Monitoring crops water needs at high spatio-temporal resolution by synergy of optical/thermal and radar observations

Abdelhakim Amazirh

THÈSE

En vue de l'obtention du
DOCTORAT DE L'UNIVERSITÉ DE TOULOUSE

Délivré par l'Université Toulouse 3 - Paul Sabatier
Cotutelle internationale : Université Cadi Ayyad

Présentée et soutenue par
Abdelhakim AMAZIRH

Le 15 juillet 2019

Monitoring crops water needs at high spatio-temporal resolution by synergy of optical / thermal and radar observations

Ecole doctorale : **SDU2E - Sciences de l'Univers, de l'Environnement et de l'Espace**

Spécialité : **Surfaces et interfaces continentales, Hydrologie**

Unité de recherche :

CESBIO - Centre d'Etudes Spatiales de la Biosphère

Thèse dirigée par
Abdelghani CHEHBOUNI et Salah ER-RAKI

Jury

Said Khabba	Proffeseur d'Univésité UCAM, Maroc	Président
Nicolas Baghdadi	Directeur de Recherche IRSTEA, France	Rapporteur
Dominique Courault	Directeur de Recherche INRA, France	Rapporteure
Abdelghani Chehbouni	Directeur de Recherche IRD, France	Directeur de thèse
Salah Er-Raki	Proffeseur d'Univésité UCAM, Maroc	Co-Directeur de thèse
Olivier Merlin	Chargé de Recherche CNRS, France	Co-Directeur de thèse
Maria José Escorihuela	Ingénieur R & D isardSAT, Espagne	Examinateur

FICHE PRÉSENTATIVE DE LA THÈSE

Nom et Prénom de l'auteur: **Amazirh Abdelhakim**

Intitulé du Travail: **Suivi des besoins en eau des cultures à haute résolution spatio- temporelle par synergie des observations optique/thermique et radar**.

Directeurs de Thèse:

- **Pr. Er-Raki Salah**, Professeur d'Enseignement Supérieur, Habilité
  Laboratoire de Procédés, Métrologie et des Matériaux pour l'Energie et l'Environnement, Département de Physique Appliquée, Faculté des Sciences et Techniques Guéliz-Marrakech (FST), Université Cadi Ayyad (UCAM)
- **DR. Chehbouni Abdelghani,** Directeur de Recherche (IRD)
  Centre d'Étude Spatiales de la BIOsphère (CESBIO)
  Université Toulouse III Paul Sabatier (UPS)

Coencadrants:

- **CR. Merlin Olivier**, Chargé de recherche (CNRS),
  Centre d'Études Spatiales de la Biosphère (CESBIO), France.
  Université Toulouse III - Paul Sabatier

Lieux de réalisation des travaux (laboratoires, institution,...) :

- Laboratoire Mixte International " Télédétection et Ressources en Eau en Méditerranée semi-Aride » (LMI-TREMA). Center Jaber, Faculté des Sciences Semlalia, Université Cadi Ayyad, Marrakech. « https://www.lmi-trema.ma/».
- Laboratoire de Procédés, Métrologie et des Matériaux pour l'Energie et l'Environnement, Département de Physique Appliquée, Faculté des Sciences et Techniques Guéliz-Marrakech (FST), Université Cadi Ayyad (UCAM)
- Centre d'Études Spatiales de la Biosphère (CESBIO), France. Université Toulouse III - Paul Sabatier
- isardSAT, Parc Tecnològic Barcelona Activa, Carrer de Marie Curie, 8, 08042 Barcelona, Spain
- LabFerrer, Centro de asesoria Dr Ferrer, Cervera, Spain

Rapporteurs autres que l'encadrant (nom, prénom, grade, laboratoire, institution) :

- **DR. Nicolas Baghdadi**, Institut national de recherche en sciences et technologies pour l'environnement et l'agriculture (IRSTEA), Antony, IRSTEA.
- **DR. Dominique Courault**, Institut national de la recherche agronomique (INRA), Avignon.
- **PR. Anas Emran**, Institut Scientifique GEOTEL, Université Mohammed V-Agdal Département de Télédétection, Rabat.

Cadres de Coopération (ou de soutien) :

- Bourse d'excellence de recherche accordée par le CNRST « Centre National pour la Recherche Scientifique et Technique »
- Projet Horizon 2020 REC "Root zone soil moisture Estimates at the daily and agricultural parcel scales for Crop irrigation management and water use impact: a multi-sensor remote sensing approach".
- Projet ANR MixMOD-E "Régionalisation et suivi multi-échelle de l'évaporation du sol à partir des

données actuellement disponibles et d'une approche de modélisation mixte"

- Projet AMETHYST ANR/TRANSMED, ANR-12-TMED-0006
- Laboratoire Mixte International LMI-TREMA

Ce travail a donné lieu aux résultats suivants (publications, communications,…) :

<u>Articles dans des revues internationales à comité de lecture</u>

- Article 1: **A. Amazirh**, O. Merlin, S. Er-Raki. 2019: Including Sentinel-1 radar data to improve the disaggregation of MODIS land surface temperature data ISPRS Journal of Photogrammetry and Remote Sensing, 150, pp.11-26, https://doi.org/10.1016/j.isprsjprs.2019.02.004.
- Article 2: **A. Amazirh**, S. Er-Raki, A. Chehbouni, V. Rivalland, A. Diarra, S. Khabba, J. Ezzahar, O. Merlin: "Modified Penman–Monteith equation for monitoring evapotranspiration of wheat crop: Relationship between the surface resistance and remotely sensed stress index", Biosystems Engineering, Volume 164, 2017, Pages 68-84, ISSN 1537-5110, https://doi.org/10.1016/j.biosystemseng.2017.09.015.
- Article 3: **A. Amazirh**, O. Merlin, S. Er-Raki, Q. Gao, V. Rivalland, Y. Malbeteau, S. Khabba, M. José Escorihuela, "Retrieving surface soil moisture at high spatio-temporal resolution from a synergy between Sentinel-1 radar and Landsat thermal data: A study case over bare soil", Remote Sensing of Environment, Volume 211, 2018, Pages 321-337, ISSN 0034-4257, https://doi.org/10.1016/j.rse.2018.04.013.
- Article 4: S. Er-Raki, **A. Amazirh**, A. Ayyoub S. Khabba, O. Merlin, J. Ezzahar and G. Chehbouni. "Integrating Thermal Surface Temperature into PenmanMonteith Model for estimating evapotranspiration and crop water stress of orange orchard in semi-arid region". April 2018; Acta horticulturae; 1197:89-96; DOI: 10.17660/ActaHortic.2018.1197.12.
- Article 5: O. Merlin, L. Olivera-Guerra, B. Aït Hssaine, **A. Amazirh**, Z. Rafi, J. Ezzahar, P. Gentine, S. Khabba, S. Gascoin, S. Er-Raki, "A phenomenological model of soil evaporative efficiency using surface soil moisture and temperature data", Agricultural and Forest Meteorology, Volumes 256–257, 2018, Pages 501-515, ISSN 0168-1923, https://doi.org/10.1016/j.agrformet.2018.04.010.
- Article 6: O. Ali Eweys, M. J. Escorihuela, J. M. Villar, S. Er-Raki, **A. Amazirh**, L. E. Olivera-Guerra, L. Jarlan, S. Khabba, O. Merlin: Disaggregation of SMOS Soil Moisture to 100 m Resolution Using MODIS Optical/Thermal and Sentinel-1 Radar Data: Evaluation over a Bare Soil Site in Morocco. 1155 (2017). Remote Sens. 2017, 9(11), 1155; doi: 10.3390/rs9111155.
- Article 7: O. Merlin., L. Olivera-Guerra., B. Aït Hssaine., **A. Amazirh**., Y. Malbéteau., V. Stefan.,B. Molero., Z. Rafi., M.J. Escorihuela., J. Ezzahar., S. Khabba., J. Walker., Y. Kerr., S. Er-Raki and V. Simonneaux. Evaporation-based disaggregation of surface soil moisture data: the DISPATCH method, the CATDS product and on-going research, IGARSS 2017. DOI: 10.1109/IGARSS.2017.8127504.
- Article 8: O. Merlin, V. Stefan, **A. Amazirh**, A. Chanzy, E. Ceschia, S. Er-Raki, P. Gentine, T. Tallec, J. Ezzahar, S. Bircher, J. Beringer, S. Khabba: Modeling soil evaporation efficiency in a range of soil and atmospheric conditions using a meta-analysis approach. Water Resources Research, 2016, doi: 10.1002/2015WR018233.
- Article 9: Z. Rafi, O. Merlin, V. Le Dantec, S. Khabba, P. Mordelet, S. Er-Raki, **A. Amazirh,** L. Olivera-Guerra, B. Aït Hssaine, V. Simonneaux, J. Ezzahar, F. Ferrer. 2019. Partitioning

evapotranspiration of drip-1 irrigated wheat crop: Intercomparing eddy covariance-, sap flow-, lysimeter- and FAO-based methods *Agricultural and Forest Meteorology*, **265, 310-326**, https://doi.org/10.1016/j.agrformet.2018.11.031.

- Article 10: N., Ojha; O., Merlin, L., Olivera-Guerra, G., Indrio; B., Ait Hssaine, **A., Amazirh**, C., Suere, A., Al Bitar; B., Molero; M., Jose Escorihuela; S., Er-Raki. Stepwise Disaggregation of SMAP Soil Moisture at 100 m Resolution Using Landsat-7 / 8 Data and a Varying Intermediate Resolution. Remote Sensing 11, 1–23. doi:10.3390/rs11161863

Communications dans des colloques nationaux et internationaux

- **A. Amazirh**, S. Er-Raki, G. Chehbouni, V. Rivalland, A. Diarra, S. Khabba, J. Ezzahar, O. Merlin. *Enhancement of Penman-Monteith equation for monitoring evapotranspiration: relationship between the surface resistance and remotely sensed stress index in semi-arid region,* Remote Sensing and Hydrology Symposium (RSHS), 8-10 May 2018, Cordoba-Spain.

- **A. Amazirh**, O. Merlin, S. Er-Raki, V. Rivalland and S. Khabba. *Disaggregation of MODIS land surface temperature to Landsat spatial resolution using high-resolution Sentinel-2 optical and Sentinel-1 radar data*. Remote Sensing and Hydrology Symposium (RSHS), 8-10 May 2018, Cordoba-Spain.

- **A. Amazirh**, O. Merlin, S. Er-Raki, V. Rivalland and S. Khabba. Disaggregation of MODIS land surface temperature using Sentinel-1 radar and Sentinel-2 optical data over an irrigated crop area: European Geophysical Union international conference (EGU), 08 - 13 April 2018, Vienne, Austria.

- **A. Amazirh**, S. Er-Raki, O. Merlin, V. Rivalland, A. Diarra , S. Khabba, A. Chehbouni. Monitoring the evapotranspiration of wheat crops using a modified Penman-Monteith equation and Landsat-derived stress index. Communication in 5th International Symposium Recent Advances in Quantitative Remote Sensing Torrent (RAQRS, Valencia), Spain, 18 to 22 September 2017.

- **A. Amazirh**, S. Er-Raki, O. Merlin, S. Khabba. Monitoring the root-zone soil moisture using remote sensing. GTWlll 'International Conference on Geospatial Technologies for Water Resources (labeled COP22)', Marrakech/Maroc, Novembre 10 - 12, 2016.

- **A. Amazirh**, O. Merlin, S. Er-Raki, S. Khabba, L. Olivera and C. Mattar, 2016. Modelling root-zone soil moisture from observed and simulated surface fluxes. International Conference on Water, Energy & Climate Change WECC, Marrakech, June 1- 4, 2016.

- **A. Amazirh**, O. Merlin, S. Er-Raki, S. Khabba, L. Olivera and C. Mattar, 2016. Modélisation de l'humidité en zone racinaire à partir des différents flux de surface observés et simulés. Workshop AMETHYST, 11 Février 2016, Auditorium-UCAM, Marrakech, Maroc. (projet ANR).

- **A. Amazirh**, S. Er-Raki, O. Merlin Estimation de l'humidité du sol et du stress de la végétation. Approches exploitant la synergie entre télédétection visible, thermique et micro-onde. *Atelier international sur l'apport des images satellitaires Sentinel pour le* développement, les 06 - 07 mars 2018, CRTS, RABAT.

- **A. Amazirh**, O. Merlin, S. Er-Raki , Q. Gao, V. Rivalland, Y. Malbeteau, S. Khabba, M.J

Escorihuela. Surface soil moisture retrieval at high spatio-temporal resolution over bare soil from Sentinel-1 radar and Landsat thermal data European Geophysical Union international conference (EGU), 07 - 12 April 2019, Vienne, Austria.

- Er-Raki S., Ayyoub A., Khabba S., **Amazirh A**., Merlin O., Ezzahar J., Chehbouni A., 2016. Integrating Thermal Surface Temperature into Penman-Monteith Model for estimating crop water stress and evapotranspiration of an orange orchard in semi-arid region. ISHS Symposium 2016 Sensing Plant Water Status Methods and Applications in Horticultural Science, Potsdam/Berlin Germany, October 5 - 7, 2016.

- S. Er-Raki, **A. Amazirh**, Luis Olivera-Guerra, S. Khabba, O. Merlin, J. Ezzahar, V. Simonneaux, A. Chehbouni, L. Jarlan. Using the selective assimilation procedure of soil moisture data in FAO-56 model for improving evapotranspiration estimates over wheat crop in a semi-arid region. *Communication in 5th International Symposium Recent Advances in Quantitative Remote Sensing Torrent (Valencia), Spain, 18 to 22 September 2017.*

- Merlin O., Olivera-Guerra L., Aït Hssaine B., **Amazirh A.**, Malbéteau Y., Stefan V., Molero B., Rafi Z., Escorihuela M.J., Ezzahar J., Khabba S., Walker J., Kerr Y., Er-Raki S. and Simonneaux V. Evaporation-based disaggregation of surface soil moisture data: the DISPATCH method, the CATDS product and on-going research *(2017) IGARSS.*

- M. J. Escorihuela, S. Er-Raki, F. Ferrer, Q. Gao, **A. Amazirh**, O. A. Eweys, M. Fontanet, V. Stefan, Y. Malbeteau and O. Merlin, Operational high temporal and spatial resolution soil moisture by multi-sensor remote sensing approach for water resources management, *10th HyMeX Workshop, 4-7 July 2017, Barcelona, Spain.*

- M. J. Escorihuela, O. Merlin, S. Er-Raki, F. Ferrer, Q. Gao, O. A. Eweys, L. Olivera, **A. Amazirh**, B. Aithssaine, M. Fontanet, S.Khabba and M. Zribi, , Estimation of high temporal and spatial resolution Soil Moisture for crop irrigation management by muti-sensor remote sensing approach. . *Communication in 5th International Symposium Recent Advances in Quantitative Remote Sensing Torrent (Valencia), Spain, 18 to 22 September 2017.*

- **A. Amazirh**, S. Er-Raki, O. Merlin, S. Khabba, L. OliveraGuerra, C. Matta. 2019. Modelling root-zone soil moisture from observed and simulated fluxes. IX International Symposium on Irrigation of Horticultural Crops-Matera (Italy). 17 to 20 June 2019 (accepted)

- S. Er-Raki, J. Ezzahar, C. Anbari , **A. Amazirh** , B. Ait Hssaine, S. Khabba, M. Fontanet, O. Merlin. 2019 Using HYDRUS-1D for estimating evapotranspiration and soil water content of irrigated winter wheat under different water managements in semi-arid region of Morocco. IX International Symposium on Irrigation of Horticultural Crops-Matera (Italy). 17 to 20 June 2019 (accepted)

...IN MEMORY OF MY FATHER

To my lovely Mother for her love and her struggle and has made an untold number of sacrifices for the entire family, and specifically for me to continue my schooling. She is a great inspiration to me

My lovely Sister "Monya"

My Brothers (Jamal, soufian and the Twins "Amine & Khalid") ...

My Family to whom I owe a great deal

...With love and eternal appreciation...

Contents

List of Figures

List of Tables

Glossary

Symbol	Signification and units
ET	Evapotranspiration, mm
rc	Surface resistance, s m^{-1}
r*	Critical bulk resistance, s m^{-1}
R_n	The net radiation, W m^{-2}
G	Soil heat flux, W m^{-2}
H_{EC}	Sensible heat flux (eddy covariance), W m^{-2}
LE_{EC}	Latent heat flux (eddy covariance), W m^{-2}
u_a	Wind speed, m s^{-1}
R_g	Solar radiation, W m^{-2}
rh_a	Relative humidity, %
T_{air}	Air temperature, °C
σ_{pp}^0	backscatter coefficient, dB
LST_{wet}	surface temperature in wet conditions
LST_{dry}	surface temperature in dry conditions
R^2	Determination coefficient
ρ_R	Red spectral reflectance, %
ρ_{PIR}	Near infrared spectral reflectance, %
ε	Surface emissivity
k	Attenuation coefficient
Δ	Slope of the saturation vapour pressure curve at air temperature, kPa °C^{-1}
γ	Psychrometric constant, kPa °C^{-1}
ρ	Mean air density at constant pressure, kg m^{-3}
c_p	Stands for the specific heat of air, MJ kg^{-1} °C^{-1}
D	Vapour pressure deficit, kPa
e_a	Air vapour pressure, kPa
e_s	Saturated water vapour pressure, kPa
$r_{ah,}$	Aerodynamic resistance, s m^{-1}
z_r	Reference height, m
kar	Von Karman constant equal to 0.44
h_c	Canopy height, m
d	Displacement height, m
z_m	Height of the dynamic soil roughness, m
ψ_m	Atmospheric stability function
ψ_h	Sensitive heat stability function
α	Surface albedo
R_{atm}	Atmospheric longwave radiation, W m^{-2}
σ	Stephan-Boltzmann constant equal to 5.67×10^{-8}, W m^{-2} K^{-4}
ε_a	Atmospheric emissivity
Γ	Fractional empirical coefficient set to 0.4
Fc	Fraction vegetation cover
f_{gv}	Fraction of green vegetation cover
F (LST)	Cost function

Abbreviation

LST	Land Surface Temperature, °C
SM	Soil moisture, $m^3. m^3$
NSSM	near surface soil moisture, $m^3. m^3$
RZSM	root zone soil moisture, $m^3. m^3$
SMP	Soil moisture proxy
SMP_{Ts}	LST-based soil moisture proxy
$SMP_{\sigma+Ts}$	LST radar-based soil moisture proxy
$SMP_{\sigma vv}$	Radar based soil moisture proxy
SI	Stress Index
IPCC	International Panel on Climate change
NDVI	Normalized Difference Vegetation Index
LAI	Leaf Area Index
SiSPAT	Simple Soil Plant Atmosphere
ISBA	Interaction Soil-Biosphere-Atmosphere
SVAT	Soil Vegetation Atmosphere Transfer
ICARE	Interactive Canopy Radiation Exchange
CERES	Crop Environment REsource Synthesis
STICS	Simulateur multidisciplinaire pour les Cultures Standard
Aquacrop	Crop-water productivity model
SEBS	Surface energy balance model
FAO-56	Food and Agriculture Organization. No 56
PM	Penman-Monteith
SEBI	Surface Energy Balance Index
WDI	Water Deficit Index
TVI	Temperature Vegetation Index
TVDI	Temperature Vegetation Dryness Index
VTCI	Vegetation Temperature Condition Index
ET_0	Evaporative demand, mm
KH21	Krypton hygrometer
HPF01	Soil heat flux plates
CSAT3	3D sonic anemometer
EC	Eddy covariance
L7	Landsat 7
L8	Landsat 8
NASA	National Aeronautics and Space Administration
USGS	United States Geological Survey
MODTRAN	MODerate resolution atmospheric TRANsmission
RMSE	Root Mean Square Error
IPI	Irrigated Priority Index
SLC	Scan line corrector
H2020	Horizon 2020
RISE	Research and Innovation Staff Exchange
REC	Root zone soil moisture Estimates at the daily and agricultural parcel scales for Crop irrigation management – a multi-sensor remote sensing approach

ACKNOWLEDGEMENTS

ABSTRACT

Optimizing water management in agriculture is essential over semi-arid areas in order to preserve water resources which are already low and erratic due to human actions and climate change. This thesis aims to use the synergy of multispectral remote sensing observations (radar, optical and thermal data) for high spatio-temporal resolution monitoring of crops water needs. In this context, different approaches using various sensors (Landsat-7/8, Sentinel-1 and MODIS) have been developed to provide information on the crop **S**oil **M**oisture (SM) and water stress at a spatio-temporal scale relevant to irrigation management. This work fits well the REC "**R**oot zone soil moisture **E**stimates at the daily and agricultural parcel scales for **C**rop irrigation management and water use impact: a multi-sensor remote sensing approach" (http://rec.isardsat.com/) project objectives, which aim to estimate the Root Zone Soil Moisture (RZSM) for optimizing the management of irrigation water. Innovative and promising approaches are set up to estimate evapotranspiration (ET), RZSM, land surface temperature (LST) and vegetation water stress through SM indices derived from multispectral observations with high spatio-temporal resolution. The proposed methodologies rely on image-based methods, radiative transfer modelling and water and energy balance modelling and are applied in a semi-arid climate region (central Morocco). In the frame of my PhD thesis, three axes have been investigated.

In the first axis, a Landsat LST-derived RZSM index is used to estimate the ET over wheat parcels and bare soil. The ET modelling estimation is explored using a modified Penman-Monteith equation obtained by introducing a simple empirical relationship between surface resistance (r_c) and a RZSM index. The later is estimated from Landsat-derived land surface temperature (LST) combined with the LST endmembers (in wet and dry conditions) simulated by a surface energy balance model driven by meteorological forcing and Landsat-derived fractional vegetation cover. The investigated method is calibrated and validated over two wheat parcels located in the same area near Marrakech City in Morocco.

In the next axis, a method to retrieve near surface (0-5 cm) SM at high spatial and temporal resolution is developed from a synergy between radar (Sentinel-1) and thermal (Landsat) data and by using a soil energy balance model. The developed approach is validated over bare soil agricultural fields and gives an accurate estimates of near surface SM with a root mean square difference compared to *in situ* SM equal to 0.03 m^3 m^{-3}.

In the final axis a new method is developed to disaggregate the 1 km resolution MODIS LST at 100 m resolution by integrating the near surface SM derived from Sentinel-1 radar data and the optical-vegetation index derived from Landsat observations. The new algorithm including the S-1 backscatter as input to the disaggregation, produces more stable and robust results during the selected year. Where, 3.35 °C and 0.75 were the lowest RMSE and the highest correlation coefficient assessed using the new algorithm.

Keywords: remote sensing, microwave, thermal, optical, evapotranspiration, Land surface temperature, soil moisture, stress index, irrigation management, energy balance model.

RESUME

L'optimisation de la gestion de l'eau en agriculture est essentielle dans les zones semi-arides afin de préserver les ressources en eau qui sont déjà faibles et erratiques dues à des actions humaines et au changement climatique. Cette thèse vise à utiliser la synergie des observations de télédétection multispectrales (données radar, optiques et thermiques) pour un suivi à haute résolution spatio-temporelle des besoins en eau des cultures. Dans ce contexte, différentes approches utilisant divers capteurs (Landsat-7/8, Sentinel-1 et MODIS) ont été développées pour apporter une information sur l'humidité du sol (SM) et le stress hydrique des cultures à une échelle spatio-temporelle pertinente pour la gestion de l'irrigation. Ce travail va parfaitement dans le sens des objectifs du projet REC "**R**oot zone soil moisture **E**stimates at the daily and agricultural parcel scales for **C**rop irrigation management and water use impact: a multi-sensor remote sensing approach" (http://rec.isardsat.com/) qui visent à estimer l'humidité du sol dans la zone racinaire (RZSM) afin d'optimiser la gestion de l'eau d'irrigation. Des approches innovantes et prometteuses sont mises en place pour estimer l'évapotranspiration (ET), RZSM, la température de surface du sol (LST) et le stress hydrique de la végétation à travers des indices de SM dérivés des observations multispectrales à haute résolution spatio-temporelle. Les méthodologies proposées reposent sur des méthodes basées sur l'imagerie, la modélisation du transfert radiatif et la modélisation du bilan hydrique et d'énergie et sont appliquées dans une région à climat semi-aride (centre du Maroc). Dans le cadre de ma thèse, trois axes ont été explorés.

Dans le premier axe, un indice de RZSM dérivé de LST-Landsat est utilisé pour estimer l'ET sur des parcelles de blé et des sols nus. L'estimation par modélisation de ET a été explorée en utilisant l'équation de Penman-monteith modifiée obtenue en introduisant une relation empirique simple entre la résistance de surface (rc) et l'indice de RZSM. Ce dernier est estimé à partir de la température de surface (LST) dérivée de Landsat, combinée avec les températures extrêmes (en conditions humides et sèches) simulée par un modèle de bilan d'énergie de surface piloté par le forçage météorologique et la fraction de couverture végétale dérivée de Landsat. La méthode utilisée est calibrée et validée sur deux parcelles de blé situées dans la même zone près de Marrakech au Maroc.

Dans l'axe suivant, une méthode permettant de récupérer la SM de la surface (0-5 cm) à une résolution spatiale et temporelle élevée est développée à partir d'une synergie entre données radar (Sentinel-1) et thermique (Landsat) et en uttilisant un modèle de bilan d'énergie du sol. L'approche développée a été validée sur des parcelles agricoles en sol nu et elle donne une estimation précise de la SM avec une différence quadratique moyenne en comparant à la SM in situ, égale à 0,03 m^3 m^{-3}.

Dans le dernier axe, une nouvelle méthode est développée pour désagréger la MODIS LST de 1 km à 100 m de résolution en intégrant le SM proche de la surface dérivée des données radar Sentinel-1 et l'indice de végétation optique dérivé des observations Landsat. Le nouvel algorithme, qui inclut la rétrodiffusion S-1 en tant qu'entrée dans la désagrégation, produit des résultats plus stables et robustes au cours de l'année sélectionnée. Dont, 3,35 ° C était le RMSE le plus bas et 0,75 le coefficient de corrélation le plus élevé évalués en utilisant le nouvel algorithme.

Mot clés: Télédétection, micro-ondes, thermique, optique, évapotranspiration, Température de surface, humidité de sol, indices de stress, gestion de l'irrigation, modèle de bilan d'énergie.

ملخص الرسالة

يعد تحسين تدبير الموارد المائية في مجال الزراعة ضرورة قصوى خاصة في المناطق شبه القاحلة من أجل الحفاظ على موارد المياه النادرة جدا والغير منتظمة بسبب الأنشطة البشرية والتغيرات المناخية. تهدف هذه الرسالة إلى مزج عمليات الرصد عبر الاستشعار عن بعد متعددة الأطياف (البيانات الرادارية، البصرية والحرارية) للمراقبة الزمنية و المكانية عالية الدقة لمتطلبات المحاصيل للمياه. في هذا السياق، تم تطوير مناهج مختلفة تستخدم أجهزة استشعار مختلفة (Landsat-7/8، Sentinel-1 و MODIS) لتوفير معلومات عن رطوبة التربة (SM) والإجهاد المائي للمحاصيل على نطاق مكاني وزماني ذي صلة تدبير مياه الري. يناسب هذا العمل جيدًا أهداف مشروع REC (http://rec.isardsat.com) الذي يهدف إلى تقدير رطوبة التربة في منطقة الجذور(RZSM) من أجل تدبير أحسن لمياه الري. تم وضع مناهج مبتكرة واعدة لتقدير التبخر و نتح المياه (ET)، RZSM، درجة حرارة سطح التربة (LST) والإجهاد المائي للنباتات من خلال مؤشرات SM المستمدة من الملاحظات المتعددة الأطياف ذات الاستبانة المكانية والزمانية العالية. تعتمد المنهجيات المقترحة على الأساليب القائمة على الصور، نمذجة النقل الإشعاعي ونمذجة توازن الماء والطاقة في منطقة مناخية شبه قاحلة (وسط المغرب). في إطار هذه الرسالة ، تم التطرق الى ثلاثة محاور.

في المحور الأول تم استخدام مؤشر RZSM، المشتق من LST-Landsat لتقدير ET على مستوى حقل القمح والتربة العارية. تم تقدير نمذجة الـ ET باستخدام معادلة Penman-monteith المعدلة (modifiée) التي تم الحصول عليها من خلال إدخال علاقة تجريبية بسيطة بين مقاومة السطح (rc) ومؤشر RZSM. ويقدر هذا الأخير من خلال درجة حرارة السطح (LST) المستمدة من Landsat، جنبا إلى جنب مع درجات الحرارة القصوى (في الظروف الرطبة والجافة على حد سواء) التي تم محاكاتها بواسطة نموذج توازن الطاقة السطحية بقيادة تأثير الطقس ونسبة الغطاء النباتي المستمد من Landsat. تم معايرة الطريقة المستخدمة والتحقق من صحتها على مستوى حقلي قمح تقعان في نفس المنطقة بالقرب من مراكش في المغرب.

في المحور التالي، تم تطوير طريقة لاستعادة SM السطحية (0-5 سم) بدقة عالية من الناحية المكانية والزمانية عن طريق المزج بين بيانات الرادار (Sentinel-1) والبيانات الحرارية (Landsat) واستخدام نموذج توازن طاقة التربة. تم التحقق من صحة النهج المطور على قطع الأراضي الزراعية العارية ويعطي تقديرا دقيقا للرطوبة SM، بما يعادل 0.03 م 3 م - 3 (RMSE) مقارنة مع SM في الموقع.

في المحور الأخير، تم تطوير طريقة جديدة لرفع استبانة LST-MODIS من 1 كم إلى 100 متر من خلال دمج نسبة الرطوبة السطحية SM المشتقة من بيانات الرادار Sentinel-1 ومؤشر الغطاء النباتي البصري المشتق من ملاحظات Landsat. الطريقة الجديدة، التي تتضمن معامل الانتثار (rétrodiffusion) S-1 ، تنتج نتائج أكثر ثباتًا وقوة في السنة المحددة. حيث ، 3.35 درجة مئوية و 0.75 كانت أدنى RMSE وأعلى معامل الارتباط التي تم تقييمها باستخدام الطريقة الجديدة.

الكلمات المفتاح: الاستشعار عن بعد، ميكروويف، الحرارية، البصرية، التبخر و نتح المياه، درجة حرارة السطح، رطوبة التربة، مؤشرات الإجهاد، إدارة الري، نموذج توازن الطاقة.

Résumé général

Dans les décennies à venir, le changement climatique et l'évolution socio-économique exerceront probablement une pression encore plus forte sur les ressources en eau, déjà insuffisantes, dans les régions arides et semi-arides. Dans ces régions, la rareté de l'eau est l'un des principaux facteurs limitant le développement agricole. La pénurie d'eau risque d'être amplifiée dans un avenir proche sous l'effet de l'altération du cycle hydrologique, du changement climatique et de l'augmentation de la demande en eau pour l'agriculture (IPCC, 2009). La question de la disponibilité et de l'accès à l'eau est sans aucun doute l'un des problèmes majeurs auxquels l'humanité sera confrontée au cours du siècle prochain. Cependant, la répartition des ressources en eau n'est pas uniforme dans le temps et l'espace, de ce fait plus de 4 milliards de personnes vivent dans des zones de pénurie en eau. Par exemple, le bassin Méditerranéen connait aujourd'hui de fortes pressions sur ses ressources en eau qui sont sollicitées par des usages domestiques croissants, mais également par une agriculture dont les besoins en eau augmentent du fait de l'extension des surfaces et de l'intensification des modes de culture. De plus, les changements climatiques annoncés dans cette région au cours de ce siècle, avec une augmentation des températures et une probable baisse des précipitations, vont accentuer cette pression. D'ici à 2040, une majorité de ces pays seront confrontés à un stress hydrique extrêmement élevé (Gassert et al., 2013).

Des pays caractérisés par un climat semi-aride à aride, comme le Maroc, connaissent déjà des crises de l'eau qui ne cessent de s'aggraver. Ceci est dû à plusieurs facteurs qui sont liés à la fois une gestion de l'eau de perfectible et aux changements naturels "variabilité imprévisible ". Ainsi, dans ces pays, la production agricole (principalement céréalière) dépend de la fréquence des précipitations. Une légère variation des régimes pluviométriques peut avoir des conséquences dramatiques sur le rendement agricole. Par conséquent, l'irrigation soutenue est le seul moyen de garantir la production agricole et garantir la sécurité alimentaire.

La détermination des besoins en eau des cultures est nécessaire pour optimiser la gestion des volumes d'irrigation. Pour ce faire, l'une des variables les plus pertinentes est l'humidité du sol ou, Soil Moisture (SM) en anglais, parce qu'elle contrôle fortement 1) les flux du bilan hydrique des parcelles agricoles, 2) la consommation d'eau (par transpiration) et le degré de stress hydrique des plantes, 3) la répartition des précipitations entre ruissellement et infiltration, 4) les échanges thermiques et hydriques entre l'interface sol-plante-atmosphère et

5) la production végétale. Ainsi, il s'agit d'une information essentielle pour une gestion optimale de l'eau d'irrigation et la prévision des sécheresses. SM est défini comme le rapport entre le volume total d'eau du sol présent dans la zone non saturée et le volume total du sol. Ce terme est correspond alors à la quantité d'eau contenue entre les particules du sol dans la zone non saturée des surfaces, qui est généralement exprimée en unités volumétriques ($m^3.m^{-3}$ ou % vol).

Même si l'humidité du sol ne représente qu'environ 0,01 % de l'eau sur terre, elle joue un rôle important dans le cycle de l'eau. Une connaissance précise de l'évolution spatio-temporelle de la SM est un élément clé pour surveiller la croissance et le développement de la végétation. Elle représente également un indicateur d'alerte dans la détection rapide d'états d'assèchement, permettant ainsi d'optimiser l'irrigation, d'améliorer la production d'une culture. La SM est donc une variable clé, aussi bien en hydrologie qu'en agronomie. Car elle affecte non seulement l'évapotranspiration (ET) mais aussi l'aptitude des sols à stocker la chaleur, donc leur conductivité thermique. C'est donc une variable clé, qui conditionne le transfert de l'eau et de la chaleur à l'interface sol-végétation-atmosphère. En effet, une partie de l'eau contenue dans les pores du sol peut retourner vers la surface par évaporation. La végétation extrait aussi l'eau de cette zone pour sa transpiration, en réaction à l'énergie fournie par le rayonnement du soleil. Les deux processus forment ce qu'on appelle l'ET.

En agriculture, l'ET joue un rôle essentiel dans la détection de l'état hydrique des plantes, l'estimation des besoins en eau des cultures et l'optimisation de la gestion de l'irrigation. Il est donc essentiel d'obtenir des estimations précises de l'ET à l'échelle de la parcelle agricole. Pendant la première phase de croissance d'une culture, l'eau est principalement perdue par évaporation, mais une fois que la culture est bien développée et recouvre le sol, la transpiration devient le processus principal (Allen et al., 1998). Pour les cultures en végétation, l'ET est synonyme de consommation d'eau.

En plus de l'humidité de surface, une autre variable pertinente est la température de la surface du sol, ou Land Surface Temperature (LST) en anglais. La LST est une variable clé qui intervient dans les quatre termes du bilan énergétique, à savoir le rayonnement net (Rn), la conduction du sol (G), la chaleur sensible (H) et la chaleur latente (LE) que l'on nomme généralement ET. Pour atteindre l'équilibre thermodynamique, un modèle de bilan énergétique recherche la LST qui minimise la différence entre l'énergie disponible à la surface

(R_n - G) et la somme des flux turbulents (H + LE). La LST est donc une résultante des flux d'eau générés par le processus ET qui couple à la fois le bilan d'énergie au bilan hydrique.

Comme l'agriculture représente la principale pression anthropique sur les ressources en eau, toute économie de l'eau agricole aura un effet levier sur la proportion d'eau disponible pour d'autres usages. Au Maroc, l'agriculture est de loin le plus grand consommateur d'eau. En moyenne, on estime qu'environ 85% des ressources en eau mobilisées sont utilisées par l'agriculture, mais avec une efficacité inférieure à 50% (Plan Bleu, 2009). Dans ce contexte, le Plan Maroc Vert établi par le Ministère de l'Agriculture et de la Pêche s'inscrit dans une nouvelle stratégie agricole visant à faire de l'agriculture le principal moteur de croissance de l'économie nationale au cours des dix à quinze prochaines années. La stratégie consiste a planifié la conservation des ressources naturelles en vue d'assurer une agriculture durable. Pour assurer cette gestion, les décideurs doivent disposer d'observations et d'outils de modélisation adaptés aux différentes échelles spatiales et temporelles concernées, que ce soit pour l'arbitrage en temps réel entre différents usages ou pour planifier les besoins futurs, par exemple.

La région du Tensift Al Haouz (nouveau nom de la région est « Marrakech-Safi »), considérée comme un bassin versant typique du sud de la Méditerranée, est caractérisée par un climat semi-aride. Dans ces conditions, l'irrigation est inévitable pour la croissance, le développement et le rendement des cultures. En raison de la forte demande climatique, les agriculteurs ont tendance à utiliser la technique traditionnelle d'irrigation (par gravité). Cette technique consiste d'abord à capter l'eau provenant du barrage Hassan 1 par le canal de la Rocade et à desservir les sorties primaires. Ensuite, un réseau de canaux secondaires et tertiaires à ciel ouvert achemine l'eau vers les parcelles cultivées. Ce système d'irrigation utilise beaucoup d'eau, dont une grande partie est perdue par infiltration et évaporation. Pour cela, une bonne gestion de l'irrigation nécessite une quantification précise des besoins en eau des cultures qui est supposée équivalente à l'ET (Allen et al., 2011).

Donc, les informations nécessaires pour une meilleure gestion de l'irrigation dépendent de l'échelle de gestion considérée. Dans le cas de quelques parcelles cultivées, l'information clé est la consommation quotidienne des cultures, ce qui permet d'ajuster l'approvisionnement en eau si celle-ci est suffisamment disponible. Pour estimer ces besoins, les agriculteurs peuvent en principe mettre en œuvre des méthodes simples, comme la méthode FAO (Food and Agriculture Organization) (Allen et al., 1998), à condition qu'ils aient accès aux données climatiques et soient capables de quantifier la végétation présente dans leur champ. Cette

estimation des besoins en eau peut être encore améliorée si l'agriculteur dispose de mesures de l'humidité dans la zone racinaire, ou Root Zone Soil Moisture (RZSM) en anglais. Dans ce contexte local, le facteur limitant réside davantage dans la capacité à maîtriser une technique d'estimation des données nécessaires. En revanche, pour le gestionnaire régional de l'irrigation, les informations les plus révélatrices sont moins accessibles.

Car à l'échelle des secteurs irrigués, le plus important est de savoir ce qui a été consommé depuis le début d'une saison, de connaître la consommation à un moment donné ou d'estimer ce qui sera nécessaire pour compléter la saison. Comme l'eau agricole provient souvent de barrages dont la capacité d'approvisionnement est limitée, cette information sur le bilan hydrique permettrait d'optimiser la distribution pour mieux répondre aux besoins. En outre, l'eau de surface étant souvent insuffisante, l'irrigation nécessite souvent l'eau souterraine comme apport d'eau supplémentaire.

À cet effet, le bilan hydrique est donc utile aux agences de bassin pour estimer les prélèvements souterrains, pour permettre une meilleure maîtrise des eaux souterraines et pour accéder à la modélisation hydrologique globale des bassins versants. Pour répondre à ces besoins, la télédétection par satellite a montré un très fort potentiel pour la surveillance des flux et des masses d'eau pour la gestion de l'irrigation à grande échelle. C'est dans le cadre de ces besoins que le projet européen REC Horizon H2020 "Root zone soil moisture Estimates at the daily and agricultural parcel scales for Crop irrigation management and water use impact : a multi-sensor remote sensing approach" a été établi. Ce projet vise à développer un système de gestion de l'irrigation par télédétection qui permet d'améliorer la fiabilité des décisions concernant l'efficacité de l'utilisation de l'eau en agriculture. Cette thèse s'inscrit dans le cadre de ce projet et vise spécifiquement à suivre les besoins en eau des cultures à haute résolution spatio-temporelle en développant de nouvelles synergies entre les observations multispectrales (optique, thermique et radar) par télédétection.

Les données de télédétection fournies par satellite offrent la possibilité de surveiller l'état des cultures à différentes échelles spatio-temporelles. Les données micro-ondes apportent une contribution significative à l'estimation de l'état de l'eau. Dans le cas d'un sol nu, l'humidité de la surface du sol, ou Near Surface Soil Moisture(NSSM) en anglais, est la principale variable qui contrôle les propriétés électriques du sol (Hallikainen et al., 1985). La réponse électromagnétique d'une surface est liée à ses propriétés diélectriques. La NSSM est déterminée à partir de la constante diélectrique, également appelée permittivité diélectrique, en fonction de la composition du sol, de l'humidité et de la température. La NSSM est une

variable d'état qui contrôle le taux d'évaporation du sol en raison de la relation entre le potentiel hydrique et la teneur en eau. En revanche, les réflectances optiques en rouge et proche infrarouge (0,4 à 12,5 µm) ont le potentiel d'accéder aux paramètres caractérisant la végétation. Ceci est dû au fait que les feuilles vertes réfléchissent moins le rayonnement incident dans la bande rouge que dans la bande proche infrarouge, tel que rapporté dans (Guyot, 1990). La combinaison de la réflectance des données optiques (comme : Normalized difference vegetation index 'NDVI', leaf area index 'LAI', f_{gv}...) permet de distinguer les surfaces nues des surfaces couvertes par la végétation. Pour la température de surface du sol, la loi de Stefan-Boltzmann indique que la puissance émise par unité de surface d'un corps noir est directement proportionnelle à la quatrième puissance de sa température absolue. Le spectre d'émission dépend de la température et la longueur d'onde dans laquelle l'émission est maximale diminue avec la température. Ce maximum est atteint pour les longueurs d'onde comprises entre 3,5 et 15 µm, qui délimitent ainsi la plage infrarouge thermique. Dans cette plage, la température de brillance mesurée est directement liée à la température de surface par la loi de Stefan-Boltzmann. La température est obtenue en inversant la loi de Planck à partir de la luminance émise par la surface observée. La LST est potentiellement une signature de l'ET et de l'eau du sol via le bilan d'énergie. Ainsi, l'utilisation des données LST acquises dans le domaine infrarouge thermique (TIR), est un bon outil pour l'estimation de l'ET (Boulet et al., 2007; Hain et al., 2009).

Dans cette thèse de doctorat, nous nous sommes concentrés sur l'amélioration de la représentation spatio-temporelle des besoins en eau des cultures en relation avec les observations satellites disponibles. Des approches novatrices et prometteuses sont présentées pour surveiller la quantité d'eau nécessaire pour compenser la perte d'eau par évapotranspiration et assurer une croissance optimale. Les besoins en eau des cultures dépendent du climat, du type de culture et des stades phénologiques des cultures, et peuvent être assuré par les précipitations ou par l'irrigation. Dans ce travail, les approches de modélisation (désagrégation et bilan d'énergie, modélisation par imagerie et par transfert radiatif) sont développées pour répondre à la question de la gestion des ressources en eau. L'idée centrale est autour de l'estimation des indices d'humidité du sol à haute résolution spatio-temporelle pour aider à estimer le stress de la végétation, l'évapotranspiration, la température de la surface et l'humidité du sol dans une zone de climat semi-aride (Maroc central).

L'objectif de ce travail est donc de contribuer à une meilleure estimation de l'humidité de la surface (5 cm) et de l'humidité du sol en zone racinaire (RZSM) pour le suivi de l'état hydrique des cultures irriguées. Le premier axe explore l'estimation de l'ET sur des pixels mixtes de blé et de sol nu en utilisant des « proxys » de l'humidité dans la zone racinaire (RZSM) dérivé des données de la température de surface (LST) à partir des observations Landsat. Le deuxième axe traite le suivi de l'humidité superficielle du sol (NSSM) à haute résolution spatio-temporelle à partir d'une synergie entre les données thermiques (Landsat-7 et -8) et radar (Sentinel-1). Le troisième axe concerne la désagrégation des données MODIS-LST de basse résolution à haute résolution spatiale en combinant les différentes données auxiliaires disponibles à haute résolution spatio-temporelle telles que l'indice de végétation (NDVI) issues des images Sentinel-2 et un proxy de NSSM dérivé des observations radar (Sentinel-1). Les trois axes sont interconnectés étant donné que i) les données NSSM/RZSM et LST peuvent être utilisées comme données d'entrée pour l'estimation d'ET (axe 1), ii) les données radar et thermiques (LST) peuvent être utilisées conjointement pour améliorer les produits NSSM (axe 2) à haute résolution spatiale et temporelle et iii) les données radar (NSSM) aident à améliorer la résolution spatiale des données LST (axe 3).

Les approches développées au cours de cette thèse ont été testées et appliquées sur cinq sites au Maroc dans la région du Tensift qui se caractérise par un climat semi-aride. Des données climatiques, d'humidité du sol, de température de surface et de différents flux énergétiques/hydriques ont été collectés dans des parcelles sélectionnées. Certaines de ces données ont été utilisées comme données d'entrée pour les modèles utilisés dans le cadre de ce travail, tandis que d'autres, comme les mesures *in situ* recueillies pendant les campagnes terrain, ont été utilisées comme données de validation pour tester la stabilité et la robustesse des modèles utilisés.

La première zone est une zone agricole irriguée (appelée R3) connue par son hétérogénéité et occupée par différents types de cultures (luzerne, blé, olivier, orange et horticulture), où le blé est la culture dominante (50 %). L'irrigation par gravitation est le principal mode d'irrigation utilisé dans cette zone. Quatre parcelles expérimentales ont été sélectionnées sur le périmètre R3 au cours de la campagne agricole 2015/2016 : deux sont maintenus en sol nu tout au long de la campagne (3 ha de superficie pour chacune d'elle) et deux autres contenaient des cultures de blé. La deuxième zone est une zone agricole pluviale (appelée Sidi Rahal) principalement dominée par les arbres (environ 80 %) tandis que le reste de la surface est constitué de sol nu, de petites forêts et de constructions (par exemple, bâtiments et routes).

D'après l'analyse du sol (Er-Raki et al., 2007), la texture du sol est, respectivement, argileuse et sableuse dans la majorité des parcelles des régions R3 et Sidi Rahal.

Des mesures *in situ*, données météorologiques et des données satellitaires sont collectées sur les deux zones dans des conditions variables, ce qui permet de tester la stabilité des approches proposées pour estimer la NSSM, l'ET et la LST sur des caractéristiques hétérogènes et différentes du sol. Les mesures *in situ* de NSSM et les échantillons sont utilisés pour valider la NSSM simulée à haute résolution à partir des données radar et thermiques. Les données du LST servent à améliorer et à spatialiser le modèle de Penman-Monteith (P-M) pour le suivi de l'ET et du stress hydrique des cultures de blé et aussi pour valider la LST satellite. Les données météorologiques servent à forcer le modèle de bilan d'énergie (EB) pour estimer les températures extrêmes. Enfin, l'ET mesuré, par le système Eddy-covariance, est utilisé pour valider l'ET simulé par le modèle P-M.

Différentes approches et modèles sont utilisés pour estimer la SM, l'évapotranspiration et la LST. En général, les nouvelles approches proposées donnent des résultats plus précis. Que celles lorsqu'on utilise des données thermiques pour calibrer la rétrodiffusion radar afin d'estimer la SM de surface sur le sol nu, ou pour intégrer le proxy d'humidité acquis à partir des données radar combinées avec la fraction de végétation verte (f_{gv}) a fin de désagréger la température de surface à haute résolution, ou pour améliorer l'équation de P-M en intégrant le stress thermique dans la résistance de surface pour estimer l'évapotranspiration des parcelles de blé.

Le premier model est le modèle de P-M qui résulte de la combinaison de l'équation du bilan d'énergie et de l'équation du transfert de masse pour estimer l'évapotranspiration d'une surface d'eau libre. Comme l'approche de P-M a été limitée par la difficulté d'estimer la résistance de la surface (r_c) puisqu'elle dépend de plusieurs facteurs liés aux caractéristiques des cultures et aux pratiques agricoles, nous avons proposé dans cette étude de relier r_c à l'indice de stress, ou Stress Index (SI) en anglais, dérivé du LST par télédétection et d'implémenter la relation développée dans le modèle P-M. Le SI a été estimé comme étant le LST observé normalisé par le LST simulé dans des conditions entièrement humides et sèches en utilisant un modèle de bilan d'énergie de surface forcé par le les données météorologique et la fraction de végétation vertes.

L'approche a été testée sur un périmètre irrigué « R3 » de 10×10 km. La stratégie de calibration/validation est implémentée sur deux sites de culture de blé équipés d'instruments

de mesures de différents fluxes hydriques et énergétiques pendant la saison agricole (2015-2016). Les deux sites ont deux systèmes d'irrigation différents un est irrigué par gravitaire et l'autre par goutte à goutte. La résistance de surface estimée à partir des mesures de la station d'Eddy covariance est premièrement corrélée avec l'indice de stress sur le site irrigué par gravitaire (en inversant l'équation de P-M). Ensuite, cette relation a été testée sur le site irrigué par goutte à goutte en utilisant les mesures *in situ* pour simuler l'évapotranspiration de surface à l'échelle de la parcelle. Finalement, cette méthode a été testée à l'échelle spatiale en termes de flux de chaleur latente en utilisant la température Landsat et de réflectance sur les deux sites. Une cartographie de l'indice de stress et de l'évapotranspiration sur la zone R3 a également été évaluée à l'aide des données LST et NDVI dérivées de Landsat. Avant de spatialiser l'ET, une occupation de sol a été effectuée afin de distinguer entre le blé, le sol nu et les autres cultures basée sur l'évolution temporelle de NDVI entre la phase de croissance et la phase mi-saison.

La relation proposée entre r_c et SI utilisée dans le modèle P-M, permet d'estimer l'ET des cultures à l'aide de données de télédétection. De plus, les résultats obtenus en termes de détection du stress hydrique des cultures peuvent être utiles pour distinguer les zones irriguées des zones non irriguées, ce qui pourrait donner une prévision du rendement du blé basée sur l'IPI (Irrigated Priority Index) développé par Belaqziz et al (2013). Cette relation a été ensuite testée sur le site irrigué par goutte à goutte en utilisant des mesures *in situ* afin de simuler l'ET de surface. Ensuite, cette méthode a été évaluée en termes de flux de chaleur latente à l'aide des données de température et de réflectance Landsat sur les deux sites. Les valeurs de RMSE sur les sites de goutte à goutte et gravitaire sont de respectivement 13 et 12 W. m^{-2}, ce qui correspond à des erreurs relatives de 5 et 4%. Comme une telle méthode a une limite, la principale limite de cette approche étant la répétitivité temporelle des données LST, qui sont une entrée essentielle de l'équation P-M. Il est intéressant de mentionner que l'équation P-M utilisée pour estimer l'ET a été appliquée à des pixels mixtes incluant les composants sol et végétation.

Le suivi du stress du blé exige une résolution spatio-temporelle élevée des données LST. Les données Landsat sont disponibles tous les 16 jours par temps clair, sinon tous les mois ou plus. Par conséquent, des données LST avec une résolution spatio-temporelles élevées sont nécessaires. L'une des solutions pratiques pour obtenir des LST à haute résolution est la désagrégation des LST du satellite qui fournissent des LST à faible résolution spatiale, mais à

haute fréquence (par ex. MODIS, chaque jour). Il s'agit de la deuxième approche développée dans le cadre de cette thèse, qui vise à désagréger les LST de 1 km à 100 m de résolution.

Pour combler ce manque de données LST, une approche de désagrégation a été développée pour améliorer la résolution spatio-temporelle des données LST afin de surveiller efficacement l'ET à haute fréquence. Deux techniques de désagrégation sont appliquées dans ce travail en utilisant les mêmes données d'entrée dérivées des données micro-ondes (radar) et optiques (NDVI). Les méthodologies sont testées sur deux zones d'étude différentes, incluant une gamme diversité de conditions (occupation de sol, état hydrique du sol, ...). Les deux sont appelées régression multilinéaire, où MultiLinear Regression (MLR) en anglais, et transfert radiatif où Radiatif Transfert Model (RTM) en anglais. Les deux méthodologies sont basées sur une échelle invariante de la relation entre le LST et d'autres variables auxiliaires, qui sont statistiquement corrélés à la LST pixel par pixel. Dans ce travail, les méthodologies de désagrégation ont été appliquées à les températures Landsat agrégées à 1 km, comme première évaluation en minimisant les incertitudes dans la température à basse résolution et ensuite appliquées à MODIS/Terra LST comme une application en cas réel. La résolution de 100 m a été choisie comme la résolution la plus fine parce qu'il s'agit de la résolution spatiale la plus faible à laquelle toutes les données HR d'entrée sont disponibles. Les approches de désagrégation sont appliquées sur une zone semi-aride irriguée et une zone pluviale.

Les méthodes de désagrégation sont appliquées aux données MODIS-Terra LST à 1 km de résolution et leur performance est évaluée en comparant les LST désagrégées à 100 m à celles de Landsat LST dans trois cas : aucune désagrégation, désagrégation utilisant uniquement la fraction de la végétation verte f_{gv} dérivée de Landsat, désagrégation utilisant à la fois Landsat f_{gv} et le coefficient de rétrodiffusion acquis des données S-1 (σ_{vv}^0).

Les meilleurs résultats de la désagrégation sont obtenus avec le nouvel algorithme développé dans ce travail en utilisant les données MODIS-LST basées sur l'équation du modèle de transfert radiatif (RTM), comparé à la procédure basée sur une régression linéaire entre f_{gv} et LST, et également comparé à la régression multilinéaire entre f_{gv}, σ_{vv}^0 et LST. Étant donné que la zone sélectionnée présente une hétérogénéité en termes de type de végétation et d'état des eaux du sol, nous concluons que le nouvel algorithme produit des résultats plus stables et plus robustes durant l'année sélectionnée. Les meilleures valeurs du RMSE et R obtenues avec le nouvel algorithme sont 0,83 °C et 0,86, respectivement. Si on inclut f_{gv} uniquement dans la procédure de désagrégation, l'erreur quadratique moyenne du LST diminue de 4,20 à 3,60 °C

et le coefficient de corrélation moyen (R) augmente de 0,45 à 0,69 comparativement au cas non désagrégé dans R3. La nouvelle méthode, en incluant en plus la rétrodiffusion S-1 à la désagrégation, apparaît systématiquement plus précise aux dates disponibles, avec une erreur moyenne qui diminue jusqu'à 3,35 °C et la valeur moyenne de R augmente à 0,75.

Ces résultats sont encourageants et peuvent être utilisés pour renforcer et améliorer l'application de la procédure de désagrégation pour les capteurs thermiques à basse résolution. Comme Sentinel-2 (S-2) est une continuité des réflectances Landsat avec une amélioration de la résolution spatio-temporelle, l'application de l'algorithme de désagrégation à la température de MODIS en utilisant des données auxiliaires S-2 améliorera la résolution temporelle à 5 jours. Ces travaux peuvent également servir comme une base à des nouvelles missions destinées à fournir des données TIR à haute résolution spatio-temporelle (mission satellite conjointe Inde-France, TRISHNA).

L'indice de stress estimé à partir de la LST pour estimer l'évapotranspiration implique un effet combiné d'évaporation du sol qui est contrôlée par l'humidité de surface du sol et de la transpiration du blé qui est contrôlée par l'humidité en zone racinaire. Les données de la LST peuvent être divisées en deux composantes : la température du sol et la température de la végétation afin d'obtenir l'ET à l'aide du modèle à deux sources. La séparation des deux composantes nécessite toutefois des données d'humidité de surface du sol, dont nous proposons dans cette étude une approche synergique entre les données radar et thermiques pour le suivi de l'humidité sur sol nu. Pour faire la distinction entre la contribution du blé et celle du sol, nous nous sommes concentrés sur le suivi de l'humidité de surface du sol nu.

Le suivi de l'humidité à partir de données radar implique l'établissement d'une relation entre l'humidité volumétrique et le coefficient de rétrodiffusion (σ°) obtenu à partir des données radar SAR. Pour un sol nu, le signal de rétrodiffusion polarisé VV et VH dépend de la SM, de la rugosité de surface et de la configuration d'observation principalement définie par l'angle d'incidence et la fréquence des micro-ondes. Deux approches ont été utilisées, la première basée uniquement sur des données radar et la seconde basée sur une approche synergique entre les données radar et thermiques. La méthodologie est basée sur le l'efficacité d'évaporation du sol ou Soil Evaporative Efficiency (SEE) en anglais, dérivée des données thermiques pour calibrer la relation de l'humidité dérivée de la rétrodiffusion radar à l'échelle du pixel (résolution de 100 m). En pratique, la relation observée entre le coefficient de rétrodiffusion polarisé VV ou VH (pp) σ^0_{pp} et le SEE thermique a été modélisée par un

modèle de régression linéaire par morceaux. La calibration du modèle de régression linéaire par morceaux a été effectué en : 1) calculant les deux « centroïdes » des points (σ_{pp}^0, SEE) avec SEE > 0,5 et SEE <= 0,5, 2) traçant la ligne passant par les deux « centroïdes » et 3) estimant les deux points de croisement de cette ligne avec les lignes définies par SEE = 0 et SEE = 1. L'approche d'estimation a été évaluée en comparant les mesures d'humidité obtenues par télédétection à des mesures *in situ* sur deux sites expérimentaux de texture de sol contrastés (Sidi Rahal a un sol sableux tandis que le périmètre R3 a un sol argileux). La méthode synergique radar/thermique a été également comparée à une méthode classique (basée uniquement sur le radar). Pour aller plus loin, l'approche de la combinaison radar-thermique est également évaluée en termes d'estimations de l'évaporation du sol. La synergie entre les données radar et les données thermiques pourrait donc servir à la fois à améliorer le suivi de l'humidité à haute résolution spatiale et à favoriser la représentation spatiale du bilan d'énergie-eau du sol.

La polarisation VV est significativement corrélée à l'humidité de surface, en comparaison avec la polarisation VH qui est corrélée avec la végétation. L'approche d'estimation de SM par synergie radar/thermique a été testée avec la polarisation VV. Le coefficient de détermination entre la SM estimée et *in situ* est de 0,64 (Sidi Rahal) et 0,59 (R3) avec la nouvelle approche, contre 0,47 (Sidi Rahal) et 0,56 (R3) pour l'approche classique. De plus, en incluant les données thermiques, le biais entre la SM estimée et *in situ* est significativement réduit de 0,14 à 0,01 m^3. m^{-3} à Sidi Rahal et de 0,04 à 0,00 m^3. m^{-3} à R3. L'approche de la combinaison radar-thermique est également évaluée en termes d'estimations de l'évaporation du sol. On a obtenu un RMSE de 26 W. m^{-2} entre l'évaporation simulée et l'évaporation observée, en comparaison de 64 et 166 W. m^{-2} en utilisant les données thermiques seulement et les données radar seulement. Ces résultats sont très encourageants car ils ouvrent des perspectives sur des synergies entre les missions spatiales (radar et optique) et les applications (humidité de sol et bilan d'eau-énergie). Deux méthodes principales pour estimer les températures extrêmes sont utilisées dans ce travail. Le premier modèle est basé sur un modèle de bilan d'énergie forcé par les données météorologiques et le second modèle est basé sur les informations contextuelles acquises à partir des polygones LST-f_{gv}.

Dans ce travail, l'indice de stress hydrique et l'évapotranspiration ont été obtenus sur des parcelles de blé. Dans une perspective, d'autres études de calibration devraient être menées pour étudier et comprendre la variabilité des paramètres r_c en fonction des différents types de cultures et des conditions de surface. Dans ce travail, l'indice d'humidité est lié à la résistance

de surface, qui est la somme des résistances du sol et de la végétation. Par conséquent, une approche de partition devrait être établie pour quantifier avec précision le stress hydrique des cultures uniquement en éliminant explicitement les contributions du sol. Le modèle Shuttleworth-Wallace à deux sources (Shuttleworth et Wallace, 1985) pourrait être utilisé pour séparer les effets sur le sol et la végétation.

De plus, pour l'estimation de la NSSM à l'aide de données thermiques/radar, la méthodologie proposée n'a été évaluée que sur des sols nus. D'autres recherches doivent être entamées pour vérifier l'applicabilité de la méthode de calibration aux sols partiellement et/ou entièrement couverts par le couvert végétal. Une solution serait d'intégrer les données VH qui sont plus sensibles aux effets de la végétation que les données VV. En outre, pour tenir en compte des effets de végétation et de rugosité, une approche synergique pourrait être testée entre les données optiques radar, thermiques et courtes langueur d'ondes à haute résolution en bénéficiant des données optiques Sentinel-2 (S-2). Le capteur S-2 fournit des réflectances à haute résolution spatiale (20 m) et temporelle (5 jours en moyenne), ce qui permettrait potentiellement d'obtenir des indices d'humidité tous les 5 jours (ciel clair) (Gao et al., 2017; Hajj et al., 2017), ce qui est suffisant pour surveiller l'état hydrique des cultures dans le cadre de la gestion des ressources en eau. Il a été démontré que les techniques de détection des changements sont un outil prometteur pour saisir la variabilité de la SM à 100 m en utilisant une interprétation des données radar S-1 à haute fréquence de répétition en synergie avec les données optiques S-2. De plus, le satellite TRISHNA fournira des données LST avec une résolution de 50 m et une revisite de 3 à 5 jours, ce qui pourrait être une excellente occasion d'utiliser les données thermiques/optiques en synergie avec les données radar pour estimer la NSSM à haute résolution.

General Introduction

Climate change is the result of the increase in the concentration of greenhouse gases in the atmosphere. These gases are almost transparent to solar radiation but absorb infrared and radiate back to the Earth, helping maintain a favorable temperature on the earth's surface. 2018 was the fourth warmest year on record since the beginning of the industrial era (Fig. 1), while 2015 was the hottest year ever since 1880, according to NASA (US National Aeronautics and Space Administration) and NOAA (US National Oceanic and Atmospheric Administration). A statement from the Copernicus Climate Change Service of the European Center for Medium-Range Weather Forecasts, mentions that the last four years are also the highest on record.

Warming will increase evaporation and precipitation, especially in tropical and equatorial regions. Rainfall will be heavier in areas where it is abundant, while areas with low water levels will experience more severe droughts. The impacts of medium- and long-term climate change on agriculture and forestry are often difficult to analyze separately from non-climate influences related to the management of resources (Hafner, 2003). According to the IPCC (Intergovernmental Panel on Climate Change) 2009, in agriculture, there is growing evidence that processes such as changes in phenology, length of growing season and northwards shift of crops and forest species can be related to climate change.
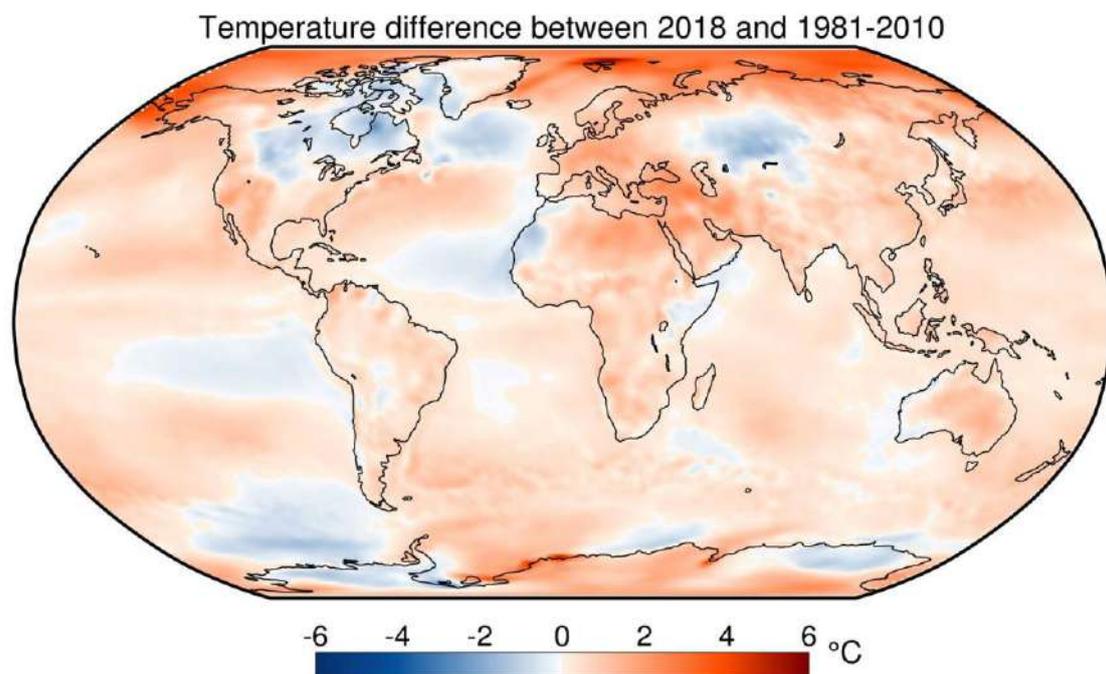
Figure 1: Temperatures anomaly between 2018 and the average 1981-2010. Source: ERA-Interim. 09-01-2019, (Credit: Copernicus Climate Change Service / ECMWF)

In the coming decades, climate change as well as socio-economic developments will likely put even greater stress on water resources, already insufficient, in arid and semi-arid regions. In these regions, water scarcity is one of the main factors limiting agricultural development. Water scarcity is likely to be exacerbated in the near future under the combined effect of the alteration of the hydrological cycle, climate change and increasing water demand for agriculture, urban and industry (IPCC, 2009).

The question of availability and access to water is undoubtedly one of the major problems that humanity will face in the coming century. Water is a vital resource for agriculture, for drinking water supply, for the health of populations, and all life on Earth depends on it. It follows a cycle which encompasses the phenomena of movement and renewal of water on the earth. In addition, water circulates constantly on Earth, undergoes changes of state and is found in the Earth's atmosphere in its three forms (liquid, gas, solid). It is anticipated that 33 countries will face extremely high water stress in 2040 (Fig. 2) especially the countries located in the Middle East.
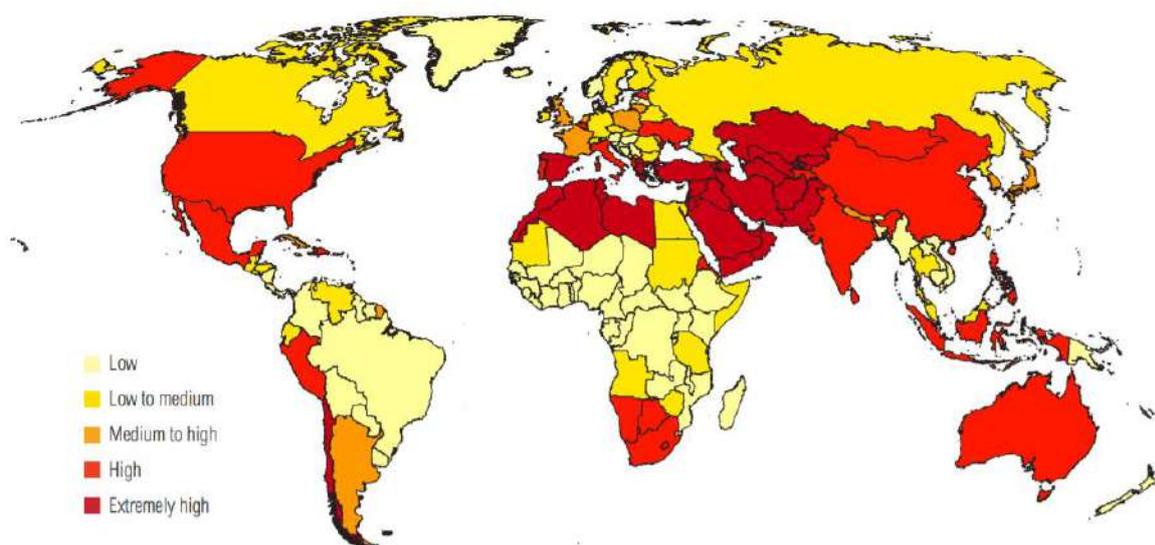
Figure 2: Ranking the world's most water-stressed countries in 2040. World resources institute. Gassert et al. (2013).

Countries characterized by an arid climate in the world, such as Morocco, are already experiencing water crises that are getting worse and worse. This is due to several factors that are linked to both human actions "water management" and climate and natural changes. Thus, in these countries, the agricultural (mainly cereal) production is dependent on the frequency of rainfall. A small variability in rainfall patterns can have dramatic consequences on agricultural yield. Consequently, irrigation is the only way to stabilize and improve production.

A calculation of crop water requirements is necessary to optimize the management of irrigation volumes. To do this, one of the most relevant variables is soil moisture (SM) because it largely controls: 1) the water balance fluxes of agricultural plots, 2) the water consumption (by transpiration) and the degree of plants water stress, 3) the distribution of precipitation between runoff and infiltration, 4) the exchanges between the surface and the atmosphere by impacting the distribution of available energy at the surface between sensible and latent heat fluxes at all spatial and temporal scales, and 5) crop production (predict quantitative and qualitative yields). In addition, it is an essential information for optimal management of irrigation water and drought forecasting. The common definition of SM is the ratio of the soil total volume of water present in the unsaturated zone to the soil total volume. This term is defined as the amount of water contained between soil particles in the unsaturated zone of continental surfaces, which is generally expressed in volumetric units ($m^3 .m^{-3}$ or % vol).

SM represents about 0.005% of the water on Earth, although so, it plays an important role in the water cycle (Fig. 3). An accurate knowledge of the spatio-temporal evolution of SM is a key element to monitor vegetation growth and development. The plant life depends on it: germination, emergence, implantation of the root system, etc. SM is a key variable in both hydrology and agronomy. It represents a fast warning indicator of the detection of dewatering stat, thus permits to optimize irrigation, to improve the production of a crop SM affects not only ET but also the ability of soils to store heat, their thermal conductivity. It is thus a key variable, which conditions the transfer of water and heat to the soil-vegetation-atmosphere interface. A part of the water contained in the soil pores can return to the atmosphere by evaporation. The vegetation also extracts water from this area for its transpiration, in response to the energy provided by the sun's radiation. Both processes form what is called evapotranspiration (ET).
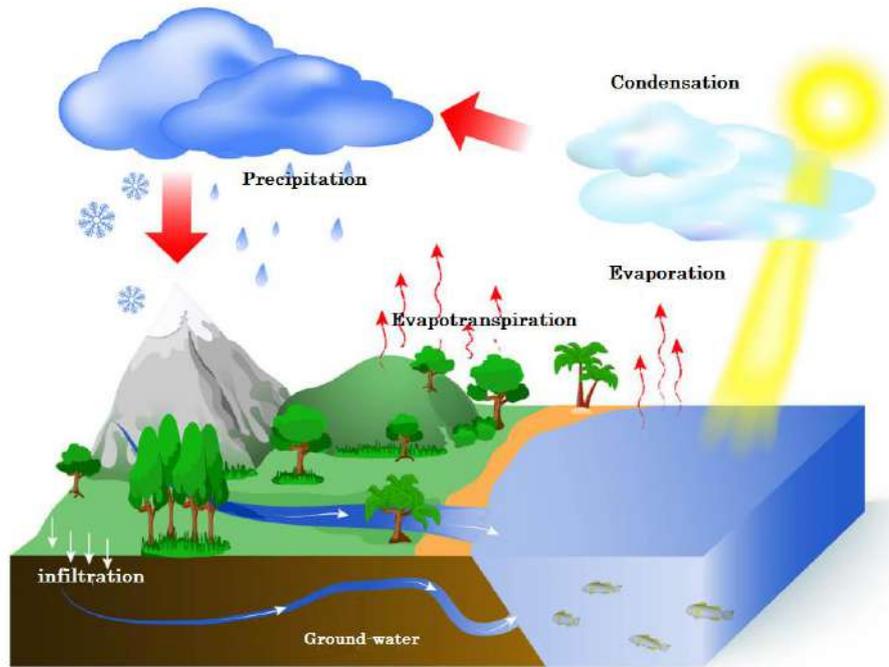
Figure 3: Illustration of the water cycle

In agriculture, ET plays an essential role for detecting plant water status, estimating crop water needs and optimizing irrigation management. Accurate estimates of ET at field scale are therefore critical. ET is the sum of soil evaporation and evaporation of the water intercepted by vegetation canopy as well as plant transpiration from the Earth's land surface to the atmosphere. During the first stage of a growing crop, water is predominantly lost by evaporation, but once the crop is well developed and covers the soil, transpiration becomes the main process (Allen et al., 1998). For vegetated land, ET is synonymous with water consumption.

Another relevant variable besides SM is the land surface temperature (LST). LST is a key parameter that intervenes in the four terms of the energy balance, namely the net radiation (Rn), ground conduction (G), sensible heat (H) and latent heat (LE) or ET. To reach the thermodynamic equilibrium, an energy balance model looks for the LST that minimizes the difference between the energy available at the surface $(R_n - G)$ and the sum of turbulent fluxes $(H + LE)$. The LST is hence a resultant of the water fluxes thought the ET process that couples both energy and water balances.

Since agriculture represents the main anthropogenic pressure on water resources, any saving made on agricultural water has an effect on the proportion of water available for other uses.

The effect is even stronger if, instead of considering water "taken", we consider water "consumed" by agriculture. However, this activity is not economical with a resource that is becoming scarce and uses up to twice as much as necessary. A rationale management of the water use actually is, in the current environmental and societal context, a major challenge. To ensure this management, decision-makers should have observations and modelling tools adapted to the different time and space scales concerned, whether for real-time arbitration between different uses or for planning future needs, for example.

In Morocco, irrigation is the biggest consumer sector of water. In average, it has been estimated that about 85% of mobilized water resources is used by agriculture with an efficiency lower than 50 % (Plan Bleu, 2009). In this context, the green Moroccan Plan established by the Ministry of Agriculture and Fishing comes as a new agriculture strategy to make agriculture the main growth engine of the national economy over the next ten to fifteen years. The strategy has planned the conservation of natural resources in view of ensuring a sustainable agriculture.

The Tensift Al Haouz region, which is considered as a typical watershed of the Southern Mediterranean, is characterized by a semi-arid climate. Under these conditions, irrigation is inevitable for crop growth, development and yield. Due to the high climatic demand, the farmers tend to use the traditional technique for (gravity) irrigation. This technique first captures water coming from the Hassan 1 dam by the "Rocade" canal (Fig. 4) and serves the primary outlets. Then, a network of secondary and tertiary open air canals convey water to the cultivated plots. This irrigation system uses a lot of water, much of it is lost through infiltration and evaporation. For that a good irrigation management requires an accurate quantification of crop water requirements which is assumed equivalent to ET (Allen et al., 2011).

Figure 4: "Rocade" canal, transporting irrigation water coming from the "Hassan 1" dam located in the neighboring catchment of Oum Erabia.

The information needed for a better irrigation management depend on the management scale considered. In case of few cultivated plots, the key information is the daily consumption of crops, which allows to adjust the water supply if water is sufficiently available. To estimate these needs, farmers can in principle implement simple methods, such as the FAO (Food and Agriculture Organization) 56 method (Allen et al., 1998), on condition that they have access to climate data and are able to quantify the vegetation present in their field. This estimate of water needs can be further improved if the farmer has root zone SM (RZSM) measurements available. In this local context, the limiting factor lies more in the ability of mastering an estimation technique of the necessary data. By contrast, for the regional irrigation manager, the more revelant information are less accessible.

At the irrigation sectors scale, the most important thing is to figure out what has been consumed since the beginning of a season, knowing the consumption at a given moment or estimating what will be necessary to complete the season. As agricultural water often comes from dams with limited supply capacity, this information on the water balance would help optimize distribution to best meet needs. In addition, as surface water is often insufficient, irrigation often requires groundwater as a supplement input water.

Closing the water balance is therefore useful for basin agencies to estimate underground withdrawals, to allow better groundwater control and to access to the global hydrological modelling of catchments. To meet these information, satellite remote sensing has shown a

very strong potential for monitoring fluxes and water masses for irrigation management at large scale. It is within the framework of these needs, that the european Horizon H2020 REC project "**R**oot zone soil moisture **E**stimates at the daily and agricultural parcel scales for **C**rop irrigation management and water use impact: a multi-sensor remote sensing approach" has been established. This project aims to develop a remote-sensing-based irrigation management system that allows for improving the reliability of decisions regarding the water use efficiency in agriculture. The irrigation management system is to be defined in accordance of user needs and requirements (Fig. 5). My thesis is a part of this project and specifically aims to monitor crops water needs at high spatio-temporal resolution by developing new synergies between multispectral (optical, thermal and radar) remotely sensed observations.
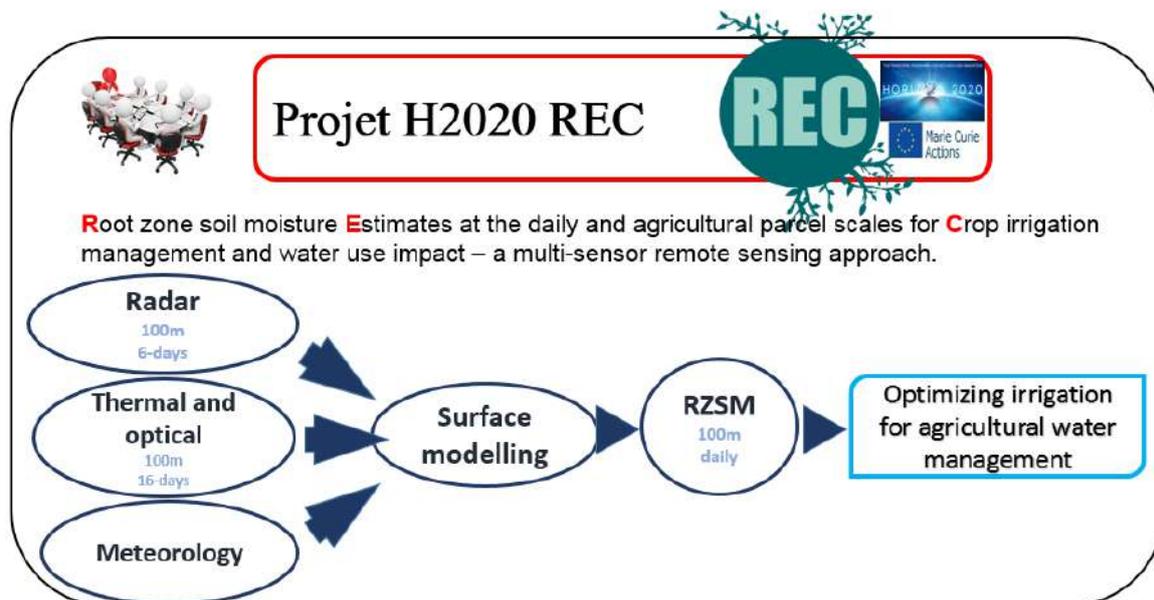
Figure 5: REC methodological approach to reach project objectives. (http://rec.isardsat.com)

The diagram in Fig. 6 illustrates the relationship between the variables discussed during my thesis: NSSM, LST and ET, as well as the potential of remote sensing to retrieve them. Remote sensing data provided by satellite, offer the possibility of monitoring the crop state at different spatio-temporal scale. Microwave data bought a significant contribution to the estimation of the water statue. In the case of a bare soil, NSSM is the main parameter of soil controlling the electrical properties of soil (Hallikainen et al., 1985). The electromagnetic response of a surface is related to its dielectric properties. The Near surface Soil Moisture (NSSM) is determined from the dielectric constant, known also as the dielectric permittivity, as a function of soil composition, moisture and temperature. The NSSM is a state variable that control the soil evaporation rate due to the relationship between water potential and water content. By contrast, Optical reflectances in red and near infrared (0.4 to 12.5 μm) have the

potential to access the parameters characterizing the vegetation. This due to the fact that green leaves reflect less incident radiation in the red band than in the near infrared band as reported in (Guyot, 1990). The reflectance combination of optical data (i.e. NDVI, LAI, Fc …) helps to distinguish between bare and vegetated surface, wich means partitioning soil evaporation and plant transpiration. The Stefan-Boltzmann Law indicates that the power emitted per unit area of the surface of a blackbody is directly proportional to the fourth power of its absolute temperature. The emission spectrum depends on the temperature and the wavelength in which the emission is maximum decreases with the temperature. This maximum is reached for wavelengths between 3.5 and 15 μm, which thus delimit the thermal infrared range. In this range the measured brightness temperature is directly related to the surface temperature by the Stefan-Boltzmann Law. The temperature is obtained by inverting the Planck's law from the luminance emitted by the observed surface. The LST is a potentially a signature of both ET and soil water availability via the energy balance. Thus, the use of LST data acquired in the TIR domain is a good tool of estimating ET (Boulet et al., 2007; Hain et al., 2009).
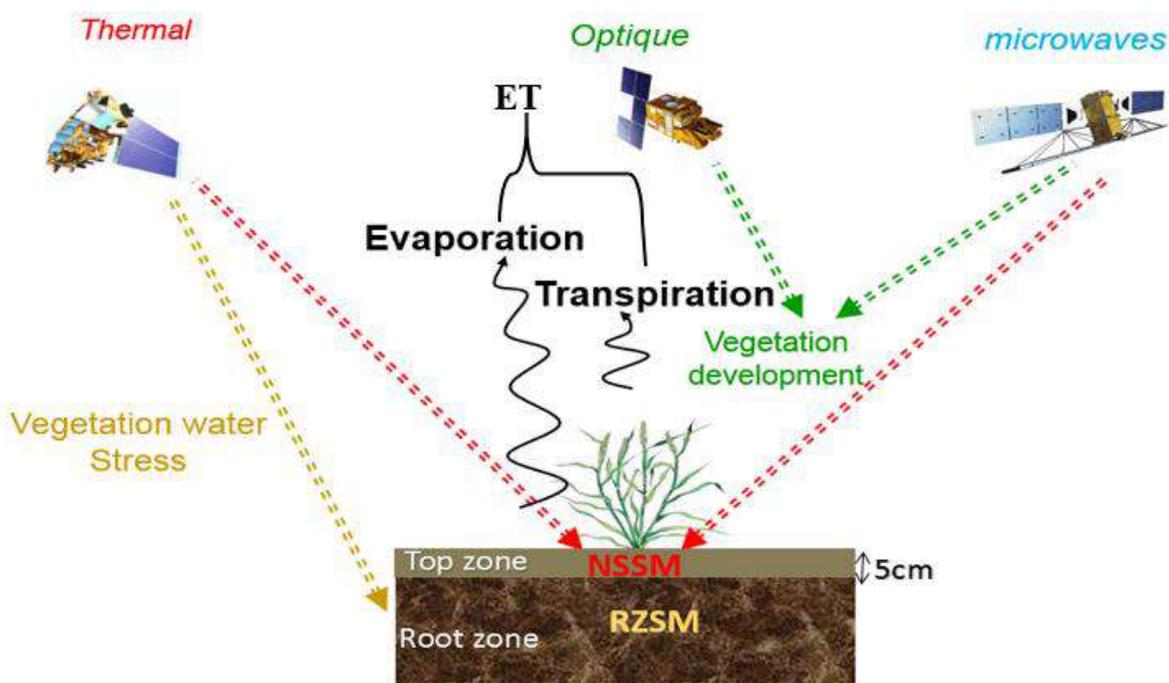
Figure 6: The ability of multi-spectral remote sensing data to characterize the soil and vegetation state and fluxes using SM as a central control variable

The objective of this work is hence to contribute to a better representation of the near surface (5 cm) soil moisture (NSSM) and the root zone soil moisture (RZSM) for monitoring the water status of irrigated crops. The three axes developed in my PhD thesis are outlined in Fig. 7. The first axis explores the estimation of ET over mixed wheat and bare soil pixels using a

RZSM index derived from (Landsat) LST data. The second axis deals with the retrieval of NSSM data at high spatio-temporal resolution from a synergy between (Landsat-7 and -8) thermal data and (Sentinel-1) radar observations. Although this approach is demonstrated over bare soil agricultural fields, its potential over vegetated pixels is discussed for further developments. The third axis involves the disaggregation of the kilometric resolution MODIS LST data using ancillary data available at high spatio-temporal resolution such as the vegetation index (NDVI) and a NSSM proxy derived from radar observations.
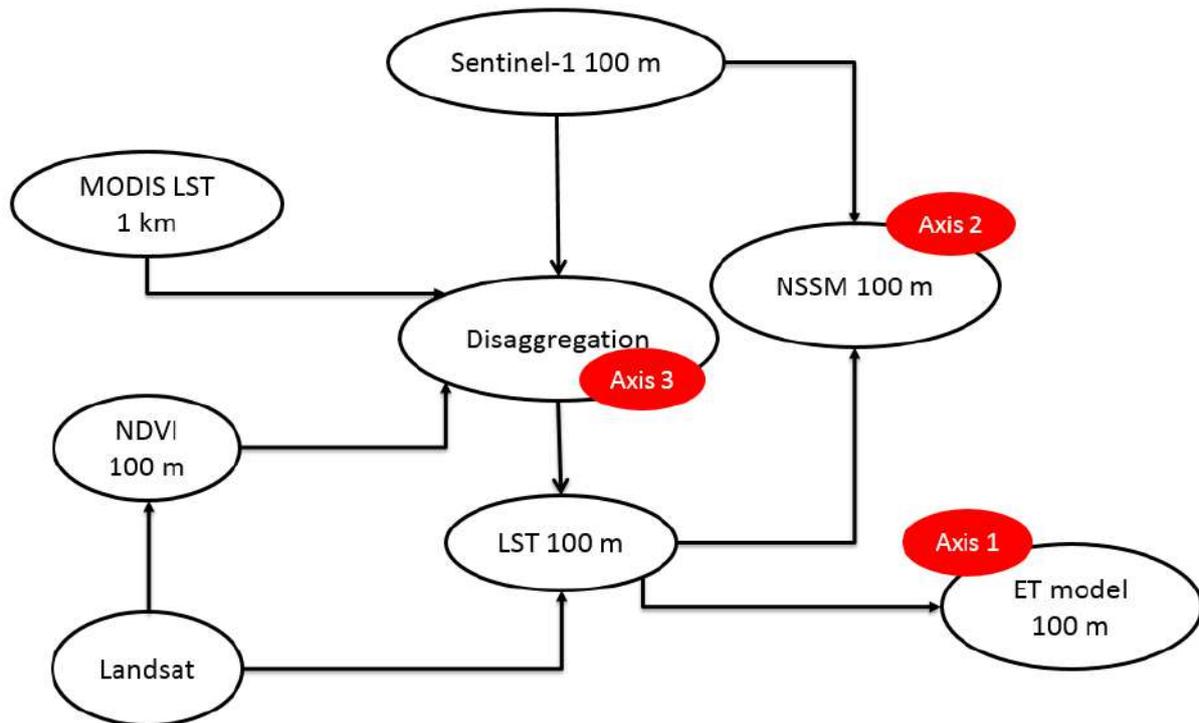
Figure 7: The three axes developed in this PhD thesis

All three axis are interconnected given that i) both NSSM and LST data can be used as input to ET models (axis 1), ii) radar (NSSM) and themal (LST) data can be used jointly to improve high spatio-temporal resolution NSSM products (axis 2), and iii) radar (NSSM) data help improve the spatial resolution of MODIS-LST data (axis 3).

This manuscript is organized in four chapters:

The first chapter "Bibliographic synthesis" presents a bibliographic survey allowing general concepts to be reviewed concerning: SM indexes derived from multispectral remote sensing data; remote sensing-based modelling approaches of ET.

The second chapter "Data & study sites description" presents the general framework of the study area (location, climate, rainfall, energy fluxes, and water and soil resources) as well as spatial and experimental databases characterizing soil surface conditions. In addition, a presentation of the remote sensing data used as well as the preprocessing satellite data steps are provided.

The third chapter "Models & methods" presents in detail methodological and analytical approaches chosen to retrieve i) NSSM ii) LST and iii) ET as well as the SM index used in each model.

The last chapter "Results and discussions" presents the obtained results of the new models used to estimate NSSM, LST and ET. An evaluation of these developed models by comparing them against in-situ measurements. A discussion of the results has been also presented by comparing the new developed models with classical ones. The obtained results and its discussion were the subject of three publications (see Appendix A). This chapter is followed by a "Conclusions and Perspectives" which presents the strengths and limitations of the key findings of this work and the methodological and operational perspectives.

Chapter I Bibliographic synthesis

Contents

_____

_____

I.1   Introduction

In this section we provide a bibliographical synthesis of the measurement and modelling methods of SM, LST and ET. A particular focus is given on the methods based on multi-spectral remote sensing data.

Remote sensing is defined as the collection of information about a given object from distance without being into physical contact with it. In spatial remote sensing, we measure the electromagnetic radiation emitted and / or reflected by the Earth's surface which is assimilated to a gray body (Gruhier, 2010).

When we want to observe a bio-geophysical variable on the surface, we must first choose a judicious frequency of observation. Indeed, the electromagnetic spectrum offers a wide range of frequencies, but not all frequencies are relevant for the observation of the surface. In certain frequencies, the atmosphere acts as a filter and blocks the natural emission of the earth at these frequencies. There are, however, a few frequency ranges to observe the earth:

- The visible (390 nm-750 nm): in a clear day when there is no cloud, it is possible to acquire information in this range that corresponds to the light visible by the human eye.
- The Near infrared (850-1050 nm): liquid water and water vapour absorption bands are sufficietly seperated to be distinguishable.
- The Short-wave infrared (1330-2400 nm): region carrying information on organic matter, soil and leaf composition.
- The thermal infrared (7 μm-25 μm): day and night, you can have the information on the detected object, because the radiation in this zone corresponds to the observed body temperature.
- The microwaves (1 mm – 1 m): observations acquired in low microwave frequencies are not affected by clouds. Information is available day and night.

I.2   Soil moisture

SM data can be acquired in two different ways: using in-situ measurements (see Table I.1) or by remote sensing methods. Each of these methods has both advantages and disadvantages. These methods are based on the amount of water in the soil or the energy status of water in the soil via the potential of water in the soil. The different approaches to measure SM, are detailed in the following.

Table I.1: Methods for measuring SM.

Method	physical basics	Utilisation
Gravimetry	weighing	Reference, destruction, labour- work
Neutron probe	nuclear method	Semi automatable, problem of radioactive sources, measurement volume = 20 cm
Capacitive probe	dielectric method	automatable, low measurement volume (1-2 cm)
TDR	dielectric method	Automatable, fast measurement, measurement volume =10 cm
Tensiometer	Measuring water potential	Most used method, measuring range 0-100 KPa
Psychrometer	Water pressure measurement in the vapor phase	Less accurate in wet conditions

I.2.1   In situ measurements

There are many methods for measuring SM (Robock et al., 2000; Walker et al., 2004). The main traditional methods are detailed below.

- *Gravimetric method*

The gravimetric method is the only one that can measure SM directly (Robock et al., 2000). It consists of taking a soil samples and you putting them in a cylinder of a known weight and volume, weighing them and then drying them by placing them in an oven at a temperature of 105 °C until the weight is constant, usually after 48 hours, and re-weigh a second time in order to deduce the mass moisture of each sample. The difference in mass between the two weighings corresponds to the volume of water evaporated. The knowledge of the soil apparent, which corresponds to its mass per unit volume of the dry soil in place, allows us to determine the volume water content of the system.

Despite the indispensability of this method to calibrate other measurement methods, it nevertheless has drawbacks: long to implement, does not integrate large areas, destructive of the soil, especially if we plan to realize a profile of moisture over several meters of soil.

- *Electromagnetic method*

According to (Robinson et al., 2003), at the moment, the majority of SM measurements are made using electromagnetic techniques from capacitive probes that use time or frequency domain reflectometry (TDR, FDR). A capacitive probe set up in ground, behaves like a resistance-inductance-capacitance (RLC) circuit whose resonance frequency can be

determined, which permits to calculate the capacitance (C) and to deduce the soil relative permittivity (ε_r). This method allows to have SM measurements over a long time period with high temporal resolution. In addition, the acquisition of these data can be automated thanks to a data-logger. The electromagnetic techniques are non-destructive, non-radioactive and non-expensive (depends on the measurement number).

The knowledge of the soil relative permittivity variation makes it possible to know the soil volume moisture using a relation SM $f(\varepsilon_r)$. This relation varies from one soil type to another.

It is therefore necessary to calibrate, using the gravimetric measurements, the measurements for each soil type in order to match the measurement (in mV) with actual SM. The accuracy is about 2% of SM volume. Those moisture probes provide only punctual spatially measurements. The *in situ* SM data used throughout this manuscript comes from the TDR and Theta-Prob (measures the dielectric constant of soil) sensors calibrated using the gravimetric technique for each field.

The TDR method is based on the fact that water has a dielectric constant (= 80) much higher than that of air and minerals (air = 1 and 2 <mineral <7). TDR measurements are based on the propagation of an electromagnetic wave. It involves measuring the propagation time of an electromagnetic wave before reflection at the end of a waveguide installed in the ground, generally consisting of a set of 2 to 4 parallel metallic needles. The propagation time permits to calculate its velocity (v) which is related to the real and imaginary parts of the relative permittivity of the ground.

Thetaprobe measures the volumetric water content of soils. A high frequency wave (100 MHz) is applied along the electrodes. The difference between the emitted and the reflected wave by the ground is a function of the dielectric properties of the surface, and therefore of the water content.

- *Neutronic method*

It is one of the easiest method to use and gives accurate measurements in real time despite the need of precautions of handling (Hillel, 1998). The operating principle is based on measuring the amount of slow neutrons reflected in a volume of soil surrounding the radioactive source. The fast neutrons emitted by the probe are progressively slowed down by the ground. The slow neutron flux is proportional to the density of hydrogen atoms at the ground, with most of the hydrogen atoms belong to the water molecules. The relationship between the amount of neutrons detected and the water content of the soil needs to be calibrated in each experimental

situation. The volume of soil prospected by radiation (sphere of influence) is about 40 cm in radius (Daudet and Vachaud, 1977).

Conveniently, the neutron probe is placed on an aluminum tube placed in the ground. This tube, is installed once for all on a given site. A detector placed near the source counts the number of slow neutrons returning to the source. The calibration of these probes should be done for each soil type and for a period of time with different SM values. The neutronic method requires a skilled labor and precautions of handling must be taken, due to radioactive materials used. In addition, the cost of these probes is high. Note that these probes cannot be used for frequent and automatic measurements.

I.2.2   Remotely sensed approaches

At the local scale and at a given time, the SM estimation is relatively easy with the methods mentioned above. However, to have representative measurements of a large area, the procedure is already complex because it involves a dedicated sampling strategy. Among these methods is remote sensing.

I.2.2.1 Soil moisture indices

Nowadays, remote sensing provides a prevailing method and approach for monitoring the spatio-temporal variations and quantitative estimations of SM. SM is difficult to be accurately evaluated, due to its strong spatial and temporal variability, resulting primarily from the variations in soil type, local topography, and land use. Many studies have attempted to establish different methods for retrieving SM based on the relationships between the SM and satellite derived land surface parameters. When such relationships are indirect, a SM index is often derived instead of the SM in absolute value. Therefore, several factors including LST and vegetation status can be indirectly used for SM estimation. Numerous indices are detailed in the literature based on remote sensing data derived from optical, thermal and microwave bands.

Other studies have been carried out, establishing a link between SM in the soil profile and drought. To this aim different indices have been developed to quantify droughts. The most commonly used drought indices are based on precipitation measurements: the Palmer Drought Severity Index (PDSI, Palmer, 1965), the Rainfall Anomaly Index (RAI, Van Rooy, 1965), the National Rainfall Index (NRI, Gommes and Petrassi, 1994), the Standardized Precipitation Index (SPI, Guttman, 1999; Mckee et al., 1993; McKee et al., 1995). Concerning drought

indices based on SM estimations, only a limited number of studies have been made, e.g. the drought index called Soil Moisture Drought Index (SMDI, Hollinger et al., 1993).

I.2.2.1.1 Shortwave-based index

These indices are mainly based on the reflectances to estimate SM. The reflectance images are available at different resolutions which makes the reflectance domain more operational. In the near-infrared band, SM can be derived from the vegetation traits that occur under water stress. The vegetation indices are sensitive to water stress, which makes them widely used to detect the drought condition.

Among those indices, (Kogan, 1995, 1990) established the vegetation condition index (VCI) which is based on the statistical Normalized Difference Vegetation Index (NDVI) time series normalized by its maximum ($NDVI_{max}$) and minimum ($NDVI_{min}$) values. The $NDVI_{min}$ and $NDVI_{max}$ are estimated are estimated on NDVI large time series's. The VCI index was used as a drought index. This index has the potential to remove the influences of weather and geographic location unlikely to NDVI. VCI is estimated as:

$$VCI = \frac{NDVI - NDVI_{min}}{NDVI_{max} - NDVI_{min}} \qquad (I.1)$$

Some research evidenced that the shortwave infrared (SWIR) region could provide better results in order to detect soil water content. Gao, (1996) proposed a Normalized Difference Water Index (NDWI, Eq. I.2) using the reflectance at 1.24 μm and 0.86 μm. The NDWI is derived from the near infrared (NIR) water absorption bands. A low NDWI value indicates canopy water stress, dry vegetation and/or bare soil (both dry and wet). On the contrary, a high NDWI index value indicates green and healthy vegetation.

$$NDWI = \frac{\rho_{0.86\mu m} - \rho_{1.24\mu m}}{\rho_{0.86\mu m} + \rho_{1.24\mu m}} \qquad (I.2)$$

Based on the NDWI, normalized multi-band drought index (NMDI) uses the NIR centered approximately 0.86 μm channel as the reference; instead of using a single liquid water absorption channel, however, it uses the difference between two liquid SWIR water absorption channels centered at 1.64 μm and 2.13 μm as the soil and vegetation moisture sensitive band. Strong differences between two water absorption bands in response to soil and leaf water content give this combination a potential to estimate SM for both bare soil and vegetated areas. Different applications have demonstrated that NMDI has the potential to

provide a quick response to SM changes (Wang et al., 2010, 2008). The NDMI is calculated as:

$$NMDI = \frac{\rho_{0.86\mu m} - (\rho_{1.64\mu m} - \rho_{2.13\mu m})}{\rho_{0.86\mu m} + (\rho_{1.64\mu m} - \rho_{2.13\mu m})} \qquad (I.3)$$

I.2.2.1.2 Thermal-based Index

For thermal infrared wavebands, SM is derived from the parameters related to the soil thermal properties. The thermal inertia and temperature index methods are two main methods for estimating SM. Both categories are based on the surface temperature variations, which are strongly correlated with the SM. In this subsection we will present the different indices that are based on the LST variations. The LST variable is an indicator of the water stress. Over bare soil LST refers to the soil temperature while over a vegetated area LST indicates the water status of the plant: an increase in the LST (for all other parameters and forcing data remaining unchanged) is a sign that the vegetation is undergoing water stress.

McVicar et al. (1992) developed an index which they called the normalized difference temperature index (NDTI) to reflect the SM status. The index is a normalization of the LST by its endmembers:

$$NDTI = \frac{LST_{\infty} - LST}{LST_{\infty} - LST_0} \qquad (I.4)$$

The LST_{∞} and LST_0 are the LST endmembers corresponding to a surface impedance (resistance) equal to infinite and zero, respectively. The extremes of LST are obtained from a surface energy balance model at specific atmospheric forcing and surface impedance.

The NDTI index reflects accurately the spatio-temporal variation of SM by eliminating the effect of the seasonal variations of LST. The limitation of this index basically comes from the availability of the atmospheric (solar radiation, air humidity, wind speed…) and vegetation (eg. Leaf area index, LAI) data.

Alternatively, other approaches are based on the relationship between SM and ET and the available energy. High ET indicates the presence of sufficient SM which leads to a lower vegetation temperature, while a weak ET indicates a water deficit in the surface. Therefore, the ratio of actual to potential ET can be used as a proxy for crop water stress:

$$SEE = \frac{ET}{ET_p} \qquad (I.5)$$

For a specific atmospheric condition, Moran et al., (1994) proposed the crop water stress (CWSI) based on the surface energy balance model. CWSI is developed as an indicator of the SM by using the vegetation canopy temperature T_c and the air temperature T_{air}:

$$CWSI = \frac{(T_c - T_{air}) - (T_c - T_{air})_{min}}{(T_c - T_{air})_{max} - (T_c - T_{air})_{min}} \qquad (I.6)$$

where $(T_c - T_{air})_{max}$ and $(T_c - T_{air})_{min}$ are the differences between the canopy and air temperature without transpiration and at potential ET, respectively. The CWSI was established based on the single canopy energy balance model, which is less effective for early crop growth. In addition, this approach requires meteorological data and the calculation process is complex. Furthermore, the extrapolation methods used for meteorological data, which are mainly obtained from ground weather stations, have important impacts on the accuracy of the CWSI determinations.

I.2.2.1.3 Thermal/shortwave-based index

The stress index can also be computed based on a combination of thermal and reflectance data. Combining remotely sensed visible and thermal infrared data can provide more information for estimating SM than the single one. It is important to determine how to combine these methods reasonably to obtain highly accurate SM. Among such indexes, the Surface Energy Balance Index (SEBI, Menenti and Choudhury, 1993), Water Deficit Index (WDI, (Moran, 2004; Moran et al., 1994) are different expressions of the stress Factor, and have been derived from a surface energy balance model, based on the same theory as the CWSI. The WDI can be used in different surface conditions, like covered area and sparsely covered one. Relying on the surface energy balance principle, the soil adjusted vegetation index (SAVI, Huete, 1988) and the temperature difference form a trapezoidal space, and the index can be directly calculated from remotely sensed data without any on leaf and air temperature measurements.

Some index like Temperature Vegetation Index (TVI, Prihodko and Goward, 1997), Temperature Vegetation Dryness Index (TVDI, Sandholt et al., 2002) and Vegetation Temperature Condition Index (VTCI, Wan et al., 2004; Wang et al., 2004), do not rely on any parameterization of the energy balance and can thus be computed directly from remote-sensing data. The above stress index can be estimated depending on the triangle/trapezoid method. These methods are usually based on the trapezoidal or triangle shape formed between

LST and other vegetation variables, the most commonly variables representing the vegetation cover fraction are NDVI or SAVI.

VTCI is defined as a ratio of the dry to actual LST difference to the dry to wet LST temperature difference, with wet/dry LST being estimated as the minimum/maximum LST that the surface can reach for a given meteorological forcing.

$$\text{VTCI} = \frac{\text{LST}_{\text{NDVI.max}} - \text{LST}}{\text{LST}_{\text{NDVI.max}} - \text{LST}_{\text{NDVI.min}}} \qquad (\text{I.7})$$

Where $\text{LST}_{\text{NDVI.max}}$ and $\text{LST}_{\text{NDVI.min}}$ are the maximum and the minimum LST of pixels which have same NDVI value in the studied area, respectively. The both extremes temperature are estimated from the dry and the wet edge in the LST-NDVI space. The most important in the image-based method is that, the number of pixels should be sufficient to cover all conditions. In the LST-VI (vegetation index) space the conservation of energy is a key elements, the surface energy maintains balance. In the LST-VI space the wet edges represents an adequate SM and higher ET and the dry edge represents that the vegetation is subjected to water stress in which evapotranspiration reaches the minimum and the SM is minimal.

I.2.2.1.4 Microwave-based index

The above thermal- and shortwave-derived SM index has a wide coverage and a fine spatial resolutions due to the existence of space-borne satellites. The thermal-based index uses the responses of the soil energy balance to soil moisture to determine SM. By contrast, the shortwave-based indexes use characteristic changes in the soil reflectance or vegetation physiology to estimate SM. One of the drawback of these methods is the temporal resolution. The thermal/optical remote sensing SM indices can be inferred only on clear sky days. In addition, using Landsat's TIR data we will have the data at best every 16 days.

Alternatively, a microwave-based SM index could be used to estimate SM. Microwave data are not affected by clouds, which allows SM to be monitored at high frequency. However, microwave-based SM indexes are easily perturbed by vegetation and surface roughness. Considerable efforts have been made for the characterization of the spatial and temporal variability of SM over vegetated areas. Passive and active microwave-based indices are developed for monitoring SM from space.

Among the active microwave-based indices, SM can be retrieved using multi-date SAR imagery. These indexes are based on change detection techniques for multi-temporal SAR data. Shoshany et al. (2000) presented the normalized radar backscatter soil moisture index

(NBMI), which is obtained from the backscatter measurements at two different times (t$_1$ and t$_2$) over the same area.

$$\text{NBMI} = \frac{\sigma_{t1}^0 + \sigma_{t2}^0}{\sigma_{t1}^0 - \sigma_{t2}^0} \qquad\qquad\qquad (I.8)$$

The advantage of these techniques is that, the difference in backscatter between two dates can be related solely to a change in the dielectric properties of the surface i.e., the NSSM, in cases where surface roughness and vegetation remain unchanged in time.

Another SM index (Δ_{index}) has been developed by Thoma et al, (2004), based on the same assumption as NBMI, that the roughness and the vegetation remain time-invariant over the selected area. The Δ_{index} index is calculated as the difference of the wet and dry backscatter images divided by the reference dry backscatter.

$$\Delta_{index} = \left| \frac{\sigma_{wet}^0 - \sigma_{dry}^0}{\sigma_{dry}^0} \right| \qquad\qquad\qquad (I.9)$$

Where the σ_{wet}^0 and σ_{dry}^0 are the average backscatter from wet and dry soil, respectively. The extremes of backscatter in wet and dry conditions must be acquired with the same view angle and the same wavelength in order to predict SM accurately and the resulting backscatter changes between repeat passes can therefore be attributed to changes in SM.

An images-difference-based index similar to the delta index, based also on the amplitude of SAR signal was developed to reflect SM variation. Wagner et al., (1999b) proposed a SM index (m$_s$(t)) by normalizing the sigma nought values by the highest and lowest σ^0, σ_{wet}^0 and σ_{dry}^0. The method compared time series data of σ^0 with standard reference incident angle 40° of ERS Scatterometer data. $\sigma_{dry}^0(40,t)$ was founded to be affected by vegetation, and increases from winter to summer due to vegetation growth, while $\sigma_{wet}^0(40,t)$ more and less depends on vegetation status. The radar observations lie between these two extreme values and the observations can be converted meaningfully to SM values from 0 to 1 relative SM by using the saturation and wilting point SM.

$$m_s(t) = \frac{\sigma^0(40,t) - \sigma_{dry}^0(40,t)}{\sigma_{wet}^0(40,t) - \sigma_{dry}^0(40,t)} \qquad\qquad\qquad (I.10)$$

Esch et al. (2018) used the SM index (SMI) which is calculated similar to m$_s$(t) developed by Wagner et al., (1999b). The SMI is used to estimate SM for each land use group (cereals,

sugar beet, and grassland). This simple linear indexing is used, because the relationship between surface SM and radar signals is well described by linear relationships.

Passive microwave data have been also used to predict surface SM. Most passive microwave-derived indexes are based on the brightness temperature TB. Paloscia et al. (2001) used the Polarization Ratio (PR) to retrieve SM using SSM/I passive microwave data (Temimi et al., 2007). The PR index is based on the brightness temperature in both polarizations V and H.

$$PR = \frac{TB_V - TB_H}{TB_V + TB_H} \qquad\qquad (I.11)$$

The PR dynamics is mainly linked to SM but it is influenced also by vegetation water content, which affects the SM accuracy because the vegetation water content and the SM have opposite effects on the PR index. This index has been used by Paloscia and Pampaloni. (1984) to detect plant water stress from Ka band, and it has been found that the PR index is correlated to CWSI index with 90% of accuracy.

Gruhier et al. (2008) evaluated the AMSR-E volumetric SM products based on ground measurements. The T_B at horizontal and vertical polarizations were used at 6.9 and 10.7 GHz (C and X bands). They found a very low RMSE equal to 0.038 % $m^3.m^{-3}$.

Liu and Shi (2012) established a new passive Microwave Soil Moisture Index (MSMI) based on the TB difference between daytime (ascending cross) and night (descending cross). The MSMI index is similar to PR index, and is calculated as:

$$MSMI = \frac{TB_{PA} - TB_{PD}}{TB_{PA} + TB_{PD}} \qquad\qquad (I.12)$$

Where the TB_{PA} and TB_{PD} are the brightness temperature in ascending and descending pass across the equator, respectively.
The results showed that the MSMI can show the spatial and temporal changes of SM at global scale. When SM is higher, the MSMI is lower, and when SM content is lower, the MSMI is higher.

Taking the advantage of both active and passive microwave techniques that are less disturbed by weather and optical/thermal data that have the potential to remove vegetation disturbance and roughness that affect easily the radar signal, the combination of optical and thermal and microwave remote sensing may have broad application prospects. Additionally, microwave

remote sensing can obtain data all-time and all-weather, which can provide great help for SM products over long time series.

Table I.2 presents the advantages and drawbacks of the SM indices derived from different multispectral data.

Table I.2: Advantages and drawbacks of several common soil moisture indices.

	index	Equation	Advantages	Disadvantages
Optical	VCI	**I.1**	Removing weather and area effects	Vegetation effects
	NDWI	**I.2**	More sensitive to SM and insensitive to atmosphere	Limitations in vegetated areas
	NMDI	**I.3**	Quick response to SM changes	Less suitable over mixed pixel of soil and vegetation
Thermal	NDTI	**I.4**	Strongly correlated to SM Eliminating the effect of the seasonal variations of LST	Availability of the atmospheric data
	CWSI	**I.6**	highly precise in regions covered by vegetation	Requires meteorological data
Active microwave	NBMI	**I.8**	More effective as it is more robust to calibration errors	Suitable when roughness and vegetation remain time-invariant
	Δ_{index}	**I.9**	Accurate estimation of SM	Suitable when roughness and vegetation remain unchangeable
	$m_s(t)$	**I.10**	Consideration of vegetation effect	Ill posted in extreme dry and wet conditions
Passive microwave	PR	**I.11**	Assess vegetation effect and retrieve SM	Vegetation interferometry
	MSMI	**I.12**	SM variation between daytime and night	Influenced by vegetation water content

I.2.2.2 Soil moisture retrieval

Remote sensing has demonstrated a strong potential for estimating the NSSM in the first cm of soil (Bruckler et al., 1988; Du et al., 2000; Engman, 2000) while SM can be estimated using optical/thermal data (Gillies and Carlson, 1995; Sandholt et al., 2002). Several studies have generally acknowledged that microwave techniques have a higher potential for retrieving SM on a regular basis, either from active (Dubois and Engman, 1995a; Ulaby et al., 1979, 1978; Zribi et al., 2005; Zribi and Dechambre, 2003; Akbar et al., 2016; Gorrab et al., 2015;

Balenzano et al., 2011; Bousbih et al., 2018, 2017; Gherboudj et al., 2011a) or passive (Akbar et al., 2016; Sabaghy et al., 2018; van der Velde et al., 2014; Kerr et al., 2010; Entekhabi et al., 2010) sensors.

Microwave methods are based on the large difference existing in the dielectric constant between a dry soil (around 4) and that of water, which is around of 80 at microwave frequencies (Ulaby et al., 1986). Radiative transfer models have hence been developed based on the SM dielectric constant relationship (Dobson et al., 1985).

There are two types of microwave sensors, depending on their source of electromagnetic energy: active and passive sensors.

The active microwave technique has its own source of electromagnetic radiation to measure the energy that is reflected and backscattered from its origin. The sensor emits a signal, an electromagnetic wave, with known frequency and polarization towards a target. The receiver records the amount of energy reflected by the target's surface as well as its polarization and the time traveled by the wave. The amount of energy perceived by the sensor is determined by the amount of energy absorbed by the surface and how the wave is reflected. The fraction of the absorbed signal will be mainly determined by the dielectric constant which is varying according to the surface conditions and especially the soil water content.

Passive sensors measure indirectly SM, by measuring the brightness temperature (TB), which is the temperature that would have a black body if it radiated at the same energy as the gray body. TB depends on the soil dielectric properties, the vegetation water content and the soil temperature. The basis for the passive microwave remote sensing of SM is that the emissivity (ε) in the microwave domain is a function of the dielectric constant of the soil-water mixture and therefore of the SM content.

Active systems are more sensitive to the structural characteristics of the surface, such as roughness or canopy structure. The surface roughness conditions the reflection of the wave, which will be specular if the surface is perfectly smooth, or affected by a large dispersion in case of high surface roughness. Among these radars, we quote the so-called SAR radar (Synthetic Aperture Radar) which measures the backscatter coefficients σ^0 (dB) that expresses the amount of energy received by the sensor after that the electromagnetic wave has come into contact with the target. On the other hand passive systems have a stronger dynamic depending on the SM.

Microwave emission is influenced by different surface conditions (SM, surface roughness, vegetation water content) depending on the frequencies ranging from 1 to 40 GHz (see Table I.3) (Kerr, 1996). The three frequency bands (L, C and X) are monstly used for SM remote sensing. These bands do not react with the same sensitivity to changes in NSSM (Schmugge et al., 1988). The L-band (1-2 GHz) has the most interesting characteristics for detecting surface SM while minimizing disruptive effects (roughness, temperature, etc.). C-band is appropriate in areas of low arid and semi-arid vegetation cover. The Soil Moisture and Ocean Salinity (SMOS) satellite (Kerr et al., 2001) is the first satellite dedicated to the study of low frequency SM. It is a radiometer that operates at L-band (1.4 GHz). It worth to mention that, the first satellite with a special sensor microwave/imager on board was launched in 1987. They operate in Ku and Ka band with a 25 km spatial resolution.

The main objection to remote sensing of SM is that direct measurement is not just about the surface layer. For example, in the X band, the first few mm are probed. For the L-band, 4-5 cm are probed on average and it can reach up to 15 cm depending on the soil characteristics and condition (soil moisture mainly). However, since it is necessary to know the total available water in the unsaturated zone, a direct approach was considered with even lower frequencies (wavelengths of several meters) to reach deeper layers. This poses major problems in terms of spatial resolution (a few hundred km) and ionospheric effects. Thus, this option is not retained at present. To address these issues, several studies have recently demonstrated the feasibility of the disaggregation approach of SMOS SM data (Malbéteau et al., 2016; Merlin et al., 2006b; Pellenq et al., 2003).

Table I.3: Correspondence between bands, wavelengths and frequency in the microwave field.

Frequency band	Frequency range (GHz)	Wavelength range (cm)
L band	1-2	15-30
S band	2-4	7.5-15
C band	4-8	3.75-7.5
X band	8-12	2.5-3.75
Ku band	12-18	1.67-2.5
K band	18-27	1.11-1.67
Ka band	27-40	0.75-1.11

In the recent past, the use of imaging radar to estimate SM has become a subject of strong interest, notably due to i) the high-spatial resolution achievable by SAR and ii) the advent of

SAR data available at high-temporal resolution. Especially, the SAR Sentinel-1 (S1) constellation (composed of two satellites S1-A and S1-B) potentially provides SAR data at 10 m resolution every 6 days in average (Torres et al., 2012). Thus, numerous studies have investigated and exploited the sensitivity of the radar signal to SM (Baghdadi et al., 2018, 2002a, n.d.; Baghdadi and Zribi, 2006; Bousbih et al., 2017; Eweys et al., 2017a; Fung, 1994; Gao et al., 2017; Gorrab et al., 2015; Hajj et al., 2017a; Holah et al., 2005a; Oh et al., 1992; Srivastava et al., 2003; Ulaby et al., 1986; Van Oevelen and Hoekmhan, 1999; Vereecken et al., 2008; Zribi et al., 2005). Retrieval approaches can be categorized into:

i) Purely empirical modelling approaches (Baghdadi et al., 2002a; Holah et al., 2005; Mathieu et al., 2003; Wickel et al., 2001; Baghdadi et al., 2017; Sikdar and Cumming, 2004; Srinivasa Rao et al., 2013; Baghdadi et al., 2016) without any physical basis, which makes them valid for the studied area solely.

ii) Semi-empirical approaches (Attema and Ulaby, 1978; Dubois and Engman, 1995a; Oh, 2004; Oh et al., 1992; Shi et al., 1997), which usually combine empirical data fits.

iii) Theoretical (physically-based) models like integral equation model (IEM) (Fung et al., 1992). In general, each model has a certain validity range in terms of observation incidence angle, soil parameters and vegetation cover (Fung et al., 1992; Karam et al., 1992).

Models, previously mentioned, do not reach the expected accuracy in SM retrievals (Alexakis et al., 2017; Bai et al., 2017; Fieuzal et al., 2011; Gao et al., 2017; Rakotoarivony L. et al., 1996; Remond et al., 1999; Zribi et al., 1997). This is owing to the various radar (incidence angle, frequency and polarization) and surface (SM and roughness) parameters that affect the behaviour of the backscattered signal. The surface roughness is one of the most important factors that impact on the SM estimation, and probably the most difficult to measure periodically when monitoring SM changes over wide areas (Loew et al., 2006). Usually, the use of such models requires a calibration step to reduce discrepancies between simulated backscatter coefficient (or inverted SM) and reference (measured) SM. Calibration is often performed using *in situ* SM measurements (Dubois and Engman, 1995b; Oh, 2004; Oh et al., 1992). In this vein, various research studies have focused on the calibration of the IEM (Baghdadi et al., 2006, 2011, 2004, 2002b; Susaki, 2008), in which *in situ* SM measurements have been used to replace the measured correlation length by a fitting/calibration parameter (autocorrelation length and standard deviation of surface height). However, calibrating IEM over large areas is not a trivial issue due to the lack of available *in situ* measurements for all

roughness values. Because of uncertainties in the estimation of roughness parameters and thus in the modelling of soil roughness, discrepancies may remain between inverted and *in situ* SM. Regarding this point, Srivastava et al. (2009) proposed a practical methodology to decouple the effect of surface roughness in SM estimation, without any assumption or prior knowledge of surface roughness distribution, exploiting multi-incidence-angle radar data. Note that the retrieval model parameters were calibrated using SM truth measurements. This method can't be used using SAR data because they are mono-incidence.

Below we present a flowchart of the main sensors dedicated for monitoring SM (Fig. I.1).
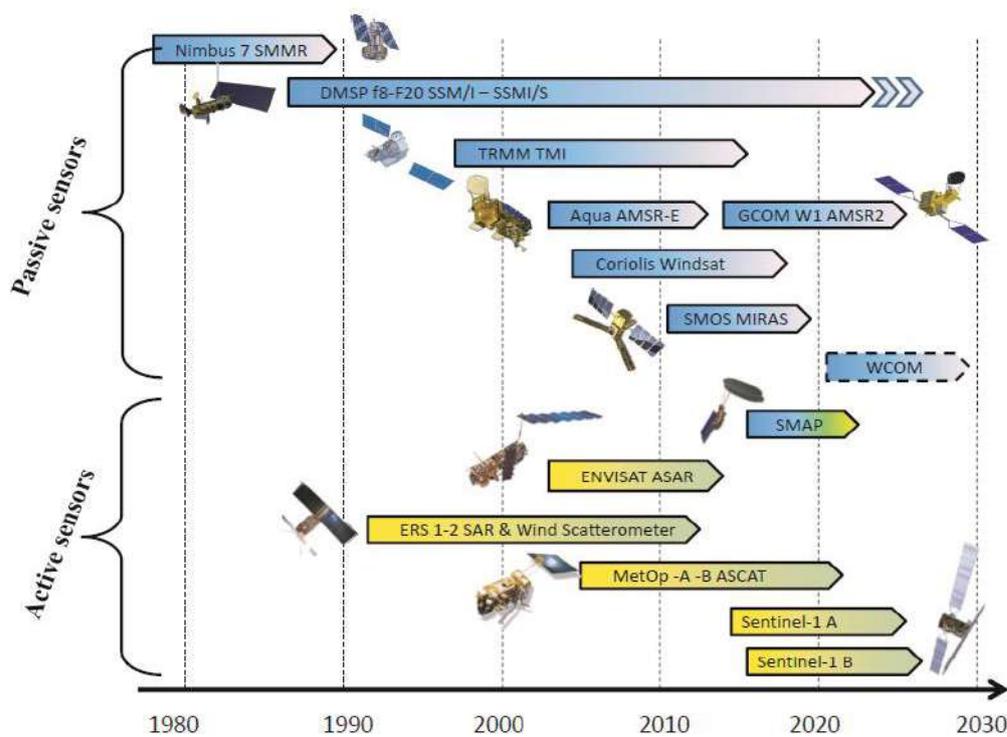
Figure I.1: Active and passive microwave sensors that have been used to retrieve SM. Source: (Malbéteau, 2016)

Alternatively to microwave approaches, thermal remote sensing has also been extensively used to monitor SM (Friedl and Davis, 1994; Gillies and Carlson, 1995; Qin et al., 2013; Schmugge, 1978) and SM-related variables such as ET (Choi et al., 2011; Desborough et al., 1996; Entekhabi et al., 1996; Verstraeten et al., 2008). The LST derived from the thermal domain, is coupled to SM via the energy balance equation when the incoming energy is not limiting. As demonstrated in Price (1990), Carlson (2007), Carlson et al. (1995), Moran et al. (1992), Smith and Choudhury (1991) and Gao et al. (2017), LST and vegetation index (VI) can provide SM information by interpreting the spatial distribution of data pixels spatial

distribution in the LST-VI feature space delimited by a triangle or a trapezoid. This has been the basis for developing thermal-derived and thermal/shortwave-based SM proxies (Sections I.2.2.1.3 and I.2.2.1.3).

A summary of the different remote sensing methods used in SM estimation is detailed in Table I.4.

Table I.4 : Remotely sensed methods for estimating SM.

Category	Methods	Advantages	Drawbacks
Optical	Visible-based methods	Good spatial resolution, mutli-bands available	Vegetation interference, night effect
	Thermal infrared-based methods	Good spatial resolution, mutli-bands available	Vegetation interference, cloudy contamination night effect and poor temporal resolution
Passive microwave	Empirical, semi-empirical, physically-based methods	High accuracy for bare soil surfaces, unlimited by clouds and/or daytime conditions, high temporal resolution	Coarse spatial resolution, influenced by vegetation cover and surface roughness
Active microwave	Empirical, semi-empirical, physically-based methods	Fine spatial resolution, unlimited by clouds and/or daytime conditions	Influenced by surface roughness & vegetation cover amount
Change detection	Image Differencing (& Ratioing)	Differences in σ^o can be related directly to soil moisture	Assumes surface roughness and vegetation remain time-invariant between dates
	Coherence	Compliments the information contained in the amplitude of σ	Several different factors contribute to the phase decorrelation of σ^o
	Principal Components Analysis (PCA)	Enhances key patterns in the data. Change can be detected in the new 'components'.	Assumes multi- temporal data are highly correlated
Synergistic methods	Optical & Thermal Infrared	High spatial resolution, simple & straightforward implementation	limited to cloud-free & daytime conditions, poor temporal resolution, low penetration depth
	Active & passive microwave (MW)	Improved temporal and spatial resolution	SM scaling & validation needs caution, different SM measurement depths
	MW & optical	Minimized vegetation and surface roughness effects	SM scaling & validation needs caution, different SM measurement depths

I.2.2.3 Soil moisture missions

Currently, the NSSM data sets available at global scale have a spatial resolution much coarser than the typical size (several ha) of fields. Especially, the SM retrieved from passive microwave observations such as C-band AMSR-E (Advanced Microwave Scanning Radiometer-EOS, Njoku et al. (2003)) and L-band SMOS data have a spatial resolution of about 60 km and 40 km, respectively. The recent SMAP (L-band, 1.4 GHz) (Soil Moisture Active and Passive, Entekhabi et al. (2010)) mission, launched in January 31, 2015, provides SM data at 10 km resolution. The spatial resolution of SM data is therefore unsuitable or even incompatible with many applications such as watershed management, flood risk prediction, irrigation management and yield prediction.

Active sensors (radars) achieve a spatial resolution much finer than that of radiometers. Sentinel-1 (Torres et al., 2012) is providing C-band SAR (Synthetic Aperture Radar) data at a spatial resolution of about 10 m with an unprecedented repeat cycle of 6 days by combining both ascending and descending overpasses combining the two available satellites (S1-A and S1-B) from 2015. The disadvantage is that there is currently no operational product for NSSM. Although radars have potential for NSSM monitoring (Balenzano et al., 2011), the impact of vegetation cover, its structure and roughness remains difficult to model at high spatial resolution over extended areas (Satalino et al., 2014). Thus, high spatial resolution radar approaches are typically based on the calibration specified for each site (Zribi et al., 2011).

Several attempts were made to improve the spatial resolution of readily available passive microwave-derived SM data using the downscaling method. DISPATCH (DISaggregation based on Physical And Theoretical scale CHange, Merlin et al., (2013, 2012b)) estimates the SM variability within a 40 km resolution SMOS (or 10 km resolution SMAP) pixel at the target 1 km resolution using MODIS data and the target 100 m resolution using Landsat data (Nitu et al. 2019; Eweys et al., 2017b; Merlin et al., 2010a, 2008b, 2008a, 2006a, 2005).

Table I.5, presents the most known spatial missions to retrieve SM based on the physical interpretation of the different variables derived from satellites. Despite the progress made to estimate SM, from physically to empirically based models, some problems have been not solved yet (Tables I.5).

Table I.5: Soil moisture mission : charactertics, advantges and drawbacks.

Sensors/ Missions	Characteristics	Advantages	Limitations
SMAP	1.41 GHz, H, V and HV or VH, Swath width: 1000 km, 3 days 1.4	High-resolution, high-accurate soil moisture, corrections for rotation	highly influenced by surface roughness, vegetation canopy structure and water content
SMOS	1.4 GHz, H and V, 3 days	Multi-angular acquisition capability, low sensitivity to cloud and vegetation contamination, high sensitivity to soil moisture fluctuation	Poor spatial resolution, highly influenced by surface roughness and vegetation cover
AMSR-E	6.6, 10.65, 18.7, 23.8, 36.5, 89GHz, H and V, Swath width: 1445 km, 2 days	Long-term observations, high revisit frequency	Coarse spatial resolution, data records overlap, small penetration depth
Sentinel-1	5.405 GHz, HH-HV and VV-VH, 6 days or less	High-accurate SM, high spatial and temporal resolution	Small penetration depth
Landsat	30 m (15 m for Band 8 of OLI), 16 days	Good spatial resolution, multi-bands available	Vegetation and cloud interference, night effects
MODIS	1000 m (250 m for panchromatic bands), 1 day	Good spatial resolution, multiple satellites available	Vegetation interference, cloudy contamination, night and atmospheric effects

I.3 Land surface temperature

Surface temperature measurement by remote sensing is indirect. A radiometer actually measures the luminance corresponding to the electromagnetic radiation emitted by a surface because of its skin temperature. Stefan-Boltzmann's law indicates that the power emitted per surface unit of a blackbody surface is directly proportional to the fourth power of its absolute temperature.

The emission spectrum depends on the temperature; the wavelength in which the emission is at its maximum decreases with the temperature. For most land surfaces, this maximum is reached for wavelengths between 3.5 and 15μm, which delimits the thermal infrared range. In this domain, we associate the luminance measured by a radiometer with an apparent temperature, we then define a spectral surface brightness temperature (K), obtained by inverting Planck's law, which amounts to considering the surface as a black body. The measured brightness temperature is directly related to the surface temperature by Stefan-Boltzmann's law:

$$T_B(\lambda) = B^{-1}(R(\lambda)) \hspace{5cm} \text{(I.13)}$$

$R(\lambda)$ is the spectral luminance measured by a radiometer near the surface and B is the luminance of the black body. This temperature thus incorporates the reflection term of atmospheric luminance by the surface assuming an emissivity equal to 1. It is therefore necessary to take into account the acquisition geometry and to make atmospheric and emissivity corrections before estimating a surface temperature that necessarily generates uncertainties.

Atmospheric corrections for space sensors have been the subject of numerous studies. For spectral measurements by spatial spectroradiometers, depending on the number of bands, we can mention the Temperature/emissivity separation (TES) algorithm (Gillespie et al., 1998) used for ASTER (Advanced Spaceborne Thermal Emission Reflection Radiometer) and MODIS, which consists of separating temperature and emissivity from spectral brightness temperatures and spectral emissivities in 3 bands at least. The "split-window" algorithms (Wan and Dozier, 1996) used with only 2 spectral bands consist in estimating the LST from the differences between the spectral measurements. This type of algorithm is used for MSG-SEVIRI for example.

I.3.1 Remote sensing approaches

Land surface temperature (LST) derived from thermal infrared remote sensing is an essential input variable for various environmental and hydro-meteorological applications. LST data are practically used for modeling the land surface processes and monitoring the functioning of agro-ecosystems (Anderson et al., 2008; Brunsell and Gillies, 2003; Karnieli et al., 2010; Kustas and Anderson, 2009; Zhang et al., 2008). Therefore, LST data have been used in a variety of applications such as, among others, climate studies (Hansen et al., 2010; Kustas and

Anderson, 2009), the monitoring of crop water consumption (Amazirh et al., 2017; Bastiaanssen et al., 1998b; Boulet et al., 2007; Er-Raki et al., 2018; Olivera-Guerra et al., 2018; Price, 1982), vegetation monitoring (Kogan, 2001; Williamson, 1988), SM estimation (Amazirh et al., 2018; Merlin et al., 2010b; Sandholt et al., 2002), hydrological studies (Crow and Wood, 2003), drought monitoring (Rhee et al., 2010), land cover monitoring (Julien and Sobrino, 2011; Karnieli et al., 2010), biodiversity studies (Albright et al., 2011), and urban heat island effects (Jin and Jin, 2012).

The LST information can be mainly acquired from TIR remote sensing, but also from passive microwave remote sensing. LST detected by IR thermal sensors provides finer spatial resolution only under clear-sky conditions. Because clouds and aerosols are essentially transparent to microwave radiation at frequencies below about 12 GHz, microwave remote sensing has the potential to eliminate the atmospheric contamination. However, passive microwave sensors have coarser spatial resolution and lower accuracy. Polar orbiting platforms such as NOAA-AVHRR, Landsat TM / ETM +, Terra / Aqua MODIS and ASTER provide images at different scales for applications in the Earth's surface processes (Zhou et al., 2012). Recently, Yu et al. (2017) specifically discussed the LST estimation progress for the NOAA JPSS and GOES-R satellite missions. While, Li and Duan (2017) discussed in general the LST estimation using remote sensing.

Spatial remote sensing offers the possibility to observe the LST in the spectral range of thermal infrared (from 8 to 14 µm) with various temporal and spatial resolutions. For example, the spatial resolution for Landsat and ASTER is about 100 m with a temporal resolution of 16 days. The MODIS sensor provides LST 4 times per day with a spatial resolution of 1 km while the sensors on the geostationary satellites (GEOS, meteosat) have the advantage of observing the LST with a temporal resolution less than 30 minutes but with a resolution of 3 to 4 km.

Large uncertainties have been detected in the current satellite LST products (Hulley and Hook, 2009; Wang et al., 2009). Taking as example, Wan (2008) reported that MODIS LST product, which is the most reliable LST product, with the accuracy of 1 K verified only for homogeneous surfaces, such as water bodies and sandy land. Wang et al. (2008) verified that the error was around -3.23°C to 0.72°C by comparing nighttime LST data with the ground TIR temperature observation of eight stations. Validation results proved that the anticipated accuracy of ASTER LST product of +1.5 K has been met (Sabol et al., 2009), under unusual

atmospheric conditions of anomalously high humidity or spatial variability, atmospheric compensation can be incomplete and errors in temperature and emissivity images can be larger than anticipated. Capelle et al. (2012) found that the standard deviation of LST from the Infrared Atmospheric Sounder Interferometer (IASI) over the tropics is about 1.3 K. As reported in (Freitas et al., 2010), the mean square error is found up to 2 K when comparing the Spinning Enhanced Visible and Infrared Imager (MSG–SEVIRI) LST product with ground measurements. Finally, the retrieval accuracy for microwave sensors is far worse than 1 K.

I.3.2   Spatio-temporal representativeness

Nowadays, there is a limitation in the existing satellite thermal sensors, since those with high revisit cycles (e.g, MODIS) do not offer high spatial resolution (HR), and those offering HR (e.g, Landsat-8) generally have low temporal resolution (Agam et al., 2007b). In contrast, the visible and near infrared (VNIR) reflectance data are available at a resolution finer than that of most thermal sensors (Ha et al., 2013). To bridge the gap, the finer-resolution VNIR data have hence been extensively used as ancillary data to disaggregate low-resolution (LR) LST at HR.

Recently, various efforts have been devoted to disaggregate LST to a finer –typically 100 m-resolution. Techniques are generally based on a relationship between LST and ancillary (vegetation cover indexes, emissivity and/or albedo) data, the obtained relationship being assumed to be scale invariant (and thus applied at both HR and LR). The statistical downscaling methods in particular, developed by Kustas et al. (2003) over a homogenous vegetated area, has been widely used. This method is based on a linear regression relationship between LST and NDVI (Normalized Difference Vegetation Index) calibrated at LR. The relation between LST and NDVI is also used in Bindhu et al. (2013), with the aim of developing a nonlinear method to estimate LST at HR. Agam et al. (2007a) used the fraction of green vegetation cover instead of NDVI. This method showed its capability and good performance over areas with relatively uniform soil and vegetation hydric status, where the temperature of bare soil is set to the average between the dry and wet soil over the studied area. Other studies reported that NDVI (or f_{gv}) shows some limitations and cannot explain all the variations in LST over agricultural areas (Agam et al., 2007b, 2007a; Inamdar and French, 2009; Merlin et al., 2010b; Olivera-Guerra et al., 2017). Especially, Agam et al. (2007b) and Merlin et al. (2010) observed a shortcoming when using the LST-NDVI or LST-f_{gv} relationship over areas with high moisture content, or with various photosynthetic activity

vegetation types. Merlin et al. (2010) adapted this method to heterogeneous vegetation status, by adding the fraction of senescent vegetation cover to include the photosynthesis activity of vegetation, and to distinguish between areas of bare soil and dry vegetation cover. Dominguez et al. (2011) integrated the surface albedo to estimate HR LST by fitting the relationship between LST, NDVI and surface albedo. Following the same idea of adding other information that affect the spatial distribution of LST, Merlin et al. (2012) used the projection technique theoretically developed in Merlin et al. (2005) that aims to strengthen the correlation between two variables (LST and NDVI) by representing the dependence of these variables on other additional variables, based on a radiative transfer equation. Moreover, other studies were further presented involving additional factors that reflect the vegetation type (Merlin et al., 2010b; Sandholt et al., 2009; Zhan et al., 2011). Sandholt et al. (2002) summarized the variables that affect LST variability, and they mentioned that, NSSM mainly controls ET and the energy balance components of the surface, which affect LST. Therefore, optimal LST disaggregation approaches should include the variability of SM in addition to NDVI (or f_{gv}), in order to represent the variability of the bare soil temperature bounded by its wet and dry endmembers. Advanced regression tools using spectral bands, have been successfully used in different studies to produce better disaggregation results than simple polynomial functions (Ghosh and Joshi, 2014)

Recently, some studies have attempted to represent the SM effect. Liu and Zhu (2012) used a NMDI for monitoring soil and vegetation moisture, based on the absorption properties of the vegetation water in the NIR and the sensitive characteristics of water absorption differences between soil and vegetation in the SWIR. However, NMDI has inconsistent relationships with vegetation and SM changes (i.e. positive correlation with vegetation water content and negative correlation with SM changes). Therefore, it poorly performed over mixed pixels of vegetation and soil. Chen et al. (2010) took into account SM variations using a soil wetness index (SWI) estimated based on the interpretation of the triangular LST–NDVI space. However, the errors were found to be larger with low fractional vegetation cover. In the same manner, Yang et al. (2010) discussed the impact of SM variations using the LST-NDVI space and assumed uniform SM conditions in a coarse pixel. Therefore this technique is only appropriate in regions where SM varies at large scale and in pixels with high f_{gv}. In general, the previously proposed proxies or indexes that aim to incorporate the SM effect on LST poorly performed over the areas with low vegetation cover.

I.4   Evapotranspiration

SM is extremely rich in information on surface states, and it is linked to ET. With decreasing SM content, the soil suction increases and the remaining SM becomes less accessible for uptake by plant roots, and ET might thus become reduced.

The ET is a process located at the interface between the water cycle, the carbon cycle, and the energy exchanges at the surface (Fig. I.2). The observation of the terrestrial surface by satellite helps access the variables characterizing each of these domains of interaction.
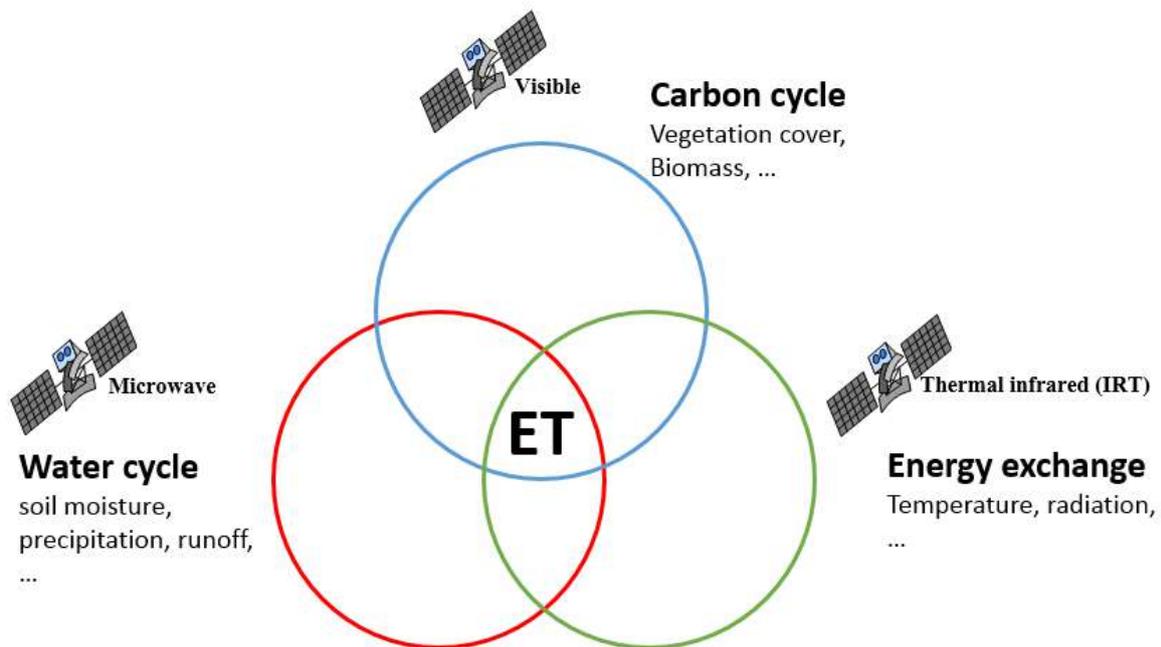
Figure I.2: Evapotranspiration, as a variable controlling water cycle, carbon cycle and surface energy exchanges.

ET can by directly measured using an instrument or estimated 'indirectly' by modeling. Modelling approaches based on using a model to get ET even that most models need in field measurements. In the following we provides the most used instruments and modelling approaches to acquire ET.

I.4.1   Direct measurements of ET

During the last decades, several techniques have been proposed to measure and estimate ET from local to global spatial scales. Different approaches are established in the literature, there are hydrological ones (weighing lysimeters and water balance model), plant physiological

approaches (sap flow, isotopy and chamber system), micrometeorological approaches (eddy covariance and scintillometry) and aerodynamic method.

At the field scale, ET can be measured by using the sap flow sensors (Smith and Allen, 2007), lysimetry (Daamen et al., 1993; Edwards, 1986), the stable isotope technique (Aouade et al., 2016). Passing from local to integrated spatial scales, the eddy covariance technique (Allen et al., 2011; Baldocchi et al., 1988) is suitable for measuring ET at the field scale over an homogeneous field (1 ha and above). The eddy covariance and sap flow techniques can be jointly use to partition the ET into plant transpiration and soil evaporation (Cammalleri et al., 2013; Er-Raki et al., 2010a). Another technique, is the scintillometry that can provide the sensible and latent heat flux over a transect ranging from 250 m to 10 km even for heterogeneous fields (Ezzahar and Chehbouni, 2009; Kohsiek et al., 2002). At global scale, remote sensing data in the optical/thermal bands provide several ET-related variables such as the Normalized Difference Vegetation Index (NDVI), surface albedo, surface emissivity, LAI (Leaf Area Index) and LST (Carlson and Buffum, 1989; Granger, 2000). Several authors have proposed the use of these methodologies (Allen et al., 2011; Er-raki et al., 2013; Hatfield, 1983; Kalma et al., 2008; Kustas and Norman, 1996; Li et al., 2009; Moran and Jackson, 1991). All the presented techniques provide ET estimates at a specific temporal and spatial scale and rely on particular assumptions. Interpolation or extrapolation is thus often necessary to infer ET rates outside application scales, which can be a source of additional uncertainty. Moreover, most *in situ* techniques are expensive, time consuming and need a well-trained staff to operate and maintain it.

Fig. I.3 shows the measurement system that can provide ET estimates at different spatio-temporal scales. In my research, the eddy covariance system was used for the ET validation.
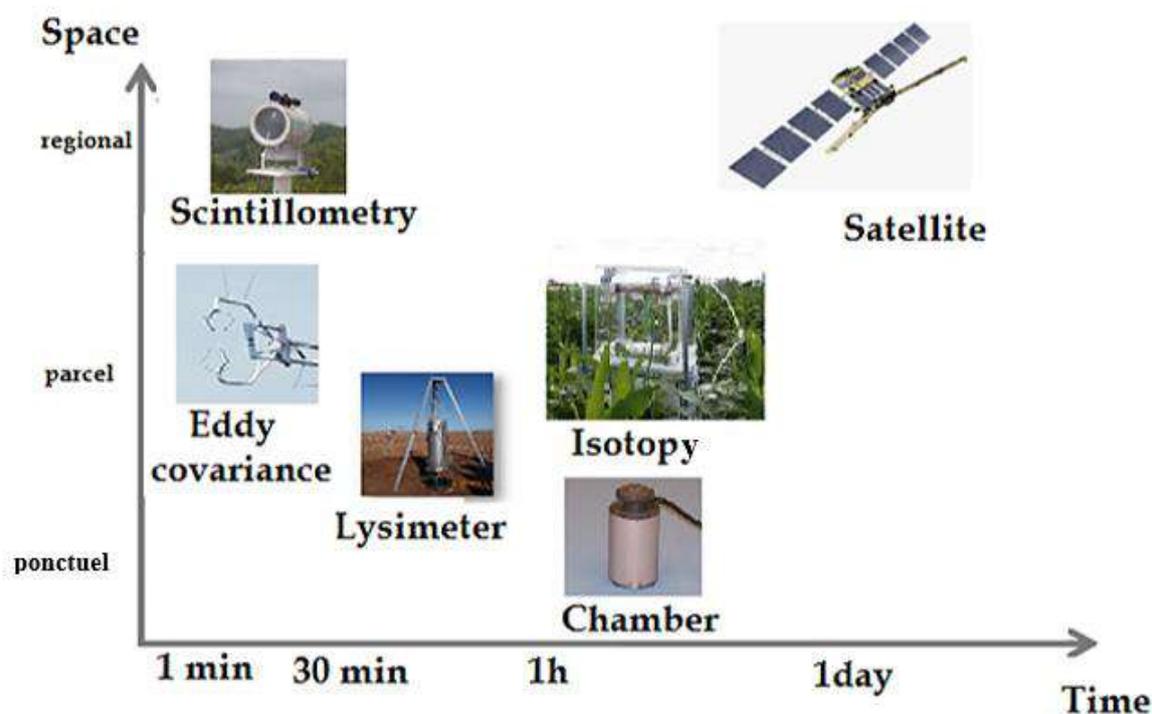
Figure I.3: Multi spatio-temporal scale measurements approaches

I.4.2   Factors conditioning ET

ET depends on two parameters: i) energy provided by solar radiation and the amount water available in the soil. Indeed, one of the main factors conditioning ET is the energy available at the surface (provided by net radiation (R_n)). Aerodynamic resistance (r_a) to sensible (H) and latent heat (LE) transfer, and water stress (related to the amount of water in the soil) are also important factors that affect ET, because when water is scarce in the soil, the stomata close again and transpiration slows down.

According to Schultz and Engman (2000), remote sensing observations combined with auxiliary meteorological data were used to estimate ET over a range of spatio-temporal scales. Much progress has been made recently in the measurement of remote sensing parameters, including: i) Solar radiation; ii) Surface albedo; iii) Vegetation cover; iv) LST; v) NSSM.

Recently satellite data have been used to estimate real ET at different scales (eg, Bastiaanssen et al., 1998; Granger, 1997). The above important parameters to estimate ET are obtained by measuring, by remote sensing of an electromagnetic radiation of a given wavelength, emitted or reflected from the surface. Incident solar radiation, albedo, and LST can be estimated using the same satellite measurements and SM can be estimated by measuring the microwaves

emitted or received by the soil (emission and reflection, or backscattering from the ground). However, there are uncertainties in these estimates due to other factors such as surface roughness and vegetation cover.

I.4.3 Remote sensing-based modelling approaches

As an alternative to observational methods of ET, numerous modelling methods have been proposed such as Simple Soil Plant Atmosphere (SiSPAT) (Braud et al., 1995), Interaction Soil-Biosphere-Atmosphere (ISBA) (Noilhan and Mahfouf, 1996) and simple SVAT (Soil Vegetation Atmosphere Transfer) (Boulet et al., 2000), Interactive Canopy Radiation Exchange (ICARE) (Gentine et al., 2007). Other models like Crop Environment REsource Synthesis (CERES) (Ritchie, 1986), Simulateur multidisciplinaire pour les Cultures Standard (STICS) (Brisson et al., 1998) and the crop-water productivity model (Aquacrop) (Raes et al., 2009) have combined the water balance with the crop growth, development and yield components. These modelling methods, whether complex or simple, are generally not easy to implement in an operational context as they require several parameters (e.g. soil and vegetation hydrodynamic properties) and forcing variables (e.g. climate and irrigation) that are often unavailable at the desired space and time scale. As a matter of fact, simpler models based on a few input data have been developed (Merlin, 2013; Merlin et al., 2014). Among them, the surface energy balance model (SEBS) estimates the turbulent fluxes and surface evaporative fraction (Su, 2002) by using remote sensing data (albedo, NDVI, emissivity and LST) in conjunction with meteorological forcing (solar radiation, air temperature, wind speed, air humidity) and surface parameters (e.g. roughness and stability correction functions for momentum and sensible heat transfer). Remote sensing energy balance using satellite imagery have been developed to estimate evaporation and ET from large areas (Allen et al., 2007; Bastiaanssen et al., 1998a, 1998c; Irmak et al., 2011; Kustas et al., 2003; Kustas and Norman, 1999). Those approaches are promising for application over a wide range of vegetation types and water availability and over large areas. Remotely sensed energy balance techniques are useful for identifying areas experiencing water stress and corresponding reductions in ET and to populate hydrologic models (Irmak and Kamble, 2009; Kamble and Irmak, 2009). There are some satellite-based energy balance models such as SEBAL (Bastiaanssen et al., 2005, 1998b, 1998c) and METRIC (Allen et al., 2007). Theses model are using inverse modeling at extreme conditions for the calibration. ET is estimated at the two conditions based on knowledge of available energy and surface conditions, usually with ties to ground-based weather data. Other more regional-scale models such as the ALEXI model (Anderson et al.,

2005) use inversion based on radiosonde profilings of temperature and specific humidity over time to estimate large-scale heat flux and evaporation.

In contrast, the FAO-56 model requires limited input parameters and it has been extensively and successfully used for estimating ET over several agricultural areas such as: wheat (Drerup et al., 2017; Er-raki et al., 2010, 2007; Jin et al., 2017), olive (Er-Raki et al., 2010b, 2008), citrus (Er-Raki et al., 2009; Rallo et al., 2017), table grapes (Er-raki et al., 2013), sugar beet (Anderson et al., 2017; Diarra et al., 2017) and for different climates (Ayyoub et al., 2017; Debnath et al., 2015). It is based on the Penman-Monteith (P-M) equation that has been formulated to include all the parameters that govern the energy exchange between vegetation and atmosphere.

During my PhD we used the P-M formulation to estimate ET at field and perimeter scale. the idea is that, in the P-M formulation, the extraction of water vapour from the surface is controlled by the surface resistance (r_c). However, the P-M approach has been limited by the difficulties to estimate r_c as it depends on several factors related to pedological, biophysical and physiological processes, which are also related to agricultural practices (Katerji and Perrier, 1983; Testi et al., 2004a).

To overcome these difficulties, many authors have used the concept of "critical bulk resistance, r*", where r* is r_c when ET is not affected by wind speed (Katerji and Perrier, 1983). The critical bulk resistance depends only on local meteorological variables. Rana et al. (2005) and Ayyoub et al. (2017) showed that r_c is linearly related to r*, allowing the ET estimates even in water shortage conditions. It has been demonstrated that the use of the critical resistance approach to estimate canopy resistance that varies with local meteorology provides more accurate ET estimates than assuming a constant value of resistance for a given canopy (Katerji and Rana, 2006). Alves and Santos Pereira (2000) further investigated the surface resistance in the P-M equation and suggested that the surface resistance integrates the combined effects of stomatal, soil surface and canopy resistances. They also showed that the surface resistance depends on meteorological variables as in Jarvis (1976). This approach has then been confirmed by Katerji and Perrier (1983) who showed that decoupling the surface resistance (function of critical resistance), from atmospheric resistance effects improves ET estimates, and this is consistent with the study of Alves and Pereira (2000). All those methods estimate the surface resistance and ET at local scale but little attention has been paid on determining r_c at large scale from remote sensing data. Since the crop water stress is related to

r_c through stomatal closure, one can estimate r_c from remotely sensed LST which can provide a good proxy for water stress level.

Among existing thermal-based SM indexes mentioned above, VTCI has two main advantages: 1) it is rather physically-based due to possibility of simulating wet/dry LST values using a surface energy balance model (Wang et al., 2001) and 2) it can be applied to mixed pixels including soil and vegetation components. In this context, in this thesis, ET is modeled based on the modified P-M equation by introducing a simple established relationship between r_c and a thermal-based proxy of vegetation water stress, since it was considered as the most relevant parameter for drought monitoring (Jackson et al., 1981a; Wan et al., 2004). The surface water stress index (SI) will be derived from the VTCI. After, the approach is calibrated and tested in terms of ET estimates over both flood and drip irrigated sites.

I.4.4   Surface evaporative efficiency

The upper limit of ET is known as the potential evapotranspiration (ET_p), which is bounded by atmospheric evaporative demand. Due to the limiting factor conditioning ET (biophysical limitations), the actual ET does not exceed the ET_p. The ratio of ET to ET_p can capture the effect of those limitations, which is known as a stress factor or the surface evaporative efficiency. The ET_p is defined as the ET under optimal unstressed conditions (low surface resistance). The ratio of ET to ET_p ratio has been used as a simple but effective approach for estimating ET in hydrological models (Caylor et al., 2005; Fisher et al., 2008; Miralles et al., 2011; Schaake et al., 1996; Van Beek et al., 2011). In agriculture, this approach is often used to quantify water availability, to estimate irrigation requirements (Allen et al., 1998), to monitor crop water stress (Anderson et al., 2011, 2007; Jackson et al., 1981b) and to monitor NSSM (Budyko, 1956; Manabe, 1969; Merlin et al., 2008b).

The reason behind choosing the ratio, is because it's generally almost constant during the day (Crago, 1996; Cragoa and Brutsaert, 1996; Gentine et al., 2007; Shuttleworth et al., 1989; Sugita and Brutsaert, 1991). In addition, it is more directly related to SM (Kustas et al., 2002) and less dependent on incident radiation than ET or LST (Nishida et al., 2003). Also, when using the P-M equation of ET and ET_p (Monteith, 1965), it is founded that the ratio is a function of the ratio surface r_c to aerodynamic resistance r_a (Eq. I.14). This ratio is referred to as the "decoupling factor," a measure of the decoupling between atmospheric conditions at the canopy surface and those in the surrounding air, introduced by Jarvis and Mcnaughton (1986).

$$\frac{\text{ET}}{\text{ET}_\text{p}} = \left(1 + \frac{\gamma}{\Delta+\gamma} \cdot \frac{\text{r}_\text{c}}{\text{r}_\text{a}}\right)^{-1} \qquad (\text{I.14})$$

Where Δ is the slope of the saturation vapor pressure curve at the temperature of interest (Pa/K), γ is the psychrometric constant (Pa/K).

The ratio $\text{ET}/\text{ET}_\text{p}$ is a useful index that indicates the partitioning between atmospheric demand control and surface biophysical control over actual ET. When the ratio tends toward 0, it means that the canopy is fully coupled with the surrounding atmospheric conditions. By contrast, when it tends to 1, it means that the canopy atmospheric conditions are fully decoupled from those of the free airstream.

I.5   Conclusion

This chapter presents the state of art of the differents methods and approaches followed to estimate and measure SM, LST and ET. Different methods have been used using either in situ data at a local scale or remote sensing data acquired from spaceborne satellites to observe how the retrieved variables are spatially distributed.

Physical, empirical or semi-empirical approaches are used in order to quantify the different variables discussed before. The purely physical models are the most accurate ones for detecting surface variables, otherwise all the parameters of the other approaches are generally empirical or semi-empirical. By contrast, the non-physical approaches have the advantage of the spatialisation (distributed calibration in space) of certain processes based on available observations, notably multi-spectral remote sensing. Multi-spectral remote sensing data help to distinguish between bare and vegetated area that allows understanding the partition of ET between soil evaporation and plant transpiration that would be very useful for estimating the consumption and the crops water needs.

Chapter II Data & study sites description

Contents

_____

_____

II.1   Introduction

The developed approaches during this thesis have been tested and applied over five sites in Morocco over the Tensift region which characterized by semi-arid climate. Climatic, soil moisture, surface temperature data and different energy/hydric fluxes were collected over the selected fields. Some of those data have been used as in put to the used models in this work, and the others such as *in situ* measurements collected during the field campain and were used as a validation data to test the stability and the robustness of the used models.

The main aim of this chapter is to present the whole data used during this thesis (study sites, *in situ* and satellite data). A first part is dedicated to give a detailed description of the study areas as well as in situ data collected over the study sites. A second part presents the satellite data used in addition, a description of the pre-processing steps applied to those data has been also presented.

II.2   Sites and in situ data description

II.2.1 Study areas

The Tensift Haouz region is situated in the Midwest Morocco-North Africa (Fig. II.1), covers 4.4% of the Moroccan territory (24 000 km^2). This area is known by a very contrasting relief with a very varying altitudes. The Tensift watershed consists of a vast semi-arid plain receiving about 250 mm/year of rainfall, while the reference evapotranspiration (ET$_0$) is about 1600 mm/year, according to the FAO-56 model (Allen et al., 1998), which leads to irrigation and increasing concerns related to optimizing the management of water resources.
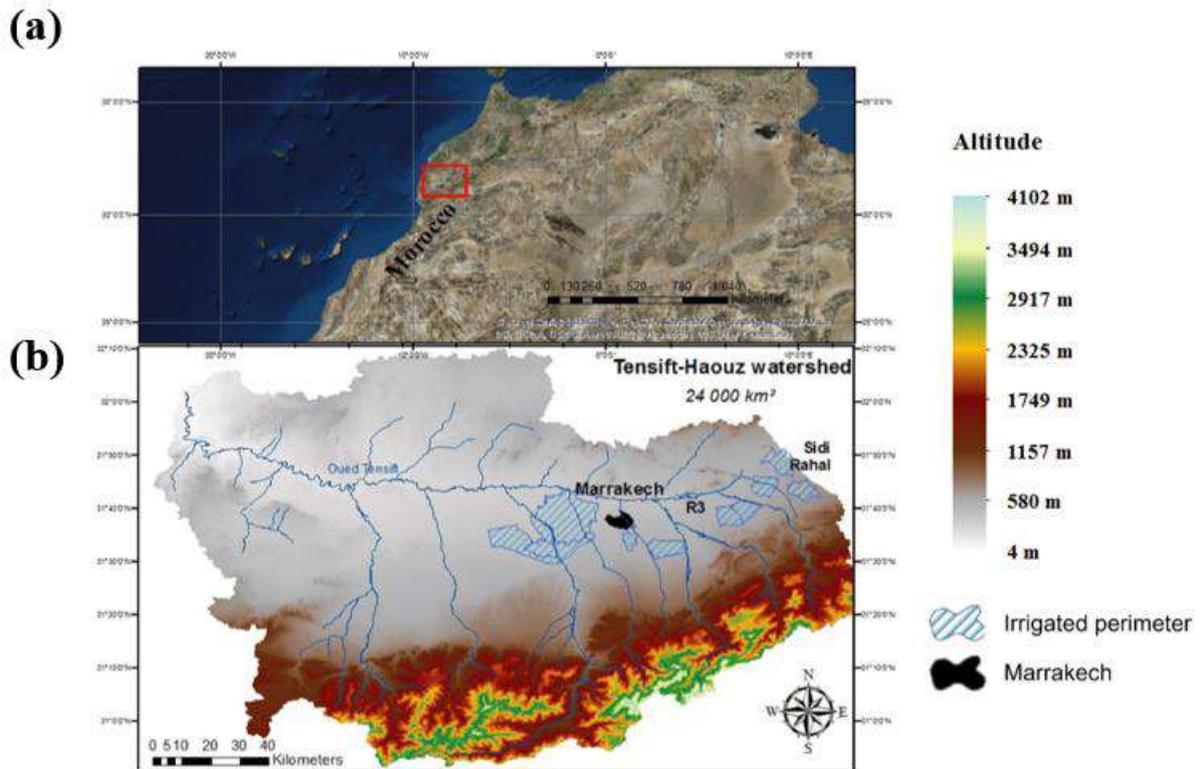
Figure II.1 : (a) Location of the Tensift Al Haouz watershed in Morocco and (b) the R3 and Sidi Rahal area location over the Tensift Al Haouz watershed.

The plain (Fig. II.2) is alimented by water from the south, a mountains area (Haut Atlas) which contains the highest reliefs of the Kingdom (4167 m, Jbel Toubkal). The massive amount of water coming from south is stored and formed "*chateau d'eau*" composed of several mountainous sub-basins. This water feeds permanently watercourses which called *L'Oued* by the North Africans "rivers" flowing to the plain. The North side is formed of low altitude mountains called Jbilet where the highest mountains do not exceed 947 m. This north area, characterized by rivers that are fed with water just in case of heavy rain, otherwise they remains dry most of the time. The plain is crossed from South to North by several *Oueds* and join the main collector river "*Oued Tensift*" which flows from East to West before to reach the Atlantic Ocean. Agriculture is the biggest consumer of water in this region, where 85 % of the mobilized water resources is consumed by the agricultural fields dominated in the plain (Duchemin et al., 2006; Er-Raki et al., 2007; Hadria et al., 2006b; M. H. Kharrou et al., 2013).

Since the Tensift Al Haouz is characterized by a semi-arid climate and under the effect of climate change, the water resources are frequently used which put a strong tension on water use. This leads to an overexploitation of water resources via irrigation. A complex network called by "*seguias*" formed the main carrying and distribution system for irrigation water. The

reached water to the agricultural area coming from the mountains, Sidi Driss and Moulay Youssef dams is controlled and managed by the Tensift basin agency (ABHT). Even the effort done by the ABHT agency, the farmer used the ground water in a non-controlled way and loss water by evaporation using the traditional flooding systems which is the dominant irrigation system in this area. Therefore, a rational management of irrigation water is important.

In this context the International Joint Laboratory (LMI-TREMA, lmi-trema.ma) installed in Marrakech (center of Morocco), aims to improve the management of irrigation water by developing tools that can help to use water in a rational way. The LMI-TREMA's selected study areas where the experiments have been conducted since 2002, R3 perimeter and Sidi Rahal study rainfed sites have been used to test our approaches. These selected sites are considered as a typical study area and they have been widely used until nowadays (Amazirh et al., 2017; Chehbouni et al., 2008; Duchemin et al., 2006; Er-raki et al., 2007; Hadria et al., 2006b; Jarlan et al., 2015; Khabba et al., 2013; Kharrou et al., 2013) due to the rich and a very large data base provided.

The first area is an irrigated agricultural zone (called R3) known by its heterogeneity and occupied by different culture types (alfalfa, wheat, olive, orange and horticulture), where wheat crops is the dominating culture (50 %) (Fig. II.3). Flood irrigation is the main irrigation mode used in this area. Four experimental fields were selected over the R3 perimeter during 2015/2016 agricultural season: two sites are slected from 22 monitored parcelles which maintained as a bare soil throughout the season (3 ha of size for each one) and two other sites permanently monitored wheat fields over this season (named drip and flood sites) (Fig. II.3).

The second area is a rainfed agricultural area (called Sidi Rahal) mainly dominated by trees (olive, about 80%) while the remaining surface is comprised of bare soil, small forest and impervious surfaces (e.g., buildings and roads). One experimental field is selected (named bare soil site): a 1 ha rainfed wheat field, this field had remained under bare soil conditions during the 2015‑2016 agricultural season.

Based on soil analysis (Er-Raki et al., 2007), soil texture is clayey and sandy in the majority of fields within the R3 and Sidi Rahal areas, respectively.

Figure II.2: Haouz Plain and Atlas mountains.

II.2.2 Meteorological data

Over the studied sites two meteorological station have been installed over an alfalfa cover near of the monitored plots for R3 perimeter and within the monitored site for the Sidi Rahal area during the 2015/2016 agricultural season as shown in Fig. II.3.
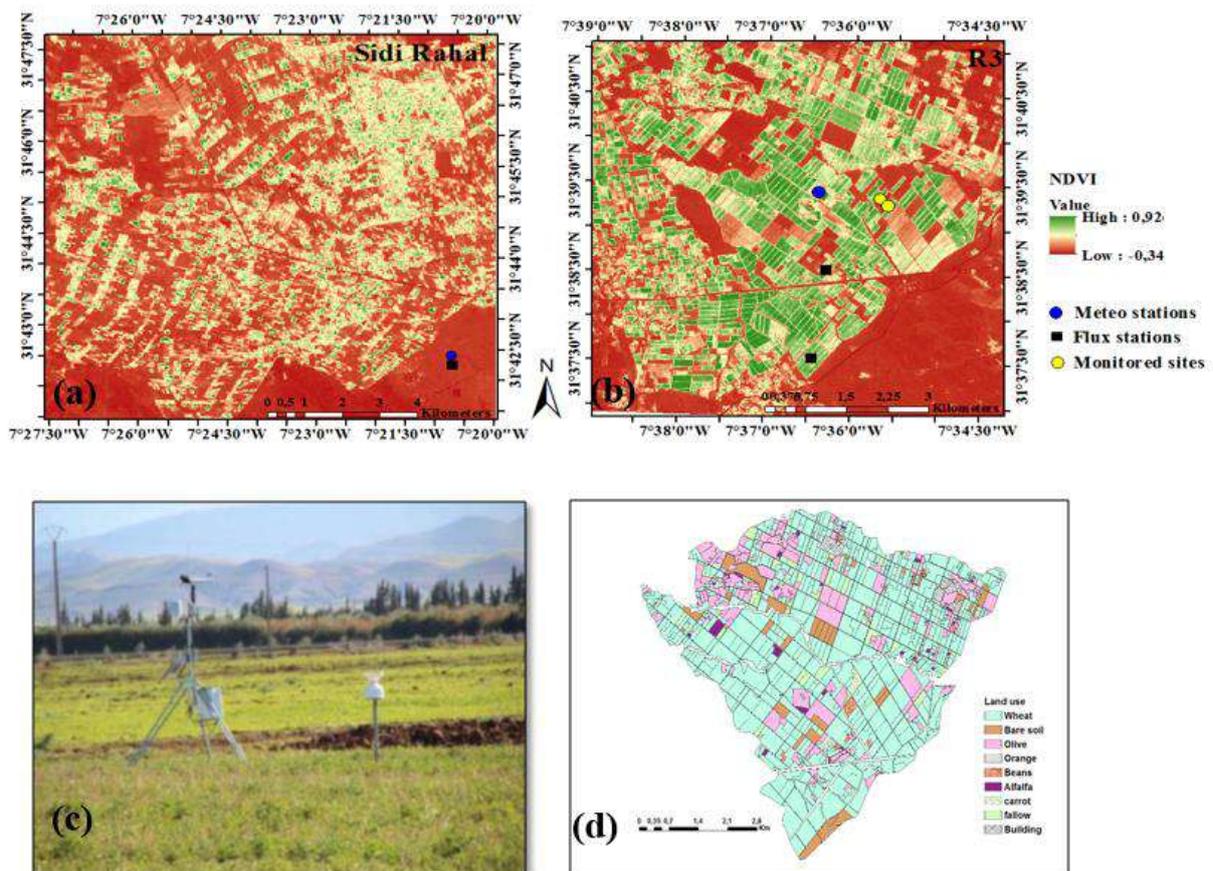
Figure II.3: Location of weather and flux stations within the study areas during the 2015/2016 agricultural season in R3 (b) and Sidi Rahal (a) sites, (c): The land use over R3 area. (d): Weather station installed over R3 site. The images are derived from Landsat data, the 07 February and the 24 July for Sidi Rahal and R3 sites, respectively.

Those stations are equipped with instruments for monitoring solar radiation, speed and direction of wind, air temperature and humidity, and rain. These meteorological forcing data was continuously monitored at the 30 min step, are stored on a central data logger, before being collected and returned to the laboratory for processing and analysis. The different parameters measured as well as the different sensors used for the measurement of meteorological variables are:

- Wind speed u_a measured by CSAT3D sonic Anemometer
- Incident solar radiation R_g measured by pyranometer
- Air temperature T_{air} and relative humidity rh_a measured by a HMP155 probe
- Precipitation measured by a rain gauge

All this variables are measured at a reference height of 2 m.

II.2.3 In situ soil moisture data

For both R3 bare parcels (P15 and P16), the near-surface (0–5 cm) soil moisture was measured within ±2 h of the L7/8 and S1 satellites overpasses using a frequency domain sensor (Theta probe) at 5 locations (10 m from the plots extrems) on both sides of each field (Fig. II.4). For each sampling date and parcels, an average of the 10 measurements was computed to reduce uncertainties in field-scale SM estimates. Soil samples over a 0 to 5 cm depth were also taken over both sites in order to calibrate Theta probe measurements using the gravimetric technique.

For Sidi Rahal rainfed site the surface soil moisture is continuously measured using time domain reflectometer probes (CS616) installed at different depths (5, 10, 20, 30, 50, 70 cm).

For this study the measured 5 cm surface soil moisture have been used as a validation data set. S1 and L7/8 never overpass the study areas on the same day. However, Table II.1 lists the dates with quasi-concurrent (one day offset) L7/8 and S1 overpasses. In the R3 area in situ SM sampling were undertaken on those particular dates, either on S1 and L7/L8 overpass date, or on both successive dates. The SM sampling dates are also reported in Table II.1.

Table II.1: Dates with quasi concurrent L7-8/S1 overpasses used in the analysis for both study sites.

Date (2016) (mm/dd-mm/dd)	S1 overpass Time (UTC)	Study Site	Thermal sensor (overpass time at 11:30 AM)	S1 orbit	R3 SM sampling
01/06-01/07	06:30 am	Sidi Rahal	L8	Ascending	No*
01/14-01/15	06:30 pm	Sidi Rahal /R3	L7	Descending	Yes
01/30-01/31	06:30 am	Sidi Rahal /R3	L7	Ascending	Yes
02/07-02/08	06:30 pm	Sidi Rahal /R3	L8	Descending	Yes
02/23-02/24	06:30 am	NO data	L8	Ascending	No*
03/02-03/03	06:30 pm	Sidi Rahal /R3	L7	Descending	Yes
03/18-03/19	06:30 am	R3	L7	Ascending	Yes
03/26-03/27	06:30 pm	R3	L8	Descending	Yes
04/11-04/12	06:30 am	NO data	L8	Ascending	No*
04/19-04/20	06:30 pm	Gap fil**	L7	Descending	Yes
05/05-05/06	06:30 am	R3	L7	Ascending	Yes
05/13-05/14	06:30 pm	NO data	L8	Descending	No*
05/29-05/30	06:30 am	Sidi Rahal	L8	Ascending	NO data
06/06-06/07	06:30 pm	Sidi Rahal	L7	Descending	NO data
06/22-06/23	06:30 am	Sidi Rahal	L7	Ascending	NO data
06/30-07/01	06:30 pm	Sidi Rahal	L8	Descending	NO data
07/16-07/17	06:30 am	Sidi Rahal	L8	Ascending	NO data
07/24-07/25	06:30 pm	Sidi Rahal	L7	Descending	NO data
08/09-08/10	06:30 am	Sidi Rahal	L7	Ascending	NO data
08/17-08/18	06:30 pm	Sidi Rahal	L8	Descending	NO data
09/02-09/03	06:30 am	NO data	L8	Ascending	NO data
09/10-09/11	06:30 pm	Sidi Rahal	L7	Descending	NO data
09/26-09/27	06:30 am	NO data	L7	Ascending	NO data
10/04-10/05	06:30 pm	Sidi Rahal	L8	Descending	NO data

*: cloudy day

**: the Landsat-7 images include data gaps due to scan line corrector failure on May 31, 2013, which on this date unfortunately covered our sites.
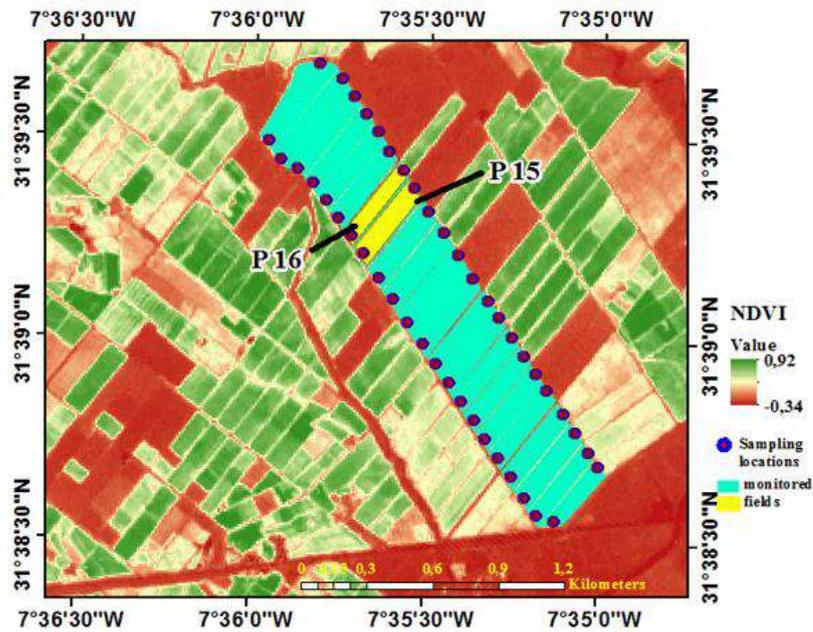
Figure II.4: Surface soil moisture sampling locations over the 22 parcels. P15 and P16 are the used two parcels which maintained as a bare soil during the investigated study.

The consistency of the SM data collected on two successive dates was checked in Fig. II.5. Both SM data sets were consistent with a root mean square difference of 0.02 m^3m^{-3} for both P15 and P16 R3 study fields, except when an irrigation or a rainfall event occurred between sampling dates. Those particular dates were removed from the data set.
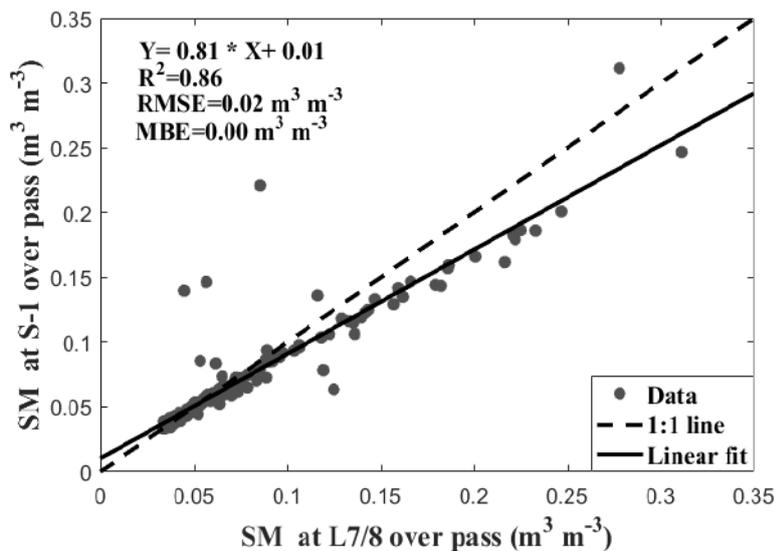
Figure II.5: Comparison of the SM collected on two successive dates corresponding to Landsat and Sentinel-1 overpasses at Sidi Rahal site.

II.2.4 In situ LST data

Land Surface Temperature (LST) is a key variable in this work which used to validate the extracted satellite temperature from Landsat sensor (see section 3). The radiometric LST was measured by an Apogee 8–14 μm thermal radiometer sensor (IRTS-P's, Apogee with a ±0.2°C of accuracy) looking at nadir, set up at a 2-m height. The apparent target temperature is corrected from sensor errors using the sensor body temperature. Then it converted to LST using surface emissivity (0.96 for vare soil and 0.98 for covred area). The in situ LST data are available each 30 min over the studied areas.

II.2.5 Flux data

During the investigated agricultural season 2016, the R3's two wheat sites and the Sidi Rahal's bare soil parcel were equipped with different sensors to collect water and heat fluxes exchanged between vegetation, soil and atmosphere. The eddy covariance systems installed on the studied sites (Fig. II.6) consists principally of a Krypton hygrometer which measures the density of water vapor in the air. Both Kh20 and Kh21 used over the study area are a UV absorption hygrometer which are suitable for applications using turbulent correlation (Eddy Correlation). The installed hygrometer provides continuous measurements of vertical sensible heat (H) and latent heat (LE) fluxes. Note that, the sensible and latent heat fluxes are not provided directly by the instrument, but they are extracted from the measured fluctuation of the vapor pressure around the mean value. If necessary, absolute readings (absolute air water vapor) can be obtained by making an independent measurement of the absolute atmospheric humidity with a humidity sensor as an example. A humidity probe (Vaissala) fixed in the tower intended for measuring the temperature and the relative humidity of the air, aims to correct the water vapor density measured by krypton. The raw data of Eddy covariance at 20 Hz are processed at the Laboratory using the EC-pack software developed by the meteorological and air quality group, Wageningen University (available for the download (http://www.met.wau.nl/)). Additional instruments are installed in the tower providing extra measurements such as the net radiation (R_n) which was measured by the net radiometer Kipp and Zonen CNR4. A Sonic 3D anemometer designed to measure the wind speed over the 3 orthogonal axes. From these measurements can be deduced the wind speed and the sonic temperature in the three orthogonal components. The provided measurements by this sensor are a key parameter to estimate the turbulent fluxes that depends on the measurement of air turbulence at a high level of accuracy.
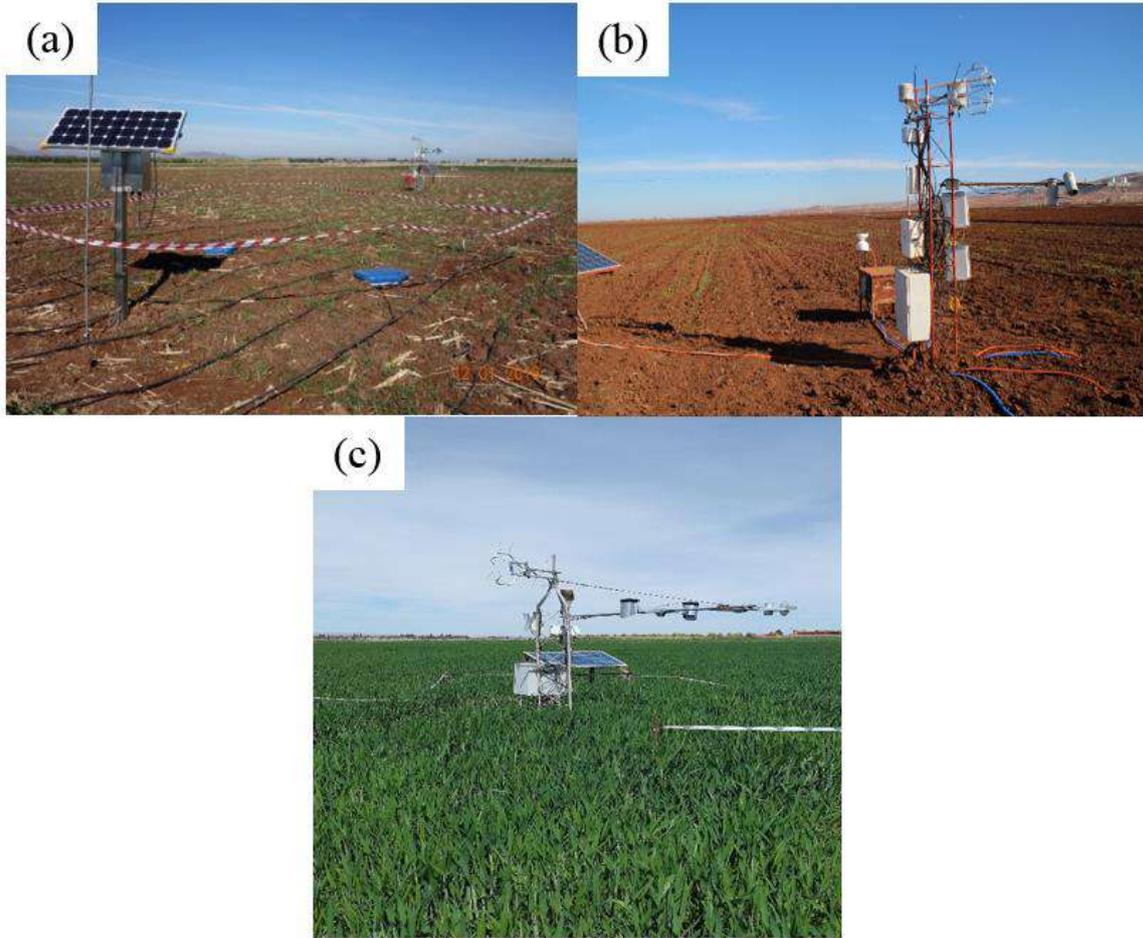
Figure II.6: Flux stations over (c) flood, (a) drip irrigated sites and (b) Sidi Rahal bare soil during the 2016 growing season.

The soil heat flux (G) is the missed component to loop the energy balance (regarding the energy storage in the canopy) which was controlled at a 5 cm depth using soil heat flux plates HPF01.

Before using the data of latent heat flux (Evapotranspiration) measured by the eddy covariance system, it is important to check the reliability and the quality of these measurements. This is undertaken through the analysis of the energy balance closure. By ignoring the term of canopy heat storage and the radiative energy used by vegetation photosynthesis (Testi et al., 2004a), the energy balance closure is defined as:

$$R_n - G = LE + H \qquad \qquad (II.1)$$

To check the budget closure during the study period, we compared the available energy at the surface (R_n - G) with the sum of turbulent fluxes measured by the Eddy covaraince (EC) sattion ($H_{EC} + LE_{EC}$) at half-hourly scale. The quality of the correlation between (R_n - G) and ($H_{EC} + LE_{EC}$) was evaluated by the regression line and the determination coefficient R^2. Fig.

II.7 shows the energy budget closure for sub-hourly data during 2016 growing season for both study sites separately.
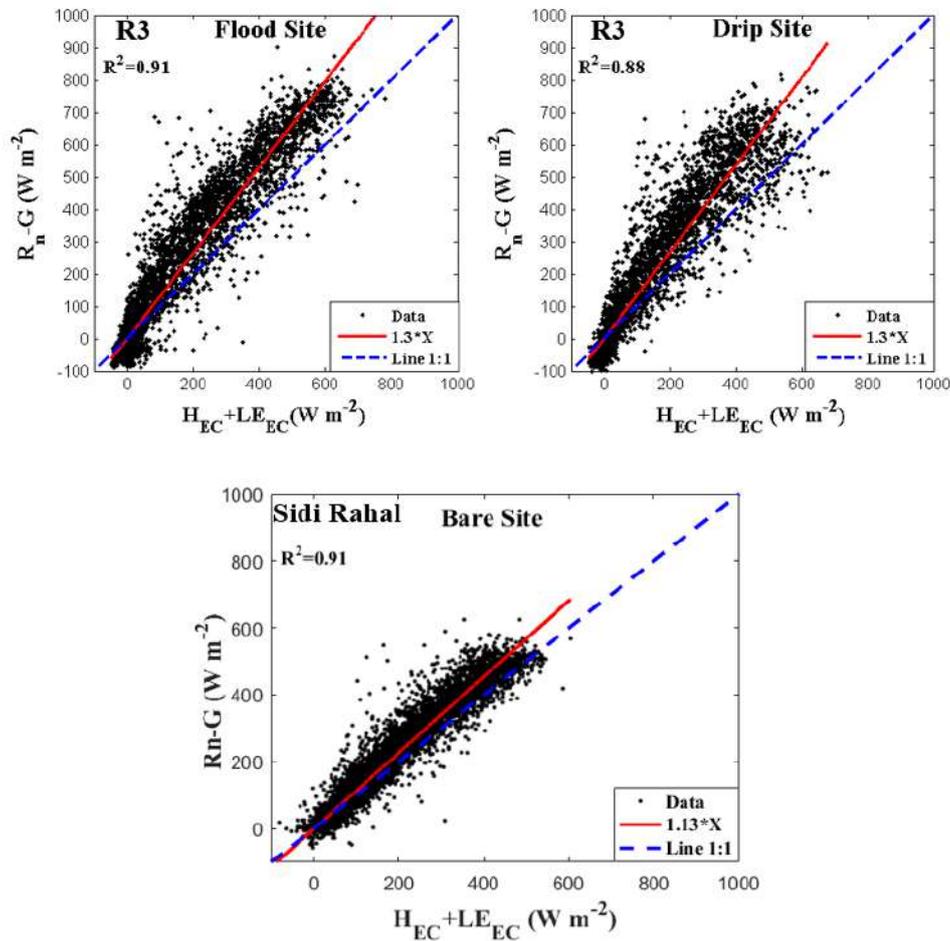
Figure II.7: Energy balance budget closure over flood and drip irrigated sites and Sidi Rahal bare soil during the 2015-2016 growing season.

Results show that the closure of the energy balance is relatively well verified by comparison with other studies (Ezzahar et al., 2009; Testi et al., 2004b). The regression lines are close to the 1:1 line and R^2 values are generally close to 1 (0.91 for both flood and bare soil sites and 0.88 for drip irrigated field). However, the slope of the regression forced through the origin was about 1.3 for both irrigated sites and 1.13 for the bare soil site (Sidi Rahal), indicating some underestimation of turbulent fluxes (H_{EC} + LE_{EC}) not exceed 30% (slope of 1.3) of the available energy (R_n - G). This due to the attenuation of turbulence at low or high frequency signals (Ezzahar et al., 2009). Also, the difference between the sensors source area has a very important impact on the energy balance closure. In fact, the surface area of the sensors measuring the available energy (net radiation and soil heat flux) is very small compared to that of EC system, which can quickly change depending on wind speed and direction and

surface conditions. Moreover, the energy absorbed by the plant has not been considered in the energy balance. In this context, Scott et al. (2003) evaluated the storage in the biomass to about 5-10 % of the available energy, which could partially explain the overestimation of available energy at the surface.

II.3   Preprocessing satellite data

In this part, a description of the different satellite data used in this work has been made. Firstly, the characteristics of the imaging satellites used are detailed, where are distinct by types (optical, thermal and microwave sensors). Then, the preprocessing steps of satellite data are detailed.

II.3.1   Satellite data characteristics

II.3.1.1 Landsat

L-7 and L-8 (Table II.2) were launched by NASA in April 1999 and February 2013, respectively. The images were downloaded from the USGS website, which freely provides surface reflectances and thermal radiances data in different spectral bands. The revisit time of each sensor is 16 days. Combining both satellites potentially (in cloud free conditions) provides optical data every 8 days. The overpass time at 11:30 AM over the studied sites. The L8 satellite is equipped with multispectral sensors including:

- Operational Land Imager (OLI) is the main instrument. This multispectral radiometer acquires images in nine spectral bands ranging from visible to infra-red. Seven of these spectral bands were already present on the Landsat-7 ETM + instrument. Two additional channels were added, mainly for atmospheric correction (440 nm blue channel) and cloud detection (1380 nm). The technology used on OLI is radically different from that of previous instruments. The oscillating mirror scanner is replaced by a fixed array of detectors that captures the data over the entire width of the optical field. The instrument uses technology tested onboard the experimental EO-1 satellite.
- Thermal Infrared Sensor (TIRS), is a two-channel infrared multispectral radiometer that provides data at the same wavelengths used by older Landsat satellites but not included in the OLI instrument. The objective of this mission is to ensure the continuity of measurements made in the past. The image resolution is 100 m compared to 60 m for the Landsat-7 thermal bands. To meet the specific characteristics of the thermal infrared, it

implements QWIP (quantum well infrared photodetector) sensors coming from recently matured technology.

Table *II.2*: Landsat 7 and 8 spectral bands.

Landsat-7 ETM+ Bands (μm)			Landsat-8 OLI and *TIRS* Bands (μm)		
			30 m Coastal/Aerosol	0.435 - 0.451	Band 1
Band 1	30 m Blue	0.441 - 0.514	30 m Blue	0.452 - 0.512	Band 2
Band 2	30 m Green	0.519 - 0.601	30 m Green	0.533 - 0.590	Band 3
Band 3	30 m Red	0.631 - 0.692	30 m Red	0.636 - 0.673	Band 4
Band 4	30 m NIR	0.772 - 0.898	30 m NIR	0.851 - 0.879	Band 5
Band 5	30 m SWIR-1	1.547 - 1.749	30 m SWIR-1	1.566 - 1.651	Band 6
Band 6	60 m TIR	10.31 - 12.36	*100 m TIR-1*	*10.60 – 11.19*	Band 10
			100 m TIR-2	*11.50 12.51*	Band 11
Band 7	30 m SWIR-2	2.064 - 2.345	30 m SWIR-2	2.107 - 2.294	Band 7
Band 8	15 m Pan	0.515 - 0.896	15 m Pan	0.503 - 0.676	Band 8
			30 m Cirrus	1.363 - 1.384	Band 9

II.3.1.2 Sentinel-1

S-1 mission is composed of a constellation of two twin satellites: S-1A was launched in April 2014 and S-1B in April 2016 by ESA in the frame of the Copernicus programme. Both S-1A and S-1B operate in C-band (frequency 5.33 GHz, wavelength 5.6 cm) synthetic aperture radar (SAR), providing data in four operational modes (Strip Map, Interferometric Wide Swath, Extra wide swath and Wave) and different polarizations for all modes. The S-1 constellation offers data with high revisit frequency (every 3-6 days). Both satellites orbit the whole earth at an altitude of ~700 km sharing the same orbital plane with a 180° orbital phasing difference. Level 1 S1 products were downloaded freely from the Sentinel-1 Data Hub website (https://scihub.copernicus.eu/).

II.3.1.3 MODIS

MODIS was launched aboard Terra satellite in December 1999 and Aqua in May 2002 by NASA Goddard Space Flight Center, providing data in 36 spectral bands at three varying spatial resolutions (250 m, 500 m and 1 km) in a 2330 km viewing swath width, covering the global world every 1 to 2 days. Aqua crosses the equator at 1:30 am and 1:30 pm local time while Terra crosses Equator at 10:30 am and 10:30 pm, which means that MODIS data is

generally available daily. The data can be freely downloaded via
http://lpdaac.usgs.gov/main.asp .

II.3.2 Data preprocessing

II.3.2.1 Thermal infrared (TIR) data

II.3.2.1.1   *MODIS*

The daily 1 km resolution LST (version 6) MOD11A1 product is available through the U.S. Land Processes Distributed Active Archive Center (LP DAAC, https://lpdaac.usgs.gov/). The generalized split-window algorithm (Wan et al., 2002; Wan and Dozier, 1996) has been used to retrieve MODIS LST products and a correction step was performed using the surface band emissivity provided also by MODIS spectral data measured in a seven infrared bands. The split window algorithm uses as input the calibrated radiance products (MOD021KM), the atmospheric temperature and the water vapor profile (MOD07), as well as the cloud masks product (MOD35). Then, The LST data were re-projected from sinusoidal to geographic latitude/longitude using the Universal Transverse Mercator (UTM), Zone 29N, World Geodetic System (WGS) 84 coordinate system.

II.3.2.1.2   *Landsat*

L-7 and L-8 sensors provide TIR data with a spatial resolution of 60 m and 100 m, respectively. The TIR radiance is used to calculate LST. To this end, the processing chain developed by Tardy et al. (2016) describes the following correction steps:

- Raw digital number is converted into top-of-the-atmosphere (TOA) radiance.
- TOA radiance is corrected for atmospheric effects by using the atmospheric downwelling and upwelling radiances and the spectral atmospheric transmissivity. Atmospheric parameters are provided by the atmospheric radiative transfer model MODTRAN (Berk et al., 2005) with input (vertical air temperature and water content) data obtained from the ECMWF European Reanalysis (ERA) Interim product (Dee et al., 2011).
- The NDVI and soil/vegetation emissivity components are used to estimate the surface emissivity via an empirical relationship described in Tardy et al. (2016). The bare soil and full-cover vegetation emissivities are taken equal to 0.96 and 0.99, respectively.
- The compensation of atmospheric effects and the surface emissivity correction allows the conversion of TOA into top-of-canopy (TOC) radiance.
- LST is obtained by applying the simplified Plank's law.

The L-7 LST is averaged (aggregated) at 100 m resolution, which is the common lowest spatial resolution between S1 and Landsat data. Note that the reliability of the Landsat-derived LST was checked by comparing remotely sensed LST with local *in situ* measurements (Fig. II.8) at three TIR stations located within the study areas.
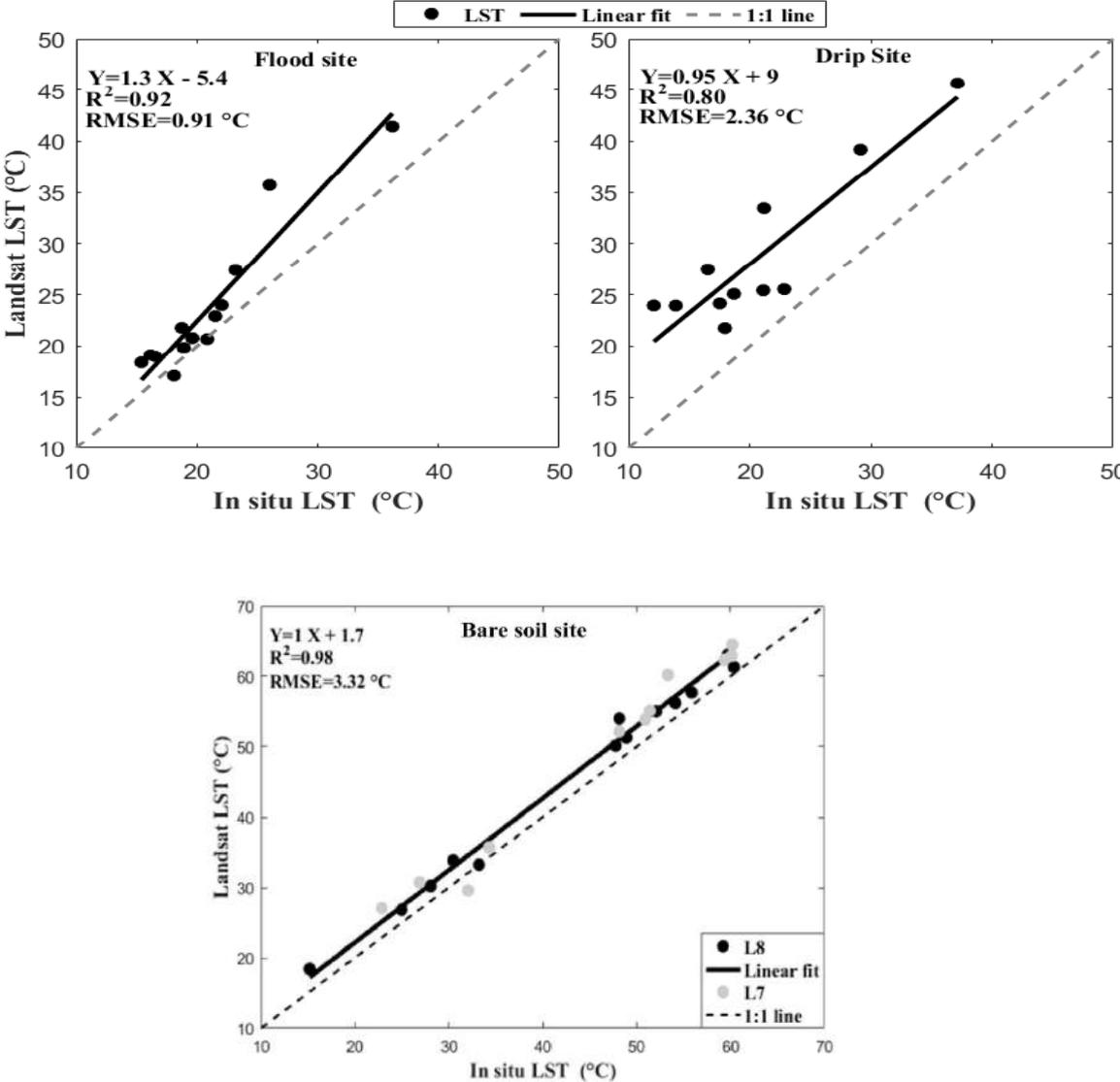
Figure II.8: LST derived from Landsat-7 and -8 versus in situ measurements for R3 two drip (top right) and flood (top left) irrgated sites and Sidi Rahal bare soil site (bottom).

Over the bare soil (Sidi Rahal) site, the maximum LST values (up to 60 °C) were acquired during the summer while it is not exceeds 50°C for both flood and drip irrigated sites.

According to this figure, a relatively good match between satellite and ground LST data is obtained for the R3-flood irrigated wheat site with a determination coefficient (R^2) of 0.92 and a RMSE equal to 0.91 °C, whereas an R^2 of 0.80 and an RMSE equal to 2.36 °C are

found for the R3-drip-irrigated site. Also, a satisfying match is observed between in situ and satellite LST with a R^2 of 0.98 and a RMSE equal to 3 °C for the Sidi Rahal rainfed site.

The systematic over-estimation observed in the R3-drip site and bare soil Sidi Rahal site is attributable to the spatial extent of *in situ* and spaceborne observations (lack of spatial representativeness of *in situ* data at the L7/8 pixel scale). In fact, the drip-irrigated site is small (in comparison with the flood one), and does not fully cover the Landsat thermal pixel size (100 m resolution). Moreover, some differences between *in situ* and Landsat data could be explained by the limited spatial representativeness of 2-m high *in situ* thermal data. LST estiamtion in R3-flood irrigated site is better than in R3-drip irrigated site, this is due to: 1) The irrigation system: as it is known, flood irrigation implies a homogeneous fraction of wetted areas, where all the pixels have the same percentage of irrigation water, which means an uniform LST within the site. In contrast, for drip irrigated site, just a part of the soil surface is wetted, which may lead to some heterogeneity in observed LST from one pixel to another. 2) The flood irrigated site is bigger (4 hectares) than the drip one (approximately 2 hectares with a surface area of 4 ha (35 Landsat pixels) and 2 ha (10 Landsat pixels), respectively. Each crop field can include a mixture of wet and dry Landsat pixels, although an average of all LST values was computed at the field scale.

Note that several 60/100 m Landsat LST pixels were partly covering the surrounding fields, causing representativeness issues especially for the smaller (drip) field. In addition 3) for the flood site, the surrounding fields are similar with the same irrigation system and crop (wheat). Contrariwise, the drip one, was surrounded by fields with different crops (beans).

The observed overestimation of LST by Landsat could also be due to an overestimation of the surface emissivity. As soil emissivity is difficult to estimate without specific measurements (unavailable in this experiment), it was fixed arbitrarily to 0.95.

II.3.2.2 Radar imagery

Over land S1 operates in Interferometric Wide Swath mode providing data at the cross polarization VH (vertical-horizontal) and co-polarization VV (vertical-vertical) mode at a spatial resolution of about 10 m. 45 S1 images were acquired for Sidi Rahal site and 23 images over the R3 sites. The incidence angle (~40°) of S1 observations is approxilatly the same for Sidi Rahal and R3 sites for ascending and descending overpasses. Several processing steps are applied before using the original S-1 data, in order to convert the radar signal to a

backscatter coefficient using the Sentinel Application Platform (SNAP). A detailed description of the retrieved processing steps are follows:

II.3.2.2.1 *Thermal noise removal*

Removing thermal noise by subtracting the additive noise from the power-detected image. The disturbing additive thermal noise (mostly in the lower range of backscatter intensity values) was removed using the calibrated noise vectors provided by ESA.

II.3.2.2.2 *Radiometric calibration*

Each pixel of a radar image is defined by a numerical account (CN). This numerical account depends on the acquisition parameters. It is therefore difficult to compare one image to another. In order to perform multi-temporal analyzes and to compare different images, it is necessary to standardize the intensity of the signal. This standardization is ensured by the radiometric calibration of the images. This process allows to calculate from the retrodiffused signal a dimensionless quantity called the backscattering coefficient. The retrodiffusion coefficient depends on the physical surface parameters such as roughness and soil moisture (in the case of bare soil), but also on the sensor parameters such as the incidence angle, the polarization and the radar length. The backscatter coefficient expresses in general in decibel (dB).

II.3.2.2.3 *Terrain correction*

Terrain correction was applied ("Range-Doppler Terrain Correction" module in the SNAP) to geocode accurately the images by correcting SAR geometric distortions (foreshortening, layover and shadow).

The purpose of geocoding is to correct the pixels displacement affected by the relief effects by replacing the pixels of the radar image at their true positions. This correction is made using a DEM (Digital Elevation Model) downloaded automatically by SNAP software at 30 metres resolution and thus eliminates geometric deformations of radar images to make them conform to reality. The use of the DEM allows to correct deformations related to the satellite view mode, as well as to the satellite viewing angle and the relief of the covered area.

II.3.2.2.4 *Filtering speckle effects*

In order to improve the quality of the radar image, it is possible to reduce the speckle by using specific filters. Among these filters, there are simple filters of linear type (median and

Page | 58

average) and more complex nonlinear type filters (Frost, Lee, Gamma-Map). Those filters allow to reduce random uncertainties related to the coherence interference of the waves reflected from the many elementary scatters. Speckle removal filters with excellent noise elimination capabilities also degrade the radiometric and spatial resolution and lead to loss of detailed information in images.

Images were filtered using one of the well-known filters for despeckling and enhancing SAR images, the refined Lee speckle filter described in Lee et al, (1994) and Lee (1999). This filter is based on the sigma probability of a Gaussian distribution. It filters the image noise by averaging only those pixels within the two-sigma range of the center pixel within a scanning window. This method gives the liberty to select the number of the neighbor pixels of the center pixel instead of the whole neighbor pixels of the center pixel being used as in the traditional Lee filter. In this work a sliding window of size 5×5 is chosen among the other (7×7, 9×9 or 3×3) beacause Larger windows provide more speckle smoothing but may smear fine details. Smaller windows should be used if image texture preservation is required.

II.3.2.3 High resolution reflectances

The VNIR Landsat reflectances are aggregated at 100 m resolution, consistent with Landsat LST spatial resolution. Surface reflectances are used to calculate the NDVI, defined as the ratio of the difference between the spectral reflectance measurements acquired in NIR and red to their sum. The fractional green vegetation cover (f_{gv}) is estimated from an empirical relationship with NDVI (Gutman and Ignatov, 1998):

$$f_{gv} = \frac{NDVI - NDVI_{bs}}{NDVI_{gv} - NDVI_{bs}} \qquad (II.2)$$

Where $NDVI_{gv}$ and $NDVI_{bs}$ are the NDVI over full-cover green vegetation and bare soil, respectively. The NDVI end-members are derived from the 2015-2016 time series of Landsat data as the minimum and maximum value of the 100 m resolution NDVI within the whole selected areas for the bare soil and full-cover green vegetation case, respectively. $NDVI_{bs}$ and $NDVI_{gv}$ are founded equal to 0.15 and 0.99, respectively.

The surface emissivity was estimated from an empirical relationship with NDVI and soil/vegetation emissivity components:

$$\varepsilon = \varepsilon_v - (\varepsilon_v - \varepsilon_s) \left(\frac{NDVI - NDVI_{gv}}{NDVI_{bs} - NDVI_{gv}} \right)^k \qquad (II.3)$$

where ε_v is the vegetation emissivity (set to 0.99), ε_s is the soil emissivity (set to 0.96), k is an attenuation coefficient relevant to the relation between LAI-NDVI and NDVI-emissivity ranging from 2 to 3. In Olioso et al. (2013) the value of k is derived from the shape of the NDVI-emissivity relationship for a range of soil moisture conditions and vegetation canopy emissivities. In our case, it was adjusted to 2 based on the NDVI-LAI relationship established in the same region by Er-raki et al. (2007). Note that this value was used in Tardy et al. (2016) over the same (semi-arid) region.

II.4 Conclusion

This chapter presents the dataset that we will use in chapter III. *In situ* measurements and satellite data are collected over two different sites in a semi-arid region. The sites used are selected in order to test and implement the different models and approaches developed in this work (see chapter III). Using different sites with varying conditions allows to test the stability of the proposed approaches to estimate NSSM, ET and LST over heterogeneous and different soil characteristics.

The in situ NSSM measurements and samples were used to validate the simulated NSSM at high resolution from radar and thermal data. LST data were used as an input to improve and spatialize the P-M model to monitor ET and hydric stress of wheat crop and also to validate satellite LST. Meteorological data are used as forcing measurements of the energy balance (EB) model to estimate the extreme temperatures used to obtain the soil evaporative efficient (SEE) independently from the measured ET. Finally the measured ET is used to validate the simulated ET by the P-M model.

Chapter III Models & methods

Contents

_____

_____

III.1 Introduction

After the description of dataset and study sites in the previous chapter, we will dedicate this chapter to the description of the different modelling approaches. The first one is the modified Penman-Monteith (P-M) equation based on the new established relationship between the surface resistance and the stress index estimated from surface temperature (LST) and extremes surface temperature.to estimate crop evapotranspiration. A mapping of the stress index and evapotranspiration over the R3 site was also assessed using LST and NDVI derived from Landsat data. Monitoring wheat stress requires high spatio-temporal LST data resolution. Landsat data are available each 16 days in clear sky conditions, otherwise every month or more. Therefore, a high spatio temporal LST data are required. One of the practical solution to get LST at high resolution is the disaggregation of the LST from satellite that provide LST at low spatial resolution but at high frequency (e.g MODIS, each day). This is the second model that aims to disaggregate LST from 1 km to 100 m resolution using two approaches: Multi-linear regressions technique (MLR) and the radiative transfer model (RTM). The stress index estimated from LST to estimate evapotranspiration is involving a mixture effect of soil evaporation which controlled by surface soil moisture and wheat transpiration which controlled by root zone soil moisture. To distinguish between the wheat and the soil contributions, we focused on retrieving surface soil moisture under bare soil. Two approaches were used, the first one based on only radar data and the second one based on a synergetic approach between radar and thermal data. The retrieval approaches are also presented in this section. The extremes temperatures mentioned above were required for the majority of the retrieved approaches that estimate LE and SM. A description of the two main methods to estimate the extremes temperatures are also detailed. The first model is based an energy balance model forced by meteorological data and the second model is based on the contextual information acquired from the LST-f_{gv} polygon, where f_{gv} is the fraction of green vegetation.

III.2 Soil moisture indices (SMP)

For soil moisture estimation using satellite data it is crucial to select a model that can best correlate remotely sensed SMP to soil moisture. During the investigated study, three soil moisture indexes have been used depending on the surface conditions (vegetation cover, bare soil): thermal-, radar- and combining thermal/radar- based SMP.

The SMP were estimated at high spatiao-temporal resolution by normalising either radar data (Sentinel-1 backscatter coefficient), thermal data (Landsat LST data) and by combining both radar and thermal data.

The LST can be used to monitor the SM because of its ability to control the biological and physical processes that occur at the land surface. For example, over bare soil area, LST refers to the soil surface temperature; and for densely vegetated areas, the LST indicates the vegetation canopy temperature under the assumption of energy balance. An increase in the vegetation canopy temperature is an initial indicator that the vegetation is subject to water stress.

Thermal based proxy that reflect the SM conditions is calculated by normalizing the LST by its endmembers, as equation (I.4 presented in chapter I). The LST based index is calculated as in Wang et al. (2001):

$$SMP_{Ts} = \frac{LST_{dry} - LST}{LST_{dry} - LST_{wet}} \qquad \text{(III.1)}$$

where LST_{wet} and LST_{dry} are the endmembers LST and corespond to the LST in fully wet and dry surface conditions.

The endmembers LST are either simulated by an energy balance model in fully wet and dry surface conditions, respectively (Merlin et al., 2016; Stefan et al., 2015) or extracted from the contextual information (image-based approach).

We therefore distinguish between stressed and unstressed conditions via the SMP_{Ts}. Especially, SMP_{Ts} equals 1 for $LST = LST_{wet}$ (energy-limited evaporation), which means that vegetation is unstressed. In the opposite case, SMP_{Ts} equals 0 for $LST = LST_{dry}$ (soil-controlled evaporation), which means that vegetation is undergoing water stress.

In this study, the thermal derived SMP is using LST data derived from Landsat-7/8 sensors combined with the LST endmembers (in wet and dry conditions) simulated by a surface energy balance model driven by meteorological forcing and Landsat-derived fractional vegetation cover. The thermal sensors receive a composite signal from the surface, which include the soil and vegetation. Therefore, the thermal-SMP is used over a mixture of wheat and bare soil pixels in the aim of retrieving the ET. ET modelling is based on a modified Penman-Monteith equation obtained by introducing a simple empirical relationship between

surface resistance (r_c) and a SMP. The P-M model is a one-source models consider the soil and vegetation as a composite leaf (big leaf model).

The issue with the thermal-based SMP is that remotely sensed LST data, are not available at high spatio-temporal resolution. The current spaceborne thermal sensors provide data at either high temporal or high spatial resolution separately which limit the number of applications domain. In addition, thermal data are affected by clouds, which further worsen the repetitiveness of the HR thermal-data. To solve the above-mentioned problems, SMP derived from S-1 data could be an appropriate alternative. The radar-based SMP can be expressed as in Fieuzal (2010) and Wagner et al. (1999a) using S-1 data:

$$SMP_\sigma = \frac{\sigma^0_{pp} - \sigma^0_{pp,min}}{\sigma^0_{pp,max} - \sigma^0_{pp,min}} \qquad\qquad (III.2)$$

with $\sigma^0_{pp,max}$ and $\sigma^0_{pp,min}$ being the maximum and minimum backscatter coefficient, respectively and p=V (Vertical) or H (Horizontal).

The radar-based SMP seems better in term of the backscatter coefficient data availability, but the σ^0_{pp} is affected by several variables (vegetation water content, roughness, polarisation,…). Therefore, to get an accurate SMP we need to incorporate theses effects over a vegetated surface.

Otherwise, disaggregating low spatial resolution LST data derived from existing satellites using ancillary data available at high spatio-temporal resolution could compensate for the lack of high spatial resolution LST observations. Note that, over bare soil, VV-polarized signal was founded to be affected by SM and surface roughness. In this context, a new method is developed to disaggregate kilometric MODIS LST at 100 m resolution by including the σ^0_{pp} derived from S-1 backscatter, which is indirectly linked to surface soil moisture $SMP_{\sigma vv}$ over bare soil. The radar derived soil moisture index $SMP_{\sigma vv}$ is estimated as in equation I.10 as follow:

$$SMP_{\sigma vv} = \frac{\sigma^0_{vv} - \sigma^0_{vv,min}}{\sigma^0_{vv,max} - \sigma^0_{vv,min}} \qquad\qquad (III.3)$$

where $\sigma^0_{vv,max}$ and $\sigma^0_{vv,min}$ are the maximum and minimum σ^0_{vv} during the season and over the study area. $\sigma^0_{vv,min}$ and $\sigma^0_{vv,max}$ hence represent the driest and the wettest pixels observed at 100 m resolution over the study site, respectively.

The SM may be accurately estimated if pure soil information can be separated from the composite context. Thermal-SMP (Eq III.1) has been also used to calibrate radar backscatter

coefficient acquired from S-1 data in order to estimate quantitative soil water content over bare soil conditions.

III.3 Endmembers temperatures estimation

III.3.1 Modelling extreme temperatures: physically based energy balance model

Estimating endmembers temperatures independently of the surface conditions within an area is reached by running a surface energy balance model forced by meteorological data. The developed algorithm is presented in this section. In practice, the wet and dry conditions are simulated by setting the surface resistance values equal to zero and infinity, respectively.

The surface net radiation R_n is expressed as:

$$R_n = (1 - \alpha)\, R_g + \varepsilon(R_{atm} - \sigma\, LST^4) \qquad\qquad (III.4)$$

with α (-) being the surface albedo (set to 0.20), R_{atm} stands for the atmospheric longwave radiation (W m^{-2}) and $\sigma = 5.67 \times 10^{-8}$ the Stephan-Boltzmann constant (W m^{-2} K^{-4}). R_g is the global radiation (W m^{-2}) and ε is the surface emissivty. The downward atmospheric radiation at surface level is expressed as:

$$R_{atm} = \varepsilon_a \times \sigma T_{air}^4 \qquad\qquad (III.5)$$

where T_{air} is the air temperature (K), ε_a is the atmospheric emissivity estimated as in Brutsaert (1975):

$$\varepsilon_a = 1.24 \times \left(\frac{e_a}{T_{air}}\right)^{\frac{1}{7}} \qquad\qquad (III.6)$$

with e_a (kPa) the saturated water vapour pressure calculated as:

$$e_a = e_s(T_{air}) \times \frac{rh_a}{100} \qquad\qquad (III.7)$$

with e_s (kPa) where the latter is calculated as:

$$e_s = 0.611 \times e^{\left(\frac{17.27 \times T_{air}}{T_{air} + 273.3}\right)} \qquad\qquad (III.8)$$

and rh_a is the air humidity (%). The ground flux G is estimated as a fraction of net radiation at the soil surface $R_{n,s}$ (Choudhury et al., 1987; Kustas and Daughtry, 1990):

$$G = \Gamma \times R_{n,s} \qquad\qquad (III.9)$$

with Γ being a fractional empirical coefficient set to 0.2 (Kustas et al., 1991), and $R_{n,s}$ is given by:

$$R_{n,s} = R_n \times (1 - f_{gv}) \tag{III.10}$$

with f_{gv}, the fraction of green vegetaion and R_n is the net rediation.

The sensible heat flux (H) is given by:

$$H = \rho \times c_p \times \beta \times \frac{LST - T_{air}}{r_{a,h}} \tag{III.11}$$

With $r_{a,h}$ is the aerodynamique resistance (s m^{-1}), ρ is the Mean air density at constant pressure, kg m^{-3} and c_p is the Specific heat of air, MJ kg^{-1} K^{-1}. LST is the surface temperature (soil + vegetation).

where β is the "β function" calculated as follows as a function of LAI:

$$\beta = 1 - \frac{l}{LAI \times m \times \sqrt{2\pi}} e^{-\frac{(\ln(LAI) - n)^2}{2 \times m^2}} \tag{III.12}$$

with l, m and n are empirical coefficients equal to 0.17 for l and 0.8 for m and n (Boulet et al., 2012). These values were calibrated for the wheat in the same R3 study site. LAI is the leaf area index. For bare soil LAI=0 which lead to β =1 and H equation transform into:

$$H = \rho \times c_p \times \frac{T_s - T_{air}}{r_{a,h}} \tag{III.13}$$

With T_s (K) is the bare soil temperature.

The latent heat flux (LE, W m^{-2}) is estimated using the following equation (Eq. III.14):

$$LE = \frac{\rho \times c_p}{\gamma} \times \frac{e_s - e_a}{r_{a,h} + r_c} \tag{III.14}$$

Over bare soil condition the resistance representing the transfer through the surface components r_c is equal to soil evaporation resistance r_s.

Finally, for running the energy balance model, it was set LST = T_{air} and search for the value of LST that minimises the following cost function F (LST):

$$\mathbf{F\ (LST) = (Rn - G - H - LE)^2} \tag{III.15}$$

F (LST) is named "cost function" as it is the function to be minimised in order to find the LST value corresponding to the energy balance closure (e.g. Merlin et al. 2016).

III.3.2 Image based extreme temperature: contextual method

As the meteorological data may not be available everywhere with sufficient accuracy, remote sensing-based temperature endmembers could be used to fill this gap. In particular, the contextual method has been successfully used to monitor evapotranspiration over large areas, by relying mainly on the distance between the observed LST and the hypothetical LST values in fully dry and wet conditions. Especially, the image-based nature of the contextual method makes it easily applicable to different areas (i.e. the method is self-calibrated). The contextual information contained in remotely sensed LST and vegetation index (such as NDVI) can be extracted by interpreting the LST-NDVI (LST-f_{gv}) feature space (in the shape of a triangle or trapezoid). This method was firstly proposed by Goward et al. (1985) and has been widely used to monitor soil water content (Kim and Hogue, 2012; Merlin et al., 2008b; Sandholt et al., 2002; Sobrino et al., 2012), evaporative fraction (Batra et al., 2006; Wang et al., 2006), evapotranspiration (Merlin, 2013; Stefan et al., 2015), drought (Wan et al., 2004), surface resistance (Nemani and Running, 1989), land use and land cover change (Julien and Sobrino, 2009). There are various popular models based on the contextual method such as: surface energy balance algorithm for land (SEBAL) (Bastiaanssen et al., 1998b), mapping evapotranspiration at high resolution with internalized calibration (METRIC) (Allen et al., 2007) and simplified surface energy balance index (S-SEBI) (Roerink et al., 2000).

The contextual method allows the estimation of LST endmembers for different surface conditions.

In this work, the contextual method is used to derive the soil temperature endmembers over the selected area covering the experimental sites. Once the polygon identified, the **$T_{bs,d}$** and **$T_{bs,w}$** correspond to fully dry (vertex A) and wet (vertex B) conditions over bare soil, which are characterised by the largest and smallest LST in the lower NDVI (f_{gv}) range (< 0.2), respectively. Vertex C correspond to fully vegetated area.

A visual representation of the LST-f_{gv} space using low/ high resolution data identifies the three extremes values for f_{gv} (0, 1) are presented in Fig III.1.
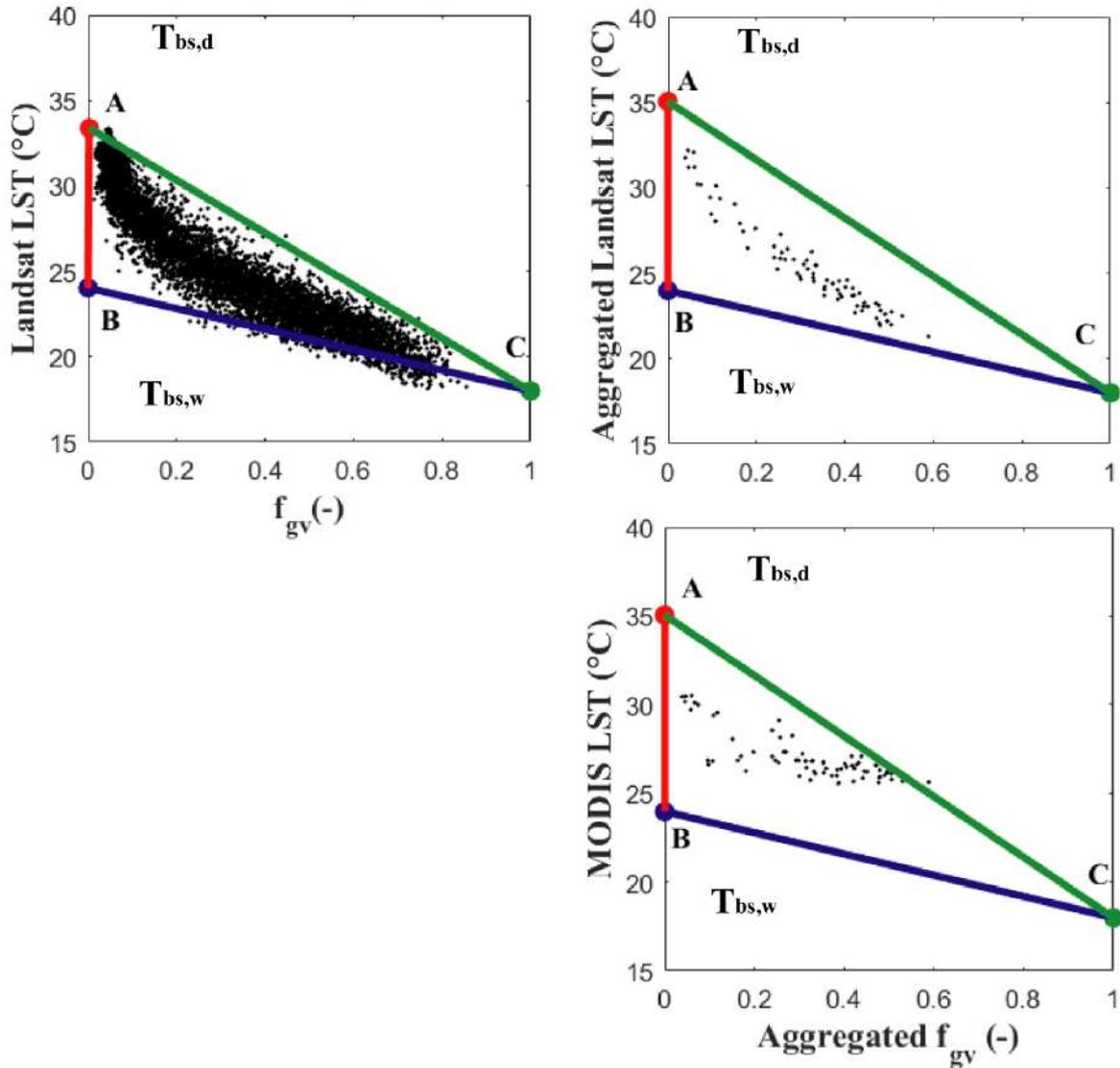
Figure III.1: Scatterplot of LST-f$_{gv}$ spaces at 100 m (left) and 1 km (right) resolution on February 07. In the LR case, extreme temperatures are estimated using a soil energy balance (EB) model over R3 site.

III.4 Integrating the SM indices to improve the water need estimates

III.4.1 Enhance Penman-Monteith method to estimate ET: thermal-based SMP

The P-M model results from the combination of the energy balance equation and the mass transfer equation for estimating the evapotranspiration of a free water surface.

The latent heat flux (LE (W. m^{-2})) of wheat was modelled by using the following P-M equation:

$$LE = \frac{\Delta(R_n - G) + \rho c_{p\frac{D}{r_{a,h}}}}{\Delta + \gamma\left(1 + \frac{r_c}{r_{ah}}\right)} \tag{III.16}$$

where Δ stands for the slope of the saturation vapour pressure curve at air temperature (kPa $°C^{-1}$). The psychrometric constant (kPa $°C^{-1}$) and the mean air density at constant pressure (kg m^{-3}) are presented by γ and ρ respectively while c_p stands for the specific heat of air (MJ kg^{-1} $°C^{-1}$). The vapour pressure deficit D (kPa) is obtained by calculating the difference between the air vapour pressure e_a (kPa) and the saturated water vapour pressure e_s (kPa) where the latter is calculated as in equation (Eq III.8):

In Eq. III.16, all parameters are deduced from the meteorological variables measured by the automatic meteorological station. However, the use of this model requires determining the aerodynamic resistance (r_{ah}, s m^{-1}) and bulk canopy resistance (r_c, s m^{-1}). r_{ah} is calculated at a reference height z_r in the boundary layer above the canopy by (Brutsaert, 1982):

$$r_{ah} = \frac{(\log[(z_r - d)/z_m] - \psi_m) \times (\log[(h_c - d)/z_m] - \psi_h)}{kar^2 \times u_a} \tag{III.17}$$

Where z_r is the reference height measurments, kar is the Von Karman constant equal to 0.44, the displacement height (to adjust the effects of vegetation height on wind displacement) and the height of the dynamic soil roughness are presented as , $d = 2/3\ h_c$ and $z_m = h_c/8$ respectively.

h_c the canopy height was derived from NDVI using the equation developed in Er-raki et al. (2007) over the same area which is applied just for wheat culture.

$$h_c = 0.0456\ e^{(3.5837 \times NDVI)} \tag{III.18}$$

The ψ_m and ψ_h presents the atmospheric stability function and the sensitive heat stability function, respectively.

$$\psi_m = 2\ln\left(\frac{1+\varphi}{2}\right) + \ln\left(\frac{1+\varphi^2}{2}\right) - 2\arctan(\varphi) + \frac{\pi}{2} \tag{III.19}$$

$$\psi_h = 2.\ln\left(\frac{1+\varphi^2}{2}\right) \tag{III.20}$$

With $\varphi = (1 - 16\xi)^{\left(\frac{1}{4}\right)}$ is a universal function that aims to stabilize the profile-flow relationship. $\xi = \frac{z_r - d}{Lmo}$ is a non-dimensional term that relies the z_r to the Monin-Obukov coefficient (Lmo), the latter is an important parameter in meteorology.

$$Lmo = -\frac{\rho\mu^{*3}}{kar\,g\left(\frac{H}{Cp\,Ta}+\frac{0,61\,LE}{\lambda v}\right)} \tag{III.21}$$

with g (m s^{-2}) being the gravitational constant, λv being the latent heat of vaporization of water (J kg^{-1} °C^{-1}) and $\mu*$ represents the friction velocity and can be found from the logarithmic wind profile relationship (Dyer, 1974) :

$$\mu^* = \frac{kar \times u_a}{\ln\left[\frac{(z_r - d)}{z_m}\right] - \psi_m} \tag{III.22}$$

For irrigated crops, the canopy resistance r_c is not assumed to be constant. It changes according to available energy, vapour pressure deficit, and other environmental factors.

Another equation is used to estimate rah as in Choudhury et al. (1986) based on the Richardson number Ri. This equation represents the importance of natural relative to forced convection.

$$r_{ah} = \frac{r_{ah0}}{(1+Ri)^\eta} \tag{III.23}$$

where η (unitless) being a coefficient equal to 0.75 in unstable conditions (Ts > T$_{air}$) and to 2 in stable conditions (Ts < T$_{air}$). r_{ah0} (s m^{-1}) being the neutral aerodynamic resistance and it symbolizes the aerodynamic resistance that neglects natural convection, is computed as:

$$r_{ah0} = \frac{\ln^2\left(\frac{z_r}{z_m}\right)}{u_a.kar^2} \tag{III.24}$$

Richardson number (unitless) is a measure of the influence of atmospheric stability on the flux-gradient relationship in the surface layer, is computed as:

$$Ri = \frac{5gz_r(LST - T_{air})}{T_{air}.u_a^2} \tag{III.25}$$

In this study, we propose to use a simple empirical relationship between r_c and a vegetation water stress index (SI) which is calculated as:

$$SI = 1 - SMP_{Ts} \tag{III.26}$$

where SMP$_{Ts}$ is the soil moisture proxy estimated using laand surface temperature. Further, The ET (LE flux) estimates are spatialized within a 10×10 km^2 area centred over the R3 sector which is mainly covered by wheat crops. The R3 perimeter is occupied by different

cultures (wheat, alfalfa, orange, and olive), so before spatializing the ET, a land use has been performed in order to distinguish between wheat/bare soil and other crops.

A flowchart of the retrieval approach is presented in Fig. III.2.
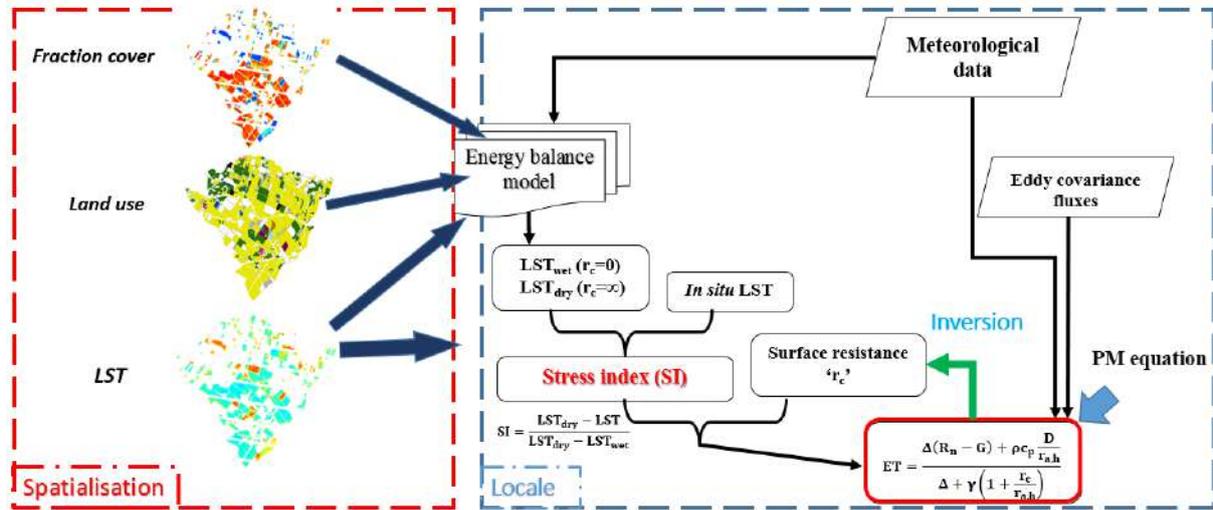
Figure III.2: Flowchart of the retrieval approach to estimates LE using locale and spatial data acquired from Landsat.

III.4.2 Calibration of the radar data to retrieve SM: radar/thermal based SMP

Retrieving SM from radar data implies establishing a relationship between the volumetric SM and the backscatter coefficient ($\sigma°$) obtained from SAR data. Over bare soil surfaces, the VV and VH polarized backscatter signal depends of SM, surface roughness and the observation configuration mainly defined by the incidence angle and microwave frequency (Lievens and Verhoest, 2011). As a first approximation, a linear relationship can be established as following (Champion and Faivre, 1997; Dobson and Ulaby, 1986; Holah et al., 2005; Le Hégarat et al., 2002; Ulaby et al., 1979):

$$SM = SM_{min} + (SM_{max} - SM_{min}) \times SMP \qquad (III.27)$$

where SMP is a radar-based SM proxy (function of $\sigma°$) and SM_{min} and SM_{max} the minimum and maximum SM values depending mainly on the soil porosity (Brisson and Perrier, 1991; Cosby et al., 1984).

As previously mentioned, we proposed a method to integrate the thermal data extracted from L7/L8 data into a S1-based retrieval approach. The performance of the radar/thermal combining approach was evaluated by comparing it to a benchmark approach based on radar only. The two (benchmark and combined radar/thermal) methods for estimating SMP and the

SM endmembers of Eq. III.27 are presented in the schematic diagram of Fig. III.3 and are described below.

III.4.2.1 Benchmark approach: based only on radar data

The radar derived soil moisture proxy (SMP_{σ}) of Eq. III.3 is used to estimate the SMP based on S-1 radar data.

As in Omer et al. (2015) and Wagner et al. (1999b), the minimum SM value is set to the residual SM, which can be related to clay fraction (f_{clay}) by the formula (Brisson and Perrier, 1991):

$$SM_{min}(m^3/m^3) = 0.15 \times f_{clay} \qquad \text{(III.28)}$$

and the maximum SM value is set to the SM at saturation, which can be estimated from sand fraction (f_{sand}) as in Cosby et al. (1984).

$$SM_{max}(m^3/m^3) = 0.489 - 0.126 \times f_{sand} \qquad \text{(III.29)}$$

III.4.2.2 New approach: combined radar/thermal data

Radar/thermal SMP is estimated using a piecewise linear relationship between SMP_{Ts} and σ^0_{pp}:

$$SMP_{\sigma+Ts} = \begin{cases} 1, & \text{if } SMP_{Ts} \geq 1 \\ a_0 \ \sigma^0_{pp} + b_0, & \text{if } 0 < SMP_{Ts} < 1 \\ 0, & \text{if } SMP_{Ts} \leq 0 \end{cases} \qquad \text{(III.30)}$$

with a_0 and b_0 being two empirical parameters and SMP_{Ts} defined as in Eq. III.1 except that, the observed LST and simulated endmembers temperatures are estimated over bare soil condition using bare soil temperature Ts. Therefore, LST_{wet} and LST_{dry} in Eq. III.1 are replaced by $T_{bs,w}$ and $T_{bs,d}$, respectively. Both a_0 and b_0 parameters were calibrated using L7/L8 thermal data by comparing $SMP_{\sigma+Ts}$ to SMP_{TS}. In this paper, T_s was derived from either *in situ* Apogee or satellite L7/8 thermal data. Both temperature endmembers were simulated by running a soil energy balance (EB) model forced by meteorological data and with a prescribed soil resistance to evaporation r_{ss} (Merlin et al., 2016; Stefan et al., 2015). In addition, a sensitivity analyses was performed using the contextual method to assess the impact of uncertainties in temperature endmembers on SM estimation.

We considered that SMP_{Ts} is a good approximation of the soil evaporative efficiency (SEE) defined as:

$$SEE = \frac{LE_s}{LE_p} \qquad (III.31)$$

with LE_s and LE_p being the actual and potential soil evaporation, respectively. SEE is known to be strongly dependent on SM (e.g. Nishida et al., 2003) and its expression as a function of soil temperature (namely SMP_{Ts} in Eq. III.1 has been found to be valid in a large range of conditions (Merlin et al., 2016). This allows for simply relating SMP_{Ts} to SM using the piecewise linear SEE model (Budyko, 1956; Manabe, 1969):

$$SEE = \frac{SM}{SM_c} \qquad (III.32)$$

with the SM_C being equal to ¾ of the soil moisture at field capacity SM_{fc} (m^3 m^{-3}). At this SM value, the SEE reaches its maximum, at which the evaporation process switches from moisture-limited to energy-limited conditions. SM_{fc} is estimated as in Mahfouf and Noilhan, (1996) by the formula:

$$SM_{fc} = 0.089 \times (f_{clay})^{0.3496} \qquad (III.33)$$

Calibration of a_0 and b_0 parameters of $SMP_{\sigma+Ts}$ (Eq. III.30) using independent SMP_{Ts} (Eq. III.1) estimates relies on the condition that SMP_{Ts} does not reach its saturation value (1), meaning that SM does not exceed SM_C. A direct consequence is that the SM endmembers in Eq. III.27 are set to SM_{res} (residual soil moisture) and SM_C for SM_{min} and SM_{max}, respectively. Unlike SMP_{Ts}, the radar signal does not reach a maximum threshold except for very moist soils (Bruckler et al., 1988; Chanzy, 1993; Dobson and Ulaby, 1981). Therefore, the SM retrieved from the combined thermal and radar data is calibrated for SM values between SM_{res} and SM_C (corresponding to $SMP_{Ts} < 1$), but it may exceed the SM_C value for backscatter values larger than $\frac{SM_C - b_0}{a_0}$.
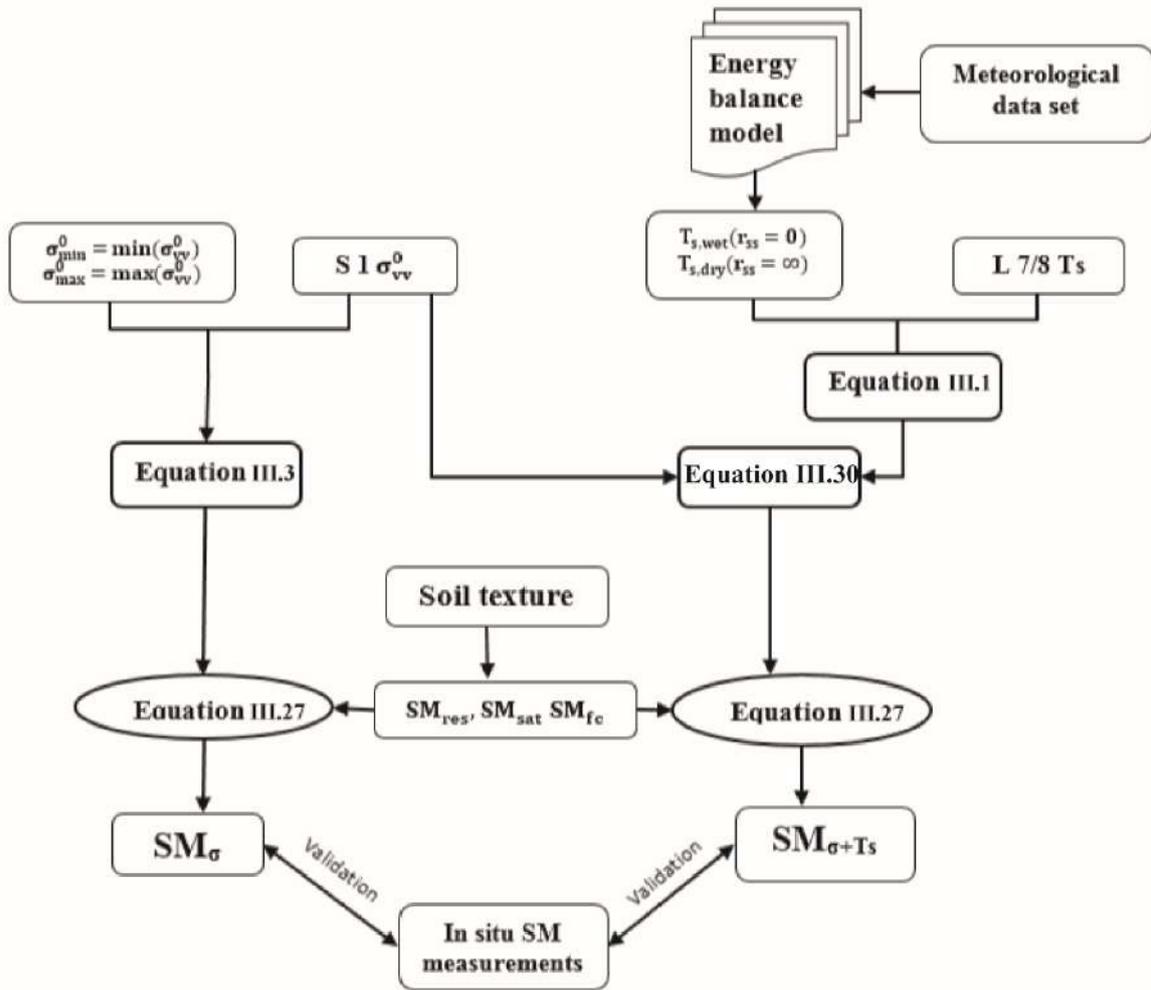
Figure III.3: Flowchart for the benchmark (radar only, on the left) and new (combined thermal and radar, on the right) SM retrieval approaches.

To assess the relationship between SMP_{Ts} and NSSM, Fig. III.4 plots the SMP_{Ts} simulated by Eq. III.1 as a function of *in situ* NSSM (at Landsat overpass time) and L7/8 data, separately. Although SMP_{Ts} generally ranges from 0 to 1, some negative values were observed in the lower SM range. This is due to the fact that $T_{bs,d}$ and $T_{bs,w}$ were estimated by the EB model, independently from T_s measurements. A nonlinear behaviour of SMP_{Ts} was obtained when considering the full SM range. The piecewise linear SEE model was superimposed for the values of SM ranging from 0 to SM_C and for SM values larger than SM_C. SMP_{Ts} value were consistent with the simple SEE model of Budyko, (1956) and Manabe (1969), for both *in situ* and satellite thermal data sets. However, note that most of the SMP_{Ts} values derived from Landsat data (blue colour) correspond to the driest period. This is due to both the relatively low temporal resolution of thermal data and also to the cloud coverage on several wet

overpass dates. Nonetheless, Landsat-derived SMP_{Ts} estimates were strongly consistent with *in situ*-derived SMP_{Ts} estimates and still range between 0 and 1.
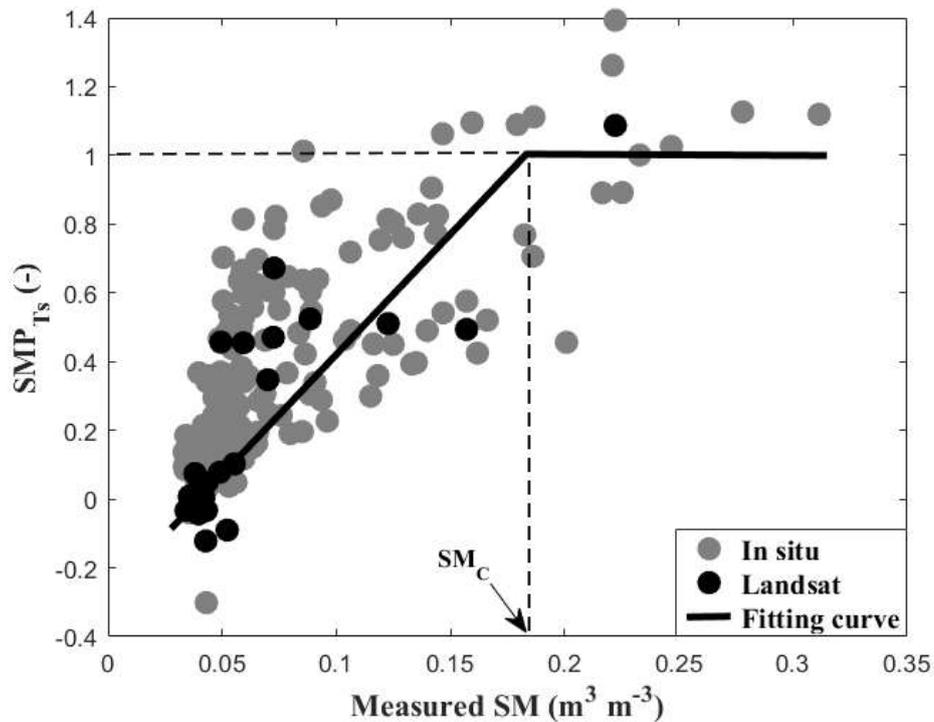
Figure III.4: The SMP_{Ts} (Eq III.1) derived from 1) in situ LST data collected at 11:00 am (Landsat overpass time) and 2) L7/8 LST-derived data is plotted as a function of in situ SM (Measured SM) at Sidi Rahal site.

III.4.3 Improve the spatio-temporal resolution of MODIS LST data: radar-based SMP

Landsat and ASTER sensors provide LST data at HR with low temporal revisit. Nevertheless, the temporal resolution of the ASTER / Landsat sensors is 16 days, which is relatively long compared to the ground surface drying time and the hydric status change especially over irrigated area. Therefore, the objective is to develop the methods for disaggregation LST with high temporal resolution but low spatial resolution as the case of MODIS data.

Two disaggregation techniques are applied in this work using the same input data derived from microwave (radar) and optical (NDVI) data. The methodologies are tested over two different study sites, including a range of conditions (land use, soil hydric status,…). The two versions are named multi-linear regression (MLR) and radiative transfer model (RTM) techniques. Both methodologies are based on a scale invariant relationship between LST and other ancillary variables, which are statistically correlated to LST pixel by pixel. In this work

the disaggregation methodologies were applied to aggregated Landsat derived-LST (as a first assessment by minimizing uncertainties in low resolution (LR) LST) and then applied to MODIS/Terra LST (as a real case application). The 100 m resolution was chosen as the target downscaling because it is the lowest spatial resolution at which all the input HR data are available.

A description of the MLR and RTM techniques is presented in the following subsections.

III.4.3.1 MLR technique

The MLR technique is based on a linear regression at LR between LST and auxiliary data. This method was firstly developed by Kustas et al. (2003) using NDVI as a biophysical indicator of LST. In practice, a least-squares fit is performed between LST (T) and the f_{gv} aggregated at 1 km. Formally, The D_1 algorithm is expressed as:

$$D_1 \qquad\qquad T_1 = LST_{km} + a \times \left(f_{gv} - f_{gv,km}\right) \qquad\qquad (III.34)$$

with a being the regression coefficient of the least squares regression between LST_{km} and $f_{gv,km}$, and LST_{km} and $f_{gv,km}$ the LR LST and the aggregated f_{gv}, respectively.

The D_1' disaggregation algorithm is proposed to improve the D1 algorithm by inserting additional information about SM (information derived from the S-1 data). A MLR is performed between LST, f_{gv} and σ_{vv}^0 at LR:

$$D_1' \qquad\qquad T_1' = LST_{km} + a' \times \left(f_{gv} - f_{gv,km}\right) + b' \times \left(\sigma_{vv}^0 - \sigma_{vv,km}^0\right) \qquad (III.35)$$

With a' and b' being the slopes of the MLR equation at 1 kilometre spatial resolution, and $\sigma_{vv,km}^0$ the aggregated σ_{vv}^0.

III.4.3.2 RTM technique

III.4.3.2.1 Model description

This technique relies on a physically based radiative transfer equation rather than empirical linear regressions (MLR). The RTM approach (Merlin et al., 2012b) is formally written as:

$$D_2' \qquad\qquad\qquad T_2' = LST_{km} + \Delta T_2' \qquad\qquad\qquad (III.36)$$

With the corrective term $\Delta T_2'$ estimated using a RTM forced by high resolution input data derived from f_{gv} and σ_{vv}^0:

$$\Delta T_2' = T_{sim}(f_{gv}, SMP_{\sigma vv}) - \langle T_{sim}(f_{gv}, SMP_{\sigma vv}) \rangle_{KM} \qquad \text{(III.37)}$$

With T_{sim} being the LST simulated by the RTM, $\langle \ \ \rangle_{KM}$ the resampling function from 100 m to 1 km resolution.

The $T_{sim}(f_{gv}, SMP_{\sigma vv})$ is calculated as:

$$T_{sim}(f_{gv}, SMP_{\sigma vv}) = f_{gv} \times T_{fc,gv} + (1 - f_{gv}) \times T_{bs}^{sm} \qquad \text{(III.38)}$$

With $T_{fc,gv}$ is the temperature of full cover green vegetation and T_{bs}^{sm} the bare soil temperature estimated using a linearized RTM:

$$T_{bs}^{sm} = T_{bs,w} \times SMP_{\sigma vv} + T_{bs,d} \times (1 - SMP_{\sigma vv}) \qquad \text{(III.39)}$$

Where $T_{bs,w}$ and $T_{bs,d}$ are the wet and dry bare soil temperatures (°C), respectively. Note that the temperature end-members ($T_{fc,gv}$, $T_{bs,w}$ and $T_{bs,d}$) are estimated based on a synergy between the LST-f_{gv} space, the LST-σ_{vv}^0 space and a soil energy balance (EB) model.

Before applying the disaggregation methodologies, the endmembers required in the RTM method, namely the three temperatures ($T_{fc,gv}$, $T_{bs,d}$ and $T_{bs,w}$) and the three backscatter coefficients (green vegetation $\sigma_{vv,gv}^0$, bare dry soil $\sigma_{vv,bs,d}^0$ and bare wet soil $\sigma_{vv,bs,w}^0$), are determined from available information. Temperature endmembers vary from date to date depending on the growing stage of vegetation and the soil hydric status over differences landscapes within the selected areas.

III.4.3.2.2 LST endmembers

In this study, the LST at high resolution is assumed to be unknown and therefore, extreme temperatures should be derived from low resolution LST and possibly other ancillary (meteorological, f_{gv}) data. Two different techniques are combined to estimate the LST endmembers: the contextual LST-f_{gv} space and the EB model forced by available meteorological data. A description of the two used methodologies is presented in the section 5. In order to estimate soil extreme temperatures independently of remote sensing data a soil EB model is run to estimate $T_{bs,w}$ and $T_{bs,d}$.

On some days over the R3 area, the maximum temperature estimated by EB modelling appears relatively low compared to the maximum (both HR and LR) observed LST especially on the hottest days (summer). This is explained by the fact that the meteorological data used as forcing to EB model are collected at a wet alfalfa site, thus underestimating the 2-m air temperature over very dry and hot surface conditions. To correct for such a slight underestimation, the $T_{bs,d}$ is set to the maximum between the maximum value (T_{max}) observed at LR and EB estimation:

$$T_{bs,d} = \max \left[T_{max}, EB(r_{ss} = \infty) \right] \qquad (III.40)$$

The temperature of full cover vegetation ($T_{fc,gv}$) is set to the air temperature measured over the studies areas (Bastiaanssen et al., 1998b; Gillies and Carlson, 1995; Merlin, 2013; Roerink et al., 2000; Stefan et al., 2015).

III.4.3.2.3   *Backscatter endmembers*

Fig. III.5 presents the spatial variability of σ^0_{vv} pixel by pixel compared to f_{gv}. Based on the observed $\sigma^0_{vv} - f_{gv}$ space, the vegetation backscatter coefficient $\sigma^0_{vv,gv}$ is estimated as the σ^0_{vv} corresponding to $f_{gv}=1$, vertex C $(1, \sigma^0_{vv,gv})$ in the σ^0_{vv}-f_{gv} space. The backscatter of bare soil in dry ($\sigma^0_{vv,bs,d}$) and wet ($\sigma^0_{vv,bs,w}$) conditions is considered as the minimum and maximum backscatters observed at low f_{gv} (<0.2), vertex A $(0, \sigma^0_{vv,bs,d})$ and B $(0, \sigma^0_{vv,bs,w})$, respectively.

Figure III.5: Identification of the σ^0_{vv} endmembers using the S-1 backscatter plotted against fractional of green vegetation cover f_{gv} space for data on February 07 over R3 site.

The triangle formed in the σ^0_{vv}-f_{gv} space is not as well defined as in the LST-f_{gv} space. In fact, the spatial correlation between σ^0_{vv} and f_{gv} is affected by variabilities of both SM and soil

roughness. Therefore, $\sigma^0_{vv,bs,d}$ more precisely corresponds to a smooth (low roughness) dry soil and larger sigma values are expected over dry bare soil pixels with larger surface roughness (the data points on the other side of the AB segment).

A visual representation of the LST-σ^0_{vv} spaces at a LR and HR are plotted side by side in Fig. III.6. The LST-σ^0_{vv} space is surrounded by the three extremes backscatter values ($\sigma^0_{vv,gv}$"vertex C", $\sigma^0_{vv,bs,d}$ "vertex A", and $\sigma^0_{vv,bs,w}$"vertex B",) derived previously from the $\sigma^0_{vv} - f_{gv}$ space.
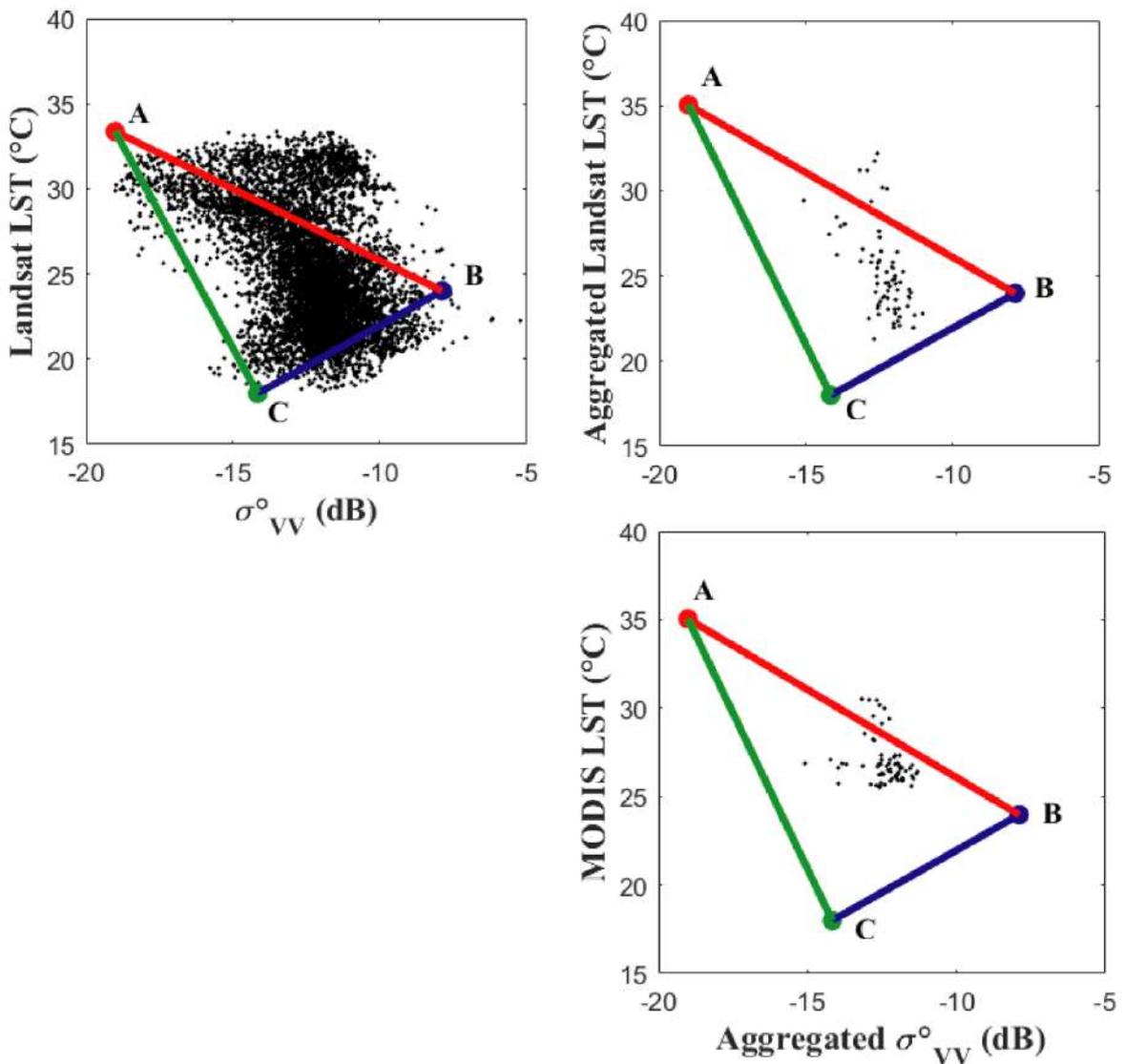
Figure III.6: Scatterplot of LST-σ^0_{vv} spaces at 100 m (left), aggregated Landsat temperature to 1 km (right) and MODIS-LST at 1 km (bottom) resolution on February 07. In the low resolution case, extreme temperatures are estimated using a soil EB model over R3 site.

The diagram in Fig. III.7 summarizes briefly the different disaggregation algorithms used in this work.
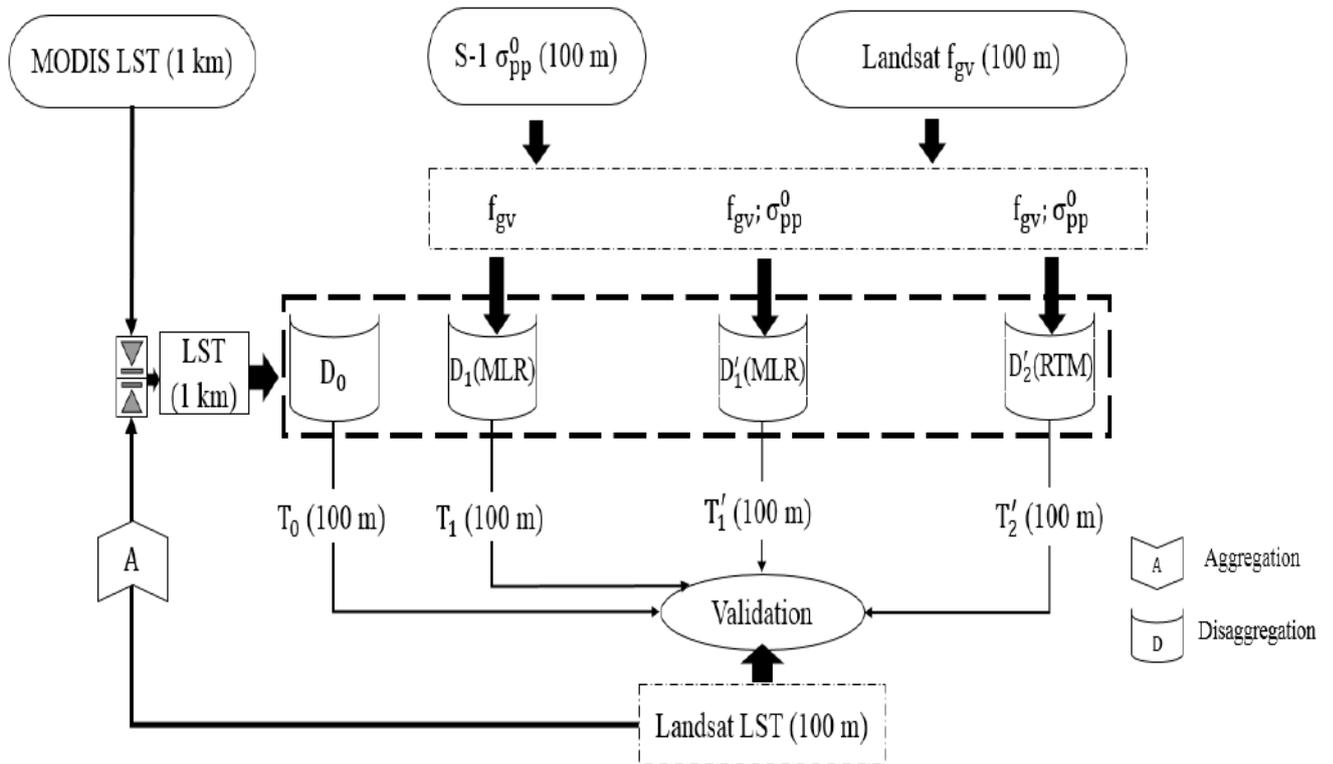
Figure III.7: Diagram showing the tow disaggregation algorithms and their input/output data.

The D_0 algorithm requires no ancillary data. By cons, D1 (MLR), D1' (MLR) and D2' (RTM) need additional data to disaggregate LST. D1 algorithm is based on f_{gv} only, while D1' and D2' are based on both f_{gv} and σ_{vv}^0.

III.5 Models evaluation

In order to judge and evaluate the performance of the modelling and the studied methods, it is possible to show the differences graphically, but it is also necessary to make a more quantitative comparison. To this end, several standard statistical criteria have been used listed in Table III.1.

Table III.1: Statistic indicators for evaluating the method performances.

Statistics	Formula	Notes
Root mean square Error	$$RMSE = \sqrt{\frac{1}{N}\sum_{i-1}^{n}(Y_i - X_i)^2}$$	Gives an indicator of model accuracy
Bias	$$MBE = \frac{1}{N}\sum_{i-1}^{n}Y_i - X_i$$	The mean error between the observations and the estimation
Correlation coefficient	$$R = \frac{\sum_{i-1}^{n}(Y_i - Ym)\times(X_i - Xm)}{\sqrt{\sum_{i-1}^{n}(Y_i - Ym)^2 \times (X_i - Xm)^2}}$$	Measures the degree of relationship between two variables
Determination coefficient	$$R^2 = \left(\frac{\sum_{i-1}^{n}(Y_i - Ym)\times(X_i - Xm)}{\sqrt{\sum_{i-1}^{n}(Y_i - Ym)^2 \times (X_i - Xm)^2}}\right)^2$$	Measures the percent of the variability explained by the model

N= Number of observations; X, Y: measured and simulated variables; Ym and Xm mean values

III.6 Conclusion

This chapter was dedicated to the description of the different approaches and models used to estimate SM, evapotranspiration and LST. A description of the P-M equation used to estimate the ET of wheat crop. Modified surface resistance linked to soil moisture proxy has been used as an input in P-M formulation instead of the common equations that depend on numerous factors related to pedological, biophysical and physiological processes. Seeing that, the used thermal data were acquired from Landsat observation (every 16 days in clear sky conditions) is not enough to monitor the hydric status of parcels, daily MODIS LSTs have been disaggregated using two different approaches: MLR and RTM techniques. The both approaches use f_{gv} or f_{gv} combined with radar-SM proxy as an ancillary data. To distinguish between the water consumed by the plants (transpiration) and evaporated one, accurate estimation of the SM over bare soil is needed. In this study SM was retrieved using a synergic approach between radar data derived from Sentinel-1 microwave observation and Landsat

thermal proxy (SMP_{Ts}). The calibration of radar-based SM retrieval approaches mainly relies on the calibration of roughness effects. This is precisely the idea behind proposing to use LST to calibrate radar data, which is less sensitive than radar to roughness. The developed approach is compared against a classical one which is based on radar data only. A description of methods used to estimates SM over bare soils have been presented. The thermal proxy were estimated using the endmembers temperature in dry and wet conditions, which are derived from the contextual information or modelled using energy balance model over bare soil to estimate SM and LST and over mixed pixels (soil + vegetation) to estimate LE.

Chapter IV Results and discussions

Contents

_____

IV.1 Introduction

This chapter contains the main results obtained during this thesis. Initially, we present the results of the P-M equation to estimate the surface ET of wheat over two different crop fields in terms of irrigation systems located in the R3 area. The proposed approach aims to modify the P-M equation by expressing r_c, which is the main parameter controlling latent heat flux, as a function of a thermal-derived Stress Index (SI). The use of LST as an indicator of the surface resistance in order to estimate the ET, is assessed by using the *in situ* measurements collected in the flood-irrigated site. The "observed" r_c is estimated by inverting P-M equation using ET measured by eddy covariance system. Then, a validation exercise is carried out over the drip irrigated-site using *in situ* data. LST data are a key variables for the P-M equation to estimate ET. Therefore, in order to enhance the temporal resolution of LST data a disaggregation of MODIS LST data is developed. The results of the disaggregation approaches MLR (D1 and D1') and RTM (D2') were presented which are applied to the seven dates when all the satellite (S-1, Landsat and MODIS) data are available. The disaggregated LST is evaluated against Landsat LST and in each case, disaggregation results are compared with those obtained in the no-disaggregation case (D0). A stepwise approach is presented by using the (1 km resolution) aggregated Landsat LST as the low resolution LST input prior to the application to MODIS LST. Finally, results of soil moisture at high resolution are presented. Two methodologies were applied to retrieve SM, the first one based on only radar data, the second based on the synergetic between radar and thermal data. The performance of the retrieved approaches is evaluated using in situ SM measurements over three study sites which had remained under bare soil condition.

IV.2 Consistency between image- and EBsoil-based extreme soil temperatures

As a first assessment of the performance of the space-based approach, the $T_{bs,d}$ and $T_{bs,w}$ estimated by the contextual method using Landsat data are compared against the ones modelled by EB model. The analysis is performed at the Landsat overpass time over the Sidi Rahal and R3 areas separately. Fig. IV.1 plots the T endmembers derived from EB model versus the space-based ones for the studied areas separately. A comparison between air temperature (T_{air}) and the $T_{bs,w}$ simulated by EB model is also presented (Fig IV. 1c, 1f). The statistical results in terms of R^2 and RMSE are shown in Fig. IV.1.
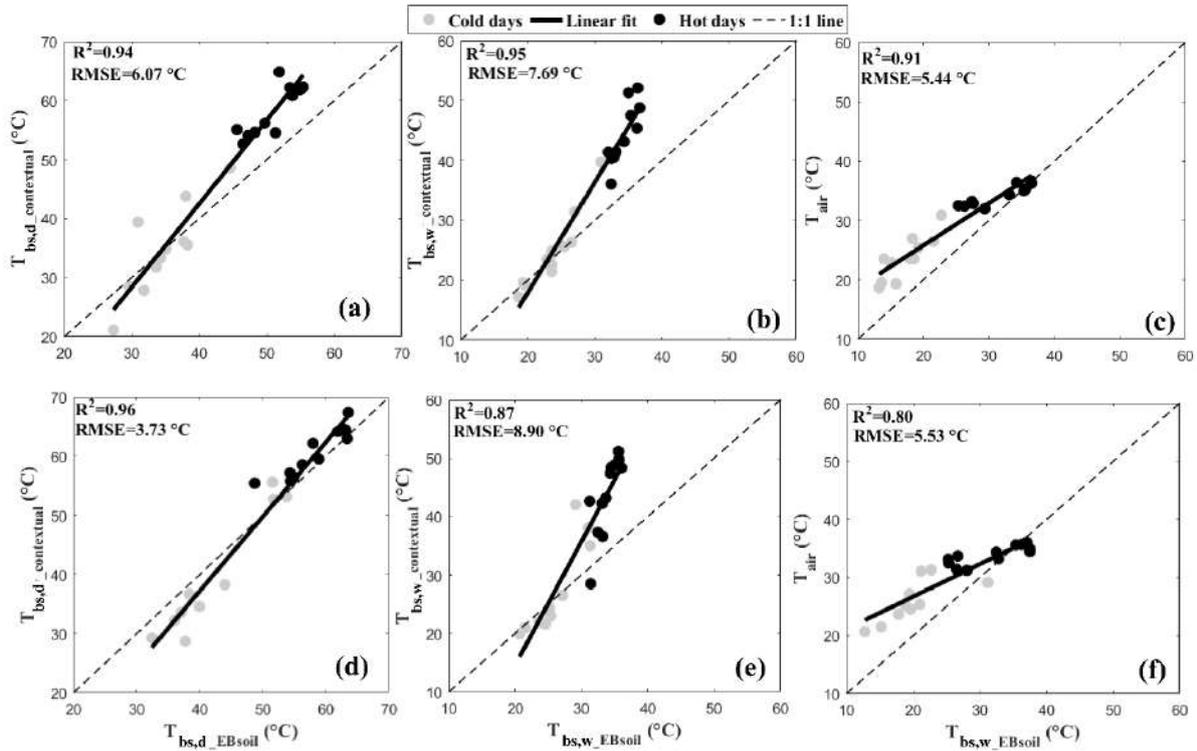
Figure IV.1: EB-simulated versus space-based soil temperature endmembers ($T_{bs,w}$ and $T_{bs,d}$) for R3 (a, b, c) and Sidi Rahal (d, e, f) sites separately.

A strong consistency is noticed between EB-derived and image-based extreme temperatures, especially for $T_{bs,d}$ (Fig IV. 1a, 1b). Statistical results in terms of R^2 and RMSE between modelled and remotely-sensed T_s endmembers indicate similar results for both sites. Results tend to be more evenly scattered along the regression line. However, the image-derived $T_{bs,w}$ clearly overestimates EB-simulated $T_{bs,w}$ in the higher range (hot days) (Fig IV. 1d, 1e). Such an overestimation especially occurs in summer (June 01st to September 25th, 2016) when wet conditions are poorly represented.

IV.3 Wheat evapotranspiration using thermal/optical-based approach

IV.3.1 Relationship between surface resistance and stress index

The time series of retrieved SI (Eq.III.26 in chapter III) and r_c over the flood site is shown in Fig. IV.2. According to this figure, daily patterns of SI and r_c are similar and respond perfectly to the water supply (rainfall or irrigation). On one hand, after water supply, the soil moisture in the root zone increases and the plant transpirates at potential rate with no limitation and the values of r_c and SI tend to decrease. On another hand, the absence of irrigation and rainfall (dry condition, e.g. from the end of April) results in an increase in the root zone depletion and generates stress (SI increased). The increase in soil water depletion is due to the removal of water by ET that induces water stress conditions and then the

stomatal closure which increases r_c. Consequently, it can be concluded that both the variables follow similar trends. This leads to look if there is any relationship between both terms. For this purpose, r_c is plotted against SI (Fig. IV.3) by using *in situ* measurements (flood site). When SI ranges from 0 to 0.4 which corresponds to unstressed vegetation with low LST values, r_c values are scattered around a mean value of about 70 s m^{-1} which corresponds to the minimum bulk surface resistance (r_{cmin}).
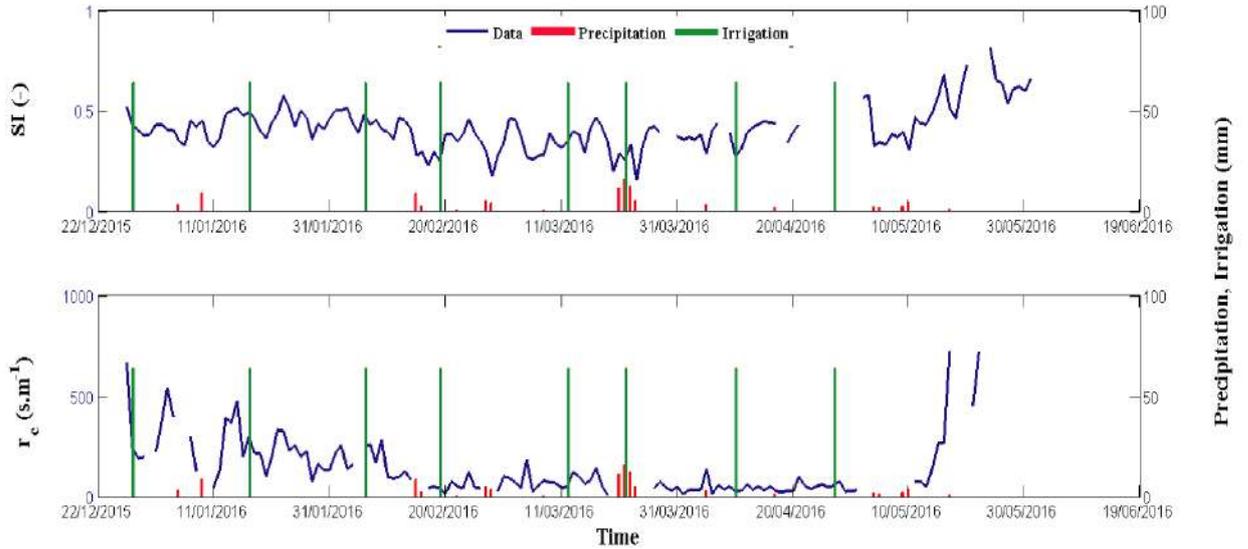
Figure IV.2: Variations of SI (top figure) and r_c (bottom figure) under different water stress conditions for the R3- flood wheat site. Rainfall (green vertical lines) and irrigation (red vertical lines) events are scaled on the secondary y-axis.

The obtained value of r_{cmin} is in agreement with values obtained for wheat crop by (Baldocchi, 1994). When SI increases above a threshold value SI = 0.4, r_c increases linearly with SI. This confirms the results reported by Autovino et al. (2016) and Er-Raki et al. (2018) who found a similar shape for olive and orange orchards, respectively. The obtained relationship, which gives the best fit between both terms, is given by:

$$r_c = r_{cmin} = 70 \ s.m^{-1} \qquad for \ SI < 0.4 \qquad\qquad \text{(IV.1)}$$
$$r_c = d * SI + e \qquad\qquad for \ SI \geq 0.4$$

where *d* and *e* are the calibration parameters, which are equal to 3000 s m^{-1} and -1130 s m^{-1}, respectively. Note that the values of r_{cmin}, *d* and *e* are expected to depend on local meteorological data, crop and soil types.
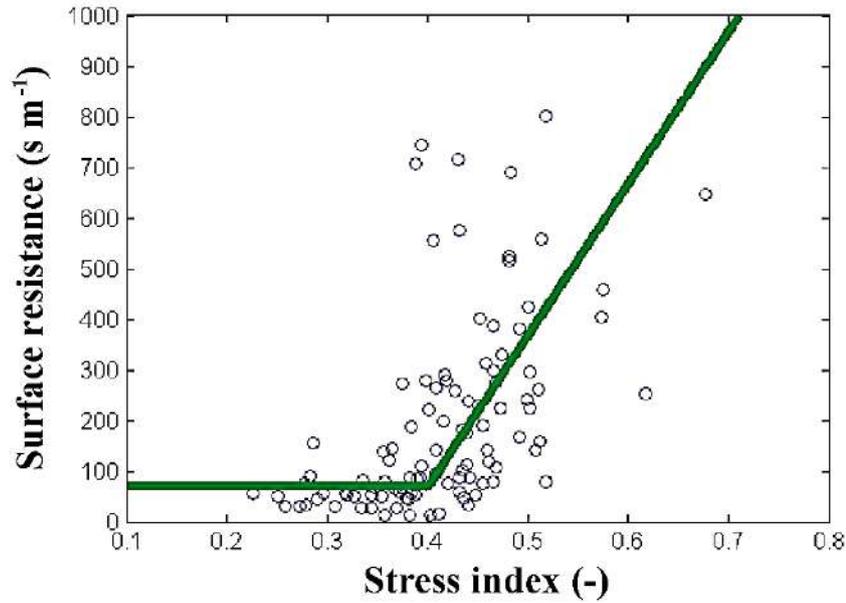
Figure IV.3: Relationship between the bulk surface resistance (r_c) and a stress index (SI) for the flood irrigated parcel. The best fit (green solid line) was presented.

IV.3.2 Evapotranspiration estimation at parcel scale

The relationship of Eq. IV.1 is validated by comparing the modelled and measured latent heat flux for the drip-irrigated wheat site at Landsat overpass time (Fig. IV.4). According to this figure, an acceptable correlation is obtained between simulated and measured LE using the proposed approach ($R^2 = 0.53$). The scatter of modelled LE estimates is probably due to the uncertainties associated to the relatively small footprint of the *in situ* thermal radiometer. Looking at the dynamics of actual LE and r_c values estimated by Eq. IV.1 (not showed in the manuscript), the proposed methodology for bulk resistance estimation allows for capturing the variability of measured LE. The significant bias in simulated LE is due to the underestimation of *in situ* LST, involving an overestimation of simulated LE especially during the dry period (Ramoelo et al., 2014; Ruhoff et al., 2013).
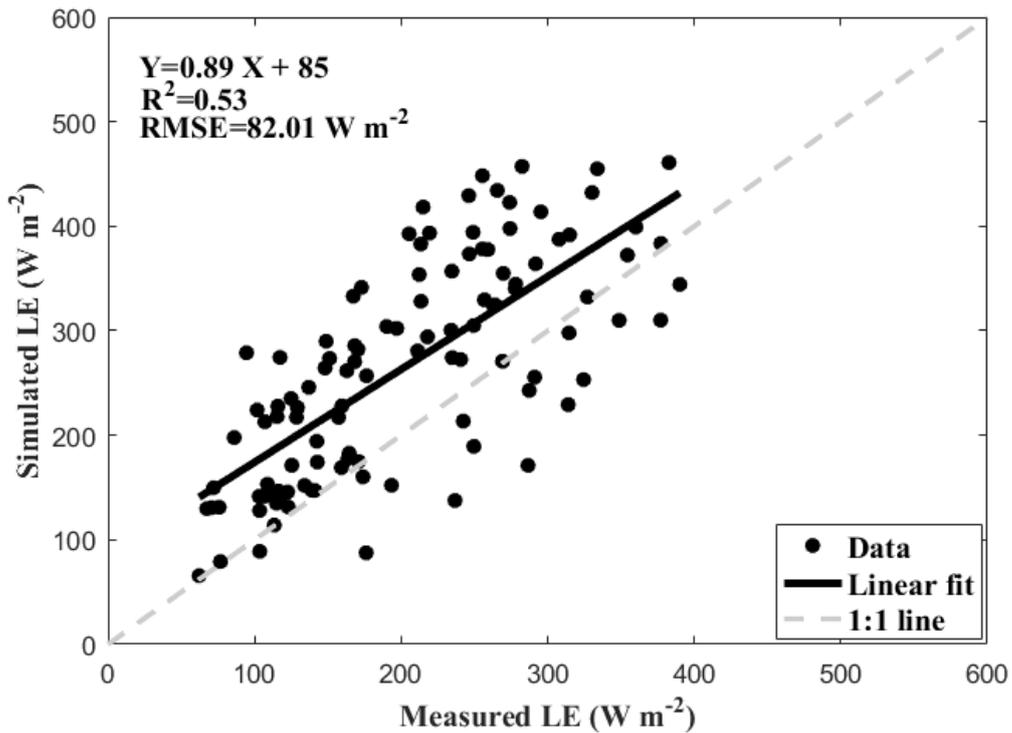
Figure IV.4: Comparison of the simulated and measured latent heat flux over the drip-irrigated site at Landsat overpass time (11:00 am).

IV.3.3 Evapotranspiration mapping at perimeter scale

IV.3.3.1   Wheat stress index mapping at 100 m resolution

The R3 site is occupied by different cultures (wheat, alfalfa, orange, and olive), so before spatializing the ET, a land use has been performed in order to distinguish between wheat and other crops. Fig. IV.5 shows the spatial and temporal variations of Landsat-derived LST and fraction cover (Fc) over wheat crops. As the entire growing season of wheat was divided into four growth stages namely: the initial, the development, the mid-season and the late season, we choose to present one image for each stage (Fig. IV.5). This figure shows that during the initial stage (06/01/2016), most of the fields were under bare soil conditions characterised by low Fc and high LST values (Fig. IV.5a, 5e) depending spatially on the water supply and atmospheric conditions. In the development stage (07/02/2016) an effective full cover is reached in some parcels while other ones are characterized by low Fc depending on the sowing date and the development of vegetation. This spatial variability of Fc has a direct effect on the variability of LST. When Fc reaches the maximum value at the mid-season (18/03/2016) (Fig. IV.5c), spatial LST values are similar around 20 °C except for some pixels where the LST values are relatively higher (about 35 °C) (Fig. IV.5g), which correspond to

the non-cultivated parcels. At the last stage (29/05/2016), from the beginning of maturity until harvest or full senescence, wheat fields are characterized by low Fc and high LST values (Fig. IV.5d, 5h).
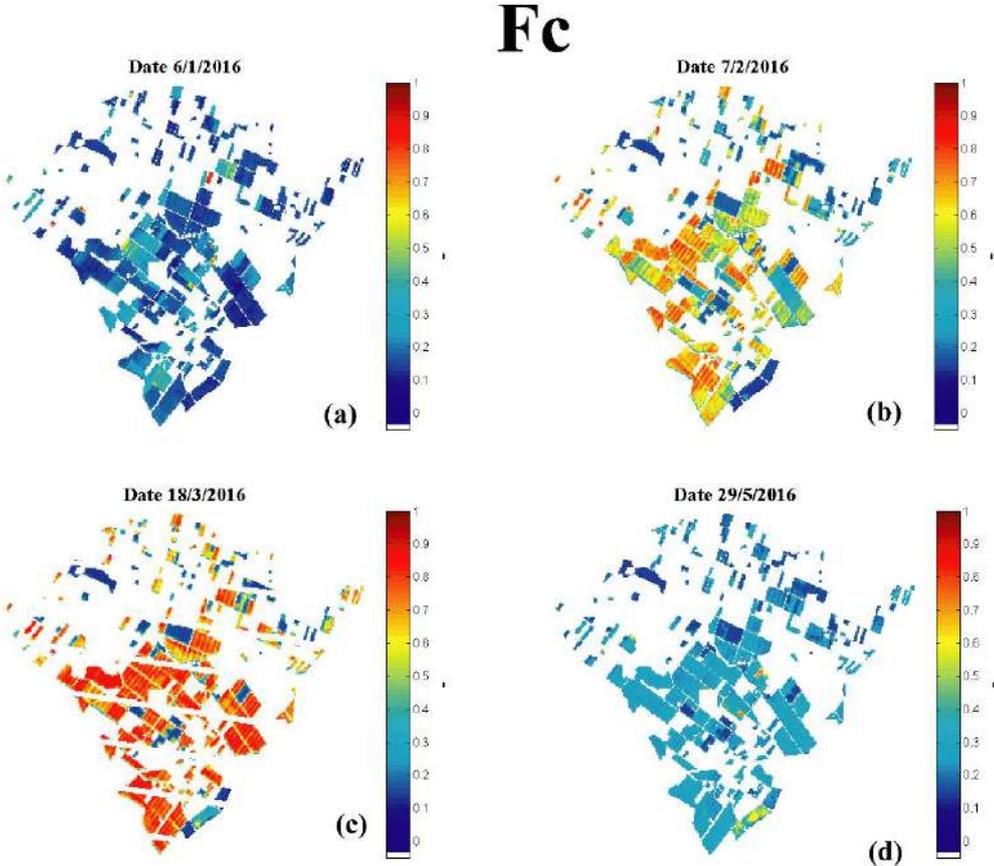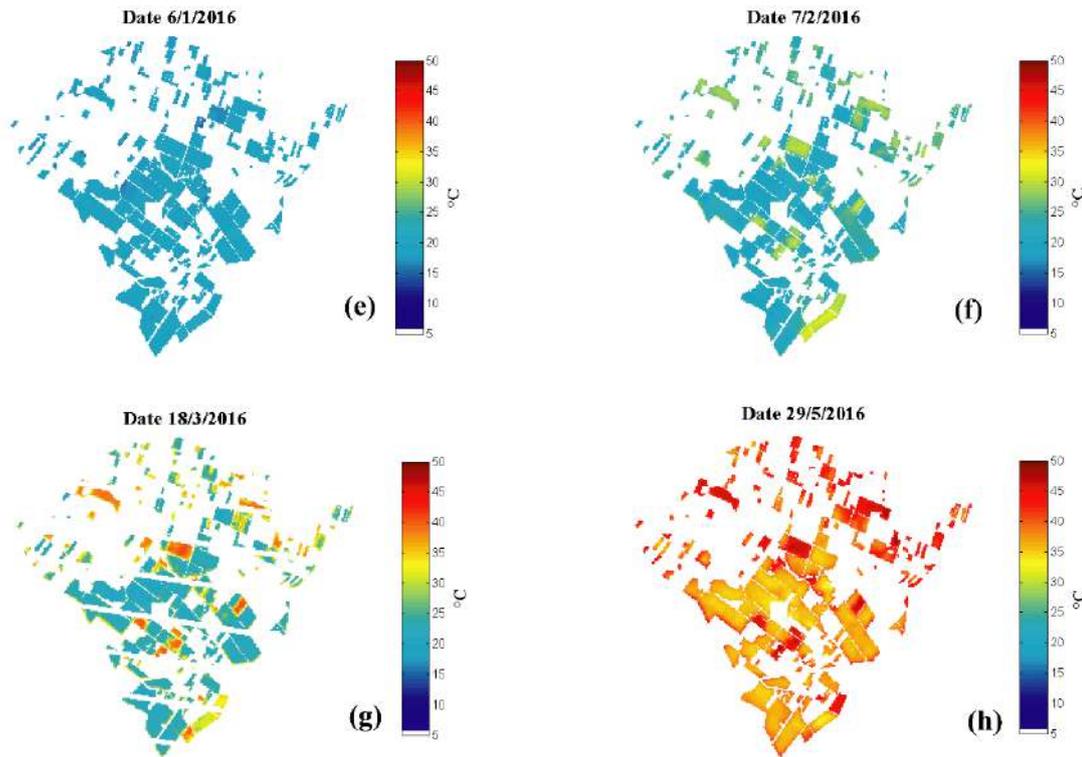
Figure IV.5: Time series of fraction cover (a, b, c, d) and Land Surface Temperature (e, f, g, h) maps over R3 area at dates corresponding to different growing stages obtained from Landsat satellite.

Our approach involves the energy balance model in order to assess the variation of LST in space and time for two extreme dry and wet conditions which depend on climatological conditions. Fig. IV.6 shows the dry and wet LST maps for the selected four dates. These maps show that, in the coldest days in winter (06/01/2016) (Fig. IV. 6a, 6e), the LST$_{dry}$ oscillated between 15 and 30 °C and the LST$_{wet}$ ranged from 10 to 17 °C. In the other hand, for the hottest days in summer (29/05/2016) (Fig. IV. 6d, 6h), the LST$_{dry}$ reached its maximum (50 °C) as well as the LST$_{wet}$ that reached 30 °C.
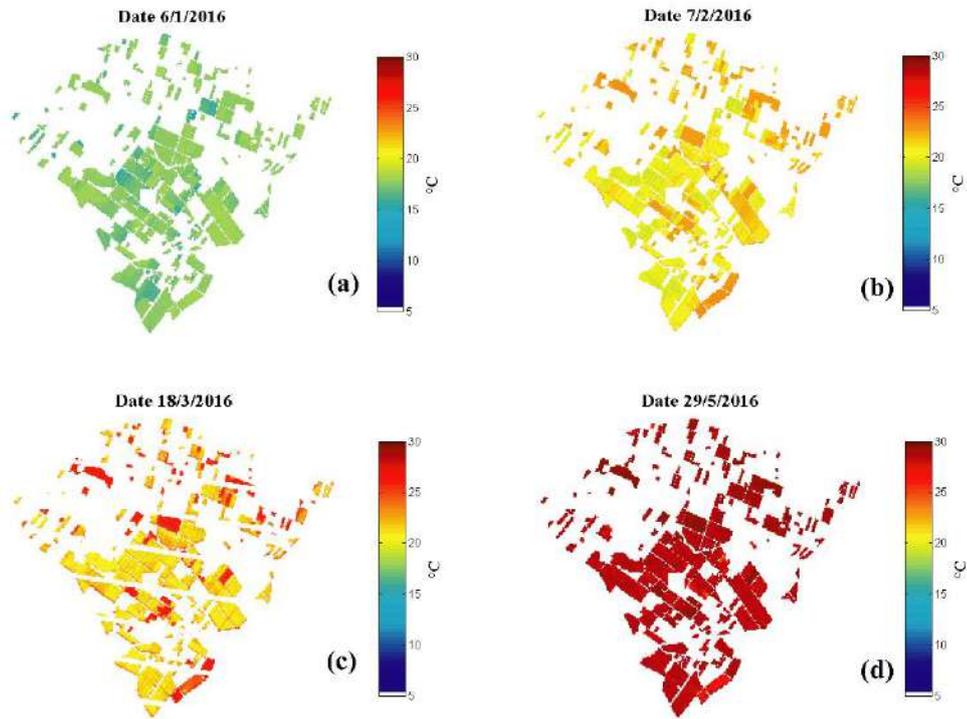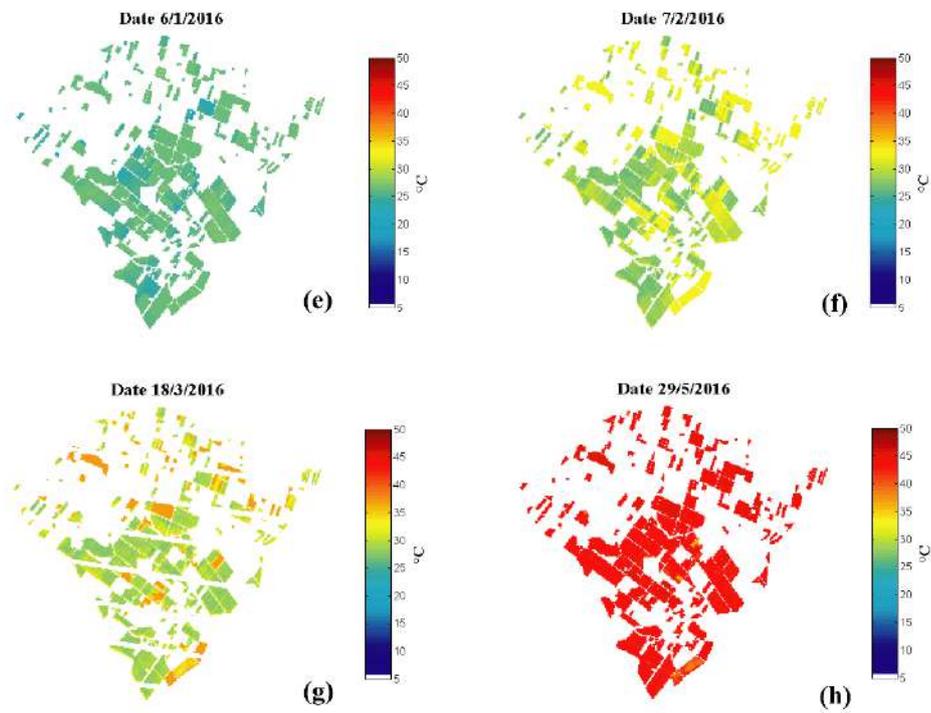
Figure IV.6: Time series of Land Surface Temperature (LST) maps in wet (a, b, c, d) and dry (e, f, g, h) conditions over R3 site on dates corresponding to different growing stages of wheat.

The use of LST time series extracted from Landsat satellite and the dry and wet LST values computed using the energy balance model appears to be a good way to monitor water stress index for irrigation scheduling. Fig. IV.7 presents the spatial distribution of SI over R3 site at the different growth stages. The maps of this figure show that Landsat-derived SI consistently ranges between 0 and 1 all along the agricultural season, regardless of the vegetation cover fraction and LST values (see Fig. IV.5). In fact, the use of Fc and LST data as input variables of the energy balance model to estimates LST_{dry} and LST_{wet}, allows taking into account all the growing stages of wheat crop. In particular, we can distinguish between the small vegetation (tillering stage) and the full developed one (mid-season stage). In this regard Barbosa Da Silva and Rao (2005) estimated SI of cotton crop using LST, surface resistance (r_c) and R_n. However, they did not take into account the vegetation parameters and their variability during the agricultural season. These parameters affect the aerodynamic resistance and hence both the sensible and latent heat fluxes.
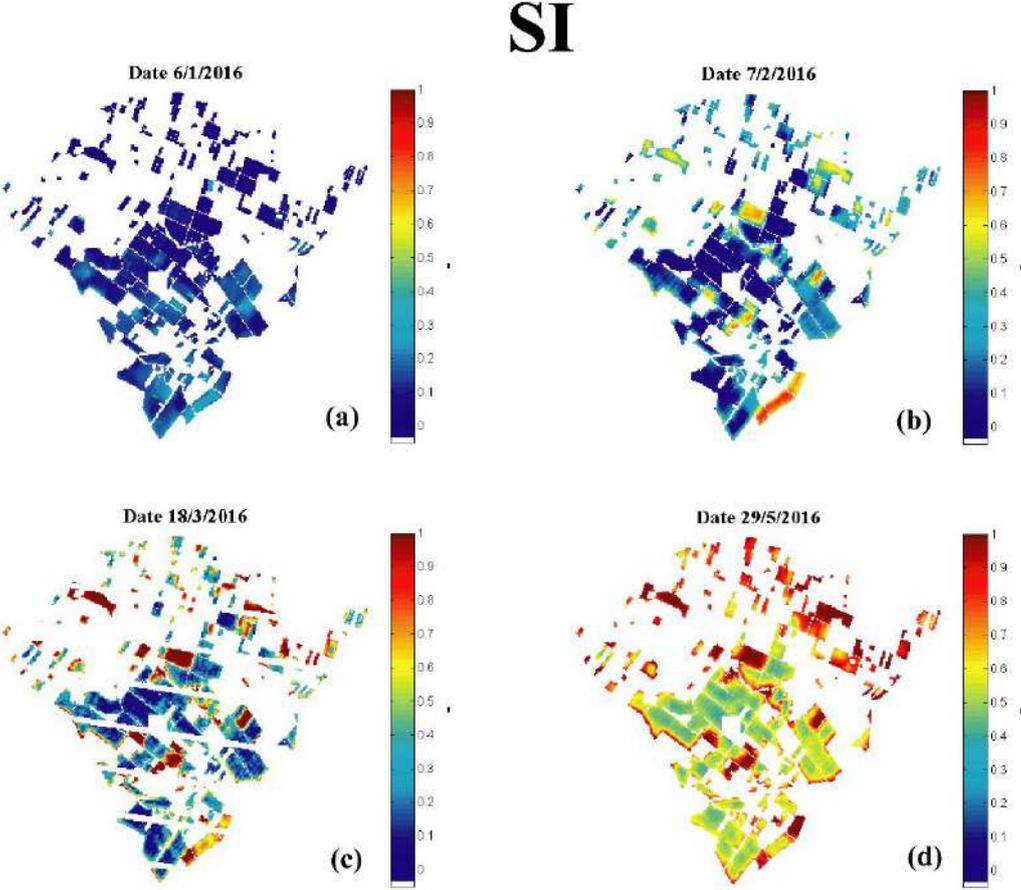
Figure IV.7: Time series of stress index (SI) maps estimated using Landsat data over R3 site.

In Fig. IV.7, the pixels having a SI value close to 1 (red colour) are characterised by a high vegetation stress due to the mismatch between water supply and water requirement (late

irrigation). The values of SI ranging between 0.3 and 0.6 are characterised by the onset of vegetation stress. This is due to the difficulty of the irrigation distribution at the right moment. Indeed, the water transported by gravity across the R3 channels may arrive to the fields before or after the optimal date (Belaqziz et al., 2014, 2013). Pixels with SI values around 0 correspond to un-stressed, meaning recently irrigated wheat. Following the evolution of SI, it appears that this index shows spatial and quantitative information about the method of irrigation distribution, and could be used to optimise the irrigation scheduling. Those results are consistent with the work of Belaqziz et al. (2013), who used another index named "Irrigated Priority Index (IPI)" in the same study area to manage the irrigation distribution. The IPI equation is mainly based on both the water stress level and irrigation dates of wheat crop. The main drawback of IPI is that it needs the amount of water supply as input, which is not the case of SI developed. This new index based on LST only might then be combined with IPI in order to detect and retrieve irrigation amount, information that is very difficult to obtain over large areas.

IV.3.3.2   Wheat evapotranspiration mapping at 100 m resolution

To overcome the spatial representativeness issue of *in situ* measurements and for further evaluating the proposed model to retrieve surface evapotranspiration, Landsat data are used as input of the modified P-M model. ET estimates are spatialized within a 10×10 km^2 area centred over the R3 site which is mainly covered by wheat crops.

Fig. IV.8 shows the spatial distribution of ET and its temporal variation across the season. We can observe a high variability of ET, which depends on the spatial heterogeneity of Fc, LST and SI over R3.
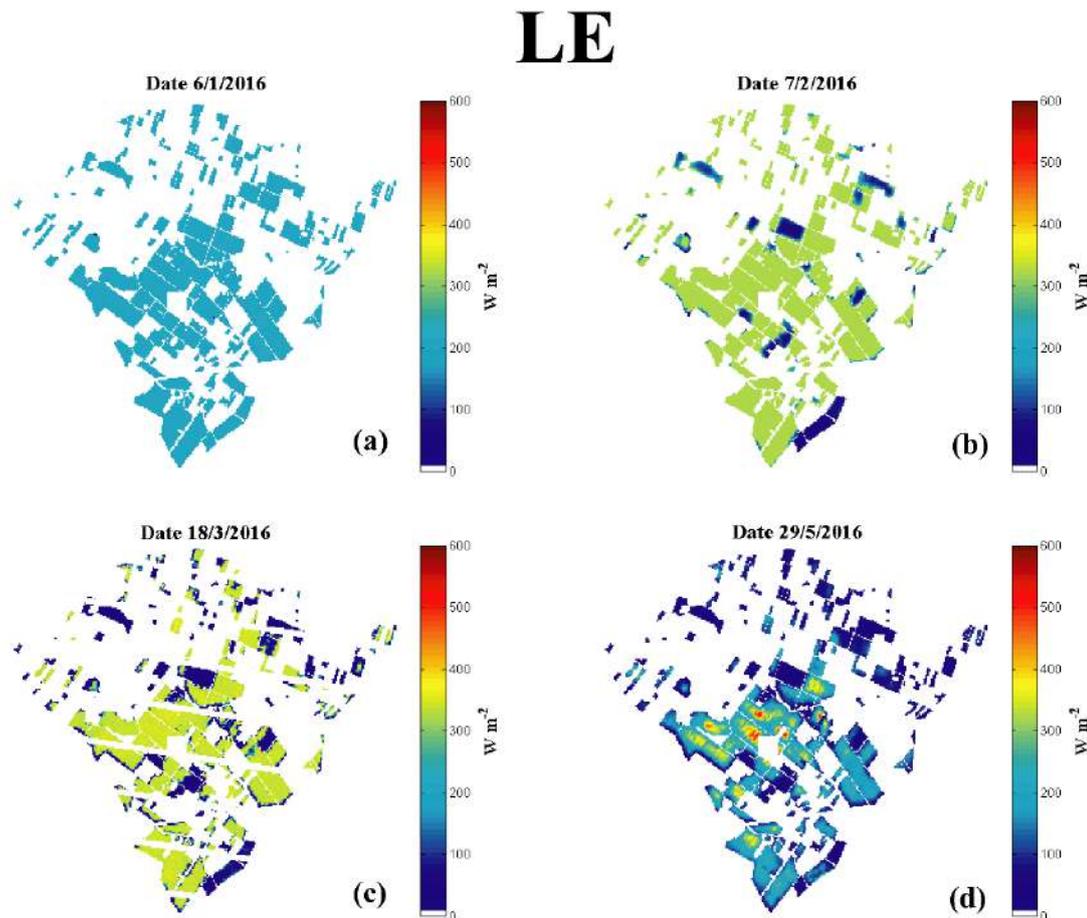
Figure IV.8: Time series of latent heat flux (LE) maps estimated over R3 site.

The spatial representation allowed to distinguish between the fields corresponding to stressed wheat (blue colour) where LE is lower and the field corresponding to un-stressed fields (other colour) that have been relatively well irrigated during the wheat growing stages, for high ET values (Fig. IV. 8d). The obtained spatial and temporal variations of ET are in accordance with the spatio-temporal variability of Fc, LST and SI (see Fig. IV.5, IV.7). To observe this more easily, the frequency histograms for remote sensing data (Fc, LST), SI and ET on one date 18/03/2016 are plotted in Fig. IV.9. The choice of this date relies on the fact that the end of March summarises the history of wheat crop growth and its development from sowing date (Hadria et al., 2006a; Karrou, 2003). By analysing the different histograms, one can be concluded that the estimates LE are coherent with other surface properties (Fc, LST, and SI). Fc values in the higher range (larger than 0.8) have a high frequency/percentage. They correspond to the fields with low LST values (lower than 25 °C), which are associated to small values of surface aerodynamic resistance (large crop height) rather than to large water availability for wheat. On this date, our model computes a

large amount of un-stressed areas with relatively small SI and large LE values. Those results seem to be representative of the real situation.
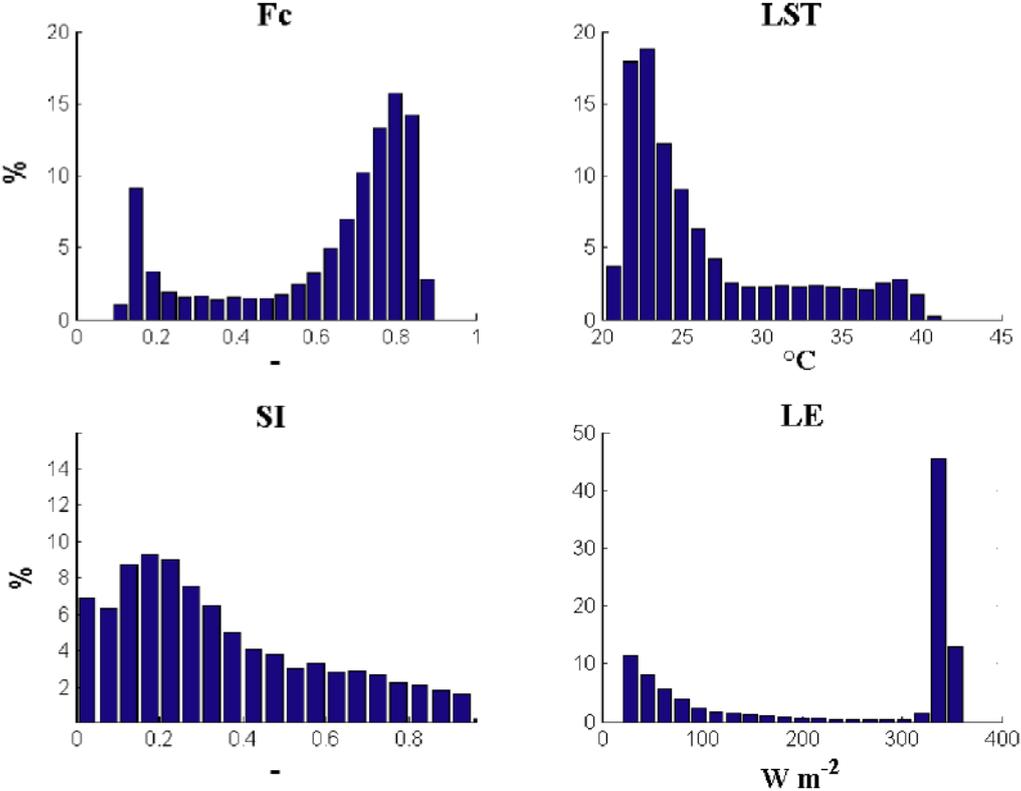
Fig. IV.9: Frequency histograms of remote sensing parameters (LST, Fc), simulated latent heat flux (LE) and Stress index (SI) on March 18, 2016.

The land surface parameters (LST, Fc, and emissivity) are obtained from Landsat data. Therefore all cloudy data (images) are discarded. In addition, the Landsat-7 images include data gaps due to scan line corrector (SLC) failure on May 31 2013, which on some dates unfortunately covered the irrigated sites.

IV.3.3.3 Validation over flood and drip irrigation parcels

The selected data are used for validating the predicted P-M ET against *in situ* ET for both flood and drip sites (Fig. IV.10). As it can be observed in this figure, the proposed approach allows to predict correctly the temporal dynamics of ET with an acceptable accuracy and a good correlation. The validations for the two sites resulted in R^2 of 0.76, 0.70 and a RMSE of 12, 13 W m^{-2} for flood-irrigated site (Fig. IV. 10b) and drip-irrigated site (Fig. IV. 10a), respectively.

A further validation of the proposed approach was performed by comparing the measured ET with the ET simulated one under fully stressed (SI=1, r_c = 1870 s m^{-1}) and un-stressed (SI=0, r_c =70 s m^{-1}) conditions. The obtained results are presented in the same Fig. IV.10 under real meteorological conditions. As expected, the model simulates very low values of ET for SI=1 whereas it simulates high values of ET for SI=0. On some dates, the ET simulations with SI=0 (r_c = 70 s m^{-1}) coincides with the ET estimated from Landsat-derived SI, which means that the fields were monitored in well-watered conditions (SI < 0.4). One key result is that the Landsat-derived SI ($0<$ SI <1, $70<$ r_c <1870 s m^{-1}) provides much more accurate ET estimates over both validation sites than when assuming fully stressed (SI = 1, r_c = 1870 s m^{-1}) or fully unstressed (SI=0, r_c = 70 s m^{-1}) condition in the P-M equation.

Figure IV.10: Comparison between the simulated and measured LE (W m^{-2}) over flood (a) and drip (b) sites in different conditions (un-stressed condition "SI = 0"; "stressed condition "SI =1"; real condition "SI as a function of LST").

Mapping ET based on the modified P-M model requires LST data. The LST data used are acquired from Landsat sensors which provide LST at high spatial resolution. Landsat thermal data are providing good results in term of evapotranspiration over wheat and bare parcels, the limiting factor to monitor efficiently parcels is the thermal data availability. Downscaling daily thermal data provided by existing sensors (MODIS, Sentinel-3…) is one of the operational method to get thermal data with high spatio-temporal resolution. In this work we propose to improve the resolution of acquired MODIS/LST data, which provide data daily at 1 km resolution.

IV.4 Improving the LST spatio-temporal resolution

IV.4.1 Application to aggregated Landsat-7/8 data: R3 and Sidi Rahal sites

As a first assessment, the disaggregation approaches are applied to aggregated Landsat LST. Moreover, in the case of RTM (D2'), the LST end-members are estimated from the spaces built from HR data in order to reduce possible uncertainties. The disaggregation results are evaluated visually and quantitatively using the 100 m Landsat LST image as reference. Fig. IV.11 shows the LST images obtained from D0, D1, D1' and D2' for the six dates over Sidi

Rahal rainfed site. The high spatial heterogeneity in soil properties and the land use over the selected areas induces strong variations in LST at the HR. All three D1, D1' and D2' algorithms provide more variability of LST than D0 algorithm which does not take into account the spatial variability at HR. It is also observed that the boxy artifact, meaning the block effect that still remains in the disaggregated LST at the LR (Agam et al., 2007b; Merlin et al., 2010b), is reduced for D2'.
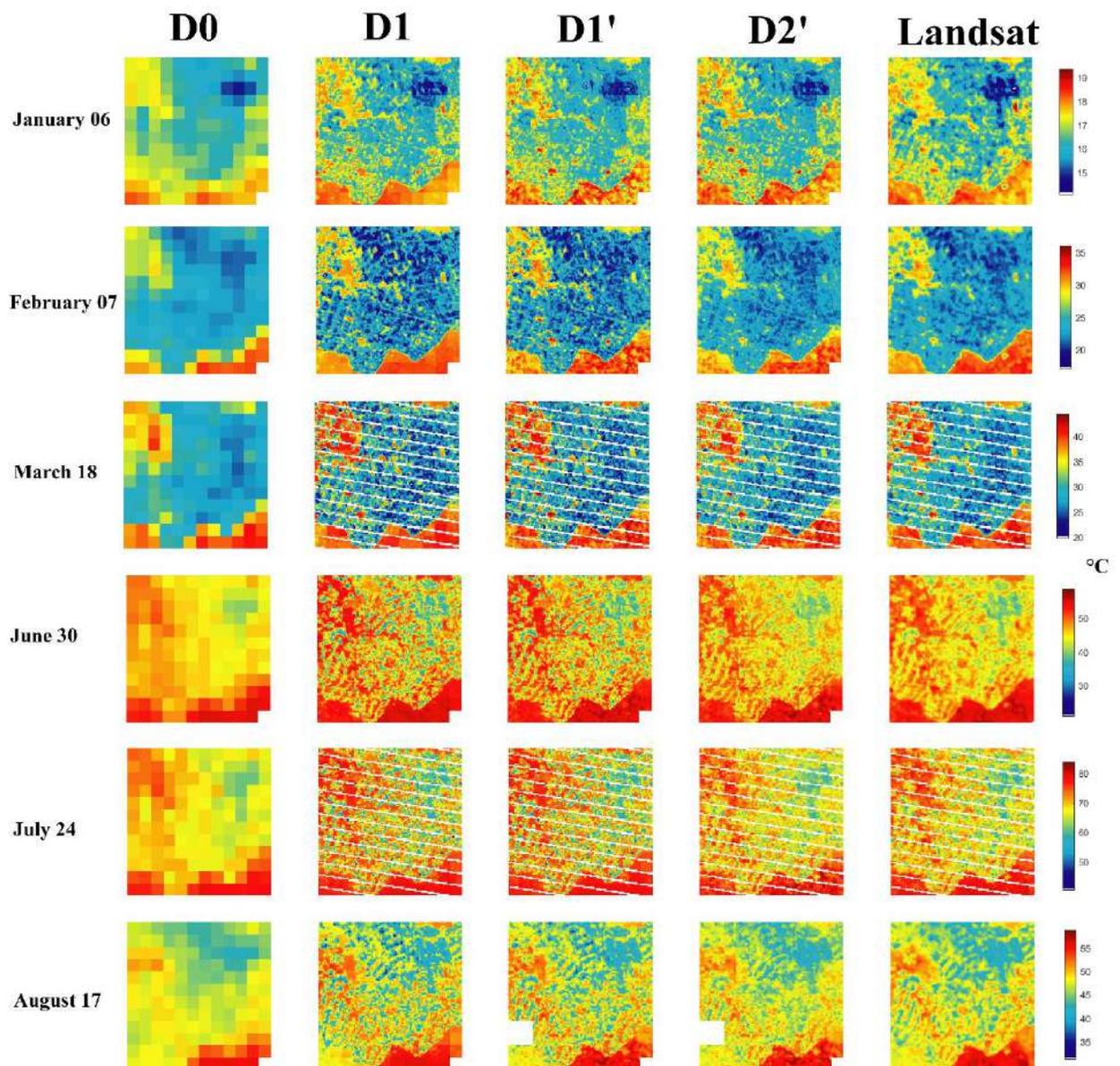
Figure IV.11: Maps of the LR (Landsat-aggregated) LST disaggregated by the four algorithms compared to the Landsat reference HR LST on six selected clear dates separately over Sidi Rahal area.
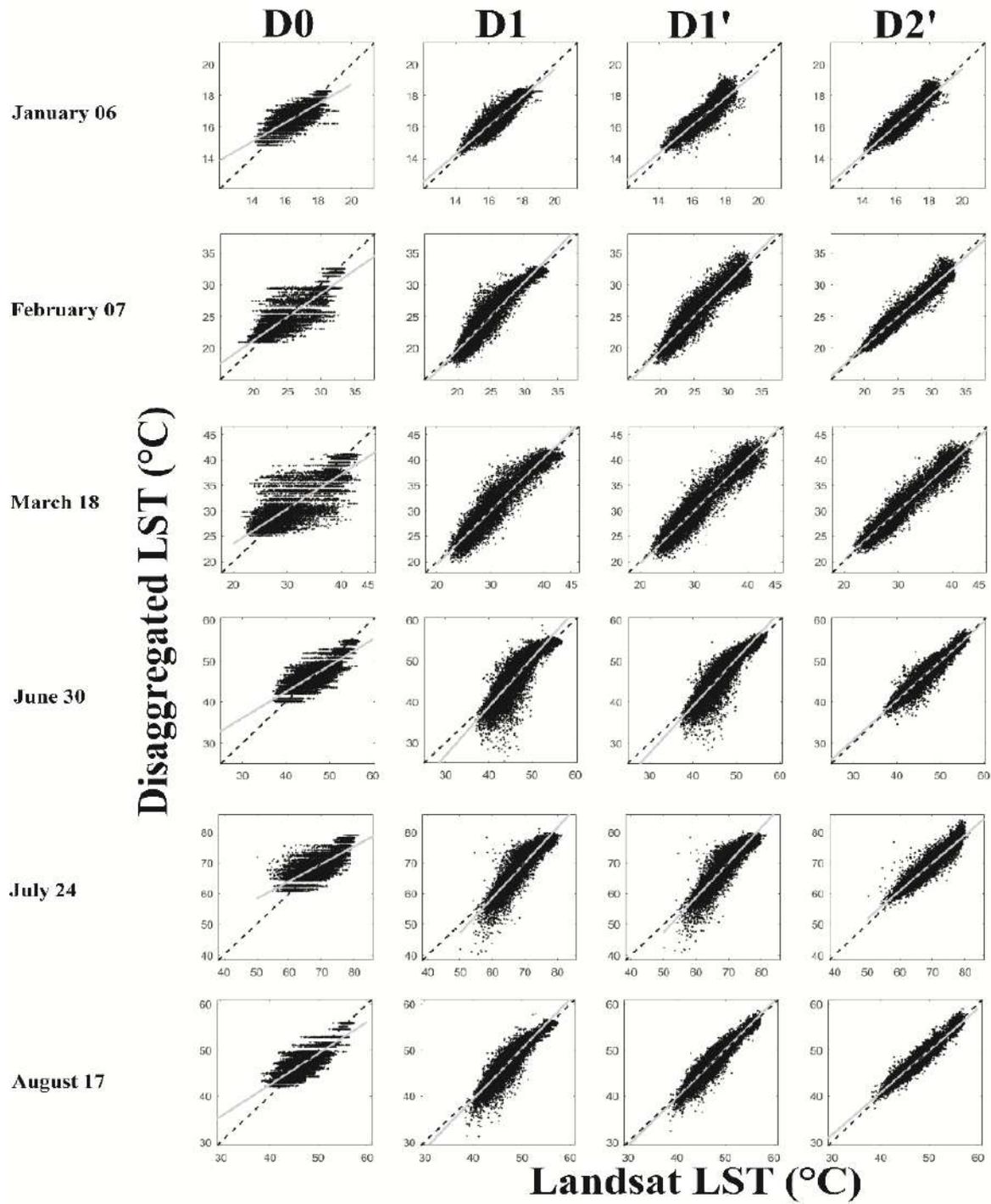
Figure IV.12: Comparison between the LST disaggregated using each algorithm against the HR Landsat LST over Sidi Rahal area.

Table IV.1: Summary statistics of the disaggregation algorithms. Temperature endmembers are estimated from HR Landsat data over the Sidi Rahal site.

Date	R (-)				RMSE (°C)				Slope (-)			
	D0	D1	D1'	D2'	D0	D1	D1'	D2'	D0	D1	D1'	D2'
February 07	0.87	0.94	0.95	0.97	1.68	1.31	1.25	0.82	0.73	1.07	1.06	0.94
March 18	0.83	0.95	0.95	0.96	2.94	1.79	1.69	1.39	0.68	1.04	1.03	0.96
June 30	0.81	0.88	0.90	0.95	2.29	2.67	2.27	1.30	0.63	1.18	1.14	0.95
July 24	0.75	0.91	0.91	0.93	3.34	2.80	2.72	1.88	0.56	1.14	1.13	0.90
August 17	0.84	0.92	0.95	0.96	1.86	1.63	1.26	0.99	0.68	1.08	1.04	0.91
All	0.82	0.92	0.93	0.95	2.42	2.04	1.83	1.27	0.65	1.10	1.08	0.93

Results (Fig. IV.12) listed in Table IV.1 show that the D2' (RTM using fraction of green vegetation and radar SM) performs systematically better than the classical approach in all the cases, and provides more accurate results over the rainfed agriculture site. 1.27 °C is the minimum mean error it has been assessed using the D2' algorithm compared to 2.04 °C by using the classical D1 approach.

A significant underestimation is observed for the low LST values during the hottest days (June 30, July 24 and August 17) using D1 and D1' (Fig.IV.12 and Table.IV.1). In contrast, the RTM D2' LST fits correctly the Landsat observation. The most significant difference in performance is found for the February 07 image, when the bare soil dominates and the soil moisture variation controls the LST distribution. This means that radar data provide useful and independent information about the LST variability that the f_{gv} does not provide. The results indicate that the additional SM proxy used in the RTM algorithm allows more of the variability in LST to be captured over this scene.

The used algorithms in this paper have been tested over the 8 km by 8 km R3 site, in order to test the stability of the new approaches. Here we test the capacity of the new algorithm to capture LST variability over the complex fields. Fig. IV.13 show the spatial distribution and the temporal variation across the season of the disaggregated and Landsat LST over the R3

site for seven clear sky selected dates. We can observe a high variability of LST, which depends on the spatial heterogeneity of f_{gv} and/or SM.
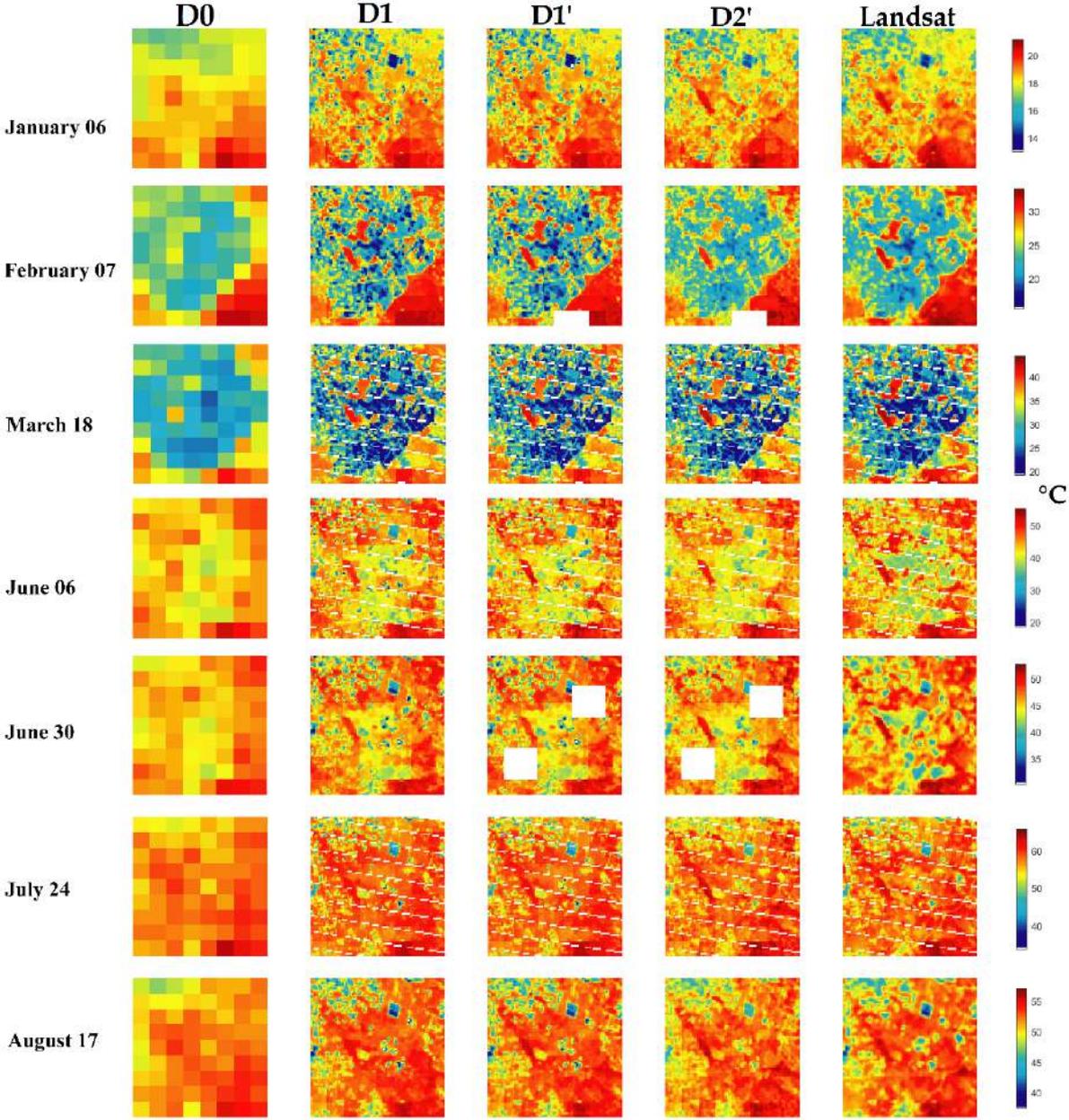
Figure IV.13: Maps of the LR (Landsat-aggregated) LST disaggregated by the four algorithms compared to the Landsat reference HR LST on the seven selected dates separately over R3 site. The data gaps on February 07 and June 30 for D1' and D2' are attributed to S-1 raw data (no data value).

To facilitate the comparison between the algorithms, they are plotted against the Landsat-derived temperature over the R3 site in Fig. IV.14. The statistical results for each algorithm are summarized in Table IV.2.
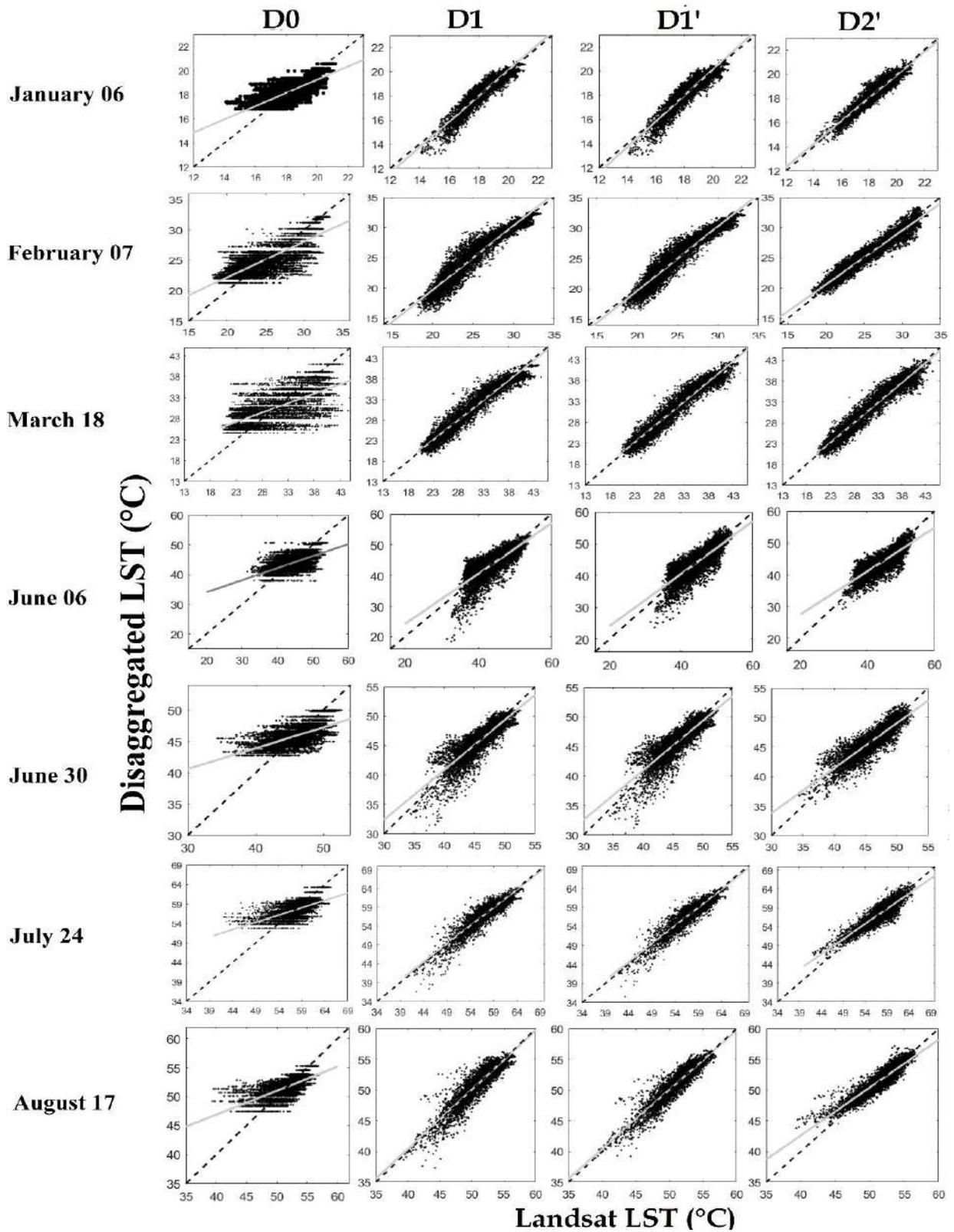
Figure IV.14: Comparison between the LST disaggregated using each algorithm against the HR Landsat LST for the seven dates over R3 site.

Table IV.2: Summary statistics of the disaggregation algorithms. For D2', LST endmembers are derived from the contextual spaces defined by HR ancillary data over R3 site.

Date	R (-)				RMSE (°C)				Slope (-)			
	D0	D1	D1'	D2'	D0	D1	D1'	D2'	D0	D1	D1'	D2'
January 06	0.76	0.93	0.93	0.94	0.71	0.45	0.47	0.36	0.55	1.06	1.06	0.95
February 07	0.78	0.95	0.96	0.97	2.26	1.26	1.15	0.91	0.59	1.06	1.06	0.89
March 18	0.66	0.97	0.97	0.97	4.42	1.48	1.44	1.46	0.45	0.96	0.97	0.96
June 06	0.63	0.80	0.82	0.83	3.31	2.78	2.61	2.37	0.40	0.82	0.82	0.68
June 30	0.61	0.86	0.86	0.88	2.25	1.47	1.54	1.39	0.33	0.84	0.84	0.76
July 24	0.61	0.91	0.92	0.90	2.54	1.37	1.27	1.40	0.37	0.96	0.95	0.80
August 17	0.67	0.92	0.94	0.92	1.81	1.01	0.87	0.97	0.41	0.96	0.96	0.78
All	0.67	0.90	0.91	0.91	2.47	1.40	1.33	1.26	0.44	0.95	0.95	0.83

Data points in the scatterplot of the new (D2') algorithm fall closer to the 1:1 line. Based on Table IV.2, D1, D1' and D2' generate better results than D0. The improved disaggregation algorithms show a decrease in the root mean square error (RMSE) with 1.26, 1.15 and 0.91 °C using the D1, D1' and D2' algorithms, respectively compared to D0, which shows an error up to 2.2°C on 07 February as an example.

The results change from date to date, but in general in our study case we found that, the MLR D1' and RTM D2' algorithms provide better results in term of correlation coefficient (R) and RMSE than the original approach D1. A better slope of the linear regression between disaggregated and Landsat LST is provided by D1 and D1' whereas D2' degrades slightly the slope on the same dates. The good results provided by the D1' algorithm are attributed to an efficient calibration at LR of the coefficients of the regression fit between LST, f_{gv} and the radar backscatter. Moreover, the RTM model is sensitive to uncertainties in extreme LST, which in this case, were derived using HR Landsat data.

The mean R between disaggregated and Landsat LST slightly increases from 0.90 to 0.91, and the mean RMSE decreases from 1.40 °C to 1.26 °C using the D1 and D2' algorithms,

respectively. In contrast, the mean slope is decreased from 0.95 to 0.83 using D1 and D2' algorithms, respectively.

Since HR Landsat LST is assumed to be unavailable in our disaggregation exercise, the LST endmembers are now derived from LR LST data only (instead of using HR LST data as previously). Table IV.3 lists the RMSE, R, and slope of the linear regression between disaggregated and Landsat LST for D2' algorithm, using the temperature endmembers derived from LR LST data combined with EB model estimates.

Table IV.3: Statistics of the disaggregation algorithms using temperature endmembers estimated by EB modelling (estimated by LST-f_{gv} spaces defined using HR data in parenthesis).

Date	R (-)	RMSE (°C)	Slope
January 06	**0.87 (0.94)**	**0.85 (0.36)**	**1.27 (0.95)**
February 07	**0.97 (0.97)**	**0.89 (0.91)**	**0.92 (0.89)**
March 18	**0.96 (0.97)**	**1.60 (1.46)**	**0.88 (0.96)**
June 06	**0.83 (0.83)**	**2.40 (2.37)**	**0.66 (0.68)**
June 30	**0.87 (0.88)**	**1.43 (1.39)**	**0.73 (0.76)**
July 24	**0.86 (0.90)**	**1.65 (1.40)**	**0.79 (0.80)**
August 17	**0.87 (0.92)**	**1.21 (0.97)**	**0.80 (0.78)**
All	**0.89 (0.91)**	**1.43 (1.26)**	**0.86 (0.83)**

A valuable discussion is presented in this paragraph that helps to see the impact of the LST endmembers estimation on the disaggregation results. Looking at the Table IV.3, the statistical results clearly show that the disaggregated LST is more accurate when using the LST endmembers derived from Landsat HR data than those derived from EB modelling (combined with LR data). In contrast, using EB-derived extreme LST provides a slightly better mean slope (0.86) than when using HR data (0.83). In order to assess the main causes behind that, the $T_{bs,d}$ estimated by the EB model is compared to the maximum value observed at HR. On January 06, an overestimation of about 8 °C of $T_{bs,d}$ is observed when using the EB model (data not shown here), which leads to slightly poorer results compared to when using temperature endmembers derived from HR spaces. It is suggested that the temperature endmembers derived from EB modeling are more uncertain than those derived from HR spaces, especially over a highly heterogeneous area like R3.

IV.4.2 Application to MODIS data: R3 area

In this section, the disaggregation methodologies D0, D1, D1' and D2' are applied to MODIS/Terra (MOD11-A1) LST product over only the R3 site. It is reminded that only the MODIS images acquired on the same dates as Landsat data are used for the evaluation. For the rainfed Sidi Rahal site, the MODIS LST data are affected by clouds where the contaminated pixel are masked with the MODIS cloud mask data product. Therefore no MODIS image is clean, which limits the application to MODIS data over this site. Fig. IV.15 compares the disaggregation images with the 100 m resolution Landsat LST for six selected dates. Note that the MODIS image on August 17 is affected by clouds and was thus removed. The MODIS LST data were derived using the generalized split-window algorithm and the cloudy pixels were detected and skipped in the LST production. The MODIS algorithm provides LST data with a good quality only for pixels in clear-sky conditions at the 99% confidence (Wan et al., 2002) otherwise, the pixels affected are set to "No data Value". On this particular day (17th August) there is a 38-minute offset between the two satellite overpasses: Landsat passes at 11:04 AM and MODIS at 11:42 AM. Such an offset is likely to explain that data gaps are different in both (MODIS and Landsat) data sets. In the implementation of D2', the temperature endmembers are estimated using EB modelling.
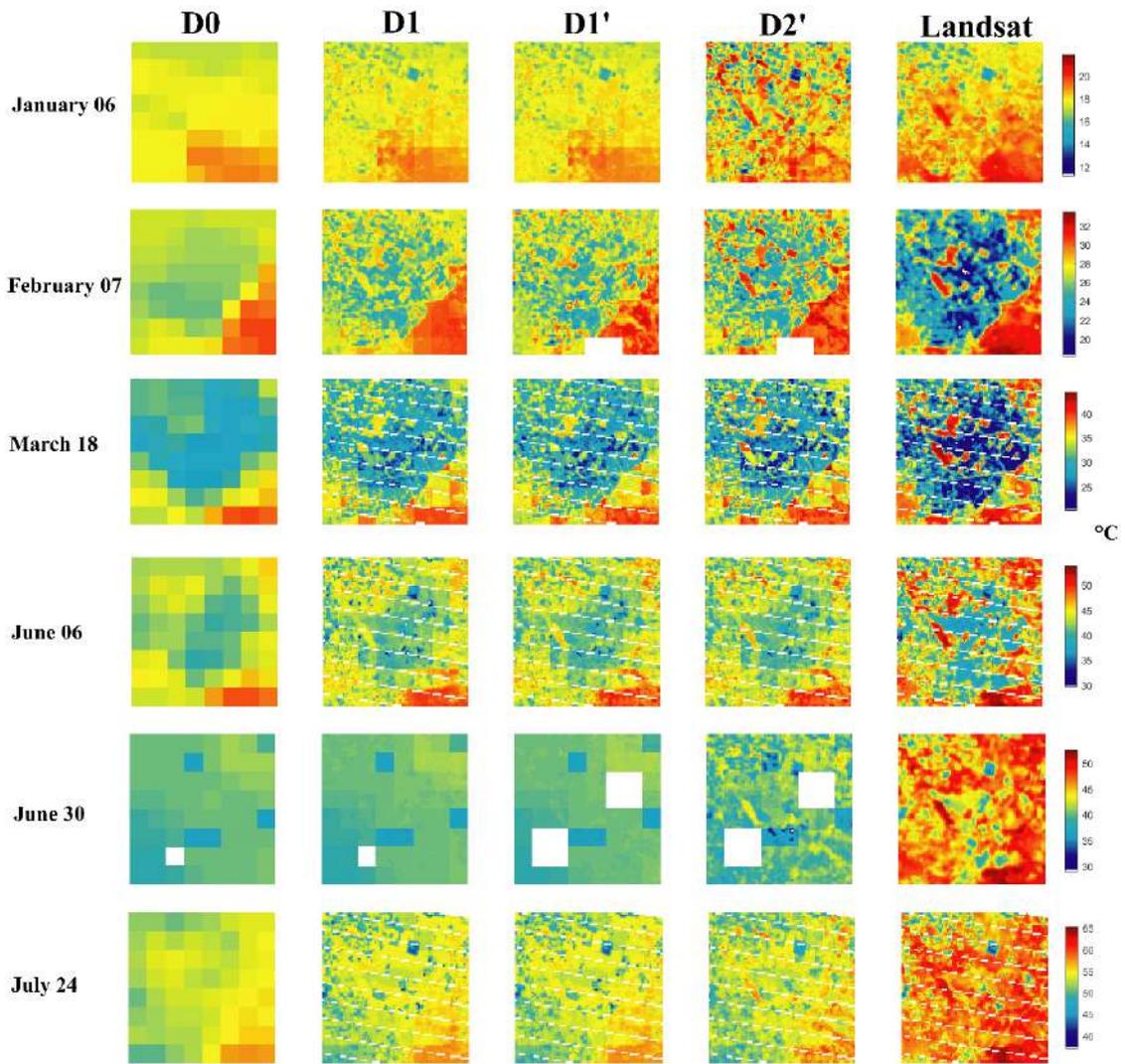
Figure IV.15: Maps of the MODIS LST disaggregated at HR by the four algorithms compared to the Landsat reference LST map on the six clear sky dates over R3 area.
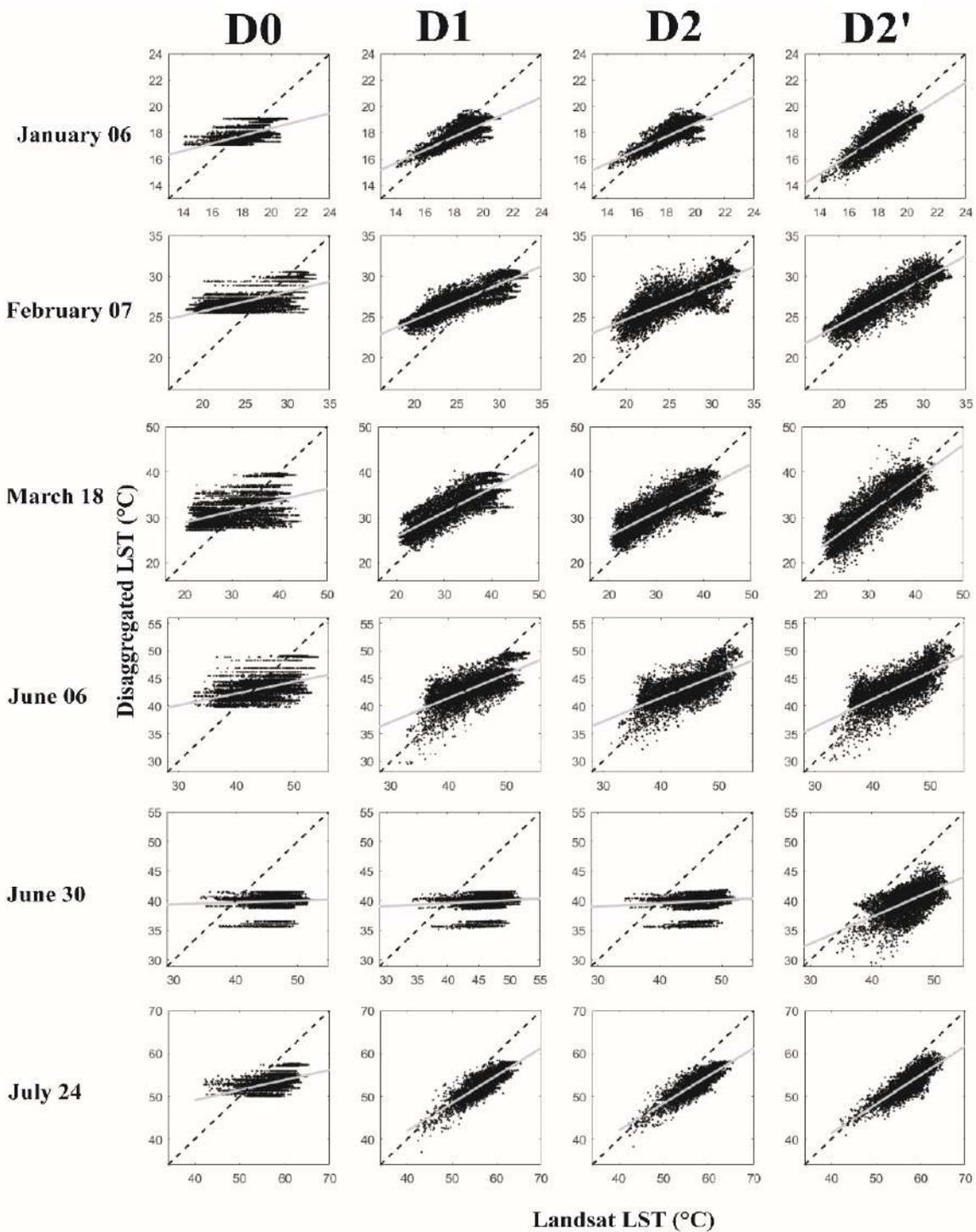
Figure IV.16: Comparison between the disaggregated LST using each algorithm against the HR Landsat LST for the seven dates over R3 area.

Table IV.4: Summary statistics of the disaggregation algorithms. Temperature endmembers are estimated from EB modelling.

Date	R (-)				RMSE (°C)				Slope			
	D0	D1	D1'	D2'	D0	D1	D1'	D2'	D0	D1	D1'	D2'
January 06	0.56	0.80	0.80	0.75	1.03	0.83	0.83	1.09	0.28	0.50	0.50	1.01
February 07	0.65	0.87	0.76	0m	3.34	2.73	2.94	2.57	0.24	0.44	0.43	0.59
March 18	0.51	0.83	0.80	0.86	5.16	3.57	3.71	2.20	0.24	0.53	0.53	0.65
June 06	0.47	0.70	0.71	0.71	3.84	3.16	3.14	3.09	0.21	0.43	0.42	0.44
June 30	0.07	0.12	0.13	0.55	6.71	6.68	6.71	6.44	0.03	0.05	0.05	0.38
July 24	0.47	0.84	0.84	0.78	5.14	4.64	4.64	4.71	0.23	0.64	0.64	0.58
All	0.45	0.69	0.67	0.75	4.20	3.60	3.66	3.35	0.20	0.43	0.43	0.61

Looking at the spatial patterns of disaggregated LST maps, the values in all maps range from 14 °C to 60 °C. The boxy effect anomalies are less apparent for D2' algorithm compared to the original algorithms. Generally, the disaggregation algorithms of MODIS LST show a lower maximum and higher minimum than Landsat LST.

The downscaling results and statistics are shown in Fig. IV.16 and reported in Table IV.4. The D2' algorithm provides better results than the MLR approaches (D1 and D1'). Results in Table IV.4 shows that the minimum mean RMSE is 3.35 °C and the highest mean R is 0.75, which are both obtained with D2' algorithm. A systematic negative bias is apparent in the disaggregated temperature using MODIS LST, quite consistent with the mean bias between MODIS and Landsat LST estimated as 4 °C in this work. As expected the disaggregation method does not yield similar results when applied to MODIS/Terra LST instead of aggregated Landsat data. This is due to the discrepancy between MODIS and Landsat data, and to different sensitivities of MLR and RTM algorithms to uncertainties (including bias) in LR input data. However, in our study case over the selected irrigated perimeter, the new algorithm D2' clearly improves the disaggregated LST against the classical approaches. When

comparing the new algorithm D2' to the classical one D1, D2' generally shows the best results with an increase of R from 0.83 to 0.86 and a decrease in the RMSE from 3.57 to 2.20 °C, respectively (18 March as an example). By comparing the performance of the disaggregation algorithms using aggregated Landsat and real MODIS LST, the aggregated Landsat LST provides better results than MODIS LST. The reason is due to the fact that real images have an additional noise in the LST data which may be related to sensor registration (Essa et al., 2013). In addition, part of the error could be attributed to differences in the algorithms used to retrieve LST, which are not the same (split-window for MODIS and single-channel for Landsat). A relatively poor performance is observed for D1 and D1' on 30 June compared to the new D2' methodology. On that date MODIS LST largely underestimates Landsat LST. However, D2' provides a much better R (0.55 instead of 0.1 for all the other approaches). We argue that the RTM method (D2'), is more accurate and more robust than MLR method (D1') especially when applying it to real data (MODIS LST). In particular, it is much less sensitive to uncertainties in LR LST than MLR method. Based on the acquired results, RTM algorithm performed better than the classical algorithm and in most cases than the RTM method where it stabilizes the errors and systematically increases the R between disaggregated and Landsat LST.

The developed algorithm to estimate ET is involving stress index based on thermal data. However, LST data is involving the bare surface temperature as well as the wheat temperature. In the P-M equation to estimate ET, we linked LST to surface resistance where a coupled effect of plant transpiration controlled by root zone soil moisture and soil evaporation which controlled by surface soil moisture is taken into account. Therefore to distinguish between the two effects we proposed to retrieve surface SM using Sentinel-1 microwave data over bare soils.

IV.5 Surface soil moisture at parcel scale

IV.5.1 Sensitivity of VV- and VH-polarized data to soil moisture

The comparison between VV and VH polarization was undertaken over the Sidi Rahal site where the longest time series of S1 data was available. As shown in Fig. IV.17, the VV polarization is significantly correlated with SM, whereas the VH polarization is poorly correlated (R^2=0.47 and 0.28, respectively). Previous studies have shown the same results (Eweys et al., 2017b; Gherboudj et al., 2011b), and our findings were consistent with the work of Baghdadi et al. (2006b), where they use a large database over ten years to study the

sensitivity of the radar signal to SM over bare soils. VH polarization was found to be sensitive to roughness and to the vegetation volume, due to the depolarization effect by vegetation-volume-scattering, which mainly depends on the vegetation characteristics (Chauhan and Srivastava, 2016; Gao et al., 2017; Karjalainen et al., 2014). The change in polarization between the radar pulse and the echo (depolarization phenomena) is related to the physical structure of the scattering surface (rough surface). In contrast, SM is linked to dielectric soil constant using the dielectric mixing model (Dobson et al., 1985).

The sensitivity of the radar backscatter to SM is estimated as 0.30 and 0.14 dB/m^3 m^{-3} for VV and VH polarization, respectively. The same sensitivity of the VV-polarized data to SM was observed in Le Hégarat et al. (2002), Quesney et al. (2000) and Srivastava et al. (2003). The dispersion and the curvilinear shape of measurements points may be attributed to roughness effects (Holah et al., 2005; Le Morvan et al., 2008).

Incorporating the roughness effect is proven to be necessary when monitoring large areas with different conditions (different soil texture and roughness). Different studies are thus attempted to incorporate the effect of surface roughness in the SM retrieval algorithm. Using data collected along multi-incidence angles requires a simultaneous availability of SAR data at lower and higher incidence angles (Srivastava, 2007). To overcome the (mostly general) unavailability of data at multi-incidence angles, several studies (Srivastava et al., 2008; Ulaby et al., 1986) have used multi-polarized SAR data. Both retrieval methodologies require ground truth measurements of soil moisture and/ or surface roughness for calibration. Contrariwise, the methodology developed in this paper relies on satellite data available world-wide, and does not require ground measurements for calibration. Future studies could make use of both thermal and multi-incidence angle radar data as additional constraints on the roughness effects on radar-based SM retrievals.
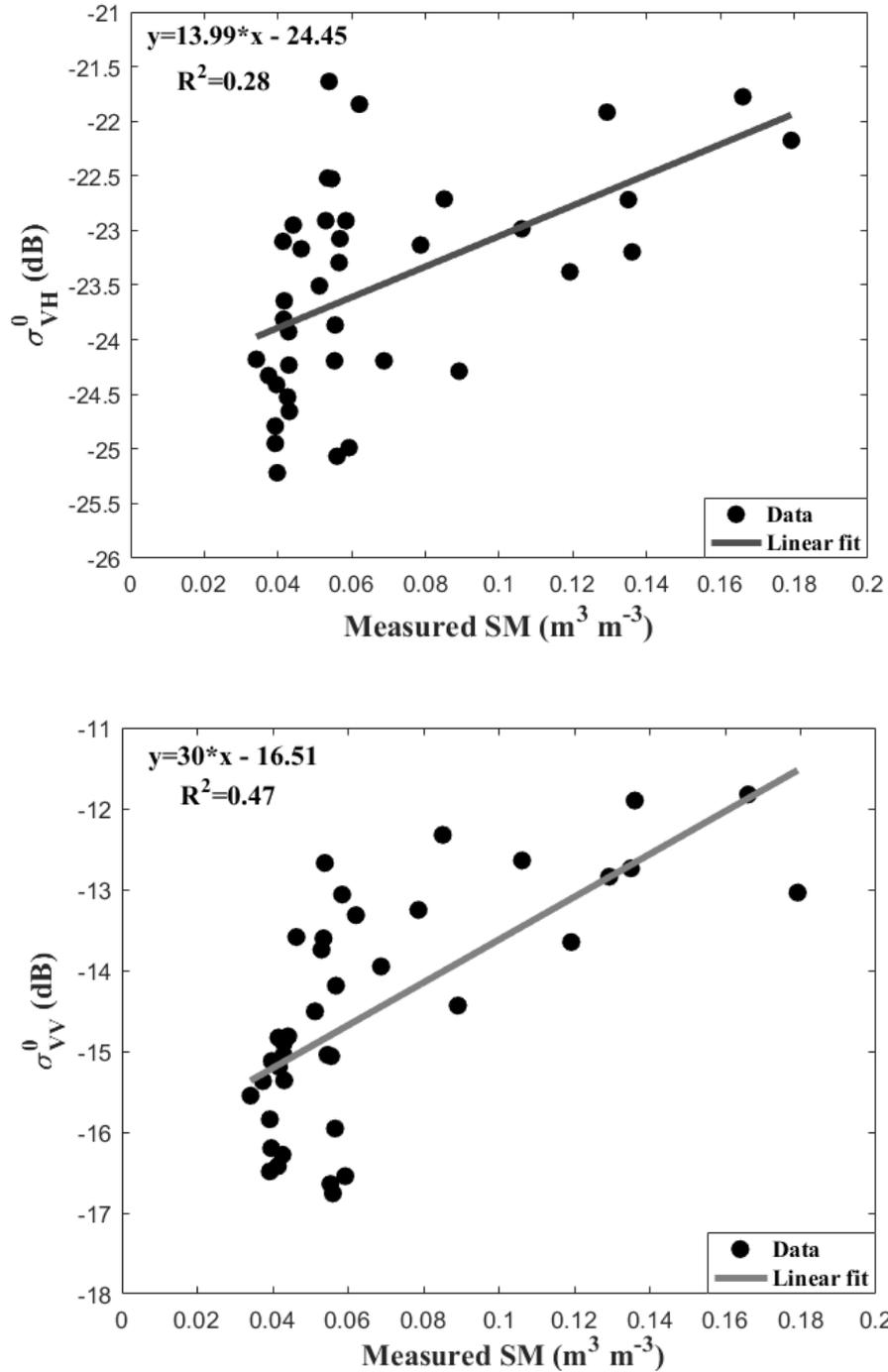
Figure IV.17: Radar signal sensitivity to SM for VH (top) and VV (bottom) polarization over the Sidi Rahal site.

The observation configuration has also an influence on the sensitivity of radar signal to SM, and hence on our capability to retrieve SM from radar data. Several studies showed that the low to medium incidence angles (20°-37°) are the most suitable for SM retrieval using C-band data (Holah et al., 2005; Le Hégarat et al., 2002; Quesney et al., 2000; Srivastava et al., 2003; Zribi et al., 2008). Baghdadi et al. (2008) and Holah et al. (2005) found that the radar

sensitivity decreases with increasing incidence angle. Moreover, the azimuthal angle changes with the ascending or descending passes. However, in our case, the study site is flat and the incidence angle is relatively constant (40°) so we observed no significant difference in terms of SM sensitivity between the data collected on ascending and descending overpasses. Hence, the sensitivity of radar data to the azimuthal angle seemed to be negligible in this study.

As a best option among the two different available polarizations to retrieve top SM, the VV polarization is used throughout the rest of the manuscript.

IV.5.2 Relationship between thermal-derived SMP$_{Ts}$ and radar signal

Fig. IV.18 plots SMP$_{Ts}$ against S1 σ^0_{vv} for the L-7/8 thermal data over the Sidi Rahal and the R3 study site, separately. For the full range of SMP$_{Ts}$ [0-1], we observed a nonlinear behaviour between the Landsat-SMP$_{Ts}$ and the σ^0_{vv}. So as an attempt to approach linearly SMP$_{Ts}$ (σ^0_{vv}) and in order to define the calibration coefficient of the piecewise linear model defined in Eq. III.30, the SMP$_{Ts}$ full range is split into 2 distinct classes separated by the mid-value (0.5). The SMP$_{Ts}$ and σ^0_{vv} values falling into each class (< and > to 0.5) provide a centroid point per class. The crossing over between the linear segment passing through the two centroid points and the line SMP = 0 and SMP = 1 allows to define the calibration parameters over each study site separately. From a physical point of view, the 0.5 was taking as a mid-value at which the evaporation process switches from mostly moisture-limited to mostly energy-limited conditions (Merlin et al., 2016). Results of the calibration using Landsat data lead to values of 0.25 dB^{-1} and 3.89 (unitless) for a_0 and b_0 over Sidi Rahal site and (0.26 dB^{-1} and 4.16 for R3 sites), respectively.

In order to detect the impact of the median value to the calibration parameters (a_0 and b_0), and to the retrieved SM, we performed a sensitivity analysis for different mid-values [0.40, 0.45, 0.50, 0.55, and 0.60]. Results are presented in Table IV.5.

Table IV.5: Sensitivity analysis of the calibration results to the mid-value.

Mid-value	Calibration parameters a_0 / b_0	SM (m^3 m^{-3})				Calibration parameters a_0 / b_0	SM (m^3 m^{-3})			
		R^2	RMSE	MBE	Slope/ intercept		R^2	RMSE	MBE	Slope/ intercept
0.40	0.20 / 3.25	0.64	0.03	0.01	1.00/0.01	0.25 / 4.03	0.59	0.04	0.01	1.01/0.01
0.45	0.20 / 3.25	0.64	0.03	0.01	1.00/0.01	0.25 / 4.03	0.59	0.04	0.01	1.01/0.01
0.50	0.25/ 3.89	0.62	0.03	0.01	1.06/0.01	0.26 / 4.16	0.59	0.04	0.0	1.03 / -0.0
0.55	0.48 / 7.44	0.51	0.06	0.02	1.37/0.00	0.25 / 4.13	0.59	0.04	0.01	1.02/0.00
0.60	0.48 / 7.44	0.51	0.06	0.02	1.37/0.00	0.25 / 4.03	0.58	0.04	0.01	0.99 /0.01

(Header spanning: "Sidi Rahal" over the first calibration+SM block, "R3" over the second.)

To help interpret these results shown in Table IV.5, a standard deviation (SD) has been calculated between the values of the a_0 parameter for the different mid-values for each site separately. We found that SD is much larger for Sidi Rahal (0.14) than for R3 (0.004) sites due to the lack of wet conditions encountered in the SEE time series at Sidi Rahal site. As it seen in Table IV.5, the sensitivity analysis shows that the method is not sensitive to the median value for the R3 sites, where the parameters slightly vary from one to another case, thus reveals very stable results in terms of SM retrievals. In contrast, the influence of the median value appears significantly over the Sidi Rahal site, which affects a lot the SM estimates. Such a sensitivity analysis indicates that the mid-value should be set appropriately, by keeping a sufficient number data points in each of both SEE classes, especially for time series containing mainly dry or mainly wet conditions.
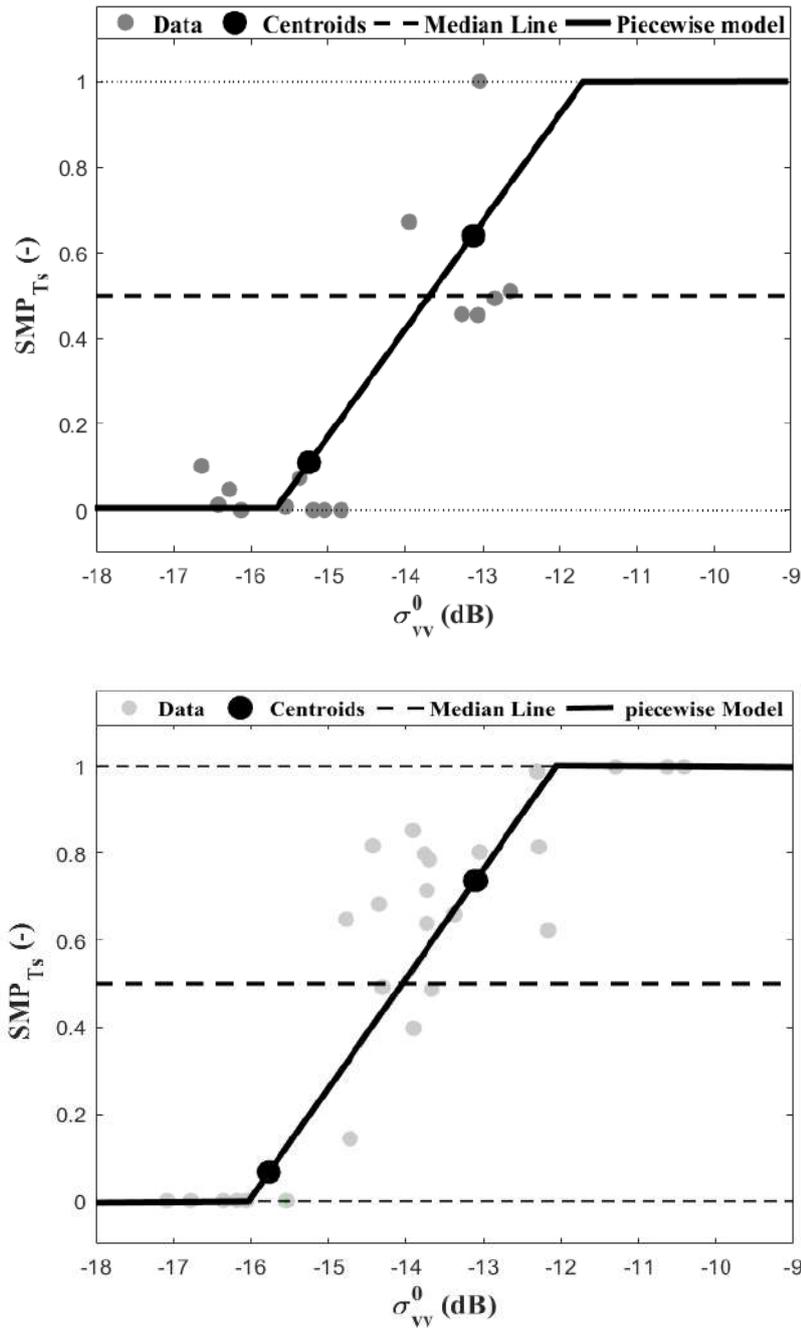
Figure IV.18: SMP_Ts – σ_{vv}^0 relationship using T_s derived from Landsat data over Sidi Rahal (top plot) and R3 (bottom plot) site. The solid line represents the assumed piecewise linear model.

IV.5.3 SM estimation at high spatio-temporal resolution

IV.5.3.1 SM retrieval

The classical and new approaches were tested and examined by comparing the retrieved SM with *in situ* measurements. The calibration and validation of the new approach was performed separately at each site (on a pixel basis), having two different soil textures: Sidi Rahal site has

a sandy soil while the two other sites in the R3 perimeter are characterised by a clayey soil. Fig. IV.19 compares SM retrievals with *in situ* measurements for the benchmark and new approach for the studied sites, and a validation of the new approach using *in situ* T_s has been also presented over Sidi Rahal site when *in situ* T_s data are available. Results of this comparison, in terms of determination coefficient (R^2), slope and intercept of the linear regression, mean bias error (MBE) and root mean square error (RMSE) are presented in Table IV.6.
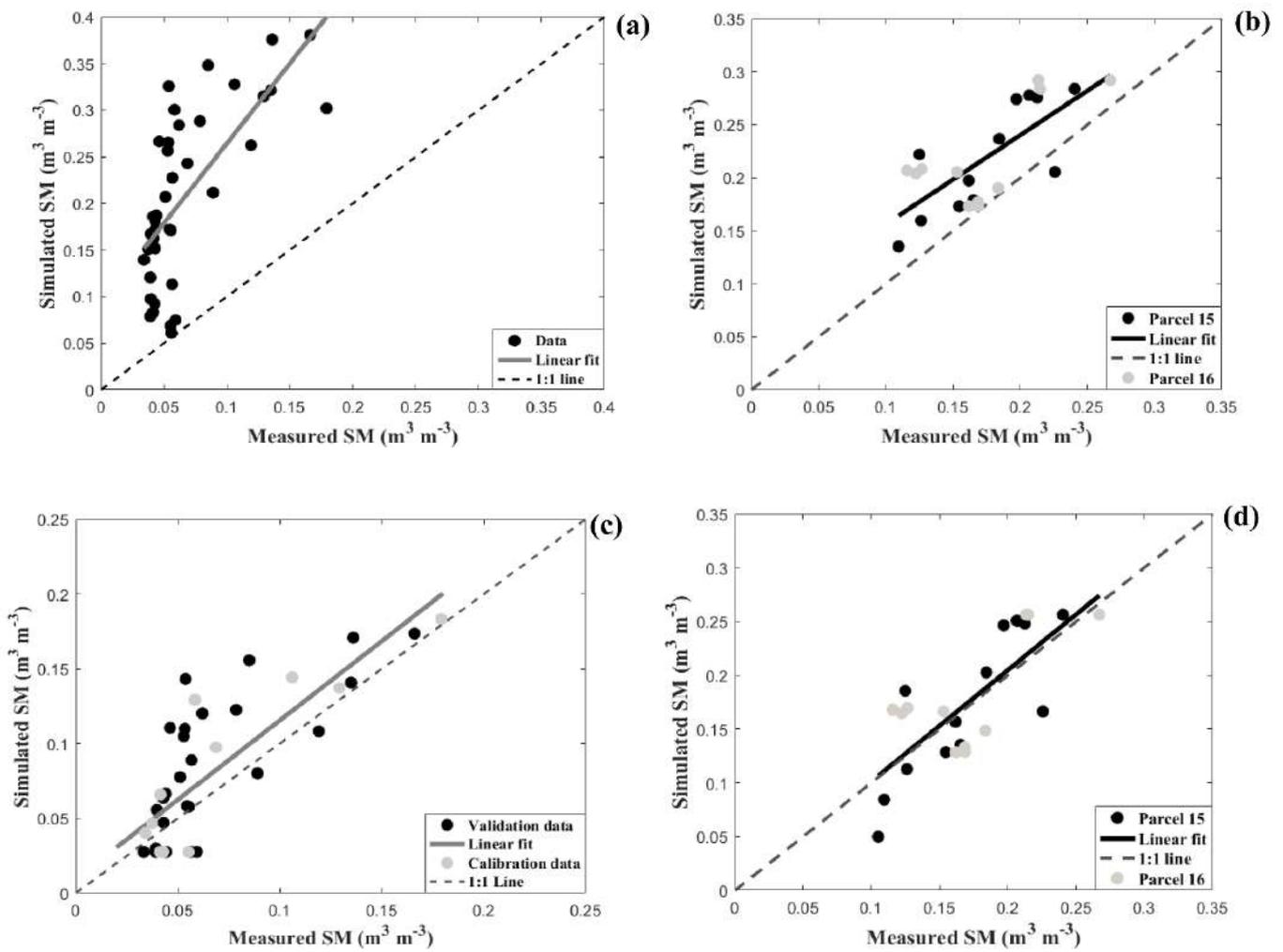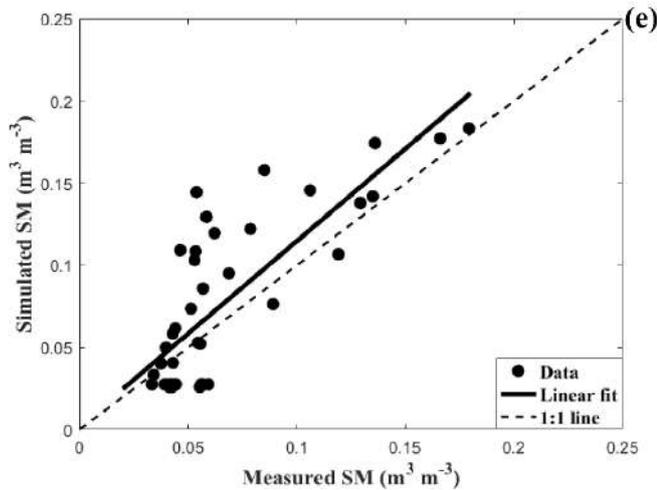
Figure IV.19: Estimated versus measured SM using the benchmark approach (a,b), new approach (c,d) and validation using in situ LST (e) over Sidi Rahal (a, c, e) and R3 (b, d) site.

Table IV.6: R^2, RMSE, MBE (simulated – observed), and the slope/intercept for the linear regression between simulated and observed SM for the classical and the new approach for Sidi Rahal and R3 sites.

Sites	Approach		R^2	RMSE (m³ m⁻³)	MBE (m³ m⁻³)	Slope/intercept (-) / (m³ m⁻³)
Sidi Rahal		Classic	0.47	0.16	0.14	1.71 / 0.09
	New	all dates	0.64	0.03	0.01	1.12 / 0.002
		dates when L7/8 & S1 data available (not shown here)	0.79	0.03	0.00	1.2 / -0.007
		Validation *using in situ LST*	0.64	0.03	0.01	1.12 / 0.002
R3		Classic	0.56	0.05	0.04	0.84 / 0.07
		New	0.59	0.04	0.00	1.03 / -0.002

The benchmark method shows a systematic overestimation, and a kind of curvilinear relationship especially in the Sidi Rahal site whereas the new methodology offers a good consistency with ground-truth measurements. The linear scaling between σ_{vv}^0 and SM can explains the overestimation observed using the classical approach, since the two coefficients of the linear relationship are derived from extreme values of SM and σ_{vv}^0. Note that this effect is all the more visible as extreme (wet) SM values have not been reached at the time of S1

overpasses, despite the high temporal resolution of S1 and the relatively long time period. We argue that the main advantage of the proposed method is to provide robust reference points for calibrating the σ^0_{vv} (SM) relationship, even for time series that do not contain extreme SM conditions. In addition, the calibration of the Eq. III.30 allows for taking into account possible nonlinear behaviours of the σ^0_{vv} (SM) relationship, especially in dry to very dry conditions. The radar signal can be only calibrated using thermal data when both satellites are concurrent or are quasi concurrent. It is reminded that over the study area both T_s and backscatter coefficients were available at approximately (one day difference) the same time. A sensitivity analysis was undertaken to assess the impact of a systematic error in LST on SM retrieval results. Based in the finding (results not shown), an error in LST estimations (±3 °C) would have a relatively small effect (maximum additional error of 0.02 m^3 m^{-3}) in the SM estimations. Note that a bias in Landsat LST would have no effect on SM retrievals in the case of using contextual methods, instead of using an energy balance model to determine $T_{bs,d}$ and $T_{bs,w}$. When L7/8 and the S1 data were available in Sidi Rahal site, the results reveal a high R^2 of 0.79 with an RMSE of 0.03 m^3 m^{-3} which decrease the bias. As seen in Table IV.6, the radar/thermal combining approach provides a slightly higher R^2 value and a lower RMSE compared to the classical (radar only) approach. This improvement result is in an almost negligible mean difference between the estimated and *in situ* SM. The statistical outputs parameters confirm that the new approach estimates SM accurately. Results in terms of SM accuracy indicate that the loss of spatial resolution (from the aggregation of radar data from 20 m resolution to crop field scale) has a lower impact than the roughness effects that need to be taken into account at the crop field scale. A slope correction is observed (close to 1) using the new approach with an almost null intercept using satellite data whereas the conventional approach provides a higher value of both slope and intercept. Note that the one-day difference between Sentinel-1 radar and Landsat LST data, which may be representative of different SM levels (difference estimated as 0.02 m^3 m^{-3} over the experimental site), explains part of the uncertainty (estimated as 0.03 m^3 m^{-3}) in the retrieved SM. We can explain the previous statement by the non-appropriate estimation of $\sigma^0_{vv,min}$ and $\sigma^0_{vv,max}$ for the classical approach, which is based on two assumptions: 1) minimum and maximum SM values are observed at the time of S1 overpasses and 2) the relationship between backscatter coefficient and SM is linear. Note that such a relationship tends to be non-linear (Zribi et al., 2011), with a saturation appearing in the radar signal in the higher range of SM values (Bruckler et al., 1988).

In Fig. IV.19 (Sidi Rahal site), a significant phenomenon was observed for the low SM values, which correspond to low backscatter values. In this range, *in situ* SM do not change with radar backscatter. This observed phenomena can be explained by the deeper penetration of the radar when the soil surface gets drier. In addition, the radar signal tends to be more sensitive to roughness variations in very dry conditions (Boisvert et al., 1997). We did not observe this effect over R3 sites because of the wetter conditions encountered over the irrigated perimeter. In addition, the SM in the top 5 cm may differ between the two sites, depending on the soil water retention properties and infiltration rates, resulting in variations in the S1 signal (Aubert et al., 2011).

IV.5.3.2   Sensitivity to temperature endmembers

In this study, soil evaporative efficiency (SEE) was derived from the temperature endmembers simulated by an EB model. Therefore, meteorological forcing data are needed as input to the calibration scheme of the radar-based SM retrieval approach.

The idea behind using the contextual method to derive temperature endmembers is to analyse the sensitivity of the SM estimation to uncertainties in $T_{bs,d}$ and $T_{bs,w}$ estimates. The extreme T_s are used as an input in Eq. III.1 in order to assess the potential of the contextual method against the EB method. The retrieved SM using the T_s endmembers extracted from LST-NDVI polygons is evaluated against *in situ* measurements over the study areas. At Sidi Rahal, the use of image-based T_s endmembers leads to small values of SMP_{Ts} (<0.3), which makes our approach inapplicable in this case as wet reference points are lacking to build the calibration equation. This is due to the overestimation of $T_{bs,w}$ by the contextual method. In addition, the Sidi Rahal (8×8 km^2) area experienced the highest observed temperature (very close to $T_{bs,d}$) leading to a small SEE values. The contextual method was also tested over the R3 area. In order to investigate the influence of $T_{bs,w}$ estimation, the new approach is also tested by using T_{air} instead of $T_{bs,w}$ (in addition to contextual $T_{bs,d}$).

Fig. IV.20 shows the estimated SM using the image-based T_s endmembers against ground measurements acquired from the R3 study site. The statistical values such as the slope of the linear regression, R^2, RMSE and MBE between retrieved and *in situ* SM are reported in Table IV.7.

Table IV.7: R^2, RMSE, MBE and slope/intercept of the linear regression between retrieved and observed SM for the classical and the new approach for R3 sites using contextual T_s endmembers.

Temperature endmembers		R^2 (-)	RMSE ($m^3 \ m^{-3}$)	MBE ($m^3 \ m^{-3}$)	Slope / intercept (-) / ($m^3 \ m^{-3}$)
Classic		0.56	0.05	0.04	0.84 / 0.07
New	Contextual $T_{bs,w}$ and $T_{bs,d}$	0.56	0.04	0.03	0.52 / 0.11
	T_{air} and contextual $T_{bs,d}$	0.50	0.04	0.01	0.99 / 0.01
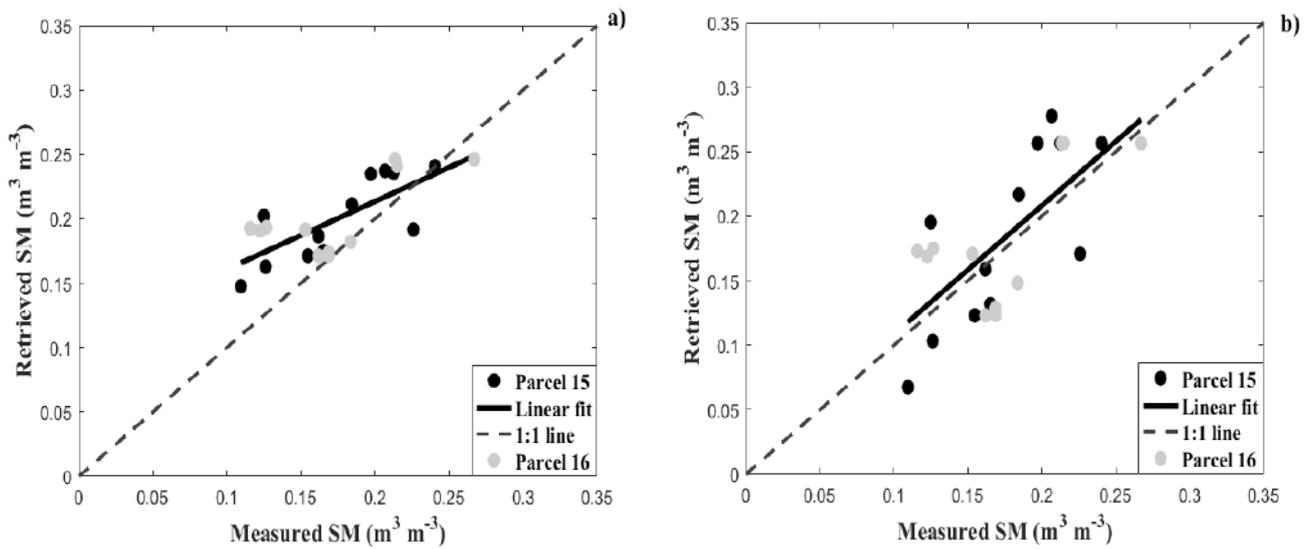
Figure IV.20: Retrieved versus measured SM using the new approach over R3 sites using: a) contextual T_s endmembers and b) contextual $T_{bs,d}$ and T_{air} instead of $T_{bs,w}$.

After using the T_s endmembers extracted from contextual information, the new method shows an improvement in terms of RMSE (0.04 $m^3 \ m^{-3}$ compared to 0.05 $m^3 \ m^{-3}$ for the classical approach). In contrast, the classical approach offers a better slope (close to 1) compared to the new approach (Fig. IV.20a). The poor slope obtained using the new approach is probably due to the overestimation of $T_{bs,w}$ by using the contextual method especially during summer, when wet conditions were not met over the study area. To discriminate the effect of image-based $T_{bs,w}$ on SM estimation, T_{air} was used as a better proxy of $T_{bs,w}$ at the satellite overpass time. Results (Fig. IV.20b) listed in Table IV.7, revealed a slightly poorer R^2 (0.50) in contrast with the classical approach (0.56), except that the new approach offers a slope equal to 1 with a null intercept in addition to smaller bias (0.01 versus 0.04 $m^3 \ m^{-3}$) compared to the classical approach. As a brief summary of this sensitivity analysis, it is found that EB temperature endmembers are generally more robust than image-based temperature endmembers.

Nevertheless, in certain conditions (e.g. semi-arid irrigated areas containing quasi continuously wet and dry conditions), the contextual method could offer an efficient alternative to calibrate the radar-based SM retrieval approach, especially in the regions where meteorological data are not available with sufficient accuracy.

An additional sensitivity analysis was performed in order to assess the impact of the surface roughness on radar and LST data, as well as on the energy balance model (represented by Z_{0h} and Z_{0m} the roughness length for heat and momentum) on the modelled extreme temperatures and the retrieved SM (via simulated $T_{bs,d}$ and $T_{bs,w}$). It is found (results not shown) that the modelled LST remains rather stable when changing the roughness parameters by 1 order of magnitude. Note that the stability of LST with respect to soil roughness is fully consistent with all contextual methods that rely on this assumption as well (ex. by setting the maximum observed LST to $T_{bs,d}$).

IV.5.3.3   SM validation: Improvement of soil evaporation estimation

The tight coupling between soil evaporation and SM in semi-arid areas is used to calibrate the radar-SM relationship using thermal-derived SEE estimates. As a step further in the assessment of the proposed methodology, the soil evaporation was estimated from either the radar-based SM, the thermal-derived SEE, or the thermal-calibrated radar-based SM. Note that soil evaporation represents an important component of the water budget over semi-arid regions. Although various evaporation formulations exist as a function of SM (Chanzy, 1991; Chanzy and Bruckler, 1993; Mahfouf J.-F. and Noilhan, 1991), the uncertainty in evaporation models remains relatively large especially when applied to a range of surface conditions (Merlin et al., 2016). Even though remote sensing data have strong potential for better constraining the evaporation process (Chanzy and Bruckler, 1993; Merlin et al., 2017), the characterisation of model parameters using available remotely sensed land surface temperature and SM observations is still not well identified.

As a complementary assessment of the synergy between radar- and thermal-based techniques for SM retrieval, both approaches were thus inter-compared in terms of soil evaporation estimates over the Sidi Rahal site, when eddy covariance measurements are available. In this sub-section, LE_s was estimated using Eq. III.31, and the potential evaporation estimated using the same energy balance model as that used to estimate temperature endmembers. The SEE used as input to Eq. III.31 was derived either from L7/8 Thermal data (Eq. III.1 or S1 backscatter (Eq. III.2).

Regarding the SM-based SEE model, two different parameterizations are suggested by setting the parameter to SM_C (Eq. III.32) or saturation soil moisture (SM_{sat}):

$$SEE = \frac{SM_{\sigma+Ts}}{SM_{sat}} \qquad\qquad (IV.2)$$

with $SM_{\sigma+Ts}$ (m^3 m^{-3}) being the SM estimated using the synergistic approach between Landsat and S1 data. Fig. IV.21 and Table IV.8 presents the results of the soil evaporation estimation using the above four models.

Table IV.8: Error statistics between simulated and observed evaporation over Sidi Rahal site.

Input data		R^2	RMSE (W m^{-2})	MBE (W m^{-2})
Thermal data only		0.36	64.2	-14.5
Radar data only		0.41	166	130
Combined radar and thermal data	Equation (III.32)	0.63	103	77
	Equation (IV.2)	0.63	26.5	-0.14
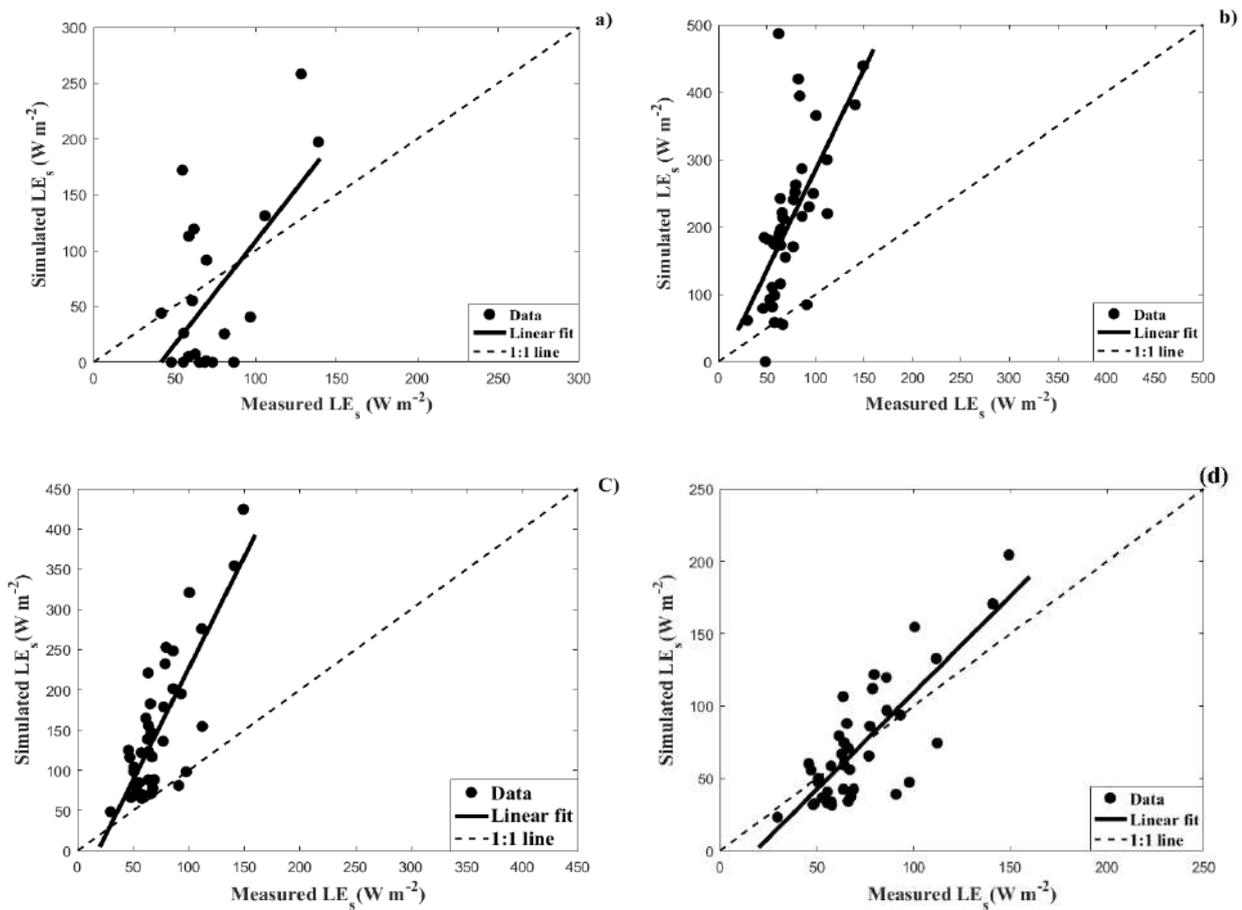
Figure IV.21: Comparison at the Sidi Rahal site between simulated and observed soil evaporation for an SEE model driven by a) LST data, b) radar data, and combined radar and Landsat data using c) SM_C and d) SM_{sat} parameter.

Table IV.8 shows that the combination between radar and thermal data (Fig. IV.21c and d) provides better evaporation results than using each satellite separately (Fig. IV.21a and b). The evaporation estimates derived from thermal data only are greatly uncertain. This could be due to the loss of sensitivity of land surface temperature to the 0-5 cm SM in very hot and dry conditions. The use of radar data only provides a much better correlation between simulated and observed soil evaporation, but estimates values are systematically larger than those observed by eddy covariance. This effect is also visible with the thermal/radar combined approach with SM_C parameter. When setting the SM-based SEE parameter to SM_{sat}, the systematic overestimation disappears with a determination coefficient and bias between simulated and observed evaporation of 0.63 and 0.14 W m^{-2}. Better results obtained by changing the SM-based SEE parameter from SM_C to SM_{sat} could be attributed to soil profile heterogeneities, which are very strong in semi-arid regions. In fact, the microwave-derived SM generally corresponds to the first cm of soil whereas the radiometric soil temperature is representative of a soil layer that is much thinner (approximately 1 mm). The discrepancy between the sensing depth of microwave and thermal data partly explains the difference in thermal-based and SM-based SEE models in this case (Merlin et al., 2017).

IV.6 Summary and conclusion

In general the proposed new approaches have given more accurate results, whether when using thermal data to calibrate radar backscatter in order to estimates surface SM over bare soil, or to integrate radar SM-proxy combined with the fraction of green vegetation information to disaggregate surface temperature at high resolution, or to improve the Penman-Monteith equation by integrating thermal stress to the surface resistance to estimate evapotranspiration over wheat parcels.

The proposed relationship between r_c and SI employed in the P-M model holds great potential for estimating crop ET using remote sensing data. Moreover, the results reached in terms of detecting crop water stress, can be helpful to distinguish between the irrigated and non-irrigated areas, which could give a prevision of the wheat yield based on the IPI developed by Belaqziz et al. (2013). This relation was then tested over the drip-irrigated site using *in situ* measurements in order to simulate the surface ET. Next, this method was evaluated in terms of latent heat flux using Landsat temperature and reflectance data over both sites. The RMSE values over drip and flood sites are 13 and 12 W m^{-2}, which correspond to the relative errors of 5 and 4%, respectively. As such a method has a limitation, the main limitation of this approach is the receptivity frequency of the LST data, which are an essential input of the P-M

equation. It is interesting to mention that the used P-M equation to retrieve ET was applied to mixed pixels including soil and vegetation components.

As an attempts to overcome the LST gap, a disaggregation approach has been developed in this work to improve the spatio-temporal resolution of LST data to monitor efficiently the ET at a high frequency. The disaggregating approaches are applied to kilometric MODIS/Terra LST data to 100 m resolution over an irrigated and rainfed semi-arid area. Further, to discretise LST into two components: soil and vegetation temperature in order to obtain the ET using Dual-source model. The separation of the two components however requires surface soil moisture data, where in this study we propose a synergistically approach between radar and thermal data to monitor SM over bare soil.

Best results are obtained with the new algorithm denoted D2' when using MODIS LST data based on the Radiative Transfer Model (RTM) equation, compared to the procedure based on a linear regression between f_{gv} and LST, and also compared to the multi-linear regression between f_{gv}, σ_{vv}^0 and LST. Since the selected area showed a heterogeneity in terms of vegetation type and soil water status, we conclude that the new algorithm produces more stable and robust results during the selected year. 0.83 °C and 0.86 were the lowest RMSE and the highest correlation coefficient assessed using the new algorithm. For the SM retrieval at field scale, the radar/thermal synergistic SM retrieval approach was tested with the VV-polarized data. The determination coefficient between remotely sensed and *in situ* SM is 0.64 and 0.59 with the new approach, compared to 0.47 and 0.56 for the classical approach over Sidi Rahal and R3 site, respectively. Moreover, the bias between remotely sensed and *in situ* SM is very significantly reduced when including thermal data, from 0.14 to 0.01 m^3 m^{-3} and from 0.04 to 0.00 m^3 m^{-3} over Sidi Rahal and R3 site, respectively. As step further, the radar-thermal combining approach is also assessed in terms of soil evaporation estimates. A RMSE of 26 W m^{-2} was obtained between simulated and observed evaporation, compared to 64 and 166 W m^{-2} when using the thermal data only and the radar data only, respectively. The synergy between radar and thermal data could thus be used to both improve the SM retrieval at high-spatial resolution and foster the spatial representation of the soil energy-water coupled budget.

Conclusions and perspectives

This Phd thesis "**Monitoring crops water needs at high spatio-temporal resolution by synergy of optical/thermal and radar observations**" is focused on improving the spatio-temporal representation of crops water needs in relation with the available satellite observations. Innovative and promising approaches are presented to monitor the amount of water needed to meet the water loss through evapotranspiration and for optimal growth. The crop water needs depend on climate, crop type and the phenological stages of the crops. The crop water needs can be supplied by rainfall or by irrigation. In this work, the modelling approaches (disaggregation and energy balance, image-based and radiative transfer modelling) are developed to answer the question of water ressource management. The central idea is around the estimation of soil moisture indices at high spatio-temporal resolution to help retrieve vegetation stress, evapotranspiration, land surface temperature and root zone soil moisture in a semi-arid climate region (central Morocco).

The first part of the thesis is dedicated to the estimation of evapotranspiration (ET) over irrigated wheat crops of semi-arid areas. Although falling within the state-of-the-art, the Penman-Monteith (P-M) approach has been limited by difficulties in estimating the bulk surface resistance (r_c), which depends on several poorly known factors related to crop characteristics and agricultural practices. We thus proposed to link r_c to the stress index (SI) derived from remotely sensed land surface temperature (LST) and to implement the developed relationship in the P-M model. SI was estimated as the observed LST normalized by the LST simulated in fully wet and dry conditions using a surface energy balance model forced by meteorological forcing and vegetation fraction.

The approach was evaluated over a 10 x 10 km^2 irrigated perimeter (R3) near Marrakech. The calibration/validation strategy implemented two instrumented wheat sites with flood and drip irrigation and Landsat shortwave and thermal imagery during one growing season (2015-2016). The r_c retrieved from eddy covariance measurements over the flood-irrigated site (by inverting P-M equation) was first correlated to SI. This relation was then tested over the drip-irrigated site using *in situ* measurements in order to simulate ET. Next, this method was evaluated in terms of latent heat flux using Landsat LST and vegetation index data over both sites.

Although tested over two wheat parcels only, the proposed relationship between r_c and SI holds great potential for estimating crop ET using remote sensing data. Moreover, the results reached in terms of crop water stress detection, could be used in the future to distinguish

between the irrigated and non-irrigated areas. Such an irrigation mapping could provide useful information for forecating the wheat yield based on the Irrigated Priority Index (IPI) developed by Belaqziz et al. (2013).

The second part is dedicated to retrieve the near-surface (5 cm) soil moisture (NSSM) over bare soils by combining Sentinel-1 C-band radar and Landsat-7/Landsat-8 thermal data. The methodology is based on the thermal-derived soil evaporation efficiency (SEE) to calibrate the radar backscatter-NSSM relationship on a (100 m resolution) pixel basis. In practice, the observed relationship between the VV or VH (pp) polarized backscatter coefficient σ_{pp}^0 and thermal-derived SEE was modelled by a piecewise linear regression model. Calibration of the piecewise model was performed by 1) computing the two centroids of the (σ_{pp}^0, SEE) points with SEE > 0.5 and SEE <= 0.5, 2) plotting the line passing through both centroids and 3) estimating the two crossing points of that line with the lines defined by SEE = 0 and SEE = 1. The retrieval approach was evaluated by comparing the remotely sensed NSSM to *in situ* measurements at two contrasted soil texture experimental sites (Sidi Rahal has sandy soil while R3 perimeter has clayey soil). The radar/thermal synergistic method was also compared to a classical (based on radar only) method. As a step further, the radar-thermal combining approach is also assessed in terms of soil evaporation estimates. The synergy between radar and thermal data could thus be used to both improve the NSSM retrieval at high-spatial resolution and foster the spatial representation of the soil energy-water coupled budget.

The above obtained results are very encouraging as they open the path for more synergies between radar and optical/thermal space missions and (NSSM and water-energy budget) applications. The methodology requires however significant NSSM variations associated with irrigation or rainfall events during the calibration periods. In addition, the temperature endmembers used to derive the SEE from thermal data are estimated from an energy balance model forced by meteorological forcing data. The point is that meteorological data may not be available everywhere with sufficient accuracy. Thus, alternative solutions could be imagined, such as the derivation of temperature endmembers from contextual methods relying on remote sensing data solely. Contextual methods are especially well adapted over semi-arid irrigated regions where extremely dry and wet conditions are present within the thermal scene (Stefan et al., 2015). Another limitation is that this method requires soil texture information to convert SM index values into absolute SM values via the residual and saturation SM derived from pedo-transfer functions.

Another potential limitation is the temporal frequency of thermal observations. The robustness of the calibration approach mainly relies on the availability of thermal data, at the same time as radar acquisitions. Unfortunately, the thermal data available at high-spatial resolution (100 m with Landsat) currently have a maximum temporal resolution of 8 days (Lagouarde et al., 2014). When the scene will be cloudy, the temporal resolution will be necessarily less. Consequently, the applicability of the proposed thermal/radar synergy over cropped fields will require sufficient thermal images during bare soil periods that is from the sowing date until emergence and during the intercropping periods. This is the objective of the third part that aims to improve the spatio-temporal resolution of remote sensing thermal data.

The third part aims to disaggregate 1 km resolution MODIS/Terra LST data to 100 m resolution over an irrigated and rainfed semi-arid area. The idea is to include the high spatial resolution NSSM variability in the disaggregation algorithm, in addition to the classical fraction of green vegetation cover. The algorithms are firstly tested using the 1 km aggregated Landsat-7/8 LST as input to avoid the errors and random uncertainties produced by the registration of 1 km resolution sensors like MODIS. Then, the performance of the used algorithms is assessed using MODIS/Terra daytime LST as input. The Landsat LST at 100 m resolution is mainly used for validation purposes.

Best results are obtained with the new algorithm when using MODIS LST data based on the radative transfer equation, compared to the procedure based on a linear regression between f_{gv} and LST, and also compared to the multi-linear regression between f_{gv}, σ^0_{vv} and LST. Since the selected area showed a heterogeneity in terms of vegetation type and soil water status, we conclude that the new algorithm produces more stable and robust results during the selected year. These results are encouraging and can be used to reinforce and to improve the application of downscaling procedures to low resolution thermal sensors. Sentinel-2 (S-2) is a continuity of Landsat reflectances with an improvement in the spatio-temporal resolution. Therefore, the application of the disaggregation algorithm to MODIS LST using S-2 ancillary data will improve the temporal resolution to 5 days.

In this work, the hydric stress index and ET have been obtained over wheat parcels. As a perspective, further calibration studies should be undertaken to investigate and understand the variability of r_c parameters over different crop types and surface conditions. In my work the SM index is linked to surface resistance, which is a sum of soil and vegetation resistances. Therefore, a partitioning approach should be established to quantify accurately the crop water stress solely by explictely removing the the soil contributions. The two-source Shuttleworth-

Wallace model (Shuttleworth and Wallace, 1985) could be used to separate soil and vegetation effects.

Additionnally, for the NSSM estimation using thermal/radar data, the proposed methodology was only assessed over bare soils. Further research must be undertaken to test the applicability of the calibration method to soils partially and/or fully covered by vegetation canopy. A solution would be to integrate the VH data that are more sensitive to vegetation effects than VV data. In addition, to take into account the vegetation and roughness effects, a synergetic approach could be tested between radar, thermal and shortwave optical data at high resolution by benefiting of S-2 optical data. The S-2 sensor provides reflectances at high spatio- (20 m) temporal (5 days in average) resolution, which would potentially allow for deriving SM indices every (clear sky) 5 days by combyining S-2 and S-1 sensors (Gao et al., 2017; Hajj et al., 2017b), which is enough to monitor the crop hydric status in the context of water resources management. It has been demonstrated that change detection techniques are a promising tool to catch the variability of SM at 100 m by using an interpretation of high repeat frequency S-1 radar data in synergy with S-2 optical data (Qi Gao 2016 thesis). Furthermore, the Thrishna satellite (India-France joint satellite mission to be launched in 2024) will provide LST data with a 50 m resolution and a 3-5-day revisit, which could be a great opportunity to use the thermal/optical data in synergy with radar data to retrieve NSSM at a high resolution.

Alternatively, the disaggregation of low (typically 40 km) spatial resolution NSSM is a promising tool for producing NSSM data sets at high spatial-temporal resolution. Pursuing this path, recently Ojha et al. (2019) proposed a new disaggregation scheme of SMOS and SMAP data at a 100 m resolution using Landsat data through an intermediate spatial resolution by using the disaggregation based on physical and theoretical scale change (DISPATCH) algorithm. The advantage of this method is that the input parametres are calibrated using remote sensing data with no in situ data needed. The problem is that DISPATCH data at 100 m are available only on cloudless days and during Landsat pass, which significantly reduces the time frequency and causes a limitation for operational applications. Synergy with radar-based approaches can fill the gap (Peng et al., 2017; Tomer et al., 2016). In this context, the calibration strategy of the main parameter of radar-based SM retrieved using a thermal-derived SM proxy established in this working complimentarily with the 100 m resolution DISPATCH SM could be used to calibrate a radar model (by integrating the effects of surface roughness and vegetation) to provide a product in any weather and that

should be quite robust, given the constraints of SMOS / SMAP / MODIS / Landsat data. The idea here is to use the 100 m resolution DISPATCH SM to calibrate a physical model based on radar and vegetal cover with no need of soil texture to estimate the SM endmembers.

Before the launch of Trishna mission, the disaggregation of existing low resolution LST data can provide LST data at high spatial resolution with a relatively satisfying accuracy. The proposed techniques provided in this work, can be considered as a basis for new missions dedicated to provide thermal infrared data at high spatio-temporal resolution (as Trishna). My work has opened up new paths of research that will make it possible to exploit the potentialities of the images provided by the new programs (S-1 and S-2) for getting LST at HR. Further research must be undertaken to incorporate the vegetation water stress into the disaggregation methods, possibly by integrating the S-1 VH polarization data, which are more sensitive to vegetation water content effects than VV polarization.

All the information provided in this thesis such as NSSM and stress index derived from thermal data at high spatio-temporal resolution are key input variables for ET models based on the hydric balance model such as FAO-56 method (Zoubair Rafi Thesis) and the energy balance model as TSEB (Bouchra ait Hssaine Thesis). They can be used as an input variable to a dual source ET model in order to improve the evaporation/transpiration partitioning for more accurate and precise estimation of the water supply by irrigation and therefore a better management of the water use. Recently (Ait Hssaine et al., 2018) proposed a new model (TSEB-SM) based on a network of resistances to represent exchanges between soil, vegetation and the atmosphere. This model has the advantage of calibrating its parameters from the MODIS LST and DISPATCH NSSM data and of being compatible with the new state of the art models of evaporation (Bouchra ait Hssaine Thesis). For further evaluation of the transpiration/ET partition, a complete in situ dataset (combining several independent techniques to quantify the uncertainties) was collected on two plots of wheat in 2016-2017 from the Chichaoua site in Morocco (Zoubair Rafi Thesis). Those data could be used as a reference to evaluate several remote sensing models based on multi-sensor data. However, NSSM and thermal-based stress index used to estimate fluxes are not always sufficient to separate the evaporation and transpiration components and to estimate the moisture stress of the vegetation. An information of the RZSM is needed, and it appears to be the key variable conditioning surface fluxes. For this reason the future incorporation of other independent observations such as fluorescence and photochemical reflectance index (PRI) could provide a solution to quantify accurately the transpired water from the plant. One of the promising paths

to better optimization of water consumption (ET) is to estimate RZSM via water stress for dense vegetated areas from the PRI or fluorescence measurements (Cerovic et al., 1996), in combination with my work, which is to estimate NSSM from S-1 radar data over bare or partially vegetated soil conditions.

Bibliography

Agam, N., Kustas, W.P., Anderson, M.C., Li, F., Colaizzi, P.D., 2007a. Utility of thermal sharpening over Texas high plains irrigated agricultural fields. Journal of Geophysical Research Atmospheres 112, 1–10. doi:10.1029/2007JD008407

Agam, N., Kustas, W.P., Anderson, M.C., Li, F., Neale, C.M.U., 2007b. A vegetation index based technique for spatial sharpening of thermal imagery. Remote Sensing of Environment 107, 545–558. doi:10.1016/j.rse.2006.10.006

Ait Hssaine, B., Ezzahar, J., Jarlan, L., Merlin, O., Khabba, S., Brut, A., Er-Raki, S., Elfarkh, J., Cappelaere, B., Chehbouni, G., 2018. Combining a two source energy balance model driven by MODIS and MSG-SEVIRI products with an aggregation approach to estimate turbulent fluxes over sparse and heterogeneous vegetation in Sahel region (Niger). Remote Sensing 10. doi:10.3390/rs10060974

Akbar, R., Das, N., Entekhabi, D., Moghaddam, M., 2016. Active and Passive Microwave Remote Sensing Synergy for Soil Moisture Estimation, Satellite Soil Moisture Retrieval. Elsevier Inc. doi:10.1016/B978-0-12-803388-3.00010-3

Albright, T.P., Pidgeon, A.M., Rittenhouse, C.D., Clayton, M.K., Flather, C.H., Culbert, P.D., Radeloff, V.C., 2011. Heat waves measured with MODIS land surface temperature data predict changes in avian community structure. Remote Sensing of Environment. 115: 245-254. 245–254.

Alexakis, D.D., Mexis, F.D.K., Vozinaki, A.E.K., Daliakopoulos, I.N., Tsanis, I.K., 2017. Soil moisture content estimation based on Sentinel-1 and auxiliary earth observation products. A hydrological approach. Sensors (Switzerland). doi:10.3390/s17061455

Allen, R.G., Pereira, L.S., Howell, T.A., Jensen, M.E., 2011. Evapotranspiration information reporting : I . Factors governing measurement accuracy Part of the Agricultural Science Commons. doi:10.1016/j.agwat.2010.12.015

Allen, R.G., Pereira, L.S., Raes, D., Smith, M., W, a B., 1998. Crop evapotranspiration - Guidelines for computing crop water requirements - FAO Irrigation and drainage paper 56, Irrigation and Drainage. doi:10.1016/j.eja.2010.12.001

Allen, R.G., Tasumi, M., Morse, A., Trezza, R., Wright, J.L., Bastiaanssen, W., Kramber, W., Lorite, I.J., C.W., R., 2007. Journal of Irrigation and Drainage Engineering Satellite-Based Energy Balance for Mapping Evapotranspiration with Internalized Calibration (METRIC)— Applications. JOURNAL OF IRRIGATION AND DRAINAGE ENGINEERING. doi:10.1061/(ASCE)0733-9437(2007)133

Allen, Tasumi, M., Morse, A., Trezza, R., Wright, J.L., Bastiaanssen, W., Kramber, W., Lorite, I., Robison, C.W., 2007. Satellite-Based Energy Balance for Mapping Evapotranspiration with Internalized Calibration (METRIC)—Applications. Journal of Irrigation and Drainage Engineering. doi:10.1061/(asce)0733-9437(2007)133:4(395)

Alves, I., Santos Pereira, L., 2000. Modelling surface resistance from climatic variables? Agricultural Water Management 42, 371–385. doi:10.1016/S0378-3774(99)00041-4

Amazirh, A., Er-Raki, S., Chehbouni, A., Rivalland, V., Diarra, A., Khabba, S., Ezzahar, J., Merlin, O., 2017. Modified Penman–Monteith equation for monitoring evapotranspiration of wheat crop: Relationship between the surface resistance and remotely sensed stress index. Biosystems Engineering 164, 68–84. doi:10.1016/j.biosystemseng.2017.09.015

Amazirh, A., Merlin, O., Er-raki, S., Gao, Q., Rivalland, V., Malbeteau, Y., Khabba, S., José, M., 2018. Retrieving surface soil moisture at high spatio-temporal resolution from a synergy between Sentinel-1 radar and Landsat thermal data : A study case over bare soil. Remote Sensing of Environment 211, 321–337. doi:10.1016/j.rse.2018.04.013

Anderson, M.C., Hain, C., Wardlow, B., Pimstein, A., Mecikalski, J.R., Kustas, W.P., 2011. Evaluation of drought indices based on Thermal remote sensing of evapotranspiration over the continental United States. Journal of Climate. doi:10.1175/2010JCLI3812.1

Anderson, M.C., Norman, J.M., Kustas, W.P., Houborg, R., Starks, P.J., Agam, N., 2008. A thermal-based remote sensing technique for routine mapping of land-surface carbon, water and energy fluxes from field to regional scales. Remote Sensing of Environment 112, 4227–4241. doi:10.1016/j.rse.2008.07.009

Anderson, M.C., Norman, J.M., Kustas, W.P., Li, F., Prueger, J.H., Mecikalski, J.R., Anderson, M.C., Norman, J.M., Kustas, W.P., Li, F., Prueger, J.H., Mecikalski, J.R., 2005. Effects of Vegetation Clumping on Two–Source Model Estimates of Surface Energy Fluxes from an Agricultural Landscape during SMACEX. Journal of Hydrometeorology 6, 892–909. doi:10.1175/JHM465.1

Anderson, M.C., Norman, J.M., Mecikalski, J.R., Otkin, J.A., Kustas, W.P., 2007. A climatological study of evapotranspiration and moisture stress across the continental United States based on thermal remote sensing: 2. Surface moisture climatology. Journal of Geophysical Research Atmospheres. doi:10.1029/2006JD007507

Anderson, R.G., Alfieri, J.G., Tirado-Corbalá, R., Gartung, J., McKee, L.G., Prueger, J.H., Wang, D., Ayars, J.E., Kustas, W.P., 2017. Assessing FAO-56 dual crop coefficients using eddy covariance flux partitioning. Agricultural Water Management. doi:10.1016/j.agwat.2016.07.027

Aouade, G., Ezzahar, J., Amenzou, N., Er-Raki, S., Benkaddour, A., Khabba, S., Jarlan, L., 2016. Combining stable isotopes, Eddy Covariance system and meteorological measurements for partitioning evapotranspiration, of winter wheat, into soil evaporation and plant transpiration in a semi-arid region. Agricultural Water Management. doi:10.1016/j.agwat.2016.07.021

Attema, E.P.W., Ulaby, F.T., 1978. Vegetation modeled as a water cloud. Radio Science. doi:10.1029/RS013i002p00357

Aubert, M., Baghdadi, N., Zribi, M., Douaoui, A., Loumagne, C., Baup, F., El Hajj, M., Garrigues, S., 2011. Analysis of TerraSAR-X data sensitivity to bare soil moisture, roughness, composition and soil crust. Remote Sensing of Environment 115, 1801–1810. doi:10.1016/j.rse.2011.02.021

Autovino, D., Minacapilli, M., Provenzano, G., 2016. Modelling bulk surface resistance by MODIS data and assessment of MOD16A2 evapotranspiration product in an irrigation district of Southern Italy. Agricultural Water Management 167, 86–94. doi:10.1016/j.agwat.2016.01.006

Ayyoub, A., Khabba, S., Er-Raki, S., Merlin, O., Bahlaoui, A., 2017. Calibration and validation of the Penman-Monteith model for estimating evapotranspiration of an orange orchard in semi-Arid region. Acta Horticulturae 1150, 15–22. doi:10.17660/ActaHortic.2017.1150.3

Baghdadi, Holah, N., Zribi, M., 2006. Soil moisture estimation using multi- incidence and multi- polarization ASAR data. International Journal of Remote Sensing 27, 1907–1920. doi:10.1080/01431160500239032

Baghdadi, N., Abou Chaaya, J., Zribi, M., 2011. Semiempirical calibration of the integral equation model for SAR data in C-Band and cross polarization using radar images and field measurements. IEEE Geoscience and Remote Sensing Letters 8, 14–18. doi:10.1109/LGRS.2010.2050054

Baghdadi, N., Choker, M., Zribi, M., Hajj, M. El, Paloscia, S., Verhoest, N.E.C., Lievens, H., Baup, F., Mattia, F., 2017. New empirical model for radar scattering from bare soils. International Geoscience and Remote Sensing Symposium (IGARSS) 2017-July, 4139–4142. doi:10.1109/IGARSS.2017.8127912

Baghdadi, N., Choker, M., Zribi, M., Hajj, M., Paloscia, S., Verhoest, N., Lievens, H., Baup, F., Mattia, F., 2016. A New Empirical Model for Radar Scattering from Bare Soil Surfaces. Remote Sensing 8, 920. doi:10.3390/rs8110920

Baghdadi, N., Gaultier, S., King, C., 2002a. Retrieving surface roughness and soil moisture from synthetic aperture radar (SAR) data using neural networks. Canadian Journal of Remote Sensing. doi:10.5589/m02-066

Baghdadi, N., Gherboudj, I., Zribi, M., Sahebi, M., King, C., Bonn, F., 2004. Semi-empirical calibration of the IEM backscattering model using radar images and moisture and roughness field measurements. International Journal of Remote Sensing 25, 3593–3623. doi:10.1080/01431160310001654392

Baghdadi, N., Hajj, M. El, Choker, M., Zribi, M., Bazzi, H., Vaudour, E., Gilliot, J.M., Ebengo, D.M., 2018. Potential of Sentinel-1 images for estimating the soil roughness over bare agricultural soils. Water (Switzerland) 10, 1–14. doi:10.3390/w10020131

Baghdadi, N., Holah, N., Zribi, M., 2006. Soil moisture estimation using multi-incidence and multi-polarization ASAR data. International Journal of Remote Sensing. doi:10.1080/01431160500239032

Baghdadi, N., King, C., Chanzy, A., Wigneron, J.P., 2002b. An empirical calibration of the integral equation model based on SAR data, soil moisture and surface roughness measurement over bare soils. International Journal of Remote Sensing 23, 4325–4340. doi:10.1080/01431160110107671

Baghdadi, N., Mallet, C., Zribi, M., n.d. Coupling Radar and Optical Data for Soil Moisture Retrieval over Agricultural Areas 1–45.

Baghdadi, N., Zribi, M., 2006. Evaluation of radar backscatter models IEM, OH and Dubois using experimental observations. International Journal of Remote Sensing 27, 3831–3852. doi:10.1080/01431160600658123

Baghdadi, N., Zribi, M., Loumagne, C., Ansart, P., Anguela, T.P., 2008. Analysis of TerraSAR-X data and their sensitivity to soil surface parameters over bare agricultural fields. Remote Sensing of Environment. doi:10.1016/j.rse.2008.08.004

Bai, X., He, B., Li, X., Zeng, J., Wang, X., Wang, Z., Zeng, Y., Su, Z., 2017. First assessment of Sentinel-1A data for surface soil moisture estimations using a coupled water cloud model and advanced integral equation model over the Tibetan Plateau. Remote Sensing. doi:10.3390/rs9070714

Baldocchi, D., 1994. A comparative study of mass and energy exchange over a closed C3 (wheat) and an open C4 (corn) canopy: I. The partitioning of available energy into latent and sensible heat exchange. Agricultural and Forest Meteorology. doi:10.1016/0168-1923(94)90003-5

Baldocchi, D.D., Hincks, B.B., Meyers, T.P., 1988. Measuring Biosphere-Atmosphere Exchanges of Biologically Related Gases with Micrometeorological Methods. Ecology 69, 1331–1340. doi:10.2307/1941631

Balenzano, A., Mattia, F., Satalino, G., Davidson, M.W.J., 2011. Dense Temporal Series of C- and L-band SAR Data for Soil Moisture Retrieval Over Agricultural Crops. IEEE Journal of Selected Topics in Applied Earth Observations and Remote Sensing 4, 439–450. doi:10.1109/JSTARS.2010.2052916

Barbosa Da Silva, B., Ramana Rao, T. V., 2005. The CWSI variations of a cotton crop in a semi-arid region of Northeast Brazil. Journal of Arid Environments 62, 649–659. doi:10.1016/j.jaridenv.2005.01.017

Bastiaanssen, Menenti, M., Feddes, R.., Holtslag, A.A.., 1998a. The surface energy balance algorithm for land (SEBAL): part 1 formulation. J. Hydrol 212–213, 198–212.

Bastiaanssen, Menenti, M., Feddes, R.A., Holtslag, A.A.M., 1998b. A remote sensing surface energy balance algorithm for land (SEBAL). Journal of Hydrology. doi:10.1016/S0022-1694(98)00253-4

Bastiaanssen, Noordman, E.J.M., Pelgrum, H., Davids, G., Thoreson, B.P., Allen, R.G., 2005. SEBAL Model with Remotely Sensed Data to Improve Water-Resources Management under Actual Field Conditions. Journal of Irrigation and Drainage Engineering 131, 85–93. doi:10.1061/(ASCE)0733-9437(2005)131:1(85)

Bastiaanssen, Pelgrum, H., Wang, J., Ma, Y., Moreno, J.F., Roerink, G.J., Van Der Wal, T., 1998c. A remote sensing surface energy balance algorithm for land (SEBAL): 2. Validation. Journal of Hydrology. doi:10.1016/S0022-1694(98)00254-6

Batra, N., Islam, S., Venturini, V., Bisht, G., Jiang, L., 2006. Estimation and comparison of evapotranspiration from MODIS and AVHRR sensors for clear sky days over the Southern Great Plains. Remote Sensing of Environment. doi:10.1016/j.rse.2006.02.019

Belaqziz, S., Khabba, S., Er-Raki, S., Jarlan, L., Le Page, M., Kharrou, M.H., Adnani, M. El,

Chehbouni, A., 2013. A new irrigation priority index based on remote sensing data for assessing the networks irrigation scheduling. Agricultural Water Management 119, 1–9. doi:10.1016/j.agwat.2012.12.011

Belaqziz, S., Mangiarotti, S., Le Page, M., Khabba, S., Er-Raki, S., Agouti, T., Drapeau, L., Kharrou, M.H., El Adnani, M., Jarlan, L., 2014. Irrigation scheduling of a classical gravity network based on the Covariance Matrix Adaptation – Evolutionary Strategy algorithm. Computers and Electronics in Agriculture 102, 64–72. doi:10.1016/J.COMPAG.2014.01.006

Berk, A., Anderson, G.P., Acharya, P.K., Bernstein, L.S., Muratov, L., Lee, J., Fox, M., Adler-Golden, S.M., Chetwynd, J.H., Hoke, M.L., Lockwood, R.B., Gardner, J.A., Cooley, T.W., Borel, C.C., Lewis, P.E., 2005. MODTRAN 5: a reformulated atmospheric band model with auxiliary species and practical multiple scattering options: update 5806, 662. doi:10.1117/12.606026

Bindhu, V.M., Narasimhan, B., Sudheer, K.P., 2013. Development and verification of a non-linear disaggregation method (NL-DisTrad) to downscale MODIS land surface temperature to the spatial scale of Landsat thermal data to estimate evapotranspiration. Remote Sensing of Environment 135, 118–129. doi:10.1016/j.rse.2013.03.023

Boisvert, J.B., Gwyn, Q.H.J., Chanzy, A., Major, D.J., Brisco, B., Brown, R.J., 1997. Effect of surface soil moisture gradients on modelling radar backscattering from bare fields. Int. J. Remote Sens. 18, 153–170. doi:10.1080/014311697219330

Boulet, G., Chehbouni, A., Braud, I., Vauclin, M., Haverkamp, R., Zammit, C., 2000. A simple water and energy balance model designed for regionalization and remote sensing data utilization. Agricultural and Forest Meteorology 105, 117–132. doi:10.1016/S0168-1923(00)00184-2

Boulet, G., Chehbouni, A., Gentine, P., Duchemin, B., Ezzahar, J., Hadria, R., 2007. Monitoring water stress using time series of observed to unstressed surface temperature difference. Agricultural and Forest Meteorology 146, 159–172. doi:10.1016/j.agrformet.2007.05.012

Boulet, G., Olioso, A., Ceschia, E., Marloie, O., Coudert, B., Rivalland, V., Chirouze, J., Chehbouni, G., 2012. An empirical expression to relate aerodynamic and surface temperatures for use within single-source energy balance models. Agricultural and Forest Meteorology 161, 148–155. doi:10.1016/j.agrformet.2012.03.008

Bousbih, S., Zribi, M., Hajj, M. El, Baghdadi, N., Lili-Chabaane, Z., Gao, Q., Fanise, P., 2018. Soil moisture and irrigation mapping in a semi-arid region, based on the synergetic use of Sentinel-1 and Sentinel-2 data. Remote Sensing 10. doi:10.3390/rs10121953

Bousbih, S., Zribi, M., Lili-Chabaane, Z., Baghdadi, N., El Hajj, M., Gao, Q., Mougenot, B., 2017. Potential of sentinel-1 radar data for the assessment of soil and cereal cover parameters. Sensors (Switzerland) 17. doi:10.3390/s17112617

Braud, I., Dantas-Antonino, A.C., Vauclin, M., Thony, J.L., Ruelle, P., 1995. A simple soil-plant-atmosphere transfer model (SiSPAT) development and field verification. Journal of Hydrology 166, 213–250. doi:10.1016/0022-1694(94)05085-C

Brisson, N., Mary, B., Ripoche, D., Jeuffroy, M.H., Ruget, F., Nicoullaud, B., Gate, P., Devienne-Barret, F., Antonioletti, R., Durr, C., Richard, G., Beaudoin, N., Recous, S., Tayot, X., Plenet, D., Cellier, P., Machet, J.-M., Meynard, J.M., Delécolle, R., 1998. STICS: a generic model for the simulation of crops and their water and nitrogen balances. I. Theory and parameterization applied to wheat and corn. Agronomie 18, 311–346. doi:10.1051/agro:19980501

Brisson, Perrier, 1991. A semi-empirical model of bare soil evaporation for crop simulation models. Water resources 27, 719–727.

Bruckler, L., Witono, H., Stengel, P., 1988. Near surface soil moisture estimation from microwave measurements. Remote Sensing of Environment. doi:10.1016/0034-4257(88)90091-0

Brunsell, N.A., Gillies, R.R., 2003. Length Scale Analysis of Surface Energy Fluxes Derived from Remote Sensing. Journal of Hydrometeorology 4, 1212–1219. doi:10.1175/1525-7541(2003)004<1212:lsaose>2.0.co;2

Brutsaert, W., 1982. Evaporation into the Atmosphere: Theory, History, and Applications. Springer, Dordrecht 299.

Brutsaert, W., 1975. On a derivable formula for long-wave radiation from clear skies. Water Resources Research 4, 742–744. doi:10.1029/WR011i005p00742

Budyko, M.I., 1956. Heat balance of the Earth's surface. Gidrometeoizdat, Leningrad. Cahill, 255.

Cammalleri, C., Rallo, G., Agnese, C., Ciraolo, G., Minacapilli, M., Provenzano, G., 2013. Combined use of eddy covariance and sap flow techniques for partition of ET fluxes and water stress assessment in an irrigated olive orchard. Agricultural Water Management 120, 89–97. doi:10.1016/j.agwat.2012.10.003

Capelle, V., Chédin, A., Péquignot, E., Schlüssel, P., Newman, S.M., Scott, N.A., 2012. Infrared continental surface emissivity spectra and skin temperature retrieved from IASI observations over the tropics. Journal of Applied Meteorology and Climatology. doi:10.1175/JAMC-D-11-0145.1

Carlson, T., 2007. An Overview of the "Triangle Method" for Estimating Surface Evapotranspiration and Soil Moisture from Satellite Imagery. Sensors. doi:10.3390/s7081612

Carlson, T.N., Buffum, M.J., 1989. On estimating total daily evapotranspiration from remote surface temperature measurements. Remote Sensing of Environment 29, 197–207. doi:10.1016/0034-4257(89)90027-8

Carlson, T.N., Gillies, R.R., Schmugge, T.J., 1995. An interpretation of methodologies for indirect measurement of soil water content. Agricultural and Forest Meteorology 77, 191–205. doi:10.1016/0168-1923(95)02261-U

Caylor, K.K., Shugart, H.H., Rodriguez-Iturbe, I., 2005. Tree canopy effects on simulated water stress in southern African Savannas. Ecosystems. doi:10.1007/s10021-004-0027-9

Cerovic, Z.G., Goulas, Y., Gorbunov, M., Briantais, J.M., Camenen, L., Moya, I., 1996. Fluorosensing of water stress in plants: Diurnal changes of the mean lifetime and yield of chlorophyll fluorescence, measured simultaneously and at distance with a τ-LIDAR and a modified PAM-fluorimeter, in maize, sugar beet, and kalanchoe. Remote Sensing of Environment. doi:10.1016/S0034-4257(96)00076-4

Champion, I., Faivre, R., 1997. Sensitivity of the radar signal to soil moisture: variation with incidence angle, frequency, and polarization. IEEE Transactions on Geoscience and Remote Sensing. doi:10.1109/36.582001

Chanzy, A., 1993. Basic soil surface characteristics derived from active microwave remote sensing. Remote Sensing Reviews.

Chanzy, A., 1991. Modélisation simplifiée de l'évaporation d'un sol nu utilisant l'humidité et la température de surface accessibles par télédétection. Institut national agronomique Paris-Grignon.

Chanzy, A., Bruckler, L., 1993. Significance of soil surface moisture with respect to daily bare soil evaporation. Water Resources Research. doi:10.1029/92WR02747

Chauhan, S., Srivastava, H.S., 2016. Comparative Evaluation of the Sensitivity of Multi-Polarised Sar and Optical Data for Various Land Cover. International Journal of Advancement in Remote Sensing, GIS and Geography COMPARATIVE 4, 1–14.

Chehbouni, A.H., Escadafal, R., Duchemin, B., Boulet, G., Simonneaux, V., Dedieu, G., Mougenot, B., Khabba, S., Kharrou, H., Maisongrande, P., Merlin, O., Chaponnière, A., Ezzahar, J., Er-Raki, S., Hoedjes, J., Hadria, R., Abourida, A., Cheggour, A., Raibi, F., Boudhar, A., Benhadj, I., Hanich, L., Benkaddour, A., Guemouria, N., Chehbouni, A.H., Lahrouni, A., Olioso, A., Jacob, F., Williams, D.G., Sobrino, J.A., 2008. An integrated modelling and remote sensing approach for hydrological study in arid and semi-arid regions: the SUDMED Programme. International Journal of Remote Sensing 29, 5161–5181. doi:10.1080/01431160802036417

Chen, L., Yan, G.J., Ren, H.Z., Li, A.H., Ieee, 2010. a Modified Vegetation Index Based Algorithm for Thermal Imagery Sharpening. 2010 Ieee International Geoscience and Remote Sensing Symposium. doi:10.1109/igarss.2010.5651428

Choi, M., Kim, T.A.E.W., Kustas, W.P., 2011. Reliable estimation of evapotranspiration on agricultural fields predicted by the Priestley – Taylor model using soil moisture data from ground and remote sensing observations compared with the Common Land Model 32, 4571–4587. doi:10.1080/01431161.2010.489065

Choudhury, B.J., Idso, S.., R.J, R., 1987. Analysis of an empirical model for soil heat flux under a growing cheat crop for estimation by an infrared-temperature based enrgy balance equation. agric. For Meteorol 39, 283–297.

Choudhury, B.J., Reginato, R.J., Idso, S.B., 1986. An analysis of infrared temperature observations over wheat and calculation of latent heat flux. Agricultural and Forest Meteorology. doi:10.1016/0168-1923(86)90029-8

Cosby, B.J., Hornberger, G.M., Clapp, R.B., Ginn, T.R., 1984. A Statistical Exploration of the Relationships of Soil Moisture Characteristics to the Physical Properties of Soils. Water

Resources Research 20, 682–690. doi:10.1029/WR020i006p00682

Crago, R.D., 1996. Conservation and variability of the evaporative fraction during the daytime. Journal of Hydrology. doi:10.1016/0022-1694(95)02903-6

Cragoa, R., Brutsaert, W., 1996. Daytime evaporation and the self-preservation of the evaporative fraction and the Bowen ratio. Journal of Hydrology 178, 241–255. doi:10.1016/0022-1694(95)02803-X

Crow, W.T., Wood, E.F., 2003. The assimilation of remotely sensed soil brightness temperature imagery into a land surface model using Ensemble Kalman filtering: A case study based on ESTAR measurements during SGP97. Advances in Water Resources 26, 137–149. doi:10.1016/S0309-1708(02)00088-X

Daamen, C.C., Simmonds, L.P., Wallace, J.S., Laryea, K.B., Sivakumar, M.V.K., 1993. Use of microlysimeters to measure evaporation from sandy soils. Agricultural and Forest Meteorology 65, 159–173. doi:10.1016/0168-1923(93)90002-Y

Daudet, F.A., Vachaud, G., 1977. La mesure neutronique du stock d'eau du sol et de ses variations. Application à la détermination du bilan hydrique. Annals of Agronomie 28, 503–519.

Debnath, S., Adamala, S., Raghuwanshi, N.S., 2015. Sensitivity Analysis of FAO-56 Penman-Monteith Method for Different Agro-ecological Regions of India. Environmental Processes 2, 689–704. doi:10.1007/s40710-015-0107-1

Dee, D., Uppala, S., Simmons, A., Berrisford, P., Poli, P., Kobayashi, S., Andrae, U., Balmaseda, M., Balsamo, G., Bauer, P., 2011. The ERA - Interim reanalysis: Configuration and performance of the data assimilation system. Quaterly Journal of the Royal Meteorological Society 137, 553–597. doi:10.1002/qj.828

Desborough, C.E., Pitman, A.J., Irannejad, P., 1996. Analysis of the relationship between bare soil evaporation and soil moisture simulated by 13 land surface schemes for a simple non-vegetated site. Global and Planetary Change. doi:10.1016/0921-8181(95)00036-4

Diarra, A., Jarlan, L., Er-Raki, S., Le Page, M., Aouade, G., Tavernier, A., Boulet, G., Ezzahar, J., Merlin, O., Khabba, S., 2017. Performance of the two-source energy budget (TSEB) model for the monitoring of evapotranspiration over irrigated annual crops in North Africa. Agricultural Water Management 193, 71–88. doi:10.1016/j.agwat.2017.08.007

Dobson, M.C., Ulaby, F., 1981. Microwave Backscatter Dependence on Surface Roughness, Soil Moisture, and Soil Texture: Part III—Soil Tension. IEEE Transactions on Geoscience and Remote Sensing. doi:10.1109/TGRS.1981.350328

Dobson, M.C., Ulaby, F.T., 1986. Active Microwave Soil Moisture Research. IEEE Transactions on Geoscience and Remote Sensing. doi:10.1109/TGRS.1986.289585

Dobson, M.C., Ulaby, F.T., Hallikainen, M.T., El-Rayes, M.A., 1985. Microwave Dielectric Behavior of Wet Soil-Part II: Dielectric Mixing Models. IEEE Transactions on Geoscience and Remote Sensing. doi:10.1109/TGRS.1985.289498

Dominguez, A., Kleissl, J., Luvall, J.C., Rickman, D.L., 2011. High-resolution urban thermal sharpener (HUTS). Remote Sensing of Environment 115, 1772–1780. doi:10.1016/j.rse.2011.03.008

Drerup, P., Brueck, H., Scherer, H.W., 2017. Evapotranspiration of winter wheat estimated with the FAO 56 approach and NDVI measurements in a temperate humid climate of NW Europe. Agricultural Water Management 192, 180–188. doi:10.1016/j.agwat.2017.07.010

Du, Y., Ulaby, F.T., Dobson, M.C., 2000. Sensitivity to soil moisture by active and passive microwave sensors. Geoscience and Remote Sensing, IEEE Transactions on.

Dubois, P.C., Engman, T., 1995a. Measuring Soil Moisture with Imaging Radars. IEEE Transactions on Geoscience and Remote Sensing. doi:10.1109/36.406677

Dubois, P.C., Engman, T., 1995b. Measuring Soil Moisture with Imaging Radars. IEEE Transactions on Geoscience and Remote Sensing 33, 915–926. doi:10.1109/36.406677

Duchemin, B., Hadria, R., Erraki, S., Boulet, G., Maisongrande, P., Chehbouni, A., Escadafal, R., Ezzahar, J., Hoedjes, J.C.B., Kharrou, M.H., Khabba, S., Mougenot, B., Olioso, A., Rodriguez, J.C., Simonneaux, V., 2006. Monitoring wheat phenology and irrigation in Central Morocco: On the use of relationships between evapotranspiration, crops coefficients, leaf area index and remotely-sensed vegetation indices. Agricultural Water Management. doi:10.1016/j.agwat.2005.02.013

Dyer, A.J., 1974. A review of flux-profile relationships. Boundary-Layer Meteorology. doi:10.1007/BF00240838

Edwards, W.R.N., 1986. Precision weighing lysimetry for trees, using a simplified tared-balance design. Tree Physiology 1, 127–144. doi:10.1093/treephys/1.2.127

Engman, E.T., 2000. Soil moisture., Ed. G.A. Schultz, E.T. Engman, . Berlin: Springer Grayson,. Remote sensing in hydrology and water management 197–216.

Entekhabi, D., Njoku, E.G., O'Neill, P.E., Kellogg, K.H., Crow, W.T., Edelstein, W.N., Entin, J.K., Goodman, S.D., Jackson, T.J., Johnson, J., Kimball, J., Piepmeier, J.R., Koster, R.D., Martin, N., McDonald, K.C., Moghaddam, M., Moran, S., Reichle, R., Shi, J.C., Spencer, M.W., Thurman, S.W., Tsang, L., Van Zyl, J., 2010. The soil moisture active passive (SMAP) mission. Proceedings of the IEEE. doi:10.1109/JPROC.2010.2043918

Entekhabi, D., Rodriguez-Iturbe, I., Castelli, F., 1996. Mutual interaction of soil moisture state and atmospheric processes. Journal of Hydrology. doi:10.1016/0022-1694(95)02965-6

Er-Raki, S., Amazirh, A., Ayyoub, A., Khabba, S., Merlin, O., Ezzahar, J., Chehbouni, A., 2018. Integrating thermal surface temperature into Penman-Monteith model for estimating evapotranspiration and crop water stress of orange orchard in semi-arid region, Acta Horticulturae. doi:10.17660/ActaHortic.2018.1197.12

Er-Raki, S., Chehbouni, A., Boulet, G., Williams, D.G., 2010a. Using the dual approach of FAO-56 for partitioning ET into soil and plant components for olive orchards in a semi-

arid region. Agricultural Water Management 97, 1769–1778.
doi:10.1016/J.AGWAT.2010.06.009

Er-Raki, S., Chehbouni, A., Boulet, G., Williams, D.G., 2010b. Using the dual approach of
FAO-56 for partitioning ET into soil and plant components for olive orchards in a semi-
arid region. Agricultural Water Management 97, 1769–1778.
doi:10.1016/J.AGWAT.2010.06.009

Er-raki, S., Chehbouni, A., Duchemin, B., 2010. Combining Satellite Remote Sensing Data
with the FAO-56 Dual Approach for Water Use Mapping In Irrigated Wheat Fields of a
Semi-Arid Region 375–387. doi:10.3390/rs2010375

Er-raki, S., Chehbouni, A., Guemouria, N., Duchemin, B., Ezzahar, J., Hadria, R., 2007.
Combining FAO-56 model and ground-based remote sensing to estimate water
consumptions of wheat crops in a semi-arid region 87, 41–54.
doi:10.1016/j.agwat.2006.02.004

Er-Raki, S., Chehbouni, A., Guemouria, N., Duchemin, B., Ezzahar, J., Hadria, R., 2007.
Combining FAO-56 model and ground-based remote sensing to estimate water
consumptions of wheat crops in a semi-arid region. Agricultural Water Management 87,
41–54. doi:10.1016/j.agwat.2006.02.004

Er-Raki, S., Chehbouni, A., Guemouria, N., Ezzahar, J., Khabba, S., Boulet, G., Hanich, L.,
2009. Citrus orchard evapotranspiration: Comparison between eddy covariance
measurements and the FAO-56 approach estimates. Plant Biosystems - An International
Journal Dealing with all Aspects of Plant Biology 143, 201–208.
doi:10.1080/11263500802709897

Er-Raki, S., Chehbouni, A., Hoedjes, J., Ezzahar, J., Duchemin, B., Jacob, F., 2008.
Improvement of FAO-56 method for olive orchards through sequential assimilation of
thermal infrared-based estimates of ET. Agricultural Water Management 95, 309–321.
doi:10.1016/j.agwat.2007.10.013

Er-raki, S., Rodriguez, J.C., Garatuza-payan, J., Watts, C.J., Chehbouni, A., 2013.
Determination of crop evapotranspiration of table grapes in a semi-arid region of
Northwest Mexico using multi-spectral vegetation index. Agricultural Water
Management 122, 12–19. doi:10.1016/j.agwat.2013.02.007

Esch, S., Korres, W., Reichenau, T.G., Schneider, K., 2018. Soil moisture index from ERS-
SAR and its application to the analysis of spatial patterns in agricultural areas. Journal of
Applied Remote Sensing 12, 1. doi:10.1117/1.JRS.12.022206

Essa, W., van der Kwast, J., Verbeiren, B., Batelaan, O., 2013. Downscaling of thermal
images over urban areas using the land surface temperature-impervious percentage
relationship. International Journal of Applied Earth Observation and Geoinformation.
doi:10.1016/j.jag.2012.12.007

Eweys, O.A., Elwan, A., Borham, T., 2017a. Retrieving topsoil moisture using RADARSAT-
2 data, a novel approach applied at the east of the Netherlands. Journal of Hydrology, In
review.

Eweys, O.A., Elwan, A., Borham, T., 2017b. Retrieving topsoil moisture using RADARSAT-

2 data, a novel approach applied at the east of the Netherlands. Journal of Hydrology 555, 670–682. doi:10.1016/j.jhydrol.2017.10.048

Eweys, O.A., Escorihuela, M.J., Villar, J.M., Er-Raki, S., Amazirh, A., Olivera, L., Jarlan, L., Khabba, S., Merlin, O., 2017c. Disaggregation of SMOS Soil Moisture to 100 m Resolution Using MODIS Optical/Thermal and Sentinel-1 Radar Data: Evaluation over a Bare Soil Site in Morocco. Remote Sensing 9, 1155. doi:10.3390/rs9111155

Ezzahar, J., Chehbouni, A., 2009. The use of scintillometry for validating aggregation schemes over heterogeneous grids. Agricultural and Forest Meteorology 149, 2098–2109. doi:10.1016/J.AGRFORMET.2009.09.004

Ezzahar, J., Chehbouni, A., Hoedjes, J., Ramier, D., Boulain, N., Boubkraoui, S., Cappelaere, B., Descroix, L., Mougenot, B., Timouk, F., 2009. Combining scintillometer measurements and an aggregation scheme to estimate area-averaged latent heat flux during the AMMA experiment. Journal of Hydrology. doi:10.1016/j.jhydrol.2009.01.010

Fieuzal, R., 2010. Interactive comment on " Combined use of optical and radar satellite data for the monitoring of irrigation and soil moisture of wheat crops " by 7–9.

Fieuzal, R., Duchemin, B., Jarlan, L., Zribi, M., Baup, F., Merlin, O., Hagolle, O., Garatuza-Payan, J., 2011. Combined use of optical and radar satellite data for the monitoring of irrigation and soil moisture of wheat crops. Hydrology and Earth System Sciences 15, 1117–1129. doi:10.5194/hess-15-1117-2011

Fisher, J.B., Tu, K.P., Baldocchi, D.D., 2008. Global estimates of the land-atmosphere water flux based on monthly AVHRR and ISLSCP-II data, validated at 16 FLUXNET sites. Remote Sensing of Environment. doi:10.1016/j.rse.2007.06.025

Freitas, S.C., Trigo, I.F., Bioucas-Dias, J.M., Gottsche, F.-M., 2010. Quantifying the Uncertainty of Land Surface Temperature Retrievals From SEVIRI/Meteosat. IEEE Transactions on Geoscience and Remote Sensing 48, 523–534. doi:10.1109/TGRS.2009.2027697

Friedl, M.A., Davis, F.W., 1994. Sources of variation in radiometric surface temperature over a tallgrass prairie. Remote Sensing of Environment 48, 1–17. doi:10.1016/0034-4257(94)90109-0

Fung, A.K., 1994. Microwave scattering and emission models and their applications. Artech House Remote Sensing Library.

Fung, A.K., Li, Z., Chen, K.S., 1992. Backscattering from a Randomly Rough Dielectric Surface. IEEE Transactions on Geoscience and Remote Sensing. doi:10.1109/36.134085

Gao, B., 1996. <NDWI—A normalized difference water index for r.pdf>. Remote Sensing of Environment 266, 257–266. doi:10.1016/S0034-4257(96)00067-3

Gao, Q., Zribi, M., Escorihuela, M., Baghdadi, N., 2017. Synergetic Use of Sentinel-1 and Sentinel-2 Data for Soil Moisture Mapping at 100 m Resolution. Sensors 17, 1966. doi:10.3390/s17091966

Gentine, P., Entekhabi, D., Chehbouni, A., Boulet, G., Duchemin, B., 2007. Analysis of

evaporative fraction diurnal behaviour. Agricultural and Forest Meteorology 143, 13–29. doi:10.1016/J.AGRFORMET.2006.11.002

Gherboudj, I., Magagi, R., Berg, A.A., Toth, B., 2011a. Soil moisture retrieval over agricultural fields from multi-polarized and multi-angular RADARSAT-2 SAR data. Remote Sensing of Environment. doi:10.1016/j.rse.2010.07.011

Gherboudj, I., Magagi, R., Berg, A.A., Toth, B., 2011b. Soil moisture retrieval over agricultural fields from multi-polarized and multi-angular RADARSAT-2 SAR data. Remote Sensing of Environment 115, 33–43. doi:10.1016/j.rse.2010.07.011

Ghosh, A., Joshi, P.K., 2014. ISPRS Journal of Photogrammetry and Remote Sensing Hyperspectral imagery for disaggregation of land surface temperature with selected regression algorithms over different land use land cover scenes. ISPRS Journal of Photogrammetry and Remote Sensing 96, 76–93. doi:10.1016/j.isprsjprs.2014.07.003

Gillespie, A., Rokugawa, S., Matsunaga, T., Steven Cothern, J., Hook, S., Kahle, A.B., 1998. A temperature and emissivity separation algorithm for advanced spaceborne thermal emission and reflection radiometer (ASTER) images. IEEE Transactions on Geoscience and Remote Sensing 36, 1113–1126. doi:10.1109/36.700995

Gillies, R.R., Carlson, T.N., 1995. Thermal Remote-Sensing of Surface Soil-Water Content with Partial Vegetation Cover for Incorporation into Climate-Models. Journal of Applied Meteorology 34, 745–756. doi:10.1175/1520-0450(1995)034<0745:trsoss>2.0.co;2

Gommes, R., Petrassi, F., 1994. Rainfall Variability and Drought in Sub-Saharan Africa since 1960. Agro-meteorology Series 9; Food and Agriculture Organization:Rome, Italy.

Gorrab, A., Zribi, M., Baghdadi, N., Mougenot, B., Chabaane, Z.L., 2015. Potential of X-band TerraSAR-X and COSMO-SkyMed SAR data for the assessment of physical soil parameters. Remote Sensing. doi:10.3390/rs70100747

Goward, S.N., Tucker, C.J., Dye, D.G., 1985. North American vegetation patterns observed with the NOAA-7 advanced very high resolution radiometer. Vegetatio. doi:{10.1007/BF00033449}

Granger, R.., 2000. Satellite-derived estimates of evapotranspiration in the Gediz basin. Journal of Hydrology 229, 70–76. doi:10.1016/S0022-1694(99)00200-0

Granger, R.., 1997. Comparison of surface and satellite derived estimates of evapotranspiration using a feedback algorithm 21–81.

Gruhier, 2010. L'humidité du sol par télédétection micro-ondes en région Sahélienne. Université Paul Sabatier, Toulouse, France Pierre et Marie Curie - Paris 6 Ecole doctorale des Sciences de l'Environnement d'IDF.

Gruhier, C., de Rosnay, P., Kerr, Y., Mougin, E., Ceschia, E., Calvet, J.-C., Richaume, P., 2008. Evaluation of AMSR-E soil moisture product based on ground measurements over temperate and semi-arid regions. Geophysical Research Letters 35. doi:10.1029/2008GL033330

Gutman, G., Ignatov, A., 1998. The derivation of the green vegetation fraction from

NOAA/AVHRR data for use in numerical weather prediction models. International Journal of Remote Sensing 19, 1533–1543. doi:10.1080/014311698215333

Guttman, N.B., 1999. Accepting the standardized precipitation index: A calculation algorithm. Journal of the American Water Resources Association 35, 311–322. doi:10.1111/j.1752-1688.1999.tb03592.x

Guyot, G., 1990. Optical properties of vegetation canopies, Butterworths, London. Applications of Remote Sensing in Agriculture. 19–43.

Ha, W., Gowda, P.H., Howell, T.A., 2013. A review of downscaling methods for remote sensing-based irrigation management: Part I. Irrigation Science 31, 831–850. doi:10.1007/s00271-012-0331-7

Hadria, R., Duchemin, B., Lahrouni, A., Khabba, S., Er-Raki, S., Dedieu, G., Chehbouni, a. G., Olioso§, A., 2006a. Monitoring of irrigated wheat in a semi-arid climate using crop modelling and remote sensing data: Impact of satellite revisit time frequency. International Journal of Remote Sensing. doi:10.1080/01431160500382980

Hadria, R., Duchemin, B., Lahrouni, A., Khabba, S., Er-raki, S., Dedieu, G., Chehbouni, A.G., Olioso§, A., 2006b. Monitoring of irrigated wheat in a semi-arid climate using crop modelling and remote sensing data: Impact of satellite revisit time frequency. International Journal of Remote Sensing 27, 1093–1117. doi:10.1080/01431160500382980

Hafner, S., 2003. Trends in maize , rice , and wheat yields for 188 nations over the past 40 years : a prevalence of linear growth 97, 275–283. doi:10.1016/S0167-8809(03)00019-7

Hain, C.R., Mecikalski, J.R., Anderson, M.C., 2008. Retrieval of an Available Water-Based Soil Moisture Proxy from Thermal Infrared Remote Sensing. Part I: Methodology and Validation. Journal of Hydrometeorology 10, 665–683. doi:10.1175/2008jhm1024.1

Hajj, M. El, Baghdadi, N., Zribi, M., Bazzi, H., 2017a. Synergic use of Sentinel-1 and Sentinel-2 images for operational soil moisture mapping at high spatial resolution over agricultural areas. Remote Sensing 9, 1–28. doi:10.3390/rs9121292

Hajj, M. El, Baghdadi, N., Zribi, M., Bazzi, H., 2017b. Synergic use of Sentinel-1 and Sentinel-2 images for operational soil moisture mapping at high spatial resolution over agricultural areas. Remote Sensing 9. doi:10.3390/rs9121292

Hallikainen, M.T., Ulaby, F.T., Dobson, M.C., El-Rayes, M. a, Wu, L.-K., 1985. Microwave Dielectric Behavior of Wet Soil-Part I: Empirical Models and Experimental Observations. Geoscience and Remote Sensing, IEEE Transactions on GE-23, 25–34. doi:10.1109/TGRS.1985.289497

Hansen, J., Ruedy, R., Sato, M., Lo, K., 2010. Global surface temperature change. Rev. Geophys. 48. doi:10.1029/2010RG000345.

Hatfield, J.L., 1983. Evapotranspiration Obtained from Remote Sensing Methods. Advances in Irrigation 2, 395–416. doi:10.1016/B978-0-12-024302-0.50017-5

Hillel, D., 1998. Introduction to Soil Physics. Academic, San Diego 365.

Holah, N., Baghdadi, N., Zribi, M., Bruand, A., King, C., 2005a. Potential of ASAR / ENVISAT for the characterization of soil surface parameters over bare agricultural fields 96, 78–86. doi:10.1016/j.rse.2005.01.008

Holah, N., Baghdadi, N., Zribi, M., Bruand, A., King, C., 2005b. Potential of ASAR/ENVISAT for the characterization of soil surface parameters over bare agricultural fields. Remote Sensing of Environment 96, 78–86. doi:10.1016/j.rse.2005.01.008

Hollinger, S. E., Isard, S.A., Welford, M.R., 1993. A new soil moisture drought index for predicting crop yields. Preprints, Eighth Conf. on Applied Climatology, Anaheim, CA, Amer. Meteor. Soc. 187–190.

Huete, A.R., 1988. A soil-adjusted vegetation index (SAVI). Remote Sensing of Environment. doi:10.1016/0034-4257(88)90106-X

Hulley, G.C., Hook, S.J., 2009. Intercomparison of versions 4, 4.1 and 5 of the MODIS Land Surface Temperature and Emissivity products and validation with laboratory measurements of sand samples from the Namib desert, Namibia. Remote Sensing of Environment. doi:10.1016/j.rse.2009.02.018

Inamdar, A.K., French, A., 2009. Disaggregation of GOES land surface temperatures using surface emissivity. Geophysical Research Letters 36, L02408. doi:10.1029/2008GL036544

IPCC, 2009. Intergovernmental Panel on Climate Change [WWW Document]. URL http://www.ipcc.ch/.%0AJones

Irmak, A., Kamble, B., 2009. Evapotranspiration data assimilation with genetic algorithms and SWAP model for on-demand irrigation. Irrigation Science 28, 101–112. doi:10.1007/s00271-009-0193-9

Irmak, A., Ratcliffe, I., Ranade, P., Hubbard, K.G., Singh, R.K., Kamble, B., Kjaersgaard, J., 2011. Estimation of land surface evapotranspiration with A satellite remote sensing procedure. Great Plains Research.

Jackson, R.D., Idso, S.B., Reginato, R.J., Pinter, P.J., 1981a. Canopy temperature as a crop water stress indicator. Water Resources Research 17, 1133–1138. doi:10.1029/WR017i004p01133

Jackson, R.D., Idso, S.B., Reginato, R.J., Pinter, P.J., 1981b. Canopy temperature as a crop water stress indicator. Water Resources Research. doi:10.1029/WR017i004p01133

Jarlan, L., Khabba, S., Er-Raki, S., Le Page, M., Hanich, L., Fakir, Y., Merlin, O., Mangiarotti, S., Gascoin, S., Ezzahar, J., Kharrou, M.H., Berjamy, B., Saaïdi, A., Boudhar, A., Benkaddour, A., Laftouhi, N., Abaoui, J., Tavernier, A., Boulet, G., Simonneaux, V., Driouech, F., El Adnani, M., El Fazziki, A., Amenzou, N., Raibi, F., El Mandour, A., Ibouh, H., Le Dantec, V., Habets, F., Tramblay, Y., Mougenot, B., Leblanc, M., El Faïz, M., Drapeau, L., Coudert, B., Hagolle, O., Filali, N., Belaqziz, S., Marchane, A., Szczypta, C., Toumi, J., Diarra, A., Aouade, G., Hajhouji, Y., Nassah, H., Bigeard, G., Chirouze, J., Boukhari, K., Abourida, A., Richard, B., Fanise, P., Kasbani, M., Chakir, A., Zribi, M., Marah, H., Naimi, A., Mokssit, A., Kerr, Y., Escadafal, R.,

2015. Remote Sensing of Water Resources in Semi-Arid Mediterranean Areas: the joint international laboratory TREMA. International Journal of Remote Sensing. doi:10.1080/01431161.2015.1093198

Jarvis, P.G., 1976. The Interpretation of the Variations in Leaf Water Potential and Stomatal Conductance Found in Canopies in the Field. Philosophical Transactions of the Royal Society B: Biological Sciences 273, 593–610. doi:10.1098/rstb.1976.0035

Jarvis, P.G., Mcnaughton, K.G., 1986. Stomatal Control of Transpiration: Scaling Up from Leaf to Region. Advances in Ecological Research. doi:10.1016/S0065-2504(08)60119-1

Jin, M.S., Jin, M.S., 2012. Developing an Index to Measure Urban Heat Island Effect Using Satellite Land Skin Temperature and Land Cover Observations. Journal of Climate 25, 6193–6201. doi:10.1175/JCLI-D-11-00509.1

Jin, X., Yang, G., Xue, X., Xu, X., Li, Z., Feng, H., 2017. Validation of two Huanjing-1A/B satellite-based FAO-56 models for estimating winter wheat crop evapotranspiration during mid-season. Agricultural Water Management 189, 27–38. doi:10.1016/J.AGWAT.2017.04.017

Julien, Y., Sobrino, J.A., 2011. Land use classification from multitemporal Landsat imagery using the Yearly Land Cover Dynamics (YLCD) method. International Journal of Applied Earth Observation and Geoinformation. doi:10.1016/j.jag.2011.05.008

Julien, Y., Sobrino, J.A., 2009. The Yearly Land Cover Dynamics (YLCD) method: An analysis of global vegetation from NDVI and LST parameters. Remote Sensing of Environment. doi:10.1016/j.rse.2008.09.016

Kalma, J.D., McVicar, T.R., McCabe, M.F., 2008. Estimating Land Surface Evaporation: A Review of Methods Using Remotely Sensed Surface Temperature Data. Surveys in Geophysics 29, 421–469. doi:10.1007/s10712-008-9037-z

Kamble, B., Irmak, A., 2009. Combining remote sensing measurements and model estimates through hybrid data assimilation scheme to predict hydrological fluxes. ProceedingsoftheIEEE International GeosciencesandRemoteSensing Symposium July 6–11, 2008. Boston, MA, USA.

Karam, M.A., Fung, A.K., Lang, R.H., Chauhan, N.S., 1992. Microwave Scattering Model for Layered Vegetation. IEEE Transactions on Geoscience and Remote Sensing. doi:10.1109/36.158872

Karjalainen, M., Harri, K., Hyyppä, J., Laurila, H., Kuittinen, R., 2014. the Use of Envisat Alternating Polarization Sar Images in Agricultural Monitoring in Comparison With Radarsat-1 Sar Images. In Proceedings of the ISPRS Congress, Istanbul, Turkey.

Karnieli, A., Agam, N., Pinker, R.T., Anderson, M., Imhoff, M.L., Gutman, G.G., Panov, N., Goldberg, A., 2010. Use of NDVI and land surface temperature for drought assessment: Merits and limitations. Journal of Climate 23, 618–633. doi:10.1175/2009JCLI2900.1

Karrou, M., 2003. Conduite du blé au Maroc. Rabat: INRA éditions.

Katerji, N., Perrier, A., 1983. Conséquence d'une contrainte hydrique appliquée à différents

stades phénologiques sur le rendement des plantes de poivron. Agronomie 11, 513–521. doi:10.1051/agro:19910805

Katerji, N., Rana, G., 2006. Modelling evapotranspiration of six irrigated crops under Mediterranean climate conditions. Agricultural and Forest Meteorology 138, 142–155. doi:10.1016/J.AGRFORMET.2006.04.006

Kerr, Y., 1996. Optimal choice for miras frequencies scientific requirements. CESBIO, p. Report.

Kerr, Y., Waldteufel, P., Wigneron, J.-P., Martinuzzi, J.-M., J, F., Berger, M., 2001. Soil Moisture retrieval from space: the Soil Moisture and Ocean Salinity (SMOS) mission. Geosci. Remote 39, 1729–1736.

Kerr, Y.H., Waldteufel, P., Wigneron, J.P., Delwart, S., Cabot, F., Boutin, J., Escorihuela, M.J., Font, J., Reul, N., Gruhier, C., Juglea, S.E., Drinkwater, M.R., Hahne, A., Martin-Neira, M., Mecklenburg, S., 2010. The SMOS Mission: New Tool for Monitoring Key Elements of the Global Water Cycle. Proceedings of the Ieee. doi:10.1109/jproc.2010.2043032

Khabba, S., Jarlan, L., Er-Raki, S., Page, M. Le, Ezzahar, J., Boulet, G., Simonneaux, V., Kharrou, M.H., Hanich, L., Chehbouni, G., 2013. The SudMed Program and the Joint International Laboratory TREMA: A Decade of Water Transfer Study in the Soil-Plant-Atmosphere System over Irrigated Crops in Semi-Arid Area. Procedia Environmental Sciences 19, 524–33.

Kharrou, H, M., L, M., Chehbouni, A., Simonneaux, V., Er-Raki, S., Jarlan, L., Ouzine, L., Khabba, S., Chehbouni, G., 2013. Assessment of Equity and Adequacy of Water Delivery in Irrigation Systems Using Remote Sensing-Based Indicators in Semi-Arid Region, Morocco. Water Resources Management 27, 4697–4714.

Kharrou, M.H., Le Page, M., Chehbouni, A., Simonneaux, V., Er-Raki, S., Jarlan, L., Ouzine, L., Khabba, S., Chehbouni, G., 2013. Assessment of Equity and Adequacy of Water Delivery in Irrigation Systems Using Remote Sensing-Based Indicators in Semi-Arid Region, Morocco. Water Resources Management. doi:10.1007/s11269-013-0438-5

Kim, J., Hogue, T.S., 2012. Improving spatial soil moisture representation through integration of AMSR-E and MODIS products. IEEE Transactions on Geoscience and Remote Sensing. doi:10.1109/TGRS.2011.2161318

Kogan, F.N., 2001. Operational space technology for global vegetation assessment. Bulletin of the American Meteorological Society 82, 1949–1964. doi:10.1175/1520-0477(2001)082<1949:OSTFGV>2.3.CO;2

Kogan, F.N., 1995. Application of vegetation index and brightness temperature for drought detection. Advances in Space Research. doi:10.1016/0273-1177(95)00079-T

Kogan, F.N., 1990. Remote sensing of weather impacts on vegetation in non-homogeneous areas. International Journal of Remote Sensing. doi:10.1080/01431169008955102

Kohsiek, W., Meijninger, W.M.L., Moene, A.F., Heusinkveld, B.G., Hartogensis, O.K., Hillen, W.C.A.M., De Bruin, H.A.R., 2002. An Extra Large Aperture Scintillometer For

Long Range Applications. Boundary-Layer Meteorology 105, 119–127. doi:10.1023/A:1019600908144

Kustas, W., Anderson, M., 2009. Advances in thermal infrared remote sensing for land surface modeling. Agricultural and Forest Meteorology 149, 2071–2081. doi:10.1016/j.agrformet.2009.05.016

Kustas, W.P., 1991. An interdisciplinary field study of the energy and water fluxes in the atmosphere-biosphere system over semiarid rangelands: description and some preliminary results. Bulletin - American Meteorological Society.

Kustas, W.P., Daughtry, C.S.T., 1990. Estimation of the soil heat flux/net radiation ratio from spectral data. Agricultural and Forest Meteorology 49, 205–223. doi:10.1016/0168-1923(90)90033-3

Kustas, W.P., Norman, J.M., 1999. Reply to comments about the basic equations of dual-source vegetation ± atmosphere transfer models 94, 275–278.

Kustas, W.P., Norman, J.M., 1996. Use of remote sensing for evapotranspiration monitoring over land surfaces. Hydrological Sciences Journal 41, 495–516. doi:10.1080/02626669609491522

Kustas, W.P., Norman, J.M., Anderson, M.C., French, A.N., 2003. Estimating subpixel surface temperatures and energy fluxes from the vegetation index-radiometric temperature relationship. Remote Sensing of Environment 85, 429–440. doi:10.1016/S0034-4257(03)00036-1

Kustas, W.P., Schmugge, T.J., Humes, K.S., Jackson, T.J., Parry, R., Weltz, M.A., Moran, M.S., 2002. Relationships between Evaporative Fraction and Remotely Sensed Vegetation Index and Microwave Brightness Temperature for Semiarid Rangelands. Journal of Applied Meteorology. doi:10.1175/1520-0450(1993)032<1781:rbefar>2.0.co;2

Lagouarde, J.P., Dayau, S., Moreau, P., Guyon, D., 2014. Directional anisotropy of brightness surface temperature over vineyards: Case study over the Medoc Region (SW France). IEEE Geoscience and Remote Sensing Letters. doi:10.1109/LGRS.2013.2282492

Le Hégarat, S., Zribi, M., Alem, F., Weisse, A., Loumagne, C., 2002. Soil moisture estimation from ERS/SAR data: Toward an operational methodology. IEEE Transactions on Geoscience and Remote Sensing. doi:10.1109/TGRS.2002.806994

Le Morvan, A., Zribi, M., Baghdadi, N., Chanzy, A., 2008. Soil Moisture Profile Effect on Radar Signal Measurement. Sensors 8, 256–270. doi:10.3390/s8010256

Lee, J.S., Jurkevich, L., Dewaele, P., Wambacq, P., Oosterlinck, A., 1994. Speckle filtering of synthetic aperture radar images: A review. Remote Sensing Reviews. doi:10.1080/02757259409532206

Lee, J. Sen, 1999. Polarimetric SAR speckle filtering and its implication for classification. IEEE Transactions on Geoscience and Remote Sensing. doi:10.1109/36.789635

Li, Z.-L., Tang, R., Wan, Z., Bi, Y., Zhou, C., Tang, B., Yan, G., Zhang, X., Li, Z.-L., Tang,

R., Wan, Z., Bi, Y., Zhou, C., Tang, B., Yan, G., Zhang, X., 2009. A Review of Current Methodologies for Regional Evapotranspiration Estimation from Remotely Sensed Data. Sensors 9, 3801–3853. doi:10.3390/s90503801

Li, Z., Duan, S., 2017. Land surface temperature. S. Liang (Ed.), Comprehensive remote sensing 5.

Lievens, H., Verhoest, N.E.C., 2011. On the Retrieval of Soil Moisture in Wheat Fields From L-Band SAR Based on Water Cloud Modeling, the IEM, and Effective Roughness Parameters. IEEE Geoscience and Remote Sensing Letters 8, 740–744. doi:10.1109/LGRS.2011.2106109

Liu, D., Zhu, X., 2012. An enhanced physical method for downscaling thermal infrared radiance. IEEE Geoscience and Remote Sensing Letters 9, 690–694. doi:10.1109/LGRS.2011.2178814

Liu, L.S., Shi, J.C., 2012. Soil moisture variations monitoring using new microwave soil moisture index (MSMI). 2012 2nd International Conference on Remote Sensing, Environment and Transportation Engineering, RSETE 2012 - Proceedings. doi:10.1109/RSETE.2012.6260727

Loew, A., Ludwig, R., Mauser, W., 2006. Derivation of surface soil moisture from ENVISAT ASAR wide swath and image mode data in agricultural areas. IEEE Transactions on Geoscience and Remote Sensing. doi:10.1109/TGRS.2005.863858

Mahfouf, J.-F., Noilhan, J., 1996. Inclusion of Gravitational Drainage in a Land Surface Scheme Based on the Force-Restore Method. Journal of Applied Meteorology 35, 987–992. doi:10.1175/1520-0450(1996)035<0987:IOGDIA>2.0.CO;2

Mahfouf J.-F., Noilhan, J., 1991. Comparative Study of Various Formulations of Evaporation from Bare Soil Using In Situ Data. Journal of Applied Meteorology.

Malbéteau, Y., 2016. Suivi des ressources en eau par une approche combinant la télédétection multi-capteur et la modélisation phénoménologique. Universit´e Toulouse 3 Paul Sabatier (UT3 Paul Sabatier).

Malbéteau, Y., Merlin, O., Molero, B., Rüdiger, C., Bacon, S., 2016. DisPATCh as a tool to evaluate coarse-scale remotely sensed soil moisture using localized in situ measurements: Application to SMOS and AMSR-E data in Southeastern Australia. International Journal of Applied Earth Observation and Geoinformation 45, 221–234. doi:10.1016/j.jag.2015.10.002

Manabe, S., 1969. Climate and the Ocean Circulation I. The Atmospheric Circulation and the Hydrology of the Earth's Surface. Monthly Weather Review. doi:10.1175/1520-0493(1969)097<0739:CATOC>2.3.CO;2

Mathieu, R., Sbih, M., Viau, A.A., Anctil, F., Parent, L.E., Boisvert, J., 2003. {R}elationships between {R}adarsat {SAR} data and surface moisture content of agricultural organic soils. INTERNATIONAL JOURNAL OF REMOTE SENSING. doi:10.1080/0143116031000115247

Mckee, T.B., Doesken, N.J., Kleist, J., 1993. THE RELATIONSHIP OF DROUGHT

FREQUENCY AND DURATION TO TIME SCALES, Eighth Conference on Applied Climatology.

McKee, T.B., Doesken, N.J., Kleist, J., 1995. Drought Monitoring with Multiple Time Scales. roceedings of the 9th Conference on Applied Climatology, Dallas, TX, American Meteorological Society 233–236.

McVicar, T.R.., Jupp, D.B.., Yang, X., 1992. Linking Regional Water Balance Models with Remote Sensing. In Proceedings of the 13th Asian Conference on Remote Sensing, Ulaanbaatar, Mongolia.

Menenti, M., Choudhury, B.J. (Laboratory for H.P.N.G.M. (USA)), 1993. Parameterization of land surface evaporation by means of location dependent potential evaporation and surface temperature range.

Merlin, O., 2013. An original interpretation of the wet edge of the surface temperature-albedo space to estimate crop evapotranspiration (SEB-1S), and its validation over an irrigated area in northwestern Mexico. Hydrology and Earth System Sciences 17, 3623–3637. doi:10.5194/hess-17-3623-2013

Merlin, O., Al Bitar, A., Walker, J.P., Kerr, Y., 2010a. An improved algorithm for disaggregating microwave-derived soil moisture based on red, near-infrared and thermal-infrared data. Remote Sensing of Environment 114, 2305–2316. doi:10.1016/j.rse.2010.05.007

Merlin, O., Chehbouni, A., Boulet, G., Kerr, Y., 2006a. Assimilation of Disaggregated Microwave Soil Moisture into a Hydrologic Model Using Coarse-Scale Meteorological Data. Journal of Hydrometeorology 7, 1308–1322. doi:10.1175/JHM552.1

Merlin, O., Chehbouni, A., Kerr, Y.H., Goodrich, D.C., 2006b. A downscaling method for distributing surface soil moisture within a microwave pixel: Application to the Monsoon '90 data. Remote Sensing of Environment 101, 379–389. doi:10.1016/j.rse.2006.01.004

Merlin, O., Chehbouni, A., Walker, J.P., Panciera, R., Kerr, Y.H., 2008a. A simple method to disaggregate passive microwave-based soil moisture. IEEE Transactions on Geoscience and Remote Sensing 46, 786–796. doi:10.1109/TGRS.2007.914807

Merlin, O., Chehbouni, A.G., Kerr, Y.H., Njoku, E.G., Entekhabi, D., 2005. A combined modeling and multipectral/multiresolution remote sensing approach for disaggregation of surface soil moisture: Application to SMOS configuration. IEEE Transactions on Geoscience and Remote Sensing 43, 2036–2050. doi:10.1109/TGRS.2005.853192

Merlin, O., Chirouze, J., Olioso, A., Jarlan, L., Chehbouni, G., Boulet, G., 2014. An image-based four-source surface energy balance model to estimate crop evapotranspiration from solar reflectance / thermal emission data (SEB-4S). Agricultural and Forest Meteorology 184, 188–203. doi:10.1016/j.agrformet.2013.10.002

Merlin, O., Duchemin, B., Hagolle, O., Jacob, F., Coudert, B., Chehbouni, G., Dedieu, G., Garatuza, J., Kerr, Y., 2010b. Disaggregation of MODIS surface temperature over an agricultural area using a time series of Formosat-2 images. Remote Sensing of Environment 114, 2500–2512. doi:10.1016/j.rse.2010.05.025

Merlin, O., Escorihuela, M.J., Mayoral, M.A., Hagolle, O., Al Bitar, A., Kerr, Y., 2013. Self-calibrated evaporation-based disaggregation of SMOS soil moisture: An evaluation study at 3km and 100m resolution in Catalunya, Spain. Remote Sensing of Environment 130, 25–38. doi:10.1016/j.rse.2012.11.008

Merlin, O., Jacob, F., Wigneron, J., Member, S., Walker, J., Chehbouni, G., 2012a. Multidimensional Disaggregation of Land Surface and Microwave-L Bands 50, 1864–1880.

Merlin, O., Jacob, F., Wigneron, J.P., Walker, J., Chehbouni, G., 2012b. Multidimensional disaggregation of land surface temperature using high-resolution red, near-infrared, shortwave-infrared, and microwave-L bands. IEEE Transactions on Geoscience and Remote Sensing 50, 1864–1880. doi:10.1109/TGRS.2011.2169802

Merlin, O., Olivera-guerra, L., Bouchra, A.H., Amazirh, A., Rafi, Z., Ezzahar, J., Gentine, P., Khabba, S., Gascoin, S., Er-raki, S., 2017. A phenomenological model of soil evaporative efficiency using readily available data. Agricultural and Forest Meteorology, In review.

Merlin, O., Rüdiger, C., Bitar, A. Al, Richaume, P., Walker, J.P., Kerr, Y.H., Member, S., 2012c. Disaggregation of SMOS Soil Moisture in Southeastern Australia 50, 1556–1571.

Merlin, O., Stefan, V.G., Amazirh, A., Chanzy, A., Ceschia, E., Tallec, T., Beringer, J., Gentine, P., Er-Raki, S., Bircher, S., Khabba, S., 2016. Modeling soil evaporation efficiency in a range of soil and atmospheric conditions using ameta-analysis approach. Water Resources Research 52, 3663–3684. doi:10.1002/2015WR018233.Received

Merlin, O., Walker, J.P., Chehbouni, A., Kerr, Y., 2008b. Towards deterministic downscaling of SMOS soil moisture using MODIS derived soil evaporative efficiency. Remote Sensing of Environment. doi:10.1016/j.rse.2008.06.012

Miralles, D.G., Holmes, T.R.H., De Jeu, R.A.M., Gash, J.H., Meesters, A.G.C.A., Dolman, A.J., 2011. Global land-surface evaporation estimated from satellite-based observations. Hydrology and Earth System Sciences. doi:10.5194/hess-15-453-2011.

Monteith, J.L., 1965. Evaporation and Environment. 19th Symposia of the Society for Experimental Biology. UniversityPress, Cambridge 19, 205–234.

Moran, M.S., 2004. Thermal infrared measurement as an indicator of plant ecosystem health. Thermal remote sensing in land surface processes / edited by Dale A. Quattrochi and Jeffrey C. Luvall.

Moran, M.S., Clarke, T.R., Inoue, Y., Vidal, A., 1994. Estimating crop water deficit using the relation between surface-air temperature and spectral vegetation index. Remote Sensing of Environment. doi:10.1016/0034-4257(94)90020-5

Moran, M.S., Jackson, R.D., 1991. Assessing the Spatial Distribution of Evapotranspiration Using Remotely Sensed Inputs. Journal of Environment Quality 20, 725. doi:10.2134/jeq1991.00472425002000040003x

Moran, M.S., Jackson, R.D., Slater, P.N., Teillet, P.M., 1992. Evaluation of simplified procedures for retrieval of land surface reflectance factors from satellite sensor output.

Remote Sensing of Environment. doi:10.1016/0034-4257(92)90076-V

Nemani, R.R., Running, S.W., 1989. Estimation of regional surface resistance to evapotranspiration from NDVI and thermal-IR AVHRR data. Journal of Applied Meteorology. doi:10.1175/1520-0450(1989)028<0276:EORSRT>2.0.CO;2

Nishida, K., Nemani, R.R., Glassy, J.M., Running, S.W., 2003. Development of an evapotranspiration index from Aqua/MODIS for monitoring surface moisture status. IEEE Transactions on Geoscience and Remote Sensing. doi:10.1109/TGRS.2003.811744

Njoku, E.G., Jackson, T.J., Lakshmi, V., Chan, T.K., Nghiem, S.V., 2003. Soil moisture retrieval from AMSR-E. IEEE Transactions on Geoscience and Remote Sensing 41, 215–229. doi:10.1109/TGRS.2002.808243

Noilhan, J., Mahfouf, J.-F., 1996. The ISBA land surface parameterisation scheme. Global and Planetary Change 13, 145–159. doi:10.1016/0921-8181(95)00043-7

Oh, Y., 2004. Quantitative retrieval of soil moisture content and surface roughness from multipolarized radar observations of bare soil surfaces. IEEE Transactions on Geoscience and Remote Sensing. doi:10.1109/TGRS.2003.821065

Oh, Y., Sarabandi, K., Ulaby, F.T., 1992. An empirical model and an inversion technique for radar scattering from bare soil surfaces. IEEE Transactions on Geoscience and Remote Sensing. doi:10.1109/36.134086

Ojha, N., Merlin, O., Molero, B., Suere, C., Olivera-guerra, L., Hssaine, B.A., Amazirh, A., Bitar, A. Al, Escorihuela, M.J., Er-raki, S., 2019. Stepwise Disaggregation of SMAP Soil Moisture at 100 m Resolution Using Landsat-7 / 8 Data and a Varying Intermediate Resolution. Remote Sensing 11, 1–23. doi:10.3390/rs11161863

Olioso, A., Mira, M., Courault, D., Marloie, O., Guillevic, P., 2013. Impact of surface emissivity and atmospheric conditions on surface temperatures estimated from top of canopy brightness temperatures derived from landsat 7 data, in: IEEE International Geoscience and Remote Sensing Symposium - IGARSS. Melbourne, VIC, Australia, pp. 3033–3036. doi:10.1109/IGARSS.2013.6723465

Olivera-Guerra, L., Mattar, C., Merlin, O., Durán-Alarcón, C., Santamaría-Artigas, A., Fuster, R., 2017. An operational method for the disaggregation of land surface temperature to estimate actual evapotranspiration in the arid region of Chile. ISPRS Journal of Photogrammetry and Remote Sensing 128, 170–181. doi:10.1016/j.isprsjprs.2017.03.014

Olivera-Guerra, L., Merlin, O., Er-Raki, S., Khabba, S., Escorihuela, M.J., 2018. Estimating the water budget components of irrigated crops: Combining the FAO-56 dual crop coefficient with surface temperature and vegetation index data. Agricultural Water Management 208, 120–131. doi:10.1016/j.agwat.2018.06.014

Omer, S.K., Bitar, A. Al, Sekhar, M., Zribi, M., Bandyopadhyay, S., 2015. Retrieval and Multi-scale Validation of Soil Moisture from 8128–8153. doi:10.3390/rs70608128

Palmer, W.C., 1965. Meteorologic Drought.

Paloscia, S., Macelloni, G., Santi, E., Koike, T., 2001. A multifrequency algorithm for the

retrieval of soil moisture on a large scale using microwave data from SMMR and SSM/I satellites. IEEE Transactions on Geoscience and Remote Sensing 39, 1655–1661. doi:10.1109/36.942543

Paloscia, S., Pampaloni, P., 1984. Microwave remote sensing of plant water stress. Remote Sensing of Environment 16, 249–255. doi:10.1016/0034-4257(84)90068-3

Pellenq, J., Kalma, J., Boulet, G., Saulnier, G.-M., Wooldridge, S., Kerr, Y., Chehbouni, A., 2003. A disaggregation scheme for soil moisture based on topography and soil depth. Journal of Hydrology 276, 112–127. doi:10.1016/S0022-1694(03)00066-0

Peng, J., Loew, A., Merlin, O., Verhoest, N.E.C., 2017. A review of spatial downscaling of satellite remotely-sensed soil moisture. Submitted to Reviews of Geophysics. doi:10.1002/2016RG000543

Plan Bleu, 2009. Etat de l'Environnement et du Développement en Méditerranée. Rapport d'activités régionales PNUD/PAM.

Price, J.C., 1990. Using spatial context in satellite data to infer regional scale evapotranspiration. IEEE Transactions on Geoscience and Remote Sensing. doi:10.1109/36.58983

Price, J.C., 1982. Estimation of Regional Scale Evapotranspiration Through Analysis of Satellite Thermal-Infrared Data. IEEE Transactions on Geoscience and Remote Sensing 20, 286–292. doi:10.1109/TGRS.1982.350445

Prihodko, L., Goward, S.N., 1997. Estimation of air temperature from remotely sensed surface observations. Remote Sensing of Environment 60, 335–346. doi:10.1016/S0034-4257(96)00216-7

Qin, J., Yang, K., Lu, N., Chen, Y., Zhao, L., Han, M., 2013. Spatial upscaling of in-situ soil moisture measurements based on MODIS-derived apparent thermal inertia. Remote Sensing of Environment. doi:10.1016/j.rse.2013.07.003

Quesney, A., Le Hégarat-Mascle, S., Taconet, O., Vidal-Madjar, D., Wigneron, J.P., Loumagne, C., Normand, M., 2000. Estimation of watershed soil moisture index from ERS/SAR data. Remote Sensing of Environment. doi:10.1016/S0034-4257(99)00102-9

Raes, D., Steduto, P., Hsiao, T.C., Fereres, E., 2009. AquaCropThe FAO Crop Model to Simulate Yield Response to Water: II. Main Algorithms and Software Description. Agronomy Journal 101, 438. doi:10.2134/agronj2008.0140s

Rakotoarivony L., O. Taconet, Vidal-Madjar, D., 1996. Radar backscattering over agricultural bare soils. Journal of Electromagnetic Waves and Applications.

Rallo, G., González-Altozano, P., Manzano-Juárez, J., Provenzano, G., 2017. Using field measurements and FAO-56 model to assess the eco-physiological response of citrus orchards under regulated deficit irrigation. Agricultural Water Management 180, 136–147. doi:10.1016/J.AGWAT.2016.11.011

Ramoelo, A., Majozi, N., Mathieu, R., Jovanovic, N., Nickless, A., Dzikiti, S., Ramoelo, A., Majozi, N., Mathieu, R., Jovanovic, N., Nickless, A., Dzikiti, S., 2014. Validation of

Global Evapotranspiration Product (MOD16) using Flux Tower Data in the African Savanna, South Africa. Remote Sensing 6, 7406–7423. doi:10.3390/rs6087406

Rana, G., Katerji, N., de Lorenzi, F., 2005. Measurement and modelling of evapotranspiration of irrigated citrus orchard under Mediterranean conditions. Agricultural and Forest Meteorology 128, 199–209. doi:10.1016/J.AGRFORMET.2004.11.001

Remond, A., Beaudoin, A., King, C., 1999. SAR imagery to estimate roughness parameters when modelling runoff risk. International Journal of Remote Sensing. doi:10.1080/014311699211967

Rhee, J., Im, J., Carbone, G.J., 2010. Monitoring agricultural drought for arid and humid regions using multi-sensor remote sensing data. Remote Sensing of Environment 114, 2875–2887. doi:10.1016/J.RSE.2010.07.005

Ritchie, J.T., 1986. The CERES-Maize model. In C. A. Jones, & J. R. Kiniry (Eds.), CERES-Maize: Simulation model of maize growth and development. College Station, TX: Texas A M University press. 3–6.

Robinson, D.A., Jones, S.B., Wraith, J.M., Or, D., Friedman, S.P., 2003. A Review of Advances in Dielectric and Electrical Conductivity Measurement in Soils Using Time Domain Reflectometry. Vadose Zone Journal 2, 444–475. doi:10.2113/2.4.444

Robock, A., Vinnikov, K.Y., Srinivasan, G., Entin, J.K., Hollinger, S.E., Speranskaya, N.A., Liu, S., Namkhai, A., 2000. The Global Soil Moisture Data Bank. Bulletin of the American Meteorological Society 81, 1281–1299. doi:10.1175/1520-0477(2000)081<1281:TGSMDB>2.3.CO;2

Roerink, G.J., Su, Z., Menenti, M., 2000. S-SEBI: A simple remote sensing algorithm to estimate the surface energy balance. Physics and Chemistry of the Earth Part B-Hydrology Oceans and Atmosphere 25, 147–157. doi:doi.org/10.1016/S1464-1909(99)00128-8

Ruhoff, A.L., Paz, A.R., Aragao, L.E.O.C., Mu, Q., Malhi, Y., Collischonn, W., Rocha, H.R., Running, S.W., 2013. Assessment of the MODIS global evapotranspiration algorithm using eddy covariance measurements and hydrological modelling in the Rio Grande basin. Hydrological Sciences Journal 58, 1658–1676. doi:10.1080/02626667.2013.837578

Sabaghy, S., Walker, J.P., Renzullo, L.J., Jackson, T.J., 2018. Spatially enhanced passive microwave derived soil moisture: Capabilities and opportunities. Remote Sensing of Environment 209, 551–580. doi:10.1016/j.rse.2018.02.065

Sabol, J., E., D., Gillespie, A.R., Abbott, E., Yamada, G., 2009. Field validation of the ASTER Temperature–Emissivity Separation algorithm. Remote Sensing of Environment 113, 2328–2344. doi:10.1016/j.rse.2009.06.008

Sandholt, I., Nielsen, C., Stisen, S., 2009. A Simple Downscaling Algorithm for Remotely Sensed Land Surface Temperature. American Geophysical Union, Spring Meeting 2009, abstract id. H24A-04.

Sandholt, I., Rasmussen, K., Andersen, J., 2002. A simple interpretation of the surface

temperature/vegetation index space for assessment of surface moisture status. Remote Sensing of Environment 79, 213–224. doi:10.1016/S0034-4257(01)00274-7

Satalino, G., Balenzano, A., Mattia, F., Davidson, M.W.J., 2014. C-band SAR data for mapping crops dominated by surface or volume scattering. IEEE Geoscience and Remote Sensing Letters. doi:10.1109/LGRS.2013.2263034

Schaake, J.C., Koren, V.I., Duan, Q.Y., Mitchell, K., Chen, F., 1996. Simple water balance model for estimating runoff at different spatial and temporal scales. Journal of Geophysical Research Atmospheres. doi:10.1029/95JD02892

Schmugge, T., 1978. Remote sensing of surface soil moisture. Design. doi:10.1029/JC080i021p03044

Schmugge, T.J., Wang, J.R., Asrar, G., 1988. Results from the Push Broom Microwave Radiometer Flights Over the Konza Prairie in 1985. IEEE Transactions on Geoscience and Remote Sensing. doi:10.1109/36.7684

Schultz, G.A., Engman, E.T., 2000. Present use and future perspectives of remote sensing in hydrology and water management, Remote Sensing and Hydrology. IAHS Publ.

Scott, R.L., Watts, C., Payan, J.G., Edwards, E., Goodrich, D.C., Williams, D., Shuttleworth, W.J., 2003. The understory and overstory partitioning of energy and water fluxes in an open canopy, semiarid woodland. Agricultural and Forest Meteorology. doi:10.1016/S0168-1923(02)00197-1

Shi, J., Wang, J., Hsu, A.Y., O'Neill, P.E., Engman, E.T., 1997. Estimation of bare surface soil moisture and surface roughness parameter using L-band SAR image data. IEEE Transactions on Geoscience and Remote Sensing. doi:10.1109/36.628792

Shoshany, M., Svoray, T., Svoray, T., Curran, P.J., Foody, G.M., Perevolotsky, A., 2000. The relationship between ERS-2 SAR backscatter and soil moisture: Generalization from a humid to semi-arid transect. International Journal of Remote Sensing. doi:10.1080/01431160050029620

Shuttleworth, W.J., Gurney, R.J.A.Y.H., Ormsby, J.P., 1989. FIFE : the variation in energy partition at surface flux sites. IAHS Publ 67–74.

Shuttleworth, W.J., Wallace, J.S., 1985. Evaporation from sparse crops-an energy combination theory. The Quarterly Journal of the Royal Meteorological Society. doi:10.1002/qj.49711146510

Sikdar, M., Cumming, I., 2004. A Modified Empirical Model for Soil Moisture Estimation in Vegetated Areas Using SAR Data. IGRASS. doi:10.1109/IGARSS.2004.1368526

Smith, D.M., Allen, S.J., 2007. Measurement of sap flow in plant stems. Journal of Experimental Botany. doi:10.1093/jxb/47.12.1833

Smith, R.C.G., Choudhury, B.J., 1991. Analysis of normalized difference and surface temperature observations over southeastern Australia. Remote Sensing. doi:10.1080/01431169108955234

Sobrino, J.A., Franch, B., Mattar, C., Jiménez-Muñoz, J.C., Corbari, C., 2012. A method to estimate soil moisture from Airborne Hyperspectral Scanner (AHS) and ASTER data: Application to SEN2FLEX and SEN3EXP campaigns. Remote Sensing of Environment. doi:10.1016/j.rse.2011.10.018

Srinivasa Rao, S., Dinesh kumar, S., Das, S.N., Nagaraju, M.S.S., Venugopal, M. V., Rajankar, P., Laghate, P., Reddy, M.S., Joshi, A.K., Sharma, J.R., 2013. Modified Dubois Model for Estimating Soil Moisture with Dual Polarized SAR Data. Journal of the Indian Society of Remote Sensing. doi:10.1007/s12524-013-0274-3

Srivastava, H.S., 2007. Development and Validation of an Improved Methodology for Operational Monitoring of Soil Moisture Over Large Agricultural Area Using Multi-Incidence Angle Radarsat-1 Sar Data and multi-polarized ENVISAT-1 ASAR Data, in: JEP-MW Conference. SAC, Ahmedabad, India, pp. 2-1-2–11.

Srivastava, H.S., Patel, P., Manchanda, M.L., Adiga, S., 2003. Use of multiincidence angle RADARSAT-1 SAR data to incorporate the effect of surface roughness in soil moisture estimation, in: IEEE Transactions on Geoscience and Remote Sensing. doi:10.1109/TGRS.2003.813356

Srivastava, H.S., Patel, P., Sharma, Y., Navalgund, R.R., 2009. Large-Area Soil Moisture Estimation Using multi-Incidence-Angle RADARSAT-1 SAR Data. IEEE TRANSACTIONS ON GEOSCIENCE AND REMOTE SENSING, 47, 2528–2535.

Srivastava, H.S., Patel, P., Sharma, Y., Navalgund, R.R., 2008. Retrieval of surface roughness using multi-polarized Envisat-1 ASAR data. Geocarto International 23, 67–77. doi:10.1080/10106040701538157

Stefan, V.G., Merlin, O., Er-Raki, S., Escorihuela, M.J., Khabba, S., 2015. Consistency between In Situ, model-derived and high-resolution-image-based soil temperature endmembers: Towards a robust data-based model for multi-resolution monitoring of crop evapotranspiration. Remote Sensing 7, 10444–10479. doi:10.3390/rs70810444

Su, Z., 2002. The Surface Energy Balance System (SEBS) for estimation of turbulent heat fluxes, Hydrology and Earth System Sciences.

Sugita, M., Brutsaert, W., 1991. Daily evaporation over a region from lower boundary layer profiles measured with radiosondes. Water Resources Research. doi:10.1029/90WR02706

Susaki, J., 2008. CALIBRATION OF IEM MODEL FOR THE SOIL MOISTURE MAPPING OF NON-INUNDATED PADDY FIELDS USING ALOS / PALSAR DATA Junichi Susaki Graduate School of Global Environmental Studies ,. Sites The Journal Of 20Th Century Contemporary French Studies 753–756.

Tardy, B., Rivalland, V., Huc, M., Hagolle, O., Marcq, S., Boulet, G., 2016a. A Software Tool for Atmospheric Correction and Surface Temperature Estimation of Landsat Infrared Thermal Data 8, 696. doi:10.3390/rs8090696

Tardy, B., Rivalland, V., Huc, M., Hagolle, O., Marcq, S., Boulet, G., 2016b. A Software Tool for Atmospheric Correction and Surface Temperature Estimation of Landsat Infrared Thermal Data 1–24. doi:10.3390/rs8090696

Temimi, M., Leconte, R., Brissette, F., Chaouch, N., 2007. Flood and soil wetness monitoring over the Mackenzie River Basin using AMSR-E 37 GHz brightness temperature. Journal of Hydrology. doi:10.1016/j.jhydrol.2006.09.002

Testi, L., Villalobos, F.., Orgaz, F., 2004a. Evapotranspiration of a young irrigated olive orchard in southern Spain. Agric.For.Meteorol 121, 1–18.

Testi, L., Villalobos, F.., Orgaz, F., 2004b. Evapotranspiration of a young irrigated olive orchard in southern Spain. Agricultural and Forest Meteorology 121, 1–18. doi:10.1016/J.AGRFORMET.2003.08.005

Thoma, D., Moran, M., Bryant, R., Collins, C.H., Rahman, M., Skirvin, S., 2004. Comparison of two methods for extracting surface soil moisture from C-band radar imagery, in: IEEE International IEEE International IEEE International Geoscience and Remote Sensing Symposium. IGARSS '04. Proceedings. 2004. IEEE, pp. 827–830. doi:10.1109/IGARSS.2004.1368532

Tomer, S., Al Bitar, A., Sekhar, M., Zribi, M., Bandyopadhyay, S., Kerr, Y., Tomer, S.K., Al Bitar, A., Sekhar, M., Zribi, M., Bandyopadhyay, S., Kerr, Y., 2016. MAPSM: A Spatio-Temporal Algorithm for Merging Soil Moisture from Active and Passive Microwave Remote Sensing. Remote Sensing 8, 990. doi:10.3390/rs8120990

Torres, R., Snoeij, P., Geudtner, D., Bibby, D., Davidson, M., Attema, E., Potin, P., Rommen, B. ??rn, Floury, N., Brown, M., Traver, I.N., Deghaye, P., Duesmann, B., Rosich, B., Miranda, N., Bruno, C., L'Abbate, M., Croci, R., Pietropaolo, A., Huchler, M., Rostan, F., 2012. GMES Sentinel-1 mission. Remote Sensing of Environment. doi:10.1016/j.rse.2011.05.028

Ulaby, F.T., Batlivala, P.P., Dobson, M.C., 1978. Microwave Backscatter Dependence on Surface Roughness, Soil Moisture, and Soil Texture: Part I–Bare Soil. IEEE Transactions on Geoscience Electronics. doi:10.1109/TGE.1978.294586

Ulaby, F.T., Bradley, G.A., Obson, M.C., 1979. Microwave Backscatter Dependence on Surface Roughness, Soil Moisture, and Soil Texture: Part II–Vegetation-Covered Soil. IEEE Transactions on Geoscience Electronics. doi:10.1109/TGE.1979.294626

Ulaby, F.T., Moore, R.K., Fung, A.K., 1986. Microwave remote sensing: Active and passive. Volume 3 - From theory to applications, Microwave Remote Sensing Active and Passive.

Van Beek, L.P.H., Wada, Y., Bierkens, M.F.P., 2011. Global monthly water stress: 1. Water balance and water availability. Water Resources Research. doi:10.1029/2010WR009791

van der Velde, R., Salama, M.S., Eweys, O.A., Wen, J., Wang, Q., Velde, R. Van Der, Salama, M.S., Eweys, O.A., Wen, J., Wang, Q., 2014. Soil Moisture Mapping Using Combined Active / Passive Microwave Observations Over the East of the Netherlands. IEEE Journal of selected topics in applied eath observation and remotesensing 8, 1–18. doi:10.1109/JSTARS.2014.2353692

Van Oevelen, P.J., Hoekman, D.H., 1999. Radar backscatter inversion techniques for estimation of surface soil moisture: EFEDA-spain and HAPEX-SAHEL case studies. IEEE Transactions on Geoscience and Remote Sensing. doi:10.1109/36.739141

Van Rooy, M.P., 1965. A rainfall anomaly index independent of time and space. Notos 14, 43.

Vereecken, H., Huisman, J.A., Bogena, H., Vanderborght, J., Vrugt, J.A., Hopmans, J.W., 2008. On the value of soil moisture measurements in vadose zone hydrology : A review 44, 1–21. doi:10.1029/2008WR006829

Verstraeten, W.W., Veroustraete, F., Feyen, J., 2008. Assessment of Evapotranspiration and Soil Moisture Content Across Different Scales of Observation 70–117.

Wagner, W., Lemoine, G., Borgeaud, M., Member, S., Rott, H., 1999a. A Study of Vegetation Cover Effects on ERS Scatterometer Data 37, 938–948.

Wagner, W., Lemoine, G., Rott, H., 1999b. A Method for Estimating Soil Moisture from ERS Scatterometer and Soil Data. Remote Sensing of Environment 4257.

Walker, J.., Willgoose, G.., Kalma, J.., 2004. In situ measurement of soil moisture: a comparison of techniques. Journal of Hydrology 293, 85–99.

Wan, Z., 2008. New refinements and validation of the MODIS Land-Surface Temperature/Emissivity products. doi:10.1016/j.rse.2006.06.026

Wan, Z., Dozier, J., 1996. A generalized split-window algorithm for retrieving land-surface temperature from space. IEEE Transactions on Geoscience and Remote Sensing 34, 892–905. doi:10.1109/36.508406

Wan, Z., Wang, P., Li, X., 2004. Using MODIS Land Surface Temperature and Normalized Difference Vegetation Index products for monitoring drought in the southern Great Plains, USA. International Journal of Remote Sensing. doi:10.1080/0143116031000115328

Wan, Z., Zhang, Y., Zhang, Q., Li, Z. liang, 2002. Validation of the land-surface temperature products retrieved from terra moderate resolution imaging spectroradiometer data. Remote Sensing of Environment 38, 163–180. doi:10.1016/S0034-4257(02)00093-7

Wang, C., Qi, S., Niu, Z., Wang, J., 2004. Evaluating soil moisture status in China using the temperature–vegetation dryness index (TVDI). Canadian Journal of Remote Sensing. doi:10.5589/m04-029

Wang, J., Bras, R.L., Sivandran, G., Knox, R.G., 2010. A simple method for the estimation of thermal inertia. Geophysical Research Letters. doi:10.1029/2009GL041851

Wang, K., Li, Z., Cribb, M., 2006. Estimation of evaporative fraction from a combination of day and night land surface temperatures and NDVI: A new method to determine the Priestley-Taylor parameter. Remote Sensing of Environment. doi:10.1016/j.rse.2006.02.007

Wang, L., Qu, J.J., Hao, X., 2008. Forest fire detection using the normalized multi-band drought index (NMDI) with satellite measurements. Agricultural and Forest Meteorology. doi:10.1016/j.agrformet.2008.06.005

Wang, P., Li, X., Gong, J., Conghe, S., 2001. Vegetation temperature condition index and its

application for drought monitoring, in: IGARSS 2001. Scanning the Present and Resolving the Future. Proceedings. IEEE 2001 International Geoscience and Remote Sensing Symposium (Cat. No.01CH37217). IEEE, pp. 141–143. doi:10.1109/IGARSS.2001.976083

Wang, W., Liang, S., Augustine, J.A., 2009. Estimating high spatial resolution clear-sky land surface upwelling longwave radiation from MODIS data. IEEE Transactions on Geoscience and Remote Sensing. doi:10.1109/TGRS.2008.2005206

Wickel, A.J., Jackson, T.J., Wood, E.F., 2001. Multi-temporal monitoring of soil moisture with RADARSAT SAR during the 1997 Southern Great Plains hydrology experiment. International Journal of Remote Sensing. doi:10.1080/01431160120291

Williamson, H.D., 1988. Evaluation of middle and thermal infrared radiance in indices used to estimate GLAI. International Journal of Remote Sensing 9, 275–283. doi:10.1080/01431168808954851

Yang, H., Cong, Z., Liu, Z., Lei, Z., 2010. Estimating sub-pixel temperatures using the triangle algorithm. International Journal of Remote Sensing 31, 6047–6060. doi:10.1080/01431160903376373

Yu, Y., Liu, Y., Yu, P., Liu, Y., Yu, P., 2017. Land Surface Temperature Product Development for JPSS and GOES-R Missions. Comprehensive Remote Sensing 284–303. doi:10.1016/b978-0-12-409548-9.10522-6

Zhan, W., Chen, Y., Zhou, J., Li, J., Liu, W., 2011. Sharpening thermal imageries: A generalized theoretical framework from an assimilation perspective. IEEE Transactions on Geoscience and Remote Sensing 49, 773–789. doi:10.1109/TGRS.2010.2060342

Zhang, R., Tian, J., Su, H., Sun, X., Chen, S., Xia, J., 2008. Two improvements of an operational two-layer model for terrestrial surface heat flux retrieval. Sensors 8, 6165–6187. doi:10.3390/s8106165

Zhou, J., Li, J., Zhang, L., Hu, D., Zhan, W., 2012. Intercomparison of methods for estimating land surface temperature from a Landsat-5 TM image in an arid region with low water vapour in the atmosphere. International Journal of Remote Sensing. doi:10.1080/01431161.2011.617396

Zribi, M., André, C., Decharme, B., 2008. A method for soil moisture estimation in Western Africa based on the ERS scatterometer, in: IEEE Transactions on Geoscience and Remote Sensing. doi:10.1109/TGRS.2007.904582

Zribi, M., Baghdadi, N., Holah, N., Fafin, O., 2005. New methodology for soil surface moisture estimation and its application to ENVISAT-ASAR multi-incidence data inversion. Remote Sensing of Environment. doi:10.1016/j.rse.2005.04.005

Zribi, M., Chahbi, A., Shabou, M., Duchemin, B., Baghdadi, N., Amri, R., 2011. Soil surface moisture estimation over a semi-arid region using ENVISAT ASAR radar data for soil evaporation evaluation 345–358. doi:10.5194/hess-15-345-2011

Zribi, M., Dechambre, M., 2003. A new empirical model to retrieve soil moisture and roughness from C-band radar data. Remote Sensing of Environment 84, 42–52.

doi:10.1016/S0034-4257(02)00069-X

Zribi, M., Taconet, O., H??garat-Mascle, S. Le, Vidal-Madjar, D., Emblanch, C., Loumagne, C., Normand, M., 1997. Backscattering behavior and simulation comparison over bare soils using SIR-C/X-SAR and ERASME 1994 data over Orgeval. Remote Sensing of Environment. doi:10.1016/S0034-4257(96)00158-7

Appendix: Papers

Available online at www.sciencedirect.com

ScienceDirect

ELSEVIER

Biosystems ENGINEERING

Research Paper

Modified Penman–Monteith equation for monitoring evapotranspiration of wheat crop: Relationship between the surface resistance and remotely sensed stress index

CrossMark

Abdelhakim Amazirh [a], Salah Er-Raki [a,*], Abdelghani Chehbouni [b], Vincent Rivalland [b], Alhousseine Diarra [c], Said Khabba [c], Jamal Ezzahar [d], Olivier Merlin [b,c]

[a] LP2M2E, Département de Physique Appliquée, Faculté des Sciences et Techniques, Université Cadi Ayyad, Marrakech, Morocco
[b] CESBIO, Université de Toulouse, CNES/CNRS/IRD/UPS, Toulouse, France
[c] LMME, Département de Physique, Faculté des Sciences Semlalia, Université Cadi Ayyad, Marrakech, Morocco
[d] MTI, ENSA, Ecole Nationale des Sciences Appliquées, Université Cadi Ayyad, Safi, Morocco

Evapotranspiration (ET) plays an essential role for detecting plant water status, estimating crop water needs and optimising irrigation management. Accurate estimates of ET at field scale are therefore critical. The present paper investigates a remote sensing and modelling coupled approach for monitoring actual ET of irrigated wheat crops in the semi-arid region of Tensift Al Haouz (Morocco). The ET modelling is based on a modified Penman–Monteith equation obtained by introducing a simple empirical relationship between surface resistance (r_c) and a stress index (SI). SI is estimated from Landsat-derived land surface temperature (LST) combined with the LST endmembers (in wet and dry conditions) simulated by a surface energy balance model driven by meteorological forcing and Landsat-derived fractional vegetation cover. The proposed model is first calibrated using eddy covariance measurements of ET during one growing season (2015–2016) over an experimental flood-irrigated wheat field located within the irrigated perimeter named R3. It is then validated during the same growing season over another drip-irrigated wheat field located in the same perimeter. Next, the proposed ET model is implemented over a 10×10 km^2 area in R3 using a time series of Landsat-7/8 reflectance and LST data. The comparison between modelled and measured ET fluxes indicates that the model works well. The Root Mean Square Error (RMSE) values over drip and flood sites were 13 and 12 W m^{-2}, respectively. The proposed approach has a great potential for detecting crop water stress and estimating crop water requirements over large areas along the agricultural season.

© 2017 IAgrE. Published by Elsevier Ltd. All rights reserved.

* *Corresponding author.* LP2M2E, Département de Physique Appliquée, Faculté des Sciences et Techniques (FSTG), Cadi Ayyad University, Av. Abdelkarim Elkhattabi. B.P 549, 40000 Marrakech, Morocco. Fax: +212 (0) 524 43 31 70.
E-mail address: s.erraki@uca.ma (S. Er-Raki).

Nomenclature		d	Calibration parameter equal to 3000, s m^{-1}

Symbol	Signification and unit
ET	Evapotranspiration, mm
ET$_0$	Evaporative demand, mm
r_c	Surface resistance, s m^{-1}
r^*	Critical bulk resistance, s m^{-1}
R_n	Net radiation, W m^{-2}
G	Soil heat flux, W m^{-2}
H$_{EC}$	Measured sensible heat flux by Eddy Covariance, W m^{-2}
LE$_{EC}$	Measured latent heat flux by Eddy Covariance, W m^{-2}
u_a	Wind speed, m s^{-1}
R_g	Solar radiation, W m^{-2}
rh$_a$	Relative humidity, %
T$_a$	Air temperature, °C
R^2	Determination coefficient
ρ_R	Red spectral reflectance, %
ρ_{PIR}	Near infrared spectral reflectance, %
ε	Surface emissivity
k	Attenuation coefficient
Δ	Slope of the saturation vapour pressure v. air temperature curve, kPa K^{-1}
γ	Psychrometric constant, kPa K^{-1}
ρ	Mean air density at constant pressure, kg m^{-3}
c_p	Specific heat of air, MJ kg^{-1} K^{-1}
D	Vapour pressure deficit, kPa
e_a	Actual vapour pressure, kPa
e_s	Saturation vapour pressure, kPa
r_{ah}	Aerodynamic resistance, s m^{-1}
z_r	Reference height, m
kar	Von Karman constant equal to 0.44
h_c	Canopy height, m
d	Displacement height, m
z_m	Height of the dynamic soil roughness, m
ψ_m	Atmospheric stability function
ψ_h	Sensitive heat stability function
a	Surface albedo
R_{atm}	Atmospheric longwave radiation, W m^{-2}
σ	Stephan–Boltzmann constant equal to 5.67×10^{-8}, W m^{-2} K^{-4}
ε_a	Atmospheric emissivity
Γ	Fractional empirical coefficient set to 0.4
Fc	Fraction vegetation cover
a	Empirical coefficient equal to 0.17
b	Empirical coefficient equal to 0.8
c	Empirical coefficient equal to 0.8
F (LST)	Cost function

e	Calibration parameter equal to −1130, s m^{-1}

Abbreviation	
LST	Land Surface Temperature, °C
SI	Stress Index
IPCC	Intergovernmental Panel on Climate Change
NDVI	Normalised Difference Vegetation Index
LAI	Leaf Area Index, m^2 m^{-2}
SiSPAT	Simple Soil Plant Atmosphere
ISBA	Interaction Soil–Biosphere–Atmosphere
SVAT	Soil Vegetation Atmosphere Transfer
ICARE	Interactive Canopy Radiation Exchange
CERES	Crop Environment REsource Synthesis
STICS	Simulateur multidisciplinaire pour les Cultures Standard
Aquacrop	Crop-water productivity model
SEBS	Surface energy balance model
FAO-56	Food and Agriculture Organization. No 56
PM	Penman–Monteith
SEBI	Surface Energy Balance Index
WDI	Water Deficit Index
TVI	Temperature Vegetation Index
TVDI	Temperature Vegetation Dryness Index
VTCI	Vegetation Temperature Condition Index
KH21	Krypton hygrometer
HPF01	Soil heat flux plates
CSAT3	3D sonic anemometer
EC	Eddy covariance
L7	Landsat 7
L8	Landsat 8
NASA	National Aeronautics and Space Administration
USGS	United States Geological Survey
MODTRAN	MODerate resolution atmospheric TRANsmission
RMSE	Root Mean Square Error
IPI	Irrigated Priority Index
SLC	Scan line corrector
H2020	Horizon 2020
RISE	Research and Innovation Staff Exchange
REC	Root zone soil moisture Estimates at the daily and agricultural parcel scales for Crop irrigation management – a multi-sensor remote sensing approach
AMETHYST	Assessment of changes in MEdiTerranean HYdro-resources in the South: river basin Trajectories

1. Introduction

In arid and semi-arid regions, water scarcity is one of the main factors limiting agricultural development. Water scarcity is likely to be exacerbated in the near future under the combined effect of the alteration of the hydrological cycle, climate change and increasing water demand for agriculture, urban and industry (IPCC, 2009).

In Morocco, irrigation is the biggest consumer sector of water, in average, it has been estimated that about 85% of

mobilised water resources is used by agriculture with an efficiency lower than 50% (Plan Bleu, 2009). The Tensift Al Haouz region, which is considered as a typical watershed of the Southern Mediterranean, is characterised by a semi-arid climate. Under these conditions, irrigation is inevitable for crop growth, development and yield. For that a good irrigation management requires an accurate quantification of crop water requirements which is assumed equivalent to evapotranspiration (ET) (Allen, Pereira, Howell, & Jensend, 2011).

During the last decades, several techniques have been proposed to estimate ET from local to global spatial scales. At the local scale, ET can be measured by using the sap flow sensors (Smith & Allen, 1996) that can provide the individual plant transpiration rate when the tree capacitance is neglected. Based on three different tree crop species, Motisi et al. (2012) verified that transpirational flow at orchard level is regulated by tree conductance, whereas capacitance effects are related to tree size or to environmental demand. ET can be also estimate at local scale by lysimetry (Daamen, Simmonds, Wallace, Laryea, & Sivakumar, 1993; Edwards, 1986). Passing from local to integrated spatial scales, the eddy covariance technique (Allen et al., 2011; Baldocchi, Hicks, & Meyers, 1988) is suitable for measuring ET at the field scale over an homogeneous fields (1 ha and above). The eddy covariance and sap flow techniques can be jointly use to partition the ET in plant transpiration and soil evaporation (Cammalleri, Anderson, Gao, Hain, & Kustas, 2013; Er-Raki, Chehbouni, Boulet, & Williams, 2010). Another technique, is the scintillometry that can provide the sensible and latent heat flux over a transect ranging from 250 m to 10 km even for heterogeneous fields (Ezzahar & Chehbouni, 2009; Kohsiek et al., 2002). At global scale, remote sensing data in the optical/thermal bands provide several ET-related variables such as the Normalised Difference Vegetation Index (NDVI), surface albedo, surface emissivity, LAI (Leaf Area Index) and Land Surface Temperature (LST) (Carlson & Buffum, 1989; Granger, 2000). Several Authors have proposed the use of these methodologies (Hatfield, 1983; Moran & Jackson, 1991; Kustas, 1996; Kalma, McVicar, & McCabe, 2008; Li et al., 2009; Allen et al., 2011; Er-Raki et al., 2013; Er-Raki, Rodriguez, Garatuza, Watts, & Chehbouni, 2013). All these techniques provide ET estimates at a specific temporal and spatial scales and rely on particular assumptions. Interpolation or extrapolation is thus often necessary to infer ET rates outside application scales, which can be a source of additional uncertainty. Moreover, most *in situ* techniques are expensive, time consuming and need a well-trained staff to operate and maintain it.

As an alternative to observational methods of ET, numerous modelling methods have been proposed such as Simple Soil Plant Atmosphere (SiSPAT) (Braud, Dantas-Antonino, Vaulcin, Throny, & Ruelle, 1995), Interaction Soil–Biosphere–Atmosphere (ISBA) (Noilhan & Mahfouf, 1996) and simple SVAT (Soil Vegetation Atmosphere Transfer) (Boulet et al., 2000), Interactive Canopy Radiation Exchange (ICARE) (Gentine, Entekhabi, Chehbouni, Boulet, & Duchemin, 2007). Others models like Crop Environment REsource Synthesis (CERES) (Ritchie, 1986), Simulateur multidisciplinaire pour les Cultures Standard (STICS) (Brisson, Mary, Ripoche, & Jeuffroy, 1998) and the crop-water productivity model (Aquacrop) (Raes, Steduto, Hsiao, & Fereres, 2009) have combined the water balance with the crop growth, development and yield components. These modelling methods, whether complex or simple, are generally not easy to implement in an operational context as they require several parameters (e.g. soil and vegetation hydrodynamic properties) and forcing variables (e.g. climate and irrigation) that are often unavailable at the desired space and time scale. As a matter of fact, simpler models based on a few input data have been developed (Merlin, 2013; Merlin et al., 2014). Among them, the surface energy balance model (SEBS) estimates the turbulent fluxes and surface evaporative fraction (Su, 2002) by using remote sensing data (albedo, NDVI, emissivity and LST) in conjunction with meteorological forcing (solar radiation, air temperature, wind speed, air humidity) and surface parameters (e.g. roughness and stability correction functions for momentum and sensible heat transfer). In contrast, the FAO-56 model requires limited input parameters and it has been extensively and successful used for estimating ET over several agricultural areas such as: wheat (Drerup, Brueck, & Scherer, 2017; Er-Raki et al., 2007, 2010; Jin et al., 2017), olive (Er-Raki et al., 2008, 2010; Rallo, Baiamonte, Manzano Juárez, & Provenzano, 2014), citrus (Er-Raki et al., 2009; Rallo, González-Altozano, Manzano-Juárez, & Provenzano, 2017), table grapes (Er-Raki et al., 2013; Er-Raki, Rodriguez, et al., 2013), sugar beet (Anderson et al., 2017; Diarra et al., 2017) and for different climate (Ayyoub, Khabba, Er-Raki, Merlin, & Bahlaoui, 2017; Ayyoub et al., 2017; Debnath, Adamala, & Raghuwanshi, 2015). It is based on the Penman–Monteith (PM) equation that has been formulated to include all the parameters that govern the energy exchange between vegetation and atmosphere. In the PM formulation, the extraction of water vapour from the surface is controlled by the surface resistance (r_c). However, the PM approach has been limited by the difficulties to estimate r_c as it depends on several factors related to pedological, biophysical and physiological processes, which are also related to agricultural practices (Katerji, Hamdy, Raad, & Mastrorilli, 1991; Testi, Villalobos, & Orgaz, 2004).

To overcome these difficulties, many authors have used the concept of "critical bulk resistance, r^*", where r^* is r_c when evapotranspiration is not affected by wind speed (Katerji & Perrier, 1983). The critical bulk resistance depends only on other local meteorological variables. Rana, Katerji, and de Lorenzi (2005), Ayyoub, Khabba, et al. (2017) and Ayyoub, Er-Raki, et al. (2017) showed that r_c is linearly related to r^*, allowing the ET estimates even in water shortage conditions. It has been demonstrated that the use of the critical resistance approach to estimate canopy resistance that varies with local meteorology provides more accurate ET estimates than assuming a constant value of resistance for a given canopy (Katerji & Rana, 2006). Alves and Pereira (2000) further investigated the surface resistance in the PM equation and suggested that the surface resistance integrates the combined effects of stomatal, soil surface and canopy resistances. They also showed that the surface resistance depends on meteorological variables as in Jarvis (1976). This approach has then been confirmed by Katerji and Perrier (1983) who showed that decoupling the surface resistance (function of critical resistance), from atmospheric resistance effects improves ET estimates, and this is consistent with the study of Alves and

Pereira (2000). All those methods estimate the surface resistance and ET at local scale but little attention has been paid on determining r_c at large scale from remote sensing data. Since the crop water stress is related to r_c through stomatal closure, one can estimate r_c from remotely sensed LST which can provide a good proxy for water stress level.

Several stress indexes have been developed such as the Surface Energy Balance Index (SEBI, Menenti and Choudhury, 1993), Water Deficit Index (WDI, Moran, Clarke Inoue, & Vidal, 1944; Moran, 2004, pp. 257–282), Temperature Vegetation Index (TVI, Prihodko & Goward, 1997), Temperature Vegetation Dryness Index (TVDI, Sandholt, Rasmussen, & Andersen, 2002) and Vegetation Temperature Condition Index (VTCI, Wang, Qi, Niu, & Wang, 2004; Wan, Wang, & Li, 2004). VTCI is defined as a ratio of the dry to actual LST difference to the dry to wet LST temperature difference, with wet/dry LST being estimated as the minimum/maximum LST that the surface can reach for a given meteorological forcing. Among existing thermal-based stress indexes, VTCI has two main advantages: 1) it is rather physically-based due to possibility of simulating wet/dry LST values using a surface energy balance model (Wang, Li, Gong, & Song, 2001) and 2) it can be applied to mixed pixels including soil and vegetation components. In this context, the objective of this study is to model ET based on the modified PM equation by introducing a simple established relationship between r_c and a thermal-based proxy of vegetation water stress, since it was considered as the most relevant parameter for drought monitoring (Jackson, Idso, & Reginato, 1981; Wan et al., 2004). The surface water stress index (SI) will be derived from the VTCI estimated either from in situ or Landsat thermal/reflectance remote sensing data. After, the approach is calibrated and tested in terms of ET estimates over both flood and drip irrigated sites.

2.   Materials and methods

2.1.   Site description

A field experiment was conducted over wheat crops in the Tensift region in central Morocco. This area has a semi-arid Mediterranean climate, characterised by low and irregular rainfall with an annual average of about 240 mm, against an evaporative demand (ET_0) of 1600 mm year^{-1}. The study site is located in the irrigated zone R3 in the Haouz plain, approximately 40 km southwest of Marrakech city (see Fig. 1). The experiment was carried out during the 2015–2016 growing season in two irrigated wheat fields: a 2 ha drip-irrigated field and a 4 ha flood-irrigated field. The surrounding of two fields is also cultivated with wheat and beans for the drip-irrigated one. The soil of both sites has low sand and high clay contents (47% clay, 35% silt, and 18% sand). The sowing dates were the 13th and 22nd December 2015 for the drip and flood irrigated sites, respectively.

2.2.   Ground data description

During the investigated agricultural season, both wheat sites were equipped with all sensors necessary for measuring different water and heat fluxes exchanged between soil, vegetation and atmosphere. The net radiation (R_n) was measured by the net radiometer (Kipp and Zonen CNR4, Campbell Sci). Soil heat flux (G) was controlled at a 5 cm depth using soil heat flux plates (HPF01, Campbell Sci). Radiometric brightness temperature was measured using an Infra-Red Thermometer (IRTS-P's, Apogee) and then converted to LST using surface emissivity. An eddy covariance system, consisting of a 3D sonic anemometer (CSAT3, Campbell Scientific Ltd.) and a Krypton hygrometer (KH21, Campbell Scientific Ltd.), was installed to provide continuous measurements of vertical sensible heat (H_{EC}) and latent heat (LE_{EC}) fluxes. Half-hourly measurements of classical meteorological data were collected over a grass cover using an automatic meteorological weather station: wind speed (u_a), incoming solar radiation (R_g), air relative humidity (rh_a) and air temperature (T_a) at a reference height (2 m).

Before using the data of latent heat flux (equivalent to ET) measured by the eddy covariance system, it is important to check the reliability and the quality of these measurements. This is undertaken through the analysis of the energy balance closure. By ignoring the term of canopy heat storage and the radiative energy used by vegetation photosynthesis (Testi et al., 2004), the energy balance closure is defined as:

$$R_n - G = H_{EC} + LE_{EC} \tag{1}$$

To check the budget closure during the study period, we compared the available energy at the surface ($R_n - G$) with the sum of turbulent fluxes ($H_{EC} + LE_{EC}$) at half-hourly scale. The quality of the correlation between ($R_n - G$) and ($H_{EC} + LE_{EC}$) was evaluated by the regression line and the determination coefficient R^2. Figure 2 shows the energy budget closure for sub-hourly data during 2015–2016 growing season for both study sites separately.

Results show that the closure of the energy balance is relatively well verified by comparison with other studies (Ezzahar, Chehbouni, Er-Raki, & Hanich, 2009; Testi et al., 2004). The regression lines are close to the 1:1 line and R^2 values are generally close to 1 (0.91 and 0.88 for the flood and drip irrigated fields, respectively). However, the slope of the regression forced through the origin was about 1.3 for both sites, indicating some underestimation of turbulent fluxes ($H_{EC} + LE_{EC}$) by about 30% of the available energy ($R_n - G$). This due to the attenuation of turbulence at low or high frequency signals (Ezzahar et al., 2009). Also, the difference between the sensors source area has a very important impact on the energy balance closure. In fact, the surface area of the sensors measuring the available energy (net radiation and soil heat flux) is very small compared to that of EC system, which can quickly change depending on wind speed and direction and surface conditions. Moreover, the energy absorbed by the plant has not been considered in the energy balance. In this context, Scott et al. (2003) evaluated the storage in the biomass to about 5–10% of the available energy, which could partially explain the overestimation of available energy at the surface.

2.3.   Remote sensing data

Landsat 7 (L7) and Landsat 8 (L8) satellites were launched by NASA on April 1999 and February 2013, respectively. The
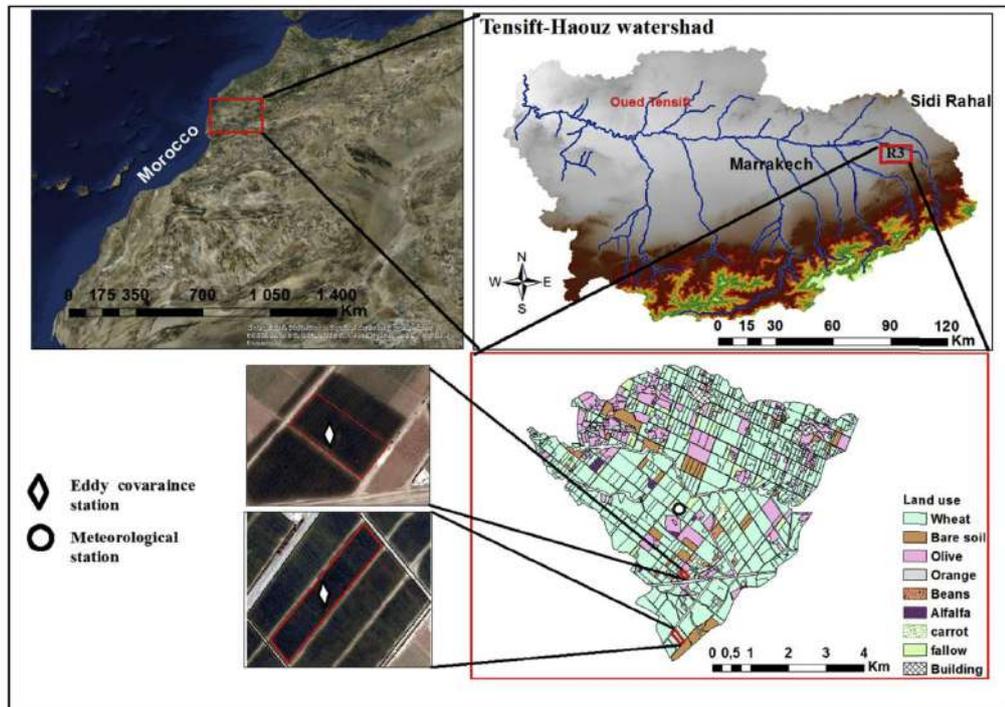
Fig. 1 – Study area and location of both experimental wheat fields (delimited with red rectangles) in the Tensift Al Haouz, Marrakech, Morocco. The meteorological station (black circle) and the towers equipped with eddy covariance systems (black diamond) are located. (For interpretation of the references to colour in this figure legend, the reader is referred to the web version of this article.)

combined use of both satellites potentially provides repetitive acquisitions every 8 days of high (30–100 m) resolution multispectral data of the Earth's surface on a global basis. The data (available for download from the USGS website, https:// earthexplorer.usgs.gov/) are resampled to 30 m resolution. A total of 14 images (6 and 8 images for L7 and L8, respectively) were used in this study. They were acquired from January 2016 until the end of the agricultural season (end of May).
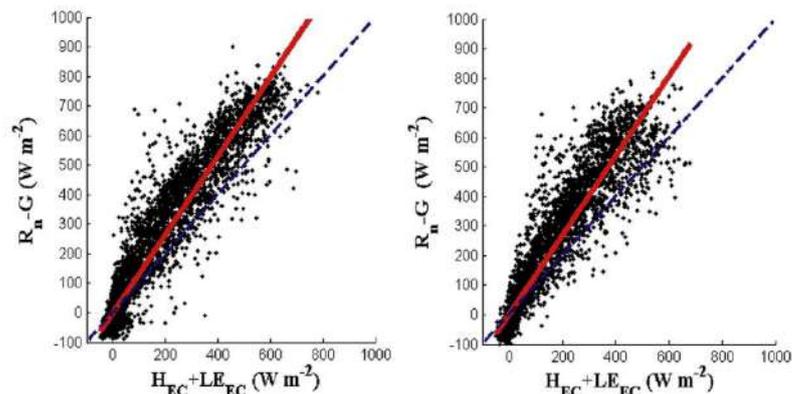
Fig. 2 – Comparison at half-hourly time scale between available energy ($R_n - G$) and the sum of the turbulent fluxes ($H_{EC} + LE_{EC}$) measured by eddy covariance at the flood (left) and drip (right) irrigated sites. Note that the regression line is forced to go through the graph origin with regression equation: $y = 1.3x$ (red solid line) with $R^2 = 0.91$ for flood site, and a regression equation: $y = 1.3x$ (red solid line) with $R^2 = 0.88$ for drip site. Line 1:1 (dotted blue line) was also presented. (For interpretation of the references to colour in this figure legend, the reader is referred to the web version of this article.)

Herein, Landsat data were used to estimate the NDVI, surface emissivity and LST over the R3 area overlaying both study sites. NDVI is calculated using the spectral reflectance measurements acquired in the visible ρ_R (red) and near-infrared regions ρ_{PIR}:

$$NDVI = \frac{\rho_{PIR} - \rho_R}{\rho_{PIR} + \rho_R}. \qquad (2)$$

The surface emissivity was estimated from an empirical relationship with NDVI and soil/vegetation emissivity components:

$$\varepsilon = \varepsilon_v - (\varepsilon_v - \varepsilon_s)\left(\frac{NDVI - NDVI_v}{NDVI_s - NDVI_v}\right)^k \qquad (3)$$

where ε_v is the vegetation emissivity (set to 0.99), ε_s is the soil emissivity (set to 0.96), $NDVI_v$ is NDVI for full vegetation (set to 0.99), $NDVI_s$ is the NDVI for bare soil (set to 0.15). k is an attenuation coefficient relevant to the relation between LAI–NDVI and NDVI–emissivity ranging from 2 to 3. In Olioso, Mira, Courault, Marloie, and Guillevic (2013) the value of k is derived from the shape of the NDVI-emissivity relationship for a range of soil moisture conditions and vegetation canopy emissivities. In our case, it was adjusted to 2 based on the NDVI-LAI relationship established in the same region by Er-Raki et al. (2007). Note that this value was used in Tardy et al. (2016) over the same (semi-arid) region.

LST was derived from the thermal infrared bands passing by different correction steps defined in Tardy et al. (2016). Those steps allowed to convert the Landsat digital number to the physical LST by inverting the Plank's low. An atmospheric correction of the thermal infrared bands data was firstly carried out using the MODTRAN atmospheric radiative transfer model software. For doing that, knowledge of the humidity and air temperature profile was needed. As second step, the at-sensor radiance was converted into surface radiance using the estimated surface emissivity. Then the LST was obtained by inverting the Plank's law. In order to evaluate the spaceborne LST, a comparison between the Landsat-derived against in situ LST measurements is presented in Fig. 3.

According to this figure, a relatively good match between satellite and ground LST data is obtained for the flood irrigated wheat parcel with a determination coefficient (R^2) of 0.92 and a RMSE equal to 0.91 °C, whereas an R^2 of 0.80 and an RMSE equal to 2.36 °C are found for the drip-irrigated field. The systematic over-estimation observed in the drip site could be attributable to the spatial extent of in situ and spaceborne observations. In fact, the drip-irrigated site is small (in comparison with the flood one), and does not fully cover the Landsat thermal pixel size (100 m resolution). Moreover, some differences between in situ and Landsat data could be explained by the limited spatial representativeness of 2-m high in situ thermal data. In addition, the better results in flood irrigated field than in drip irrigated field is due to: 1) The irrigation system: as it is known, flood irrigation implies a homogeneous fraction of wetted areas, where all the pixels have the same percentage of irrigation water, which means an uniform LST within the site. In contrast, just a part of the soil surface is wetted in the drip irrigated site, which may lead to some heterogeneity in observed LST from one pixel to another. 2) The flood irrigated site is bigger (4 ha) than the drip one (approximately 2 ha with a surface area of 4 ha (35 Landsat pixels) and 2 ha (10 Landsat pixels), respectively. Note that several 60/100 m Landsat LST pixels were partly covering the surrounding fields, causing representativeness issues especially for the smaller (drip) field. In addition 3) for the flood site, the surrounding fields are similar with the same irrigation system and crop (wheat). Contrariwise, the drip one, was surrounded by fields with different crops (beans).

The observed overestimation of LST by Landsat could also be due to an overestimation of the surface emissivity. As soil emissivity is difficult to estimate without specific measurements (unavailable in this experiment), it was fixed arbitrarily
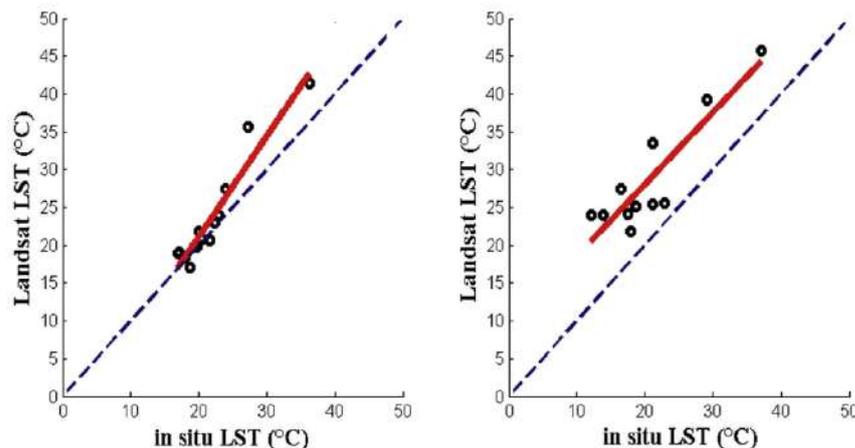
Fig. 3 – Land Surface Temperature (LST) acquired by Landsat versus *in situ* measurements for both sites: flood (left) and drip (right) wheat. The regression equations (red solid line) are: $y = 1.3x - 5.4$ with $R^2 = 0.92$ and RMSE = 0.91 °C, and $y = 0.95x + 9$, with $R^2 = 0.80$ and RMSE = 2.36 °C, for flood and drip wheat, respectively. Line 1:1 (dotted blue line) was also shown. (For interpretation of the references to colour in this figure legend, the reader is referred to the web version of this article.)

to 0.95. Moreover, we would like to underline that the field measurements of LST are representative of a small square of the surface only, which is much smaller than a Landsat pixel. Last each crop field can include a mixture of wet and dry Landsat pixels, although an average of all LST values was computed at the field scale.

2.4. Evapotranspiration monitoring approach

2.4.1. Evapotranspiration modelling
The latent heat flux (LE (W m^{-2})) of wheat was modelled by using the following PM equation:

$$LE = \frac{\Delta(R_n - G) + \rho c_p \frac{D}{r_{a,h}}}{\Delta + \gamma\left(1 + \frac{r_c}{r_{a,h}}\right)} \tag{4}$$

where Δ stands for the slope of the saturation vapour pressure curve at air temperature (kPa °C^{-1}). The psychrometric constant (kPa °C^{-1}) and the mean air density at constant pressure (kg m^{-3}) are presented by γ and ρ respectively while c_p stands for the specific heat of air (MJ kg^{-1} °C^{-1}). The vapour pressure deficit; D (kPa) is obtained by calculating the difference between the air vapour pressure; e_a (kPa) and the saturated water vapour pressure; e_s (kPa) where the latter is calculated as addressed in Equation (5).

$$e_s = 0.611 \times e^{\left(\frac{17.27 \times T_a}{T_a + 273.3}\right)} \tag{5}$$

In Equation (4), all parameters are deduced from the meteorological variables measured by the automatic meteorological station. However, the use of this model requires determining the aerodynamic resistance (r_{ah}, s m^{-1}) and bulk canopy resistance (r_c, s m^{-1}). r_{ah} is calculated at a reference height z_r in the boundary layer above the canopy by:

$$r_{ah} = \frac{\left(\log\left[(z_r - d)/zm\right] - \psi_m\right) \times \left(\log\left[(h_c - d)/zm\right] - \psi_h\right)}{kar^2 \times u_a} \tag{6}$$

where kar is the Von Karman constant equal to 0.44, h_c the canopy height, the displacement height (to adjust the effects of vegetation height on wind displacement) and the height of the dynamic soil roughness are presented as, $d = 2/3\ h_c$ and $z_m = h_c/8$ respectively. The ψ_m and ψ_h presents the atmospheric stability function and the sensitive heat stability function, respectively.

For irrigated crops, the canopy resistance r_c is not assumed to be constant. It changes according to available energy, vapour pressure deficit, and other environmental factors. In this study, we propose to use a simple empirical relationship between r_c and a vegetation water stress index (SI) which is calculated as:

$$SI = 1 - VTCI \tag{7}$$

where VTCI is calculated as follow:

$$VTCI = \frac{LST_{dry} - LST}{LST_{dry} - LST_{wet}} \tag{8}$$

where LST_{wet} and LST_{dry} are the LST simulated by an energy balance model in fully wet and dry surface conditions, respectively (Merlin et al., 2016; Stefan, Merlin, Er-Raki,

Escorihuela, & Khabba, 2015). We therefore distinguish between stressed and unstressed conditions via the VTCI. Especially, VTCI equals 1 (SI = 0) for LST = LST_{wet} (energy-limited evaporation), which means that vegetation is unstressed and the value of r_c is low. In the opposite case, VTCI equals 0 (SI = 1) for LST = LST_{dry} (soil-controlled evaporation), which means that vegetation is undergoing water stress and the value of r_c is large.

2.4.2. Energy balance model
The two extreme temperatures (LST_{wet} and LST_{dry}) of Equation (8) are simulated by running an energy balance model forced by $r_c \approx 0$ s m^{-1} and $r_c \approx \infty$, respectively. The surface net radiation is expressed as:

$$R_n = (1 - \alpha)\ R_g + \varepsilon(R_{atm} - \sigma\ LST^4) \tag{9}$$

with α (–) being the surface albedo (set to 0.20), R_{atm} stands for the atmospheric longwave radiation (W m^{-2}) and $\sigma = 5.67 \times 10^{-8}$ the Stephan–Boltzmann constant (W m^{-2} K^{-4}). The downward atmospheric radiation at surface level is expressed as:

$$R_{atm} = \varepsilon_a \times \sigma T_a^4 \tag{10}$$

where ε_a is the atmospheric emissivity estimated as in Brutsaert (1975):

$$\varepsilon_a = 1.24 \times \left(\frac{e_a}{T_a}\right)^{\frac{1}{7}} \tag{11}$$

with $e_a = e_s(T_a) \times (rh_a)/100$

The ground flux G is estimated as a fraction of net radiation at the soil surface $R_{n,s}$:

$$G = \Gamma \cdot R_{n,s} \tag{12}$$

with Γ being a fractional empirical coefficient set to 0.4, and $R_{n,s}$ is given by:

$$R_{n,s} = R_n \times (1 - Fc) \tag{13}$$

with Fc being the fraction vegetation cover calculated as:

$$Fc = \left(\frac{NDVI - NDVIs}{NDVI_V - NDVI_S}\right) \tag{14}$$

The sensible heat flux is given by:

$$H = \rho c_p \beta \frac{LST - T_a}{r_{a,h}} \tag{15}$$

where β is the "β function" calculated as follows as a function of LAI:

$$\beta = 1 - \frac{a}{LAI \cdot b \cdot \sqrt{2\pi}} e^{\frac{[\ln(LAI) - c]^2}{2 \cdot b^2}} \tag{16}$$

with a, b and c are empirical coefficients equal to 0.17 for a and 0.8 for b and c (Boulet, Olioso, Ceschia, Marloie, & Coudert, 2012). These values are calibrated for the wheat in the same study site.

The latent heat flux is estimated using the following equation:

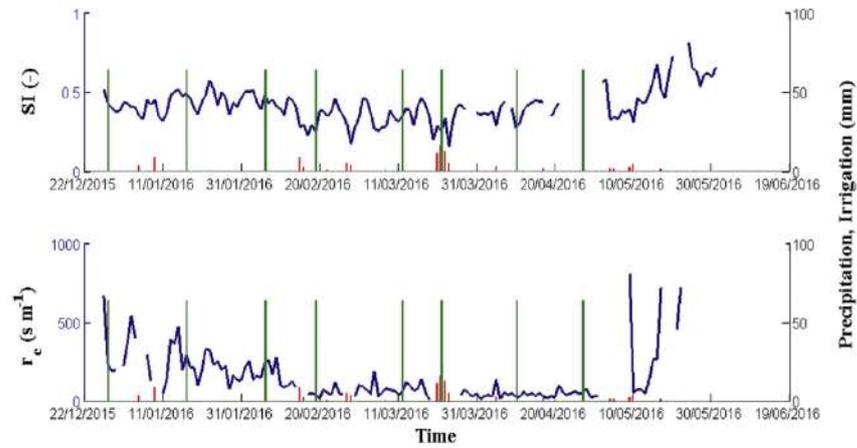$$LE = \frac{\rho c_p}{\gamma}\ \frac{e_s - e_a}{r_{a,h} + r_c} \tag{17}$$

Fig. 4 – Variations of SI (top figure) and r_c (bottom figure) under different water stress conditions for the flood wheat site. Rainfall (green vertical lines) and irrigation (red vertical lines) events are scaled on the secondary y-axis. (For interpretation of the references to colour in this figure legend, the reader is referred to the web version of this article.)

Finally, for running the energy balance model, it was set LST = Ta and search for the value of LST that minimises the following cost function F (LST):

$$F(LST) = (Rn - G - H - LE)^2 \qquad (18)$$

F (LST) is named "cost function" as it is the function to be minimised in order to find the LST value corresponding to the energy balance closure (e.g. Merlin et al., 2016).

3.   Results and discussions

The PM equation is used in this study to estimate the surface ET of wheat over two different crop fields in terms of irrigation systems loc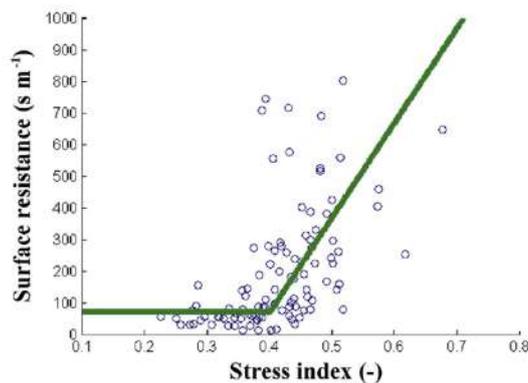ated in the R3 area. The proposed approach aims to modify the PM equation by expressing r_c, which is the main parameter controlling latent heat flux, as a function of a thermal-derived SI. The use of LST as an indicator of the surface resistance in order to estimate the ET, is assessed by using the in situ measurements collected in the flood-irrigated site. The "observed" r_c is estimated by inverting Equation (3) using ET measured by eddy covariance system. Then, a validation exercise is carried out over the drip irrigated-site using in situ data. Finally, an evaluation of the method is undertaken using Landsat data over both sites.

Fig. 5 – Relationship between the bulk surface resistance (r_c) and a stress index (SI) for the flood irrigated parcel. The best fit (green solid line) was presented. (For interpretation of the references to colour in this figure legend, the reader is referred to the web version of this article.)
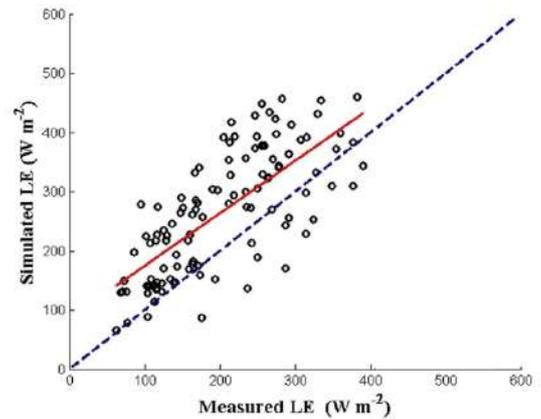
Fig. 6 – Comparison of the simulated and measured latent heat flux over the drip-irrigated site at Landsat overpass time (11:00 am). The red solid line represents the regression equation: y = 0.89x + 85, with R^2 = 0.53 and RMSE = 82.01 W m^{-2}. Line 1:1 (dotted blue line) was also shown. (For interpretation of the references to colour in this figure legend, the reader is referred to the web version of this article.)

Fig. 7 — Time series of fraction cover (Fc) and Land Surface Temperature (LST) maps over R3 area at dates corresponding to different growing stages obtained from Landsat satellite.

LST (wet conditions)

Fig. 8 – Time series of Land Surface Temperature (LST) maps in dry and wet conditions over R3 area on dates corresponding to different growing stages of wheat.
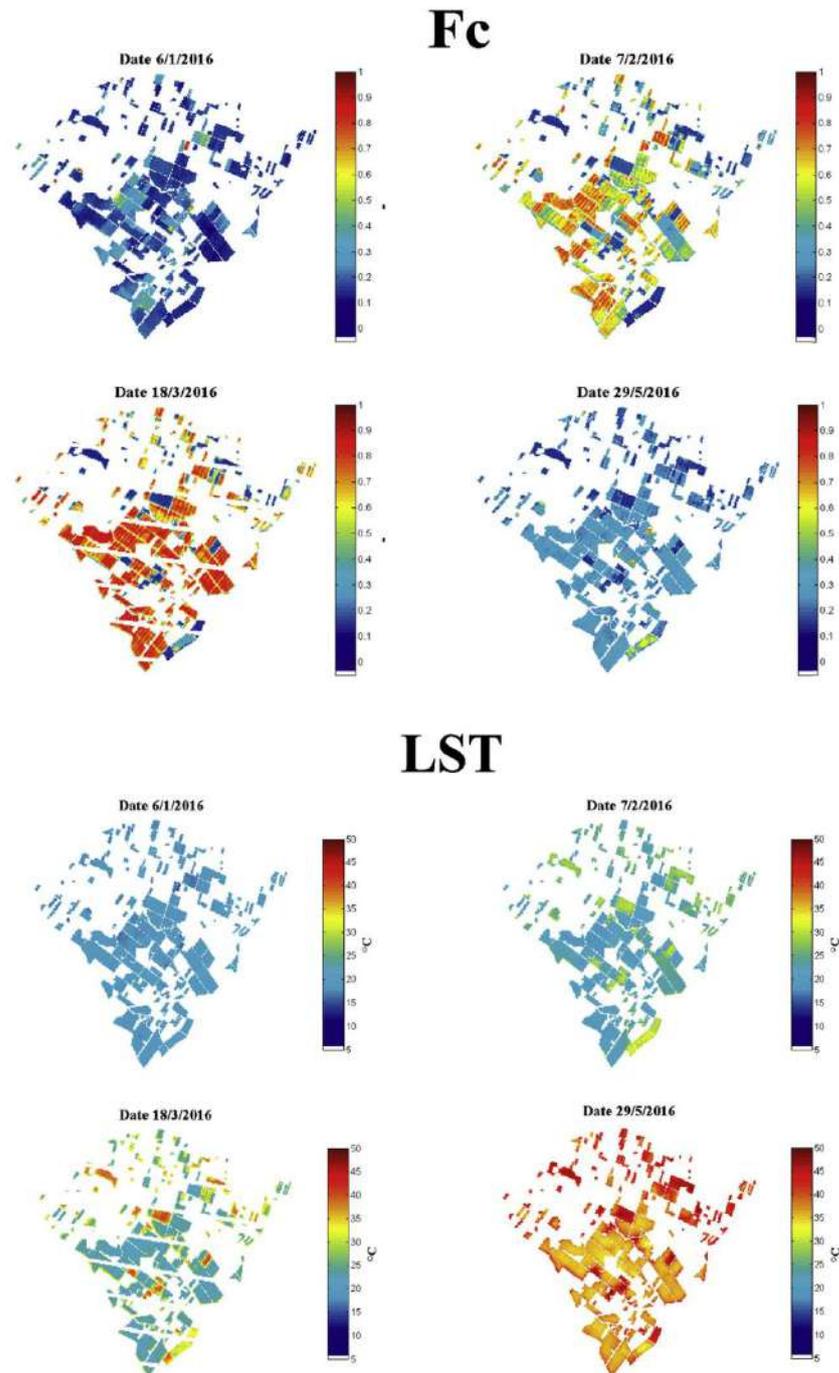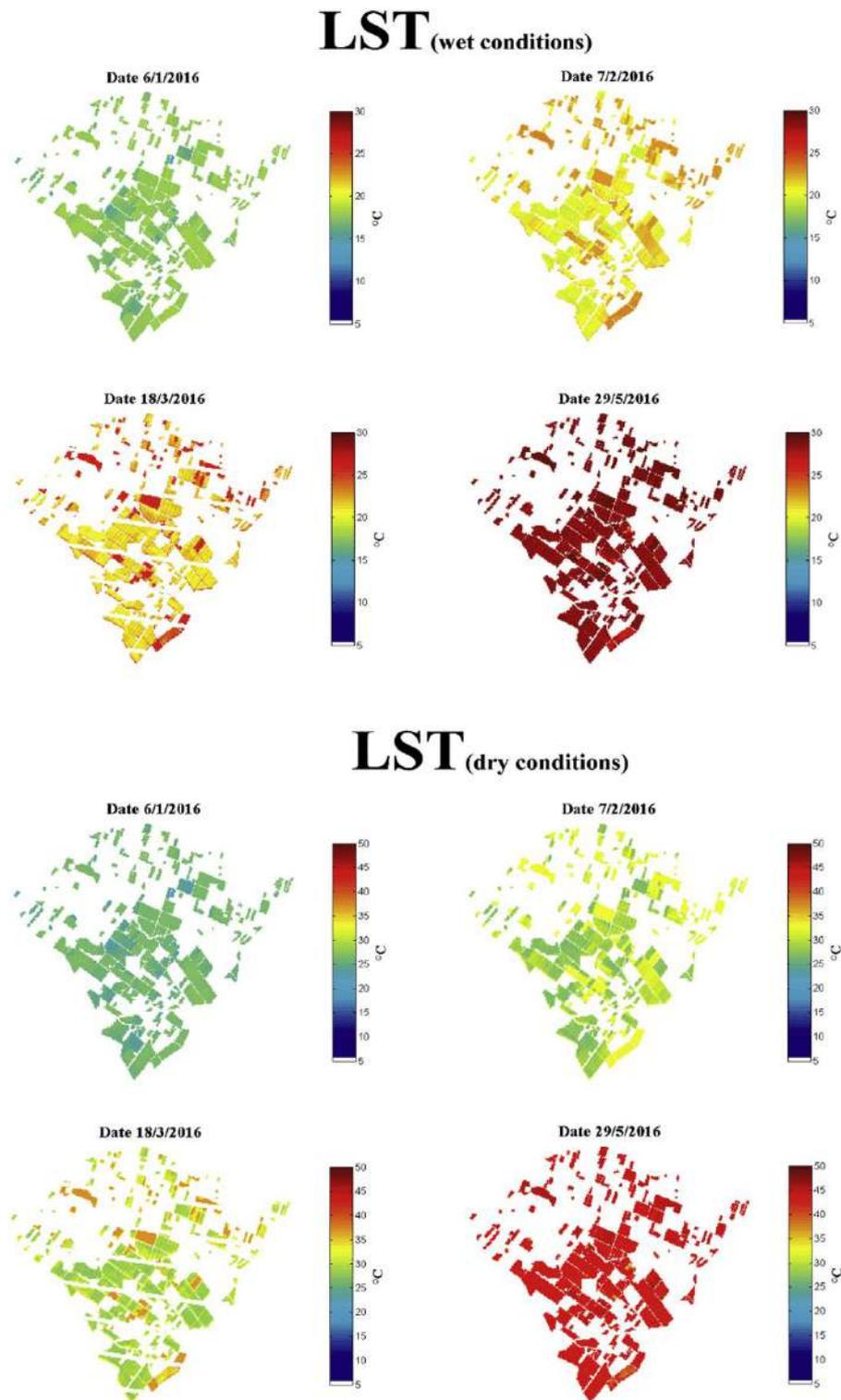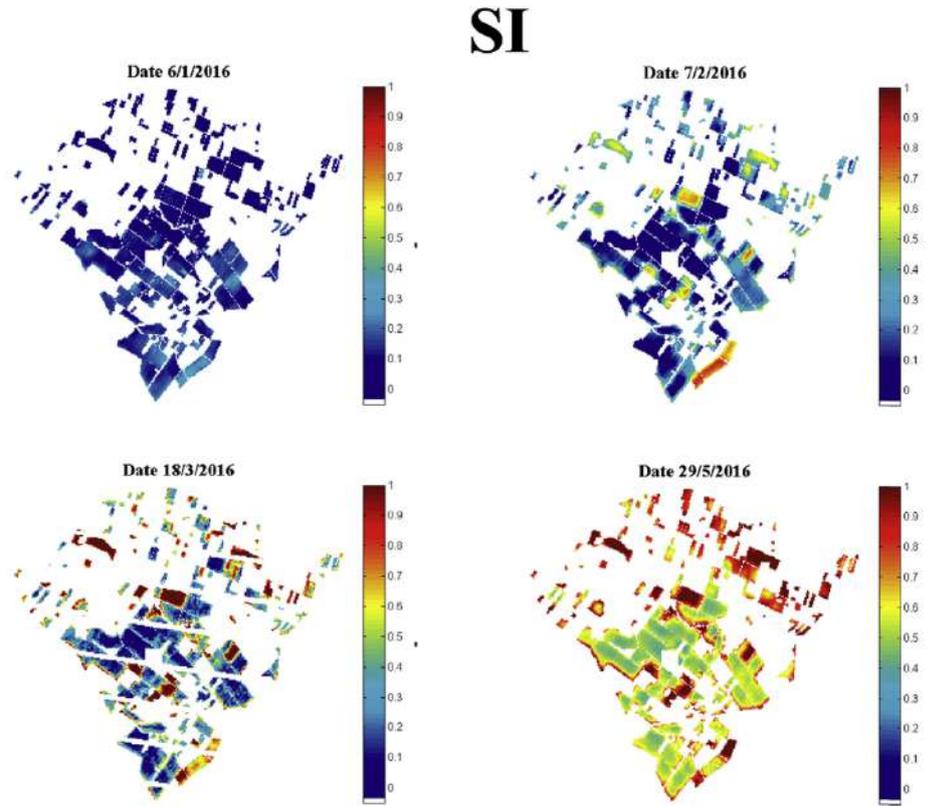
SI

Date 6/1/2016

Date 7/2/2016

Date 18/3/2016

Date 29/5/2016

Fig. 9 − Time series of stress index (SI) maps estimated using Landsat data over R3 area.

3.1. *In situ evaluation of the proposed approach*

The time series of retrieved SI and r_c over the flood site is shown in Fig. 4. According to this figure, daily patterns of SI and r_c are similar and respond perfectly to the water supply (rainfall or irrigation). On one hand, after water supply, the soil moisture in the root zone increases and the plant transpirates at potential rate with no limitation and the values of r_c and SI tend to decrease. On another hand, the absence of irrigation and rainfall (dry condition, e.g. from the end of April) results in an increase in the root zone depletion and generates stress (SI increased). The increase in soil water depletion is due to the removal of water by ET that induces water stress conditions and then the stomatal closure which increases r_c. Consequently, it can be concluded that both the variables follow similar trends. This leads to look if there is any relationship between both terms. For this purpose, r_c is plotted against SI (Fig. 5) by using *in situ* measurements (flood site). When SI ranges from 0 to 0.4 which corresponds to unstressed vegetation with low LST values, r_c values are scattered around a mean value of about 70 s m^{-1} which corresponds to the minimum bulk surface resistance (r_{cmin}).

The obtained value of r_{cmin} is in agreement with values obtained for wheat crop by Baldocchi (1994). When SI increases above a threshold value SI = 0.4, r_c increases linearly with SI. This confirms the results reported by Autovino,

Minacapilli, and Provenzano (2016) and Er-Raki et al. (2017) who found a similar shape for olive and orange orchards, respectively. The obtained relationship, which gives the best fit between both terms, is given by:

$$r_c = r_{cmin} = 70s \ m^{-1} \quad \text{for } SI < 0.4$$

$$r_c = d*SI + e \quad \text{for } SI \geq 0.4 \tag{19}$$

where d and e are the calibration parameters, which are equal to 3000 s m^{-1} and −1130 s m^{-1}, respectively. Note that the values of r_{cmin}, d and e are expected to depend on local meteorological data, crop and soil types.

The relationship of Equation (19) is validated by comparing the modelled and measured latent heat flux for the drip-irrigated wheat site at Landsat overpass time (Fig. 6). According to this figure, an acceptable correlation is obtained between simulated and measured LE using the proposed approach ($R^2 = 0.53$). The scatter of modelled LE estimates is probably due to the uncertainties associated to the relatively small footprint of the *in situ* thermal radiometer. Looking at the dynamics of actual LE and r_c values estimated by Equation (19) (not showed in the manuscript), the proposed methodology for bulk resistance estimation allows for capturing the variability of measured LE. The significant bias in simulated LE is probably due to the underestimation of *in situ* LST, involving
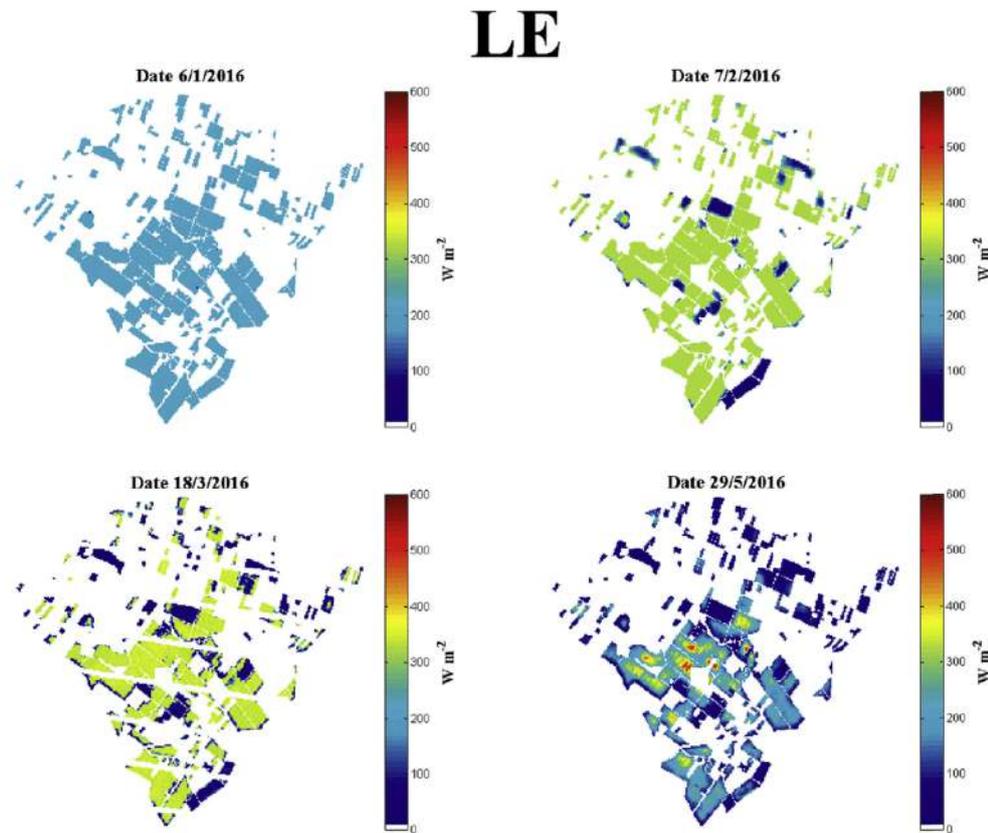
LE

Fig. 10 – Time series of latent heat flux (LE) maps estimated over R3 area.

an overestimation of simulated LE especially during the dry period (Ramoelo et al., 2014; Ruhoff at al., 2013). Those explanations were added to the revised version.

3.2. Spatial analysis

To overcome the spatial representativeness issue of *in situ* measurements and for further evaluating the proposed model, Landsat data are used as input of the modified PM model. ET estimates are spatialised within a 10×10 km^2 area centred over the R3 sector which is mainly covered by wheat crops. The R3 perimeter is occupied by different cultures (wheat, alfalfa, orange, and olive), so before spatializing the ET, a land use has been performed in order to distinguish between wheat and other crops. Figure 7 shows the spatial and temporal variations of Landsat-derived LST and Fc over wheat crops. As the entire growing season of wheat was divided into four growth stages namely: the initial, the development, the mid-season and the late season, we choose to present one image for each stage (Fig. 7). This figure shows that during the initial stage (06/01/2016), most of the fields were under bare soil conditions characterised by low Fc and high LST values depending spatially on the water supply and atmospheric conditions. In the development stage (07/02/

2016) an effective full cover is reached in some parcels while other ones are characterised by low Fc depending on the sowing date and the development of vegetation. This spatial variability of Fc has a direct effect on the variability of LST. When Fc reaches the maximum value at the mid-season (18/03/2016), spatial LST values are similar around 20 °C except for some pixels where the LST values are relatively higher (about 35 °C), which correspond to the non-cultivated parcels. At the last stage (29/05/2016), from the beginning of maturity until harvest or full senescence, wheat fields are characterised by low Fc and high LST values.

Our approach involves the energy balance model in order to assess the variation of LST in space and time for two extreme dry and wet conditions which depend on climatological conditions. Figure 8 shows the dry and wet LST maps for the selected four dates. These maps show that, in the coldest days in winter (06/01/2016), the LST$_{dry}$ oscillated between 15 and 30 °C and the LST$_{wet}$ ranged from 10 to 17 °C. In the other hand, for the hottest days in summer (29/05/2016), the LST$_{dry}$ reached its maximum (50 °C) as well as the LST$_{wet}$ that reached 30 °C.

The use of LST time series extracted from Landsat satellite and the dry and wet LST values computed using the energy balance model appears to be a good way to monitor water
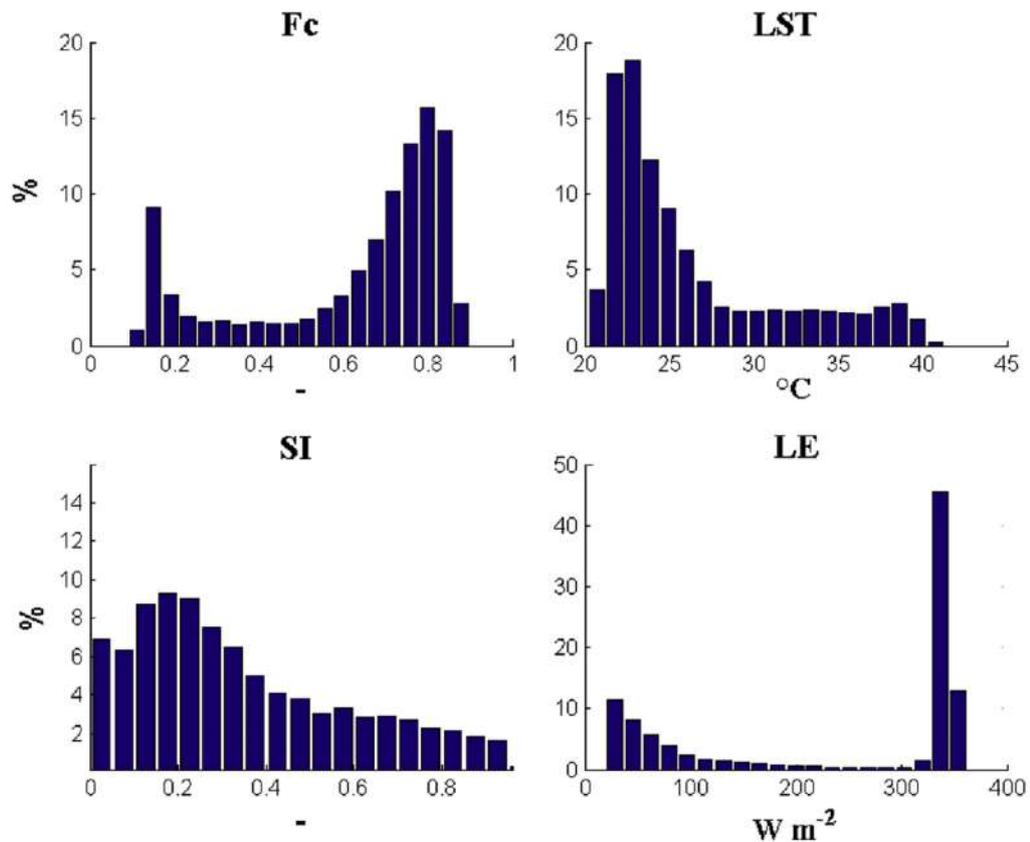
Fig. 11 – Frequency histograms of remote sensing parameters (LST, Fc), simulated latent heat flux (LE) and Stress index (SI) on March 18, 2016.

stress index for irrigation scheduling. Figure 9 presents the spatial distribution of SI over R3 perimeter at the different growth stages. The maps of this figure show that Landsat-derived SI consistently ranges between 0 and 1 all along the agricultural season, regardless of the vegetation cover fraction and LST values (see Fig. 7). In fact, the use of Fc and LST data as input variables of the energy balance model to estimates LST_{dry} and LST_{wet}, allows taking into account all the growing stages of wheat crop. In particular, we can distinguish between the small vegetation (tillering stage) and the full developed one (mid-season stage). In this regard Barbosa da Silva and Ramana Rao (2005) estimated SI of cotton crop using LST, r_c and R_n. However, they did not take into account the vegetation parameters and their variability during the agricultural season. These parameters affect the aerodynamic resistance and hence both the sensible and latent heat fluxes.

In Fig. 9, the pixels having a SI value close to 1 (red colour) are characterised by a high vegetation stress due to the mismatch between water supply and water requirement (late irrigation). The values of SI ranging between 0.3 and 0.6 are characterised by the onset of vegetation stress. This is due to the difficulty of the irrigation distribution at the right moment. Indeed, the water transported by gravity across the R3

channels may arrive to the fields before or after the optimal date (Belaqziz et al., 2013, 2014). Pixels with SI values around 0 correspond to un-stressed, meaning recently irrigated wheat. Following the evolution of SI, it appears that this index shows spatial and quantitative information about the method of irrigation distribution, and could be used to optimise the irrigation scheduling. Those results are consistent with the work of Belaqziz et al. (2013), who used another index named "Irrigated Priority Index (IPI)" in the same study area to manage the irrigation distribution. The IPI equation is mainly based on both the water stress level and irrigation dates of wheat crop. The main drawback of IPI is that it needs the amount of water supply as input, which is not the case of SI developed. This new index based on LST only might then be combined with IPI in order to detect and retrieve irrigation amount, information that is very difficult to obtain over large areas.

Figure 10 shows the spatial distribution of ET and its temporal variation across the season. We can observe a high variability of ET, which depends on the spatial heterogeneity of Fc, LST and SI over R3.

The spatial representation allowed to distinguish between the fields corresponding to stressed wheat (blue colour) where
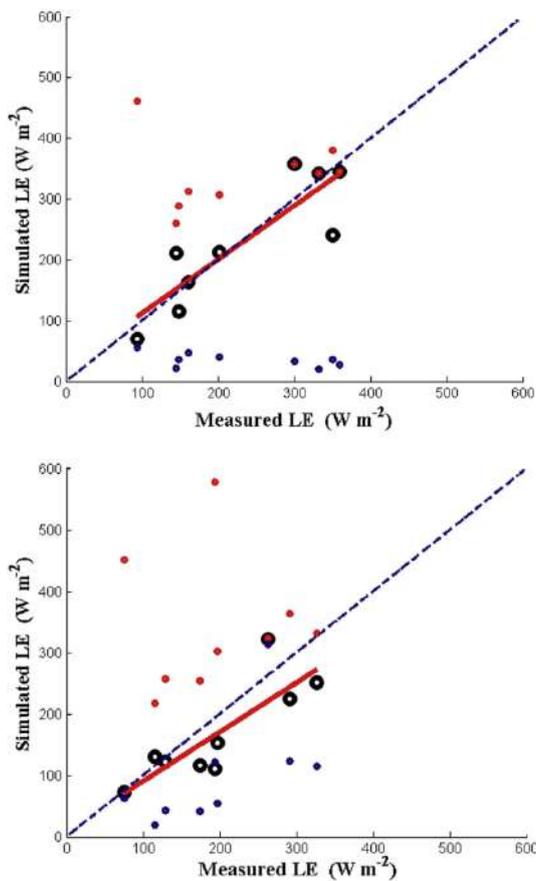
Fig. 12 – Comparison between the simulated and measured LE (W m^{-2}) over flood (top) and drip (bottom) sites in different conditions (Red: un-stressed condition "SI = 0"; Blue: stressed condition "SI = 1"; Black: real condition "SI as a function of LST"). The red solid line represents the regression equations: y = 0.88x + 23, with R^2 = 0.76 and RMSE = 11.77 W m^{-2} for flood site, and y = 0.80x + 9.3, with R^2 = 0.70 and RMSE = 13.39 W m^{-2} for drip site. The dotted blue line represents the Line 1:1. (For interpretation of the references to colour in this figure legend, the reader is referred to the web version of this article.)

LE is lower and the field corresponding to un-stressed fields (other colour) that have been relatively well irrigated during the wheat growing stages, for high ET values. The obtained spatial and temporal variations of ET are in accordance with the spatio-temporal variability of Fc, LST and SI (see Figs. 7 and 9). To observe this more easily, the frequency histograms for remote sensing data (Fc, LST), SI and ET on one date 18/03/2016 are plotted in Fig. 11. The choice of this date relies on the fact that the end of March summarises the history of wheat crop growth and its development from sowing date (Hadria., 2006, p. 174; Karrou, 2003). By analysing the different histograms, one can be concluded that the estimates LE are

coherent with other surface properties (Fc, LST, and SI). Fc values in the higher range (larger than 0.8) have a high frequency/percentage. They correspond to the fields with low LST values (lower than 25 °C), which are associated to small values of surface aerodynamic resistance (large crop height) rather than to large water availability for wheat. On this date, our model computes a large amount of un-stressed areas with relatively small SI and large LE values. Those results seem to be representative of the real situation.

The land surface parameters (LST, Fc, and emissivity) are obtained from Landsat data. Therefore all cloudy data (images) are discarded. In addition, the Landsat-7 images include data gaps due to scan line corrector (SLC) failure on May 31 2013, which on some dates unfortunately covered the irrigated sites. The selected data are used for validating the predicted ET (Equation (4)) against *in situ* ET for both flood and drip sites (Fig. 12). As it can be observed in this figure, the proposed approach allows to predict correctly the temporal dynamics of ET with an acceptable accuracy and a good correlation. The validations for the two sites resulted in R^2 of 0.76, 0.70 and a RMSE of 12, 13 W m^{-2} for flood-irrigated site and drip-irrigated site, respectively.

A further validation of the proposed approach was performed by comparing the measured ET with the ET simulated one under fully stressed (SI = 1, r$_c$ = 1870 s m^{-1}) and un-stressed (SI = 0, r$_c$ = 70 s m^{-1}) conditions. The obtained results are presented in the same Fig. 12 under real meteorological conditions. As expected, the model simulates very low values of ET for SI = 1 whereas it simulates high values of ET for SI = 0. On some dates, the ET simulations with SI = 0 (r$_c$ = 70 s m^{-1}) coincides with the ET estimated from Landsat-derived SI, which means that the fields were monitored in well-watered conditions (SI < 0.4). One key result is that the Landsat-derived SI (0 < SI < 1, 70 < r$_c$ < 1870 s m^{-1}) provides much more accurate ET estimates over both validation sites than when assuming fully stressed (SI = 1, r$_c$ = 1870 s m^{-1}) or fully unstressed (SI = 0, r$_c$ = 70 s m^{-1}) condition in the PM equation.

4.   Conclusion

The aim of this study was to use the PM equation to estimate the evapotranspiration (ET) over irrigated wheat crops of semi-arid areas. As the PM approach has been limited by the difficulties to estimate the bulk surface resistance (r$_c$) since it depends on several factors related to crop characteristics and agricultural practices, we proposed in this study to link r$_c$ to the stress index (SI) derived from remotely sensed LST and to implement the developed relationship in the PM model. SI was estimated as the observed LST normalised by the LST simulated in fully wet and dry conditions using a surface energy balance model forced by meteorological forcing and vegetation fraction.

The approach was tested over a 10 × 10 km^2 irrigated perimeter R3. The calibration/validation strategy implements two instrumented wheat sites with flood and drip irrigation and Landsat shortwave and thermal imagery during one growing season (2015–2016). The r$_c$ retrieved from eddy covariance measurements over the flood-irrigated site (by inverting PM equation) was first correlated to SI. This relation was then

tested over the drip-irrigated site using *in situ* measurements in order to simulate the surface ET. Next, this method was evaluated in terms of latent heat flux using Landsat temperature and reflectance data over both sites. The RMSE values over drip and flood sites are 13 and 12 W m^{-2}, which correspond to the relative errors of 5 and 4%, respectively.

The proposed relationship between r_c and SI employed in the PM model holds great potential for estimating crop ET using remote sensing data. Moreover, the results reached in terms of detecting crop water stress, can be helpful to distinguish between the irrigated and non-irrigated areas, which could give a prevision of the wheat yield based on the IPI developed by Belaqziz et al. (2013). Note however that the proposed methodology has been tested over two wheat parcels only. Further calibration studies should be undertaken to investigate and understand the variability of r_c parameters over different crop types and surface conditions.

Acknowledgement

REFERENCES

Allen, R. G., Pereira, L. S., Howell, T. A., & Jensend, M. E. (2011). Evapotranspiration information reporting: I. Factors governing measurement accuracy. *Agricultural Water Management, 98*, 899–920.

Alves, I., & Pereira, L. S. (2000). Modelling surface resistance from climatic variables? *Agricultural Water Management, 42*, 371–385.

Anderson, R. G., Alfieri, J. G., Tirado-Corbalá, R., Gartung, J., McKee, L. G., Prueger, J. H., et al. (2017). Assessing FAO-56 dual crop coefficients using eddy covariance flux partitioning. *Agricultural Water Management.* ISSN: 0378-3774, 179, 92–102. https://doi.org/10.1016/j.agwat.2016.07.027.

Autovino, D., Minacapilli, M., & Provenzano, G. (2016). Modelling bulk surface resistance by MODIS data and assessment of MOD16A2 evapotranspiration product in an irrigation district of Southern Italy. *Agricultural Water Management, 167*, 86–94.

Ayyoub, A., Khabba, S., Er-Raki, S., Merlin, O., & Bahlaoui, A. (2017b). Calibration and validation of the Penman-Monteith Model for estimating evapotranspiration of an orange orchard in semi-arid region. *Acta Horticulturae, 1150*, 15–22.

Ayyoub, A., Er-Raki, S., Khabba, S., Merlin, O., Ezzahar, J., Rodriguez, J. C., et al. (2017a). A simple and alternative approach based on reference evapotranspiration and leaf area index for estimating tree transpiration in semi-arid regions. *Agricultural Water Management.* ISSN: 0378-3774, 188, 61–68. https://doi.org/10.1016/j.agwat.2017.04.005.

Baldocchi, D. (1994). A comparative study of mass and energy exchange over a closed (wheat) and an open (corn) canopy: I. The partitioning of available energy into latent and sensible heat exchange. *Agricultural and Forest Meteorology, 67*, 191–220.

Baldocchi, D. D., Hicks, B. B., & Meyers, T. P. (1988). Measuring biosphere-atmosphere exchanges of biologically related gases with micrometeorological methods. *Ecology, 69*, 1331–1340.

Barbosa da Silva, B., & Ramana Rao, T. V. (2005). The CWSI variations of a cotton crop in a semi-arid region of Northeast Brazil. *Journal of Arid Environments, 62*, 649–659.

Belaqziz, S., Khabba, S., Er-Raki, S., Jarlan, L., Le Page, M. H., Kharrou, M., et al. (2013). A new irrigation priority index based on remote sensing data for assessing the networks irrigation scheduling. *Agricultural Water Management, 119*, 1–9.

Belaqziz, S., Mangiarotti, S., Le Page, M., Khabba, S., Er-Raki, S., Agouti, T., et al. (2014). Irrigation scheduling of a classical gravity network based on the covariance matrix adaptation – evolutionary strategy algorithm. *Computers and Electronics in Agriculture, 102*, 64–72.

Boulet, G., Chehbouni, A., Braud, I., Vauclin, M., Haverkamp, R., & Zammit, C. (2000). A simple water and energy balance model designed for specialization and remote sensing data utilization. *Agricultural and Forest Meteorology, 105*, 117–132.

Boulet, G., Olioso, A., Ceschia, E., Marloie, O., & Coudert, B. (2012). An empirical expression to relate aerodynamic and surface temperatures for use within single-source energy balance models. *Agricultural and Forest Meteorology, 161*, 148–155 (Elsevier Masson).

Braud, I., Dantas-Antonino, A. C., Vauclin, M., Throny, J. L., & Ruelle, P. (1995). A simple Soil_Plant-Atmosphere Transfert model (SiSPAT), development and field verification. *Journal of Hydrology, 166*, 231–260.

Brisson, N., Mary, B., Ripoche, D., & Jeuffroy, M. H. (1998). STICS: Ageneric model for the simulation of crops and their water and nitrogen balances. 1. Theory and parameterization applied to wheat and corn. *Agronomie, 18*, 311–346.

Brutsaert, W. (1975). On a derivable formula for long-wave radiation from clear skies. *Water Resources Research, 11*(5), 742–744.

Cammalleri, C., Anderson, M. C., Gao, F., Hain, C. R., & Kustas, W. P. (2013). A data fusion approach for mapping daily evapotranspiration at field scale. *Water Resources Research, 49*, 4672–4686. https://doi.org/10.1002/wrcr.20349.

Carlson, T. N., & Buffum, M. J. (1989). On estimating total daily evapotranspiration from remote sensing surface temperature measurements. *Remote Sensing of Environment, 29*(2), 197–207.

Daamen, C. C., Simmonds, L. P., Wallace, J. S., Laryea, K. B., & Sivakumar, M. V. K. (1993). Use of microlysimeters to measure evaporation from sandy soils. *Agricultural and Forest Meteorology, 65*, 159–173.

Debnath, S., Adamala, S., & Raghuwanshi, N. S. (2015). Sensitivity analysis of FAO-56 Penman-Monteith method for different agro-ecological regions of India. *Environmental Processes, 2*(4), 689–704.

Diarra, A., Jarlan, L., Er-Raki, S., Le Page, M., Aouade, G., Tavernier, A., et al. (2017). Performance of the two-source energy budget (TSEB) model for the monitoring of evapotranspiration over irrigated annual crops in North Africa. *Agricultural Water Management.* ISSN: 0378-3774, 193, 71–88. https://doi.org/10.1016/j.agwat.2017.08.007.

Drerup, P., Brueck, H., & Scherer, H. W. (2017). Evapotranspiration of winter wheat estimated with the FAO 56 approach and NDVI measurements in a temperate humid climate of NW Europe. *Agricultural Water Management.* ISSN: 0378-3774, 192, 180–188. https://doi.org/10.1016/j.agwat.2017.07.010.

Edwards, W. R. N. (1986). Precision weighing lysimetry for trees, using a simplified tared-balance design. *Tree Physiology, 1*, 127–144.

Er-Raki, S., Amazirh, A., Ayyoub, A., Khabba, S., Merlin, O., Ezzahar, J., et al. (2017). Integrating thermal surface

temperature into Penman-Monteith model for estimating crop water stress and evapotranspiration of an orange orchard in semi-arid region. *Acta Horticulturae Journal* (in press).

Er-Raki, S., Chehbouni, A., Boulet, G., & Williams, D. G. (2010). Using the dual approach of FAO-56 for partitioning ET into soil and plant components for olive orchards in a semi-arid region. *Agricultural Water Management, 97*, 1769–1778.

Er-Raki, S., Chehbouni, A., Guemouria, N., Duchemin, B., Ezzahar, J., & Hadria, R. (2007). Combining FAO-56 model and ground-based remote sensing to estimate water consumptions of wheat crops in a semi-arid region. *Agricultural Water Management, 87*, 41–54.

Er-Raki, S., Chehbouni, A., Guemouria, N., Ezzahar, J., Khabba, S., Boulet, G., et al. (2009). Citrus orchard evapotranspiration: Comparison between eddy covariance measurements and the FAO 56 approach estimates. *Plant Biosystems, 143*(1), 201–208.

Er-Raki, S., Chehbouni, A., Hoedjes, J., Ezzahar, J., Duchemin, B., & Jacob, F. (2008). Improvement of FAO-56 method for olive orchards through sequential assimilation of thermal infrared based estimates of ET. *Agricultural Water Management, 95*, 309–321.

Er-Raki, S., Ezzahar, J., Khabba, S., Jarlan, L., Kharrou, M. H., & Chehbouni, G. (2013). Micrometeorology tools for measuring evapotranspiration from the leaf to the region. In S. Er-Raki (Ed.), *Evapotranspiration: Processes, sources and environmental implications* (pp. 1–22). Nova Publishers, ISBN 978-1-62417-138-3.

Er-Raki, S., Rodriguez, J. C., Garatuza, J. P., Watts, C., & Chehbouni, G. (2013). Determination of crop evapotranspiration of table grapes in a semi-arid region of Northwest Mexico using multi-spectral vegetation index. *Agricultural Water Management, 122*, 12–19.

Ezzahar, J., & Chehbouni, A. (2009). The use of the scintillometry for validating the spatial and temporal aggregation schema over heterogeneous grid. *Agricultural and Forest Meteorology, 149*, 2098–2109.

Ezzahar, J., Chehbouni, A., Er-Raki, S., & Hanich, L. (2009). Combining a large aperture scintillometer and estimates of available energy to derive evapotranspiration over several agricultural fields in semi-arid regions. *Plant Biosystems, 143*, 209–221.

Gentine, P., Entekhabi, D., Chehbouni, A., Boulet, G., & Duchemin, B. (2007). Analysis of evaporative fraction diurnal behaviour. *Agricultural and Forest Meteorology, 143*(1–2), 13–29.

Granger, R. J. (2000). Satellite-derived estimates of evapotranspiration in the Gediz Bsin. *Journal of Hydrology, 229*, 70–76.

Hadria, R. (2006). *Adaptation et spatialisation du modèle de cultures STICS pour la gestion d'un périmètre céréalier irrigué en milieu semi-aride*. Thèse de doctorat. Marrakech, Maroc.: Faculté des Sciences Semlalia.

Hatfield, J. L. (1983). Evapotranspiration obtained from remote sensing methods. *Advances in Irrigation, 2*, 395–416.

IPCC. (2009). *Intergovernmental Panel on Climate Change (IPCC)*. http://www.ipcc.ch/.

Jackson, R. D., Idso, S. B., & Reginato, R. J. (1981). Canopy temperature as a crop water stress indicator. *Water Resources Research, 17*, 1133–1138.

Jarvis, P. G. (1976). The interpretation of the variations in leaf water potential and stomatal conductance found in canopies in the field. *Philosophical Transactions of the Royal Society, 273*, 593–610.

Jin, X., Yang, G., Xue, X., Xu, X., Li, Z., & Feng, H. (2017). Validation of two Huanjing-1A/B satellite-based FAO-56 models for estimating winter wheat crop evapotranspiration during mid-season. *Agricultural Water Management, 189*, 27–38.

Kalma, J. D., McVicar, T. R., & McCabe, M. F. (2008). Estimating land surface evaporation: A review of methods using remotely sensed surface temperature data. *Surveys in Geophysics, 29*, 421–469.

Karrou, M. (2003). *Conduite du blé au Maroc*. Rabat: INRA éditions.

Katerji, N., Hamdy, A., Raad, A., & Mastrorilli, M. (1991). Conséquence d'une contrainte hydrique appliquée à différents stades phénologiques sur le rendement des plantes de poivron. *Agronomie, 11*, 679–687.

Katerji, N., & Perrier, A. (1983). Modélisation de l'évapotranpsiration réelle ETR d'une parcelle de luzerne: Rôle d'un coefficient cultural. *Agronomie, 3*, 513–521.

Katerji, N., & Rana, G. (2006). Modelling evapotranspiration of six irrigated crops under Mediterranean climate conditions. *Agricultural and Forest Meteorology, 138*, 142–155.

Kohsiek, W., Meijninger, W. M. L., Moene, A. F., Heusinkveld, B. G., Hartogensis, O. K., Hillen, W. C. A. M., et al. (2002). An extra large aperture scintillometer for long range application. *Boundary Layer Meteorology, 105*, 119–127.

Kustas, W. P., & Norman, J. M. (1996). Use of remote sensing for evapotranspiration monitoring over land surfaces. *Hydrological Sciences Journal, 41*, 495–516.

Li, Z. L., Tang, R., Wan, Z., Bi, Y., Zhou, C., Tang, B., et al. (2009). A review of current methodologies for regional evapotranspiration estimation from remotely sensed data. *Sensors, 9*, 3801–3853.

Menenti, M., & Choudhury, B. J. (1993). Parameterization of land surface evaporation by means of location dependent potential evaporation and surface temperature range. In *Exchange processes at the land surface for a range of space and time scales*, Yokohama, Japan, IAHS.

Merlin, O. (2013). An original interpretation of the wet edge of the surface temperature–albedo space to estimate crop evapotranspiration (SEB–1S), and its validation over an irrigated area in northwestern Mexico. *Hydrology and Earth System Sciences, 17*, 3623–3637.

Merlin, O., Chirouze, J., Olioso, A., Jarlan, L., Chehbouni, A., & Boulet, G. (2014). An image–based four–source surface energy balance model to estimate crop evapotranspiration from solar reflectance/thermal emission data (SEB–4S). *Agricultural and Forest Meteorology, 184*, 188–203.

Merlin, O., Stefan, V. G., Amazirh, A., Chanzy, A., Ceschia, E., Er-Raki, S., et al. (2016). Modeling soil evaporation efficiency in a range of soil and atmospheric conditions using a meta-analysis approach. *Water Resources Research, 52*(5), 3663–3684.

Moran, M. S. (2004). Thermal infrared measurement as an indicator of ecosystem health. In *Thermal remote sensing in land surface processes*. CRC – Taylor & Francis. D. Quattrochi.

Moran, M. S., Clarke, T. R., Inoue, Y., & Vidal, A. (1994). Estimating crop water deficit using the relation between surface-air temperature and spectral vegetation index. *Remote Sensing of Environment, 49*(3), 246–263.

Moran, M. S., & Jackson, R. D. (1991). Assessing the spatial distribution of evapotranspiration using remotely sensed inputs. *Journal of Environmental Quality, 20*, 525–737.

Motisi, A., Consoli, S., Papa, R., Cammalleri, C., Rossi, F., Minacapilli, M., et al. (2012). Eddy covariance and sap flow measurement of energy and mass exchanges of woody crops in a Mediterranean environment. *Acta Horticulturae, 951*, 121–128.

Noilhan, J., & Mahfouf, J. F. (1996). The ISBA land surface parameterisation scheme. *Global and Planetary Change, 13*, 145–159.

Olioso, A., Mira, M., Courault, D., Marloie, O., & Guillevic, P. (2013). Impact of surface emissivity and atmospheric conditions on surface temperatures estimated from top of canopy brightness temperatures derived from Landsat 7 data. In *Proceedings of the 2013 IEEE International geoscience and remote sensing symposium, Melbourne, Australia* (pp. 3033–3036).

Plan Bleu. (2009). *Etat de L'environnement et du Développement en Méditerranée* (p. 208). Centre d'activités régionales PNUD/PAM.

Available http://www.planbleu.org/publications/. (Accessed 28 June 2012).

Prihodko, I., & Goward, S. N. (1997). Estimation of air temperature from remotely sensed surface observations. *Remote Sensing of Environment, 60*(3), 335–346.

Raes, D., Steduto, P., Hsiao, T. C., & Fereres, E. (2009). AquaCrop-the FAO crop modelto simulate yield response to water: II. Main algorithms and software description. *Agronomy Journal, 101*, 438–447.

Rallo, G., Baiamonte, G., Manzano Juárez, J., & Provenzano, G. (2014). Improvement of FAO-56 model to estimate transpiration fluxes of drought tolerant crops under soil water deficit: Application for olive groves. *Journal of Irrigation and Drainage Engineering, 140*(9). art. no. A4014001.

Rallo, G., González-Altozano, P., Manzano-Juárez, J., & Provenzano, G. (2017). Using field measurements and FAO-56 model to assess the eco-physiological response of citrus orchards under regulated deficit irrigation. *Agricultural Water Management, 180*, 136–147.

Ramoelo, A., Majozi, N., Mathieu, R., Jovanovic, N., Nickless, A., & Dzikiti, S. (2014). Validation of global evapotranspiration product (MOD16) using flux tower data in the African savanna, South Africa. *Remote Sensing, 6*(8), 7406–7423.

Rana, G., Katerji, N., & de Lorenzi, F. (2005). Measurement and modelling of evapotranspiration of irrigated citrus orchard under Mediterranean conditions. *Agricultural and Forest Meteorology, 128*, 199–209.

Ritchie, J. T. (1986). The CERES-Maize model. In C. A. Jones, & J. R. Kiniry (Eds.), *CERES-Maize: Simulation model of maize growth and development* (pp. 3–6). College Station, TX: Texas A M University press.

Ruhoff, A. L., Paz, A. R., Aragao, L. E. O. C., Mu, Q., Malhi, Y., Collischonn, W., et al. (2013). Assessment of the MODIS global evapotranspiration algorithm using eddy covariance measurements and hydrological modelling inthe Rio Grande basin. *Hydrological Sciences Journal, 58*, 1–19. https://doi.org/10.1080/02626667.2013.837578.

Sandholt, I., Rasmussen, K., & Andersen, J. (2002). A simple interpretation of the temperature/vegetation index space for assessment of surface moisture status. *Remote Sensing of Environment, 79*(2–3), 213–224.

Scott, R. W. C., Garatuza-Payan, J., Edwards, E., Goodrich, D. C., Williams, D. G., & Shuttleworth, W. J. (2003). The understory and overstory partitioning of energy and water fluxes in an open canopy, semi-arid woodland. *Agricultural and Forest Meteorology, 114*, 127–139.

Smith, D. M., & Allen, S. J. (1996). Measurement of sap flow in plant stems. *Journal of Experimental Botany, 47*, 1833–1844.

Stefan, V. G., Merlin, O., Er-Raki, S., Escorihuela, M. J., & Khabba, S. (2015). Consistency between in situ, model-derived and high-resolution-image-based soil temperature endmembers: Towards a robust data-based model for multi-resolution monitoring of crop evapotranspiration. *Remote Sensing, 7*(8), 10444–10479.

Su, Z. (2002). The surface energy balance (SEBS) for estimation of turbulent heat fluxes. *Hydrology and Earth System Sciences, 6*(1), 85–99.

Tardy, B., Rivalland, V., Huc, M., Olivier, H., Sebastien, M., & Gilles, B. (2016). A software tool for atmospheric correction and surface temperature estimation of Landsat infrared thermal data. *Remote Sensing*, 1–24.

Testi, L., Villalobos, F. J., & Orgaz, F. (2004). Evapotranspiration of a young irrigated olive orchard in southern Spain. *Agricultural and Forest Meteorology, 121*, 1–18.

Wan, Z., Wang, P., & Li, X. (2004). Using MODIS land surface temperature and normalised difference vegetation index products for monitoring drought in the southern great plains, USA. *International Journal of Remote Sensing, 25*(1), 61–72.

Wang, P.-X., Li, X.-W., Gong, J.-Y., & Song, C.-H. (2001). Vegetation temperature condition index and its application for drought monitoring. In *Proceedings of International geoscience and remote sensing symposium, 9–14 July 2001, Sydney, Australia* (pp. 141–143). Piscataway, NJ: IEEE.

Wang, C. Y., Qi, S. H., Niu, Z., & Wang, J. B. (2004). Evaluating soil moisture status in China using the temperature-vegetation dryness index (TVDI). *Canadian Journal of Remote Sensing, 30*(5), 671–679.
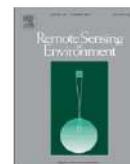
Review

Retrieving surface soil moisture at high spatio-temporal resolution from a synergy between Sentinel-1 radar and Landsat thermal data: A study case over bare soil

Abdelhakim Amazirh[a,b,*], Olivier Merlin[b,e], Salah Er-Raki[a], Qi Gao[c,b], Vincent Rivalland[b], Yoann Malbeteau[b,d], Said Khabba[e], Maria José Escorihuela[c]

[a] LP2M2E, Département de Physique Appliquée, Faculté des Sciences et Techniques, Université Cadi Ayyad, Marrakech, Morocco
[b] CESBIO, Université de Toulouse, CNES/CNRS/IRD/UPS, Toulouse, France
[c] isardSAT, Parc Tecnològic Barcelona Activa, Carrer de Marie Curie, 8, 08042 Barcelona, Spain
[d] Water Desalination and Reuse Center, King Abdullah University of Science and Technology, Thuwal, Saudi Arabia
[e] LMME, Département de Physique, Faculté des Sciences Semlalia, Université Cadi Ayyad, Marrakech, Morocco

ARTICLE INFO

ABSTRACT

Radar data have been used to retrieve and monitor the surface soil moisture (SM) changes in various conditions. However, the calibration of radar models whether empirically or physically-based, is still subject to large uncertainties especially at high-spatial resolution. To help calibrate radar-based retrieval approaches to supervising SM at high resolution, this paper presents an innovative synergistic method combining Sentinel-1 (S1) microwave and Landsat-7/8 (L7/8) thermal data. First, the S1 backscatter coefficient was normalized by its maximum and minimum values obtained during 2015–2016 agriculture season. Second, the normalized S1 backscatter coefficient was calibrated from reference points provided by a thermal-derived SM proxy named soil evaporative efficiency (SEE, defined as the ratio of actual to potential soil evaporation). SEE was estimated as the radiometric soil temperature normalized by its minimum and maximum values reached in a water-saturated and dry soil, respectively. We estimated both soil temperature endmembers by using a soil energy balance model forced by available meteorological forcing. The proposed approach was evaluated against *in situ* SM measurements collected over three bare soil fields in a semi-arid region in Morocco and we compared it against a classical approach based on radar data only. The two polarizations VV (vertical transmit and receive) and VH (vertical transmit and horizontal receive) of the S1 data available over the area are tested to analyse the sensitivity of radar signal to SM at high incidence angles (39°–43°). We found that the VV polarization was better correlated to SM than the VH polarization with a determination coefficient of 0.47 and 0.28, respectively. By combining S1 (VV) and L7/8 data, we reduced the root mean square difference between satellite and *in situ* SM to 0.03 $m^3 m^{-3}$, which is far smaller than 0.16 $m^3 m^{-3}$ when using S1 (VV) only.

1. Introduction

Soil moisture plays a very important role in many domains, such as agriculture, hydrology and meteorology. Consequently, the development of innovative techniques to monitor this variable from space becomes crucial. Remote sensing has demonstrated a strong potential for estimating the surface soil moisture (SM) in the first cm of soil (Bruckler et al., 1988; Du et al., 2000; Engman, 2000) while SM can be estimated using optical/thermal data (Gillies and Carlson, 1995; Sandholt et al.,

2002). Several studies have generally acknowledged that microwave techniques have a higher potential for retrieving SM on a regular basis, either from active (Dubois and Engman, 1995; Ulaby et al., 1978, 1979; Zribi et al., 2005; Zribi and Dechambre, 2003) or passive (Kerr et al., 2010; Entekhabi et al., 2010) sensors.

Microwave methods are based on the large difference existing in the dielectric constant between a dry soil (around 4) and that of water, which is around of 80 at microwave frequencies (Ulaby et al., 1986). Radiative transfer models have hence been developed based on the SM-

dielectric constant relationship (Dobson et al., 1985).

In the recent past, the use of imaging radar to estimate SM has become a subject of strong interest, notably due to i) the high-spatial resolution achievable by synthetic aperture radars (SAR) and ii) the advent of SAR data available at high-temporal resolution. Especially, the Sentinel-1 (S1) constellation (composed of two satellites S1-A and S1-B) potentially provides SAR data at 20 m resolution every 3 days (Torres et al., 2012). Thus, numerous studies have investigated and exploited the sensitivity of the radar signal to SM (Baghdadi et al., 2002a; Baghdadi and Zribi, 2006; Fung, 1994; Holah et al., 2005; Oh et al., 1992; Srivastava et al., 2003; Ulaby et al., 1986; Van Oevelen and Hoekman, 1999; Vereecken et al., 2008; Zribi et al., 2005). Retrieval approaches can be categorized into i) purely empirical modelling approaches (Baghdadi et al., 2002a; Holah et al., 2005; Mathieu et al., 2003; Wickel et al., 2001; Baghdadi et al., 2016) without any physical basis, which makes them valid for the studied area solely, and ii) semi-empirical approaches (Attema and Ulaby, 1978; Dubois and Engman, 1995; Oh, 2004; Oh et al., 1992; Shi et al., 1997), which usually combine empirical (data fits) and theoretical (physically-based) models like integral equation model (IEM) (Fung et al., 1992). In general, each model has a certain validity range in terms of observation incidence angle, soil parameters and vegetation cover (Fung et al., 1992; Karam et al., 1992).

Models, previously mentioned, do not reach the expected accuracy in SM retrievals (Alexakis et al., 2017; Bai et al., 2017; Fieuzal et al., 2011; Gao et al., 2017; Rakotoarivony et al., 1996; Remond et al., 1999; Zribi et al., 1997). This is owing to the various radar (incidence angle, frequency and polarization) and surface (soil moisture and roughness) parameters that affect the behaviour of the backscattered signal. The surface roughness is one of the most important factors that impact on the SM estimation, and probably the most difficult to measure periodically when monitoring

thermal-derived SM proxies. McVicar et al. (1992) developed the normalized difference temperature index (NDTI) using the upper and lower boundary conditions for LST, which were simulated by an energy balance model forced by atmospheric forcing data. The spatio-temporal variations in NDTI and SM ground measurements were found to be consistent. Other indexes have been proposed which help to estimate SM using the trapezoid method (Zhang and Zhou, 2016), such as the crop water stress index (CWSI, Jackson and Pinter, 1981), water deficit index (WDI, Moran et al., 1994) and temperature–vegetation dryness index (TVDI, Sandholt et al., 2002). Zhang et al. (2014) recently argued that TDVI is an ideal proxy to retrieve SM. Such thermal-derived SM proxies have also been extensively used to downscale global scale microwave-derived SM products (Molero et al., 2016; Peng et al., 2017). In addition, recent works about the synergy between microwave and optical data, have demonstrated the potential to retrieve surface SM including the effect of vegetation (Gao et al., 2017; Mattar et al., 2012; Santamaria-Artigas et al., 2016). However, both radar- and thermal-based SM retrieval approaches have inherent limitations. While, the radar backscatter is highly sensitive to surface roughness effects and to the structure of vegetation canopy, thermal data are unavailable under cloudy conditions and may be weakly linked to SM when the incoming energy is limiting (*e.g.* during the night and when the evaporative demand is low) or over densely vegetated surfaces. Hence the idea to combine radar- and thermal-based approaches is to benefit from the advantages of i) all-weather and day/night capabilities of microwave sensors, and ii) the physical basis of the LST-SM relationship that occurs *via* the surface energy budget under relatively large evaporative demand conditions.

In this context, the overall objective of the present paper is to develop a new methodology to retrieve SM from Sentinel-1 (S1) C-band microwave (MW) and Landsat-7/8 (L7/8) thermal data, by taking ad-

Y=1 X + 1.7
R²=0.98
RMSE=3.32 °C
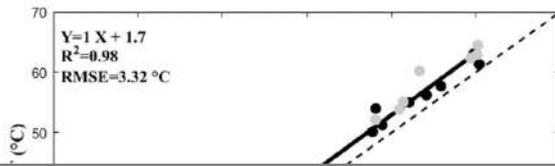
speckle effects to reduce random uncertainties related to the coherence interference of the waves reflected from the many elementary scatters. Images were filtered using the 5 × 5 refined Lee speckle filter described in Lee et al. (1994) and Lee (1999).

The mean backscatter radiation (linear units) is calculated from previously calibrated S1 images, and converted to decibel (dB) using

Table 2
Dates with quasi concurrent L7/8/S1 overpasses used in the analysis for both study sites.

Date (mm/dd–dd/yyyy)	S1 overpass Time (UTC)	Study site	Thermal sensor	S1 orbit	R3 SM sampling
01/06–07/2016	06:30 am	Sidi Rahal	L8	Ascending	No[a]
01/14–15/2016	06:30 pm	Sidi Rahal/R3	L7	Descending	Yes
01/30–31/2016	06:30 am	Sidi Rahal/R3	L7	Ascending	Yes
02/07–08/2016	06:30 pm	Sidi Rahal/R3	L8	Descending	Yes
02/23–24/2016	06:30 am	–	L8	Ascending	No[a]
03/02–03/2016	06:30 pm	Sidi Rahal/R3	L7	Descending	Yes
03/18–19/2016	06:30 am	R3	L7	Ascending	Yes
03/26–27/2016	06:30 pm	R3	L8	Descending	Yes
04/11–12/2016	06:30 am	–	L8	Ascending	No[a]
04/19–20/2016	06:30 pm	Gap fil[b]	L7	Descending	Yes
05/05–06/2016	06:30 am	R3	L7	Ascending	Yes
05/13–14/2016	06:30 pm	–	L8	Descending	No[a]
05/29–30/2016	06:30 am	Sidi Rahal	L8	Ascending	–
06/06–07/2016	06:30 pm	Sidi Rahal	L7	Descending	–
06/22–23/2016	06:30 am	Sidi Rahal	L7	Ascending	–
06/30–07/01/2016	06:30 pm	Sidi Rahal	L8	Descending	–
07/16–17/2016	06:30 am	Sidi Rahal	L8	Ascending	–
07/24–25/2016	06:30 pm	Sidi Rahal	L7	Descending	–
08/09–10/2016	06:30 am	Sidi Rahal	L7	Ascending	–
08/17–18/2016	06:30 pm	Sidi Rahal	L8	Descending	–
09/02–03/2016	06:30 am	–	L8	Ascending	–
09/10–11/2016	06:30 pm	Sidi Rahal	L7	Descending	–
09/26–27/2016	06:30 am	–	L7	Ascending	–
10/04–05/2016	06:30 pm	Sidi Rahal	L8	Descending	–

[a] Cloudy day.
[b] The Landsat-7 images include data gaps due to scan line corrector failure on May 31, 2013, which on this date unfortunately covered our sites.
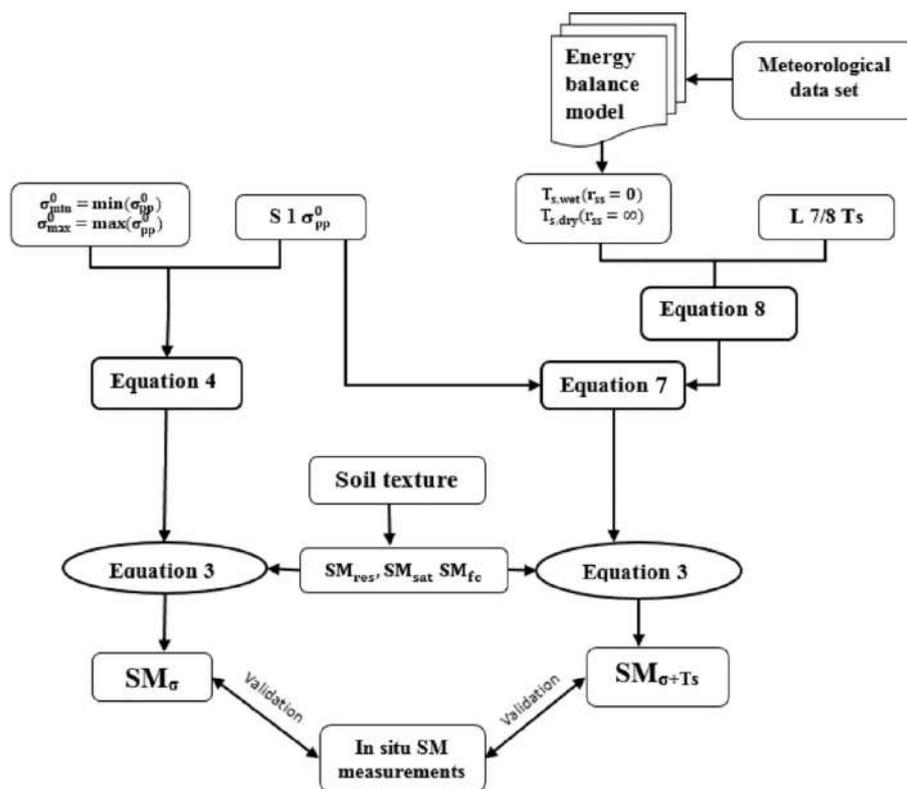
Fig. 3. Flowchart for the benchmark (radar only, on the left) and new (combined thermal and radar, on the right) SM retrieval approaches.

Page | 181
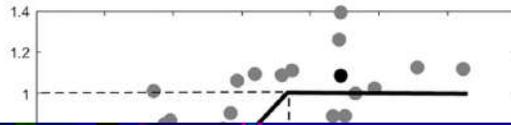
situ Apogee or satellite L7/8 thermal data. Both temperature end-members were simulated by running a soil energy balance (EB) model forced by meteorological data and with a prescribed soil resistance to evaporation r_{ss} (Merlin et al., 2016; Stefan et al., 2015). In addition, a sensitivity analyses was performed using the
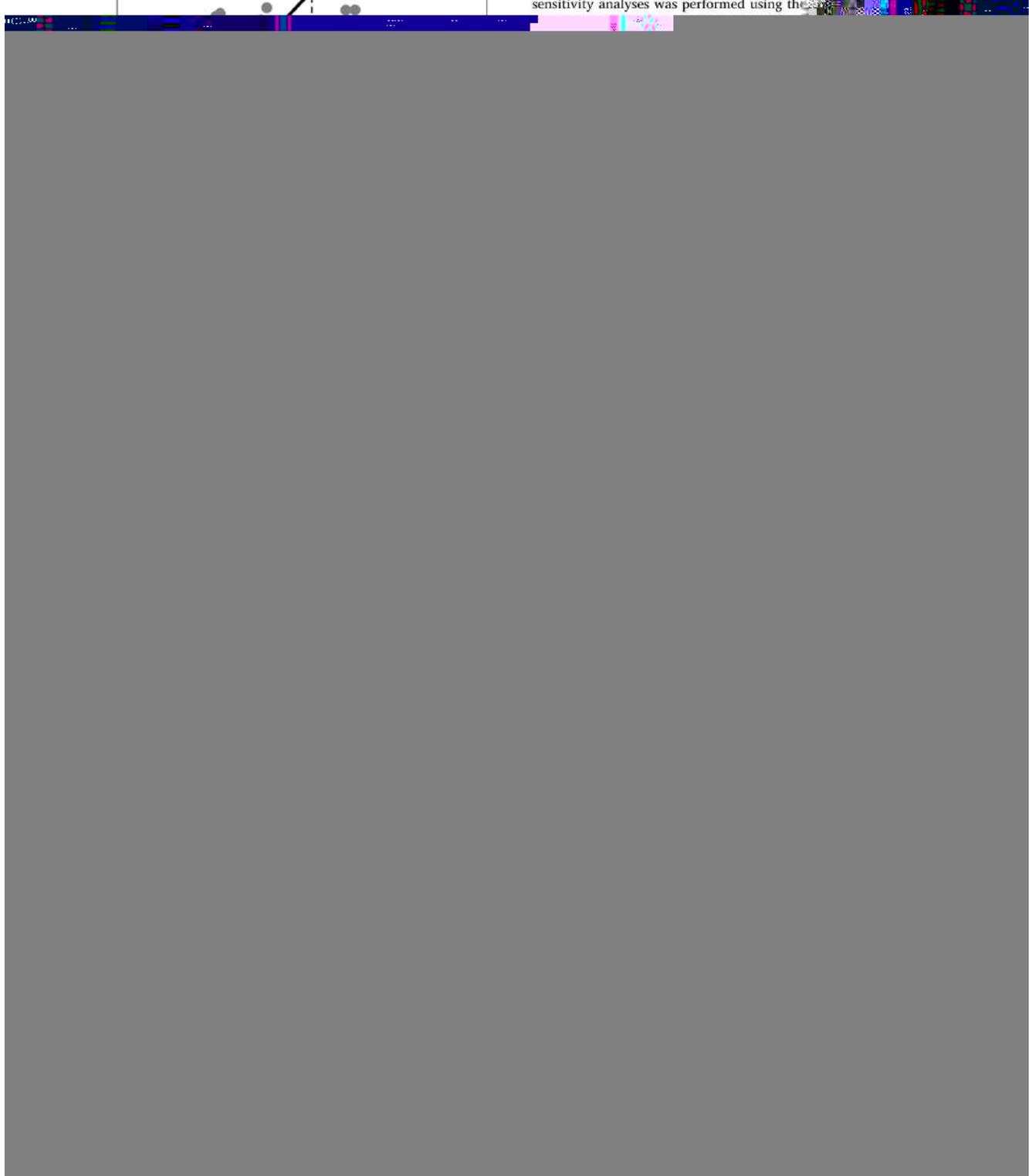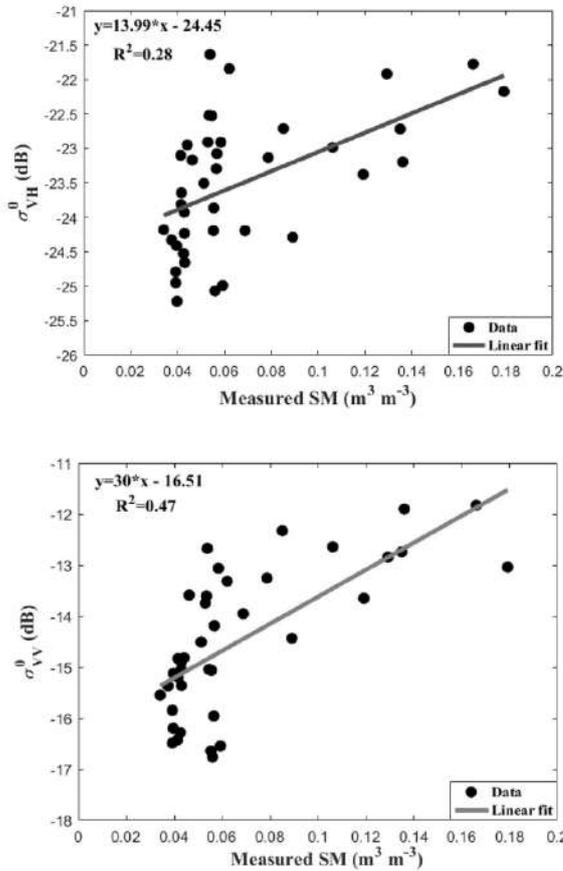
Fig. 5. Radar signal sensitivity to SM for VH (top) and VV (bottom) polarization over the Sidi Rahal site.

correlated with SM, whereas the VH polarization is poorly correlated ($R^2 = 0.47$ and 0.28, respectively). Previous studies have shown the same results (Eweys et al., 2017; Gherboudj et al., 2011), and our findings were consistent with the work of Baghdadi et al. (2006), where they use a large database over ten years to study the sensitivity of the radar signal to SM over bare soils. VH polarization was found to be sensitive to roughness and to the vegetation volume, due to the depolarization effect by vegetation-volume-scattering, which mainly de-

collected along multi-incidence angles requires a simultaneous availability of SAR data at lower and higher incidence angles (Srivastava, 2007). To overcome the (mostly general) unavailability of data at multi-incidence angles, several studies (Srivastava et al., 2008; Ulaby et al., 1986) have used multi-polarized SAR data. Both retrieval methodologies require ground truth measurements of soil moisture and/or surface roughness for calibration. Contrariwise, the methodology developed in this paper relies on satellite data available world-wide, and does not require ground measurements for calibration. Future studies could make use of both thermal and multi-polarized radar data as additional constraints on the roughness effects on radar-based SM retrievals.

The observation configuration has also an influence on the sensitivity of radar signal to SM, and hence on our capability to retrieve SM from radar data. Several studies showed that the low to medium incidence angles (20°–37°) are the most suitable for SM retrieval using C-band data (Holah et al., 2005; Le Hégarat-Mascle et al., 2002; Quesney et al., 2000; Srivastava et al., 2003; Zribi et al., 2008). Baghdadi et al. (2008) and Holah et al. (2005) found that the radar sensitivity decreases with increasing incidence angle. Moreover, the azimuthal angle changes with the ascending or descending passes. However, in our case, the study site is flat and the incidence angle is relatively constant (40°) so we observed no significant difference in terms of SM sensitivity between the data collected on ascending and descending overpasses. Hence, the sensitivity of radar data to the azimuthal angle seemed to be negligible in this study.

As a best option among the two different available polarizations to retrieve top SM, the VV polarization is used throughout the rest of the manuscript.

4.2. Relationship between thermal-derived SMP_{Ts} and radar signal

Fig. 6 plots SMP_{Ts} against S1 σ_{vv}^{0} for the L7/8 thermal data over the Sidi Rahal and the R3 study site, separately. For the full range of SMP_{Ts} [0–1], we observed a nonlinear behaviour between the Landsat-SMP_{Ts} and the σ_{vv}^{0}. So as an attempt to approach linearly SMP_{Ts} (σ_{vv}^{0}) and in order to define the calibration coefficient of the piecewise linear model defined in Eq. (7), the SMP_{Ts} full range is split into 2 distinct classes separated by the mid-value (0.5). The SMP_{Ts} and σ_{vv}^{0} values falling into each class (< and > to 0.5) provide a centroid point per class. The crossing over between the linear segment passing through the two centroid points and the line SMP = 0 and SMP = 1 allows to define the calibration parameters over each study site separately. From a physical point of view, the 0.5 was taking as a mid-value at which the evaporation process switches from mostly moisture-limited to mostly energy-limited conditions (Merlin et al., 2016). Results of the calibration using Landsat data lead to values of 0.25 dB^{-1} and 3.89 (unitless) for a and b over Sidi Rahal site and (0.26 dB^{-1} and 4.16 for R3 sites), re-
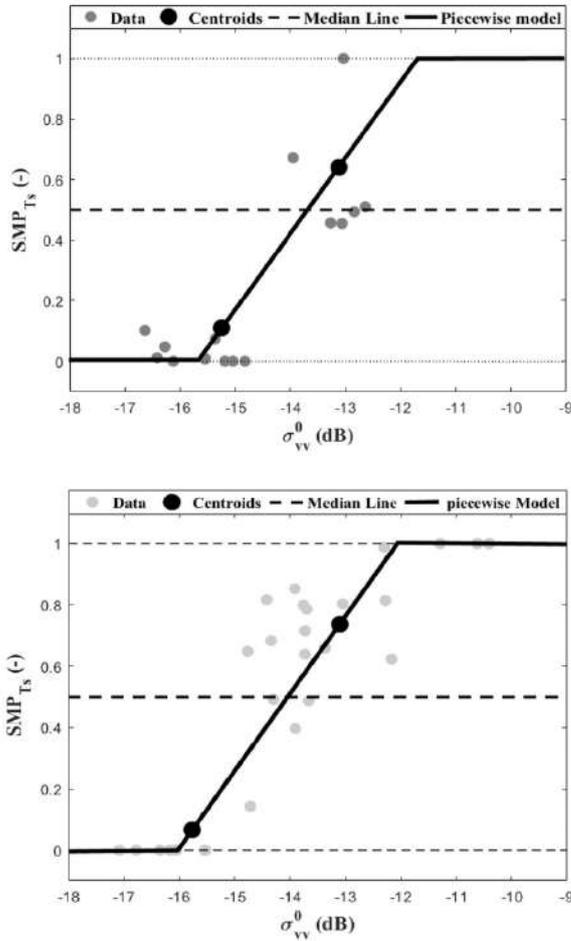
Fig. 6. SMP_{Ts} – σ_{vv}^0 relationship using T_s derived from Landsat data over Sidi Rahal (top plot) and R3 (bottom plot) site. The solid line represents the assumed piecewise linear model.

mainly dry or mainly wet conditions.

4.3. SM retrievals

The classical and new approaches were tested and examined by comparing the retrieved SM with *in situ* measurements. The calibration and validation of the new approach was performed separately at each site (on a pixel basis), having two different soil textures: Sidi Rahal site

has a sandy soil while the two other sites in the R3 perimeter are characterised by a clayey soil. Fig. 7 compares SM retrievals with *in situ* measurements for the benchmark and new approach for the studied sites, and a validation of the new approach using *in situ* T_s has been also presented over Sidi Rahal site when *in situ* T_s data are available. Results of this comparison, in terms of determination coefficient (R^2), slope and intercept of the linear regression, mean bias error (MBE) and root mean square error (RMSE) are presented in Table 4.

The benchmark method shows a systematic overestimation, and a kind of curvilinear relationship especially in the Sidi Rahal site whereas the new methodology offers a good consistency with ground-truth measurements. The linear scaling between σ_{vv}^0 and SM can explains the overestimation observed using the classical approach, since the two coefficients of the linear relationship are derived from extreme values of SM and σ_{vv}^0. Note that this effect is all the more visible as extreme (wet) SM values have not been reached at the time of S1 overpasses, despite the high temporal resolution of S1 and the relatively long time period. We argue that the main advantage of the proposed method is to provide robust reference points for calibrating the σ_{vv}^0 (SM) relationship, even for time series that do not contain extreme SM conditions. In addition, the calibration of the Eq. (7) allows for taking into account possible nonlinear behaviours of the σ_{vv}^0 (SM) relationship, especially in dry to very dry conditions. The radar signal can be only calibrated using thermal data when both satellites are concurrent or are quasi concurrent. It is reminded that over the study area both T_s and backscatter coefficients were available at approximately (one day difference) the same time. A sensitivity analysis was undertaken to assess the impact of a systematic error in LST on SM retrieval results. Based in the finding (results not shown), an error in LST estimations ($\pm$ 3 °C) would have a relatively small effect (maximum additional error of $0.02\,m^3\,m^{-3}$) in the SM estimations. Note that a bias in Landsat LST would have no effect on SM retrievals in the case of using contextual methods, instead of using an energy balance model to determine $T_{s,dry}$ and $T_{s,wet}$. When L7/8 and the S1 data were available in Sidi Rahal site, the results reveal a high R^2 of 0.79 with an RMSE of $0.03\,m^3\,m^{-3}$ which decrease the bias. As seen in Table 4, the radar/thermal combining approach provides a slightly higher R^2 value and a lower RMSE compared to the classical (radar only) approach. This improvement result is in an almost negligible mean difference between the estimated and *in situ* SM. The statistical outputs parameters confirm that the new approach estimates SM accurately, regardless of the soil composition. Results in terms of SM accuracy indicate that the loss of spatial resolution (from the aggregation of radar data from 20 m resolution to crop field scale) has a lower impact than the roughness effects that need to be taken into account at the crop field scale. A slope correction is observed (close to 1) using the new approach with an almost null intercept using satellite data whereas the conventional approach provides a higher value of both slope and intercept. Note that the one-day difference between Sentinel-1 radar and Landsat LST data, which may be representative of different SM levels (difference estimated as $0.02\,m^3\,m^{-3}$ over the experimental site), explains part of the uncertainty (estimated as $0.03\,m^3\,m^{-3}$) in the retrieved SM. We can

Table 3
Sensitivity analysis of the calibration results to the mid-value.

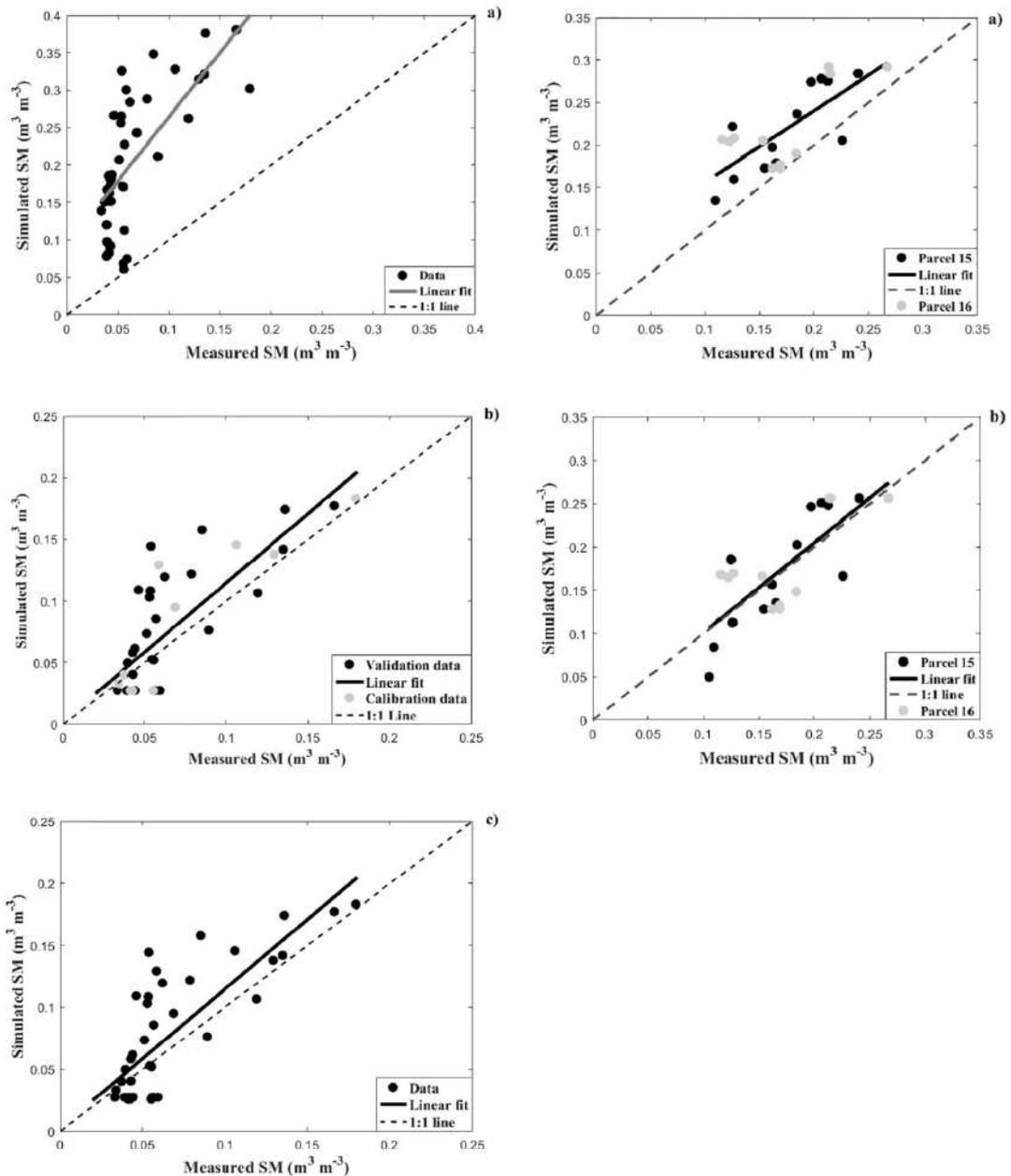|	Sidi Rahal					R3				
Mid-value	Calibration parameters a/b	SM ($m^3\,m^{-3}$)				Calibration parameters a/b	SM ($m^3\,m^{-3}$)			
		R^2	RMSE	MBE	Slope/intercept		R^2	RMSE	MBE	Slope/intercept
0.40	0.20/3.25	0.64	0.03	0.01	1.00/0.01	0.25/4.03	0.59	0.04	0.01	1.01/0.01
0.45	0.20/3.25	0.64	0.03	0.01	1.00/0.01	0.25/4.03	0.59	0.04	0.01	1.01/0.01
0.50	0.25/3.89	0.62	0.03	0.01	1.06/0.01	0.26/4.16	0.59	0.04	0.0	1.03/−0.0
0.55	0.48/7.44	0.51	0.06	0.02	1.37/0.00	0.25/4.13	0.59	0.04	0.01	1.02/0.00
0.60	0.48/7.44	0.51	0.06	0.02	1.37/0.00	0.25/4.03	0.58	0.04	0.01	0.99/0.01

Fig. 7. Estimated *versus* measured SM using the benchmark approach (a), new approach (b) and *in situ* validation (c) over Sidi Rahal (left plots) and R3 (right plots) site.

explain the previous statement by the non-appropriate estimation of $\sigma_{vv,\,min}^0$ and $\sigma_{vv,\,max}^0$ for the classical approach, which is based on two assumptions: 1) minimum and maximum SM values are observed at the time of S1 overpasses and 2) the relationship between backscatter coefficient and SM is linear. Note that such a relationship tends to be non-linear (Zribi et al., 2011), with a saturation appearing in the radar signal in the higher range of SM values (Bruckler et al., 1988).

In Fig. 7 (Sidi Rahal site), a significant phenomenon was observed for the low SM values, which correspond to low backscatter values. In

this range, *in situ* SM do not change with radar backscatter. This observed phenomena can be explained by the deeper penetration of the radar when the soil surface gets drier. In addition, the radar signal tends to be more sensitive to roughness variations in very dry conditions (Boisvert et al., 1997). We did not observe this effect over R3 sites because of the wetter conditions encountered over the irrigated perimeter. In addition, the SM in the top 5 cm may differ between the two sites, depending on the soil water retention properties and infiltration rates, resulting in variations in the S1 signal (Aubert et al., 2011).

Page | 185

Table 4

R^2, RMSE, MBE (simulated − observed), and the slope/intercept for the linear regression between simulated and observed SM for the classical and the new approach for Sidi Rahal and R3 sites.

Sites	Approach		R^2	RMSE ($m^3 m^{-3}$)	MBE ($m^3 m^{-3}$)	Slope/intercept ($-$)/($m^3 m^{-3}$)
Sidi Rahal	Classic		0.47	0.16	0.14	1.71/0.09
	New	All dates	0.64	0.03	0.01	1.12/0.002
		Dates when L7/8 & S1 data available (not shown here)	0.79	0.03	0.00	1.2/−0.007
		In situ validation	0.64	0.03	0.01	1.12/0.002
R3	Classic		0.56	0.05	0.04	0.84/0.07
	New		0.59			
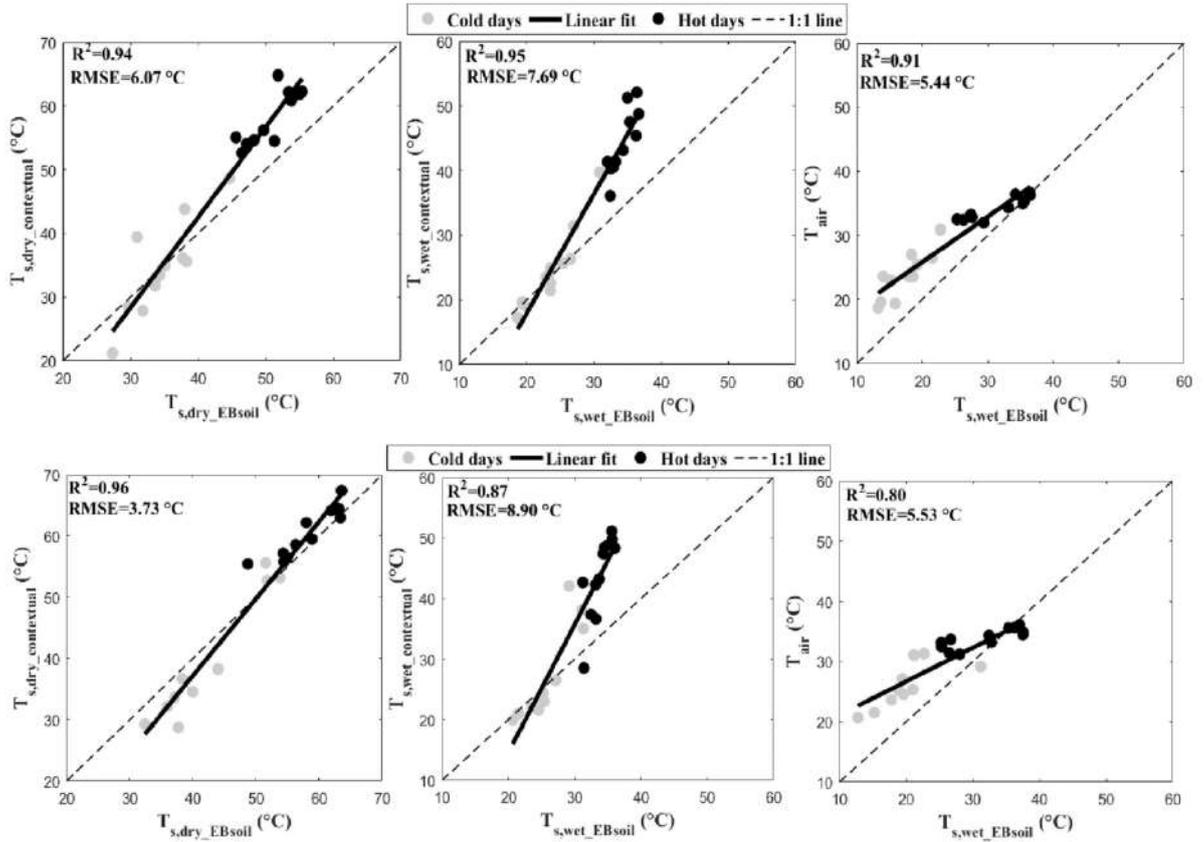
Fig. 9. EB-simulated *versus* space-based soil temperature endmembers ($T_{s,wet}$ and $T_{s,dry}$) for R3 (top plots) and Sidi Rahal (bottom plots) sites separately.

compared to the classical approach. As a brief summary of this sensitivity analysis, it is found that EB temperature endmembers are generally more robust than image-based temperature endmembers

the impact of the surface roughness on radar and LST data, as well as on the energy balance model (represented by Z_{0h} and Z_{0m} the roughness length for heat and momentum) on the modelled extreme temperatures
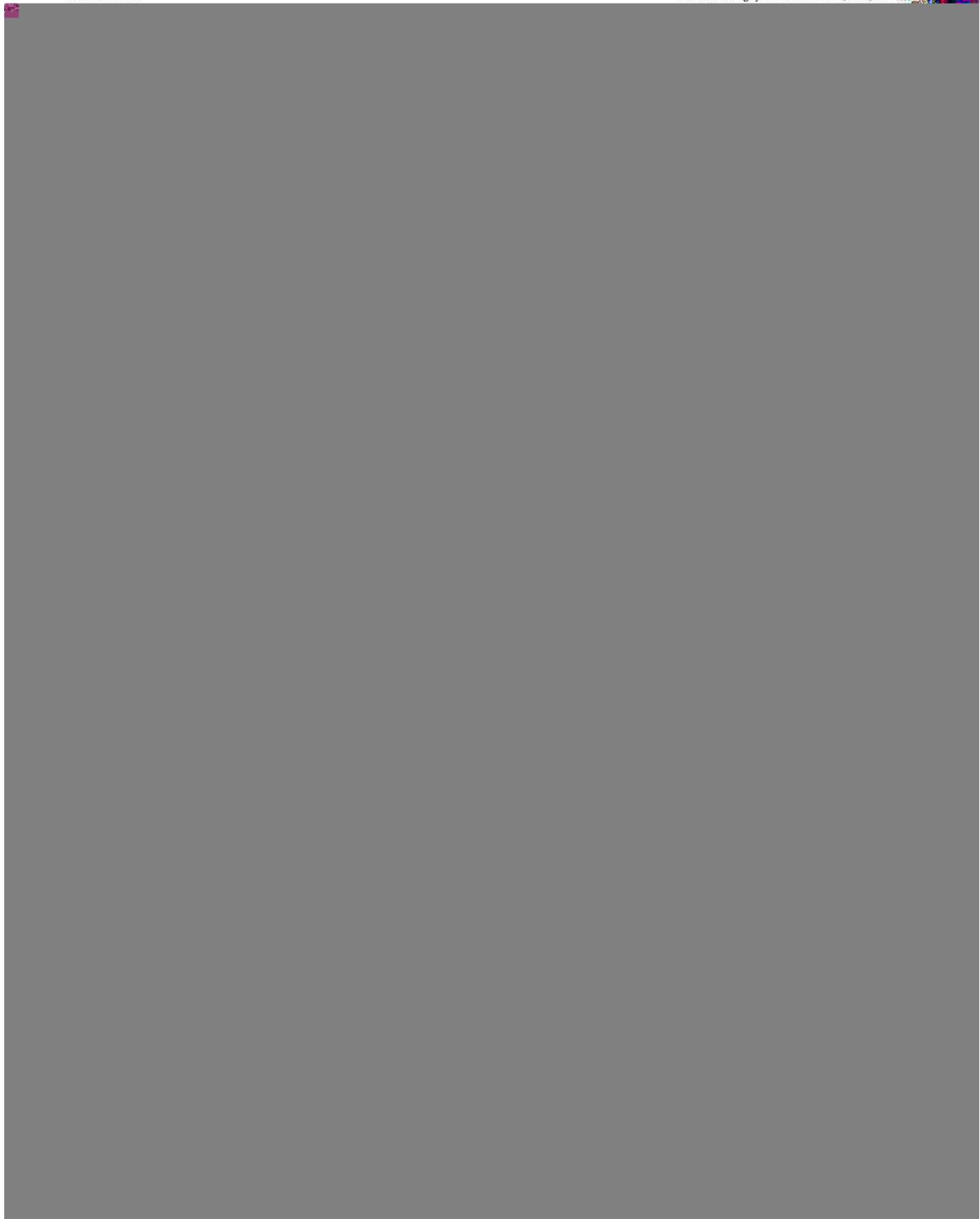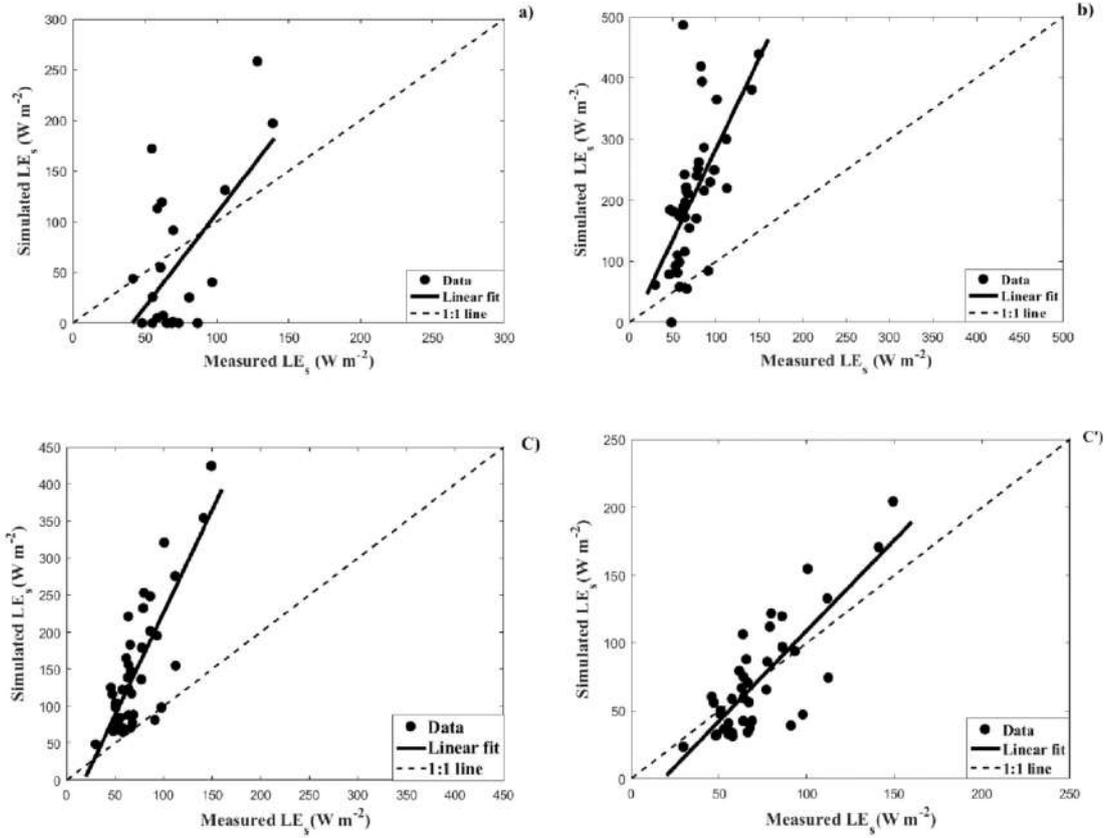
Fig. 11. Comparison at the Sidi Rahal site between simulated and observed soil evaporation for an SEE model driven by a) LST data, b) radar data, and combined radar and Landsat data using c) SM_C and c') SM_{sat} parameter.

high-spatial resolution (100 m with Landsat) currently have a maximum temporal resolution of 8 days (Lagouarde et al., 2014). When the scene will be cloudy, the temporal resolution will be necessarily less. Consequently, the applicability of the proposed thermal

thermal data are estimated from an energy balance model forced by meteorological forcing data. The point is that meteorological data may not be available everywhere with sufficient accuracy. Thus, alternative

Appendix A

A.1. Soil energy balance model

Surface energy balance model equation based on the partition of available energy on the surface (R_n-G) into sensible and latent heat flux (H and LE):

$$R_n - G = LE + H \tag{A.1}$$

with R_n is the surface net radiation is expressed as:

$$R_n = (1 - \alpha)R_g + \varepsilon(R_{atm} - \sigma T_s^4) \tag{A.2}$$

with α (−) being the surface albedo (set to 0.15), R_g (W m^{-2}) the global radiation, ε (−) is the surface emissivity (set to 0.95), R_{atm} the atmospheric longwave radiation (W m^{-2}) and $\sigma = 5.67 \times 10^{-8}$ the Stephan-Boltzmann constant (W m^{-2} K^{-4}). The downward atmospheric radiation at surface level is expressed as:

$$R_{atm} = \varepsilon_a \times \sigma T_{air}^4 \tag{A.3}$$

where ε_a is the atmospheric emissivity estimated as in (Brutsaert, 1975):

$$\varepsilon_a = 1.24 \times \left(\frac{e_a}{T_{air}}\right)^{\frac{1}{7}} \tag{A.4}$$

with $e_a = e_s(T_{air}) \times \dfrac{rh_a}{100}$ \tag{A.5}

rh_a (%) being the air relative humidity and e_s the saturated water vapour pressure (kPa) given by:

$$e_s = 0.611 \times e^{\left(\frac{17.27 \times T_{air}}{T_{air}+273.3}\right)} \tag{A.6}$$

The ground flux G is estimated as a fraction of net radiation at the surface R_n:

$$G = cg \cdot R_n \tag{A.7}$$

with cg being a fractional empirical coefficient set to 0.2.
The sensible heat flux is given by:

$$H = \rho c_p \frac{T_s - T_{air}}{r_{a,h}} \tag{A.8}$$

The latent heat flux is estimated as:

$$LE = \frac{\rho c_p}{\gamma} \frac{e_s - e_a}{r_{a,h} + r_c} \tag{A.9}$$

Finally, for running the energy balance model, we set LST = T_{air} and look for the value of LST that minimizes the following cost function F (LST):

$$F(T_s) = (R_n - G - H - LE)^2 \tag{A.10}$$

References

Alexakis, D.D., Mexis, F.D.K., Vozinaki, A.E.K., Daliakopoulos, I.N., Tsanis, I.K., 2017. Soil moisture content estimation based on Sentinel-1 and auxiliary earth observation products. A hydrological approach. Sensors (Switzerland). http://dx.doi.org/10.3390/s17061455.

Allen, R.G., Tasumi, M., Morse, A., Trezza, R., Wright, J.L., Bastiaanssen, W., Kramber, W., Lorite, I.J., Robison, C.W., 2007. Satellite-based energy balance for mapping evapotranspiration with internalized calibration (METRIC)—applications. J. Irrig. Drain. Eng. http://dx.doi.org/10.1061/(ASCE)0733-9437(2007)133.

Amazirh, A., Er-Raki, S., Chehbouni, A., Rivalland, V., Diarra, A., Khabba, S., Ezzahar, J., Merlin, O., 2017. Modified Penman–Monteith equation for monitoring evapotranspiration of wheat crop: relationship between the surface resistance and remotely sensed stress index. Biosyst. Eng. 164, 68–84. http://dx.doi.org/10.1016/j.biosystemseng.2017.09.015.

Attema, E.P.W., Ulaby, F.T., 1978. Vegetation modeled as a water cloud. Radio Sci. http://dx.doi.org/10.1029/RS013i002p00357.

Aubert, M., Baghdadi, N., Zribi, M., Douaoui, A., Loumagne, C., Baup, F., El Hajj, M., Garrigues, S., 2011. Analysis of TerraSAR-X data sensitivity to bare soil moisture, roughness, composition and soil crust. Remote Sens. Environ. 115, 1801–1810. http://dx.doi.org/10.1016/j.rse.2011.02.021.

Baghdadi, N., Zribi, M., 2006. Evaluation of radar backscatter models IEM, OH and Dubois using experimental observations. Int. J. Remote Sens. 27, 3831–3852. http://dx.doi.org/10.1080/01431160600658123.

Baghdadi, N., Gaultier, S., King, C., 2002a. Retrieving surface roughness and soil moisture from synthetic aperture radar (SAR) data using neural networks. Can. J. Remote. Sens. http://dx.doi.org/10.5589/m02-066.

Baghdadi, N., King, C., Chanzy, A., Wigneron, J.P., 2002b. An empirical calibration of the integral equation model based on SAR data, soil moisture and surface roughness measurement over bare soils. Int. J. Remote Sens. 23, 4325–4340. http://dx.doi.org/10.1080/01431160110107671.

Baghdadi, N., Gherboudj, I., Zribi, M., Sahebi, M., King, C., Bonn, F., 2004. Semi-empirical calibration of the IEM backscattering model using radar images and moisture and roughness field measurements. Int. J. Remote Sens. 25, 3593–3623. http://dx.doi.org/10.1080/01431160310001654392.

Baghdadi, N., Holah, N., Zribi, M., 2006. Soil moisture estimation using multi-incidence and multi-polarization ASAR data. Int. J. Remote Sens. 27, 1907–1920. http://dx.doi.org/10.1080/01431160500239032.

Baghdadi, N., Zribi, M., Loumagne, C., Ansart, P., Anguela, T.P., 2008. Analysis of

334

Page | 190

TerraSAR-X data and their sensitivity to soil surface parameters over bare agricultural fields. Remote Sens. Environ. http://dx.doi.org/10.1016/j.rse.2008.08.004.

Baghdadi, N., Abou Chaaya, J., Zribi, M., 2011. Semiempirical calibration of the integral equation model for SAR data in C-band and cross polarization using radar images and field measurements. IEEE Geosci. Remote Sens. Lett. 8, 14–18. http://dx.doi.org/10.1109/LGRS.2010.2050054.

Baghdadi, N., Choker, M., Zribi, M., Hajj, M., Paloscia, S., Verhoest, N., Lievens, H., Baup, F., Mattia, F., 2016. A new empirical model for radar scattering from bare soil surfaces. Remote Sens. 8, 920. http://dx.doi.org/10.3390/rs8110920.

Bai, X., He, B., Li, X., Zeng, J., Wang, X., Wang, Z., Zeng, Y., Su, Z., 2017. First assessment of Sentinel-1A data for surface soil moisture estimations using a coupled water cloud model and advanced integral equation model over the Tibetan Plateau. Remote Sens. http://dx.doi.org/10.3390/rs9070714.

Bastiaanssen, W.G.M., Menenti, M., Feddes, R.A., Holtslag, A.A.M., 1998. A remote sensing surface energy balance algorithm for land (SEBAL). J. Hydrol. http://dx.doi.org/10.1016/S0022-1694(98)00253-4.

Batra, N., Islam, S., Venturini, V., Bisht, G., Jiang, L., 2006. Estimation and comparison of evapotranspiration from MODIS and AVHRR sensors for clear sky days over the Southern Great Plains. Remote Sens. Environ. http://dx.doi.org/10.1016/j.rse.2006.02.019.

Berk, A., Anderson, G.P., Acharya, P.K., Bernstein, L.S., Muratov, L., Lee, J., Fox, M., Adler-Golden, S.M., Chetwynd, J.H., Hoke, M.L., Lockwood, R.B., Gardner, J.A., Cooley, T.W., Borel, C.C., Lewis, P.E., 2005. MODTRAN 5: A Reformulated Atmospheric Band Model With Auxiliary Species and Practical Multiple Scattering Options: Update. vol. 5806. pp. 662. http://dx.doi.org/10.1117/12.606026.

Boisvert, J.B., Gwyn, Q.H.J., Chanzy, A., Major, D.J., Brisco, B., Brown, R.J., 1997. Effect of surface soil moisture gradients on modelling radar backscattering from bare fields. Int. J. Remote Sens. 18, 153–170. http://dx.doi.org/10.1080/014311697219330.

Brisson, Perrier, 1991. A semi-empirical model of bare soil evaporation for crop simulation models. Water Resour. Res. 27, 719–727.

Bruckler, L., Witono, H., Stengel, P., 1988. Near surface soil moisture estimation from microwave measurements. Remote Sens. Environ. http://dx.doi.org/10.1016/0034-4257(88)90091-0.

Brutsaert, W., 1975. On a derivable formula for long-wave radiation from clear skies. Water Resour. Res. http://dx.doi.org/10.1029/WR011i005p00742.

Budyko, M.I., 1956. Heat Balance of the Earth's Surface. Gidrometeoizdat, Leningrad. Cahill, pp. 255.

Carlson, T., 2007. An overview of the "triangle method" for estimating surface evapotranspiration and soil moisture from satellite imagery. Sensors http://dx.doi.org/10.3390/s7081612.

Carlson, T.N., Gillies, R.R., Schmugge, T.J., 1995. An interpretation of methodologies for indirect measurement of soil water content. Agric. For. Meteorol. 77, 191–205. http://dx.doi.org/10.1016/0168-1923(95)02261-U.

Champion, I., Faivre, R., 1997. Sensitivity of the radar signal to soil moisture: variation with incidence angle, frequency, and polarization. IEEE Trans. Geosci. Remote Sens. http://dx.doi.org/10.1109/36.582001.

Chanzy, A., 1991. Modélisation simplifiée de l'évaporation d'un sol nu utilisant l'humidité et la température de surface accessibles par télédétection. Institut National Agronomique Paris-Grignon.

Chanzy, A., 1993. Basic soil surface characteristics derived from active microwave remote sensing. Remote Sens. Rev. 7, 303–319.

Chanzy, A., Bruckler, L., 1993. Significance of soil surface moisture with respect to daily bare soil evaporation. Water Resour. Res. http://dx.doi.org/10.1029/92WR02747.

Chauhan, S., Srivastava, H., 2016. Comparative evaluation of the sensitivity of multipolarised Sar and optical data for various land cover. Int. J. Adv. Remote Sens. GIS Geogr. 4, 1–14.

Chehbouni, A.H., Escadafal, R., Duchemin, B., Boulet, G., Simonneaux, V., Dedieu, G., Mougenot, B., Khabba, S., Kharrou, H., Maisongrande, P., Merlin, O., Chaponnière, A., Ezzahar, J., Er-Raki, S., Hoedjes, J., Hadria, R., Abourida, A., Cheggour, A., Raibi, F., Boudhar, A., Benhadj, I., Hanich, L., Benkaddour, A., Guemouria, N., Chehbouni, A.H., Lahrouni, A., Olioso, A., Jacob, F., Williams, D.G., Sobrino, J.A., 2008. An integrated modelling and remote sensing approach for hydrological study in arid and semi-arid regions: the SUDMED Programme. Int. J. Remote Sens. 29, 5161–5181. http://dx.doi.org/10.1080/01431160802036417.

Choi, M., Kim, T.A.E.W., Kustas, W.P., 2011. Reliable Estimation of Evapotranspiration on Agricultural Fields Predicted by the Priestley – Taylor Model Using Soil Moisture Data from Ground and Remote Sensing Observations Compared With the Common Land Model. 32. pp. 4571–4587. http://dx.doi.org/10.1080/01431161.2010.489065.

Cosby, B.J., Hornberger, G.M., Clapp, R.B., Ginn, T.R., 1984. A statistical exploration of the relationships of soil moisture characteristics to the physical properties of soils. Water Resour. Res. 20, 682–690. http://dx.doi.org/10.1029/WR020i006p00682.

Dee, D., Uppala, S., Simmons, A., Berrisford, P., Poli, P., Kobayashi, S., Andrae, U., Balmaseda, M., Balsamo, G., Bauer, P., 2011. The ERA - interim reanalysis: configuration and performance of the data assimilation system. Q. J. R. Meteorol. Soc. http://dx.doi.org/10.1002/qj.828.

Desborough, C.E., Pitman, A.J., Irannejad, P., 1996. Analysis of the relationship between bare soil evaporation and soil moisture simulated by 13 land surface schemes for a simple non-vegetated site. Glob. Planet. Chang. http://dx.doi.org/10.1016/0921-8181(95)00036-4.

Dobson, M.C., Ulaby, F., 1981. Microwave backscatter dependence on surface roughness, soil moisture, and soil texture: part III—soil tension. IEEE Trans. Geosci. Remote Sens. http://dx.doi.org/10.1109/TGRS.1981.350328.

Dobson, M.C., Ulaby, F.T., 1986. Active microwave soil moisture research. IEEE Trans. Geosci. Remote Sens. http://dx.doi.org/10.1109/TGRS.1986.289585.

Dobson, M.C., Ulaby, F.T., Hallikainen, M.T., El-Rayes, M.A., 1985. Microwave dielectric behavior of wet soil-part ii: dielectric mixing models. IEEE Trans. Geosci. Remote Sens. http://dx.doi.org/10.1109/TGRS.1985.289498.

Du, Y., Ulaby, F.T., Dobson, M.C., 2000. Sensitivity to soil moisture by active and passive microwave sensors. IEEE Trans. Geosci. Remote Sens. 38 (1), 105–114.

Dubois, P.C., Engman, T., 1995. Measuring soil moisture with imaging radars. IEEE Trans. Geosci. Remote Sens. 33, 915–926. http://dx.doi.org/10.1109/36.406677.

Duchemin, B., Hadria, R., Erraki, S., Boulet, G., Maisongrande, P., Chehbouni, A., Escadafal, R., Ezzahar, J., Hoedjes, J.C.B., Kharrou, M.H., Khabba, S., Mougenot, B., Olioso, A., Rodriguez, J.C., Simonneaux, V., 2006. Monitoring wheat phenology and irrigation in Central Morocco: on the use of relationships between evapotranspiration, crops coefficients, leaf area index and remotely-sensed vegetation indices. Agric. Water Manag. http://dx.doi.org/10.1016/j.agwat.2005.02.013.

Engman, E.T., 2000. Soil moisture. In: Schultz, G.A., Engman, E.T. (Eds.), Remote Sensing in Hydrology and Water Management. Springer Grayson, Berlin, pp. 197–216.

Entekhabi, D., Rodriguez-Iturbe, I., Castelli, F., 1996. Mutual interaction of soil moisture state and atmospheric processes. J. Hydrol. http://dx.doi.org/10.1016/0022-1694(95)02965-6.

Entekhabi, D., Njoku, E.G., O'Neill, P.E., Kellogg, K.H., Crow, W.T., Edelstein, W.N., Entin, J.K., Goodman, S.D., Jackson, T.J., Johnson, J., Kimball, J., Piepmeier, J.R., Koster, R.D., Martin, N., McDonald, K.C., Moghaddam, M., Moran, S., Reichle, R., Shi, J.C., Spencer, M.W., Thurman, S.W., Tsang, L., Van Zyl, J., 2010. The soil moisture active passive (SMAP) mission. Proc. IEEE. http://dx.doi.org/10.1109/JPROC.2010.2043918.

Er-Raki, S., Chehbouni, A., Guemouria, N., Duchemin, B., Ezzahar, J., Hadria, R., 2007. Combining FAO-56 model and ground-based remote sensing to estimate water consumptions of wheat crops in a semi-arid region. Agric. Water Manag. 87, 41–54. http://dx.doi.org/10.1016/j.agwat.2006.02.004.

Eweys, O.A., Elwan, A., Borham, T., 2017. Retrieving topsoil moisture using RADARSAT-2 data, a novel approach applied at the east of the Netherlands. J. Hydrol. 555, 670–682. http://dx.doi.org/10.1016/j.jhydrol.2017.10.048.

Fieuzal, R., 2010. Interactive Comment on "Combined Use of Optical and Radar Satellite Data for the Monitoring of Irrigation and Soil Moisture of Wheat Crops" by 7–9.

Fieuzal, R., Duchemin, B., Jarlan, L., Zribi, M., Baup, F., Merlin, O., Hagolle, O., Garatuza-Payan, J., 2011. Combined use of optical and radar satellite data for the monitoring of irrigation and soil moisture of wheat crops. Hydrol. Earth Syst. Sci. 15, 1117–1129. http://dx.doi.org/10.5194/hess-15-1117-2011.

Friedl, M.A., Davis, F.W., 1994. Sources of variation in radiometric surface temperature over a tallgrass prairie. Remote Sens. Environ. 48, 1–17. http://dx.doi.org/10.1016/0034-4257(94)90109-0.

Fung, A.K., 1994. Microwave Scattering and Emission Models and Their Applications. Artech House Remote Sensing Library.

Fung, A.K., Li, Z., Chen, K.S., 1992. Backscattering from a randomly rough dielectric surface. IEEE Trans. Geosci. Remote Sens. http://dx.doi.org/10.1109/36.134085.

Gao, Q., Zribi, M., Escorihuela, M., Baghdadi, N., 2017. Synergetic use of Sentinel-1 and Sentinel-2 data for soil moisture mapping at 100 m resolution. Sensors 17, 1966. http://dx.doi.org/10.3390/s17091966.

Gherboudj, I., Magagi, R., Berg, A.A., Toth, B., 2011. Soil moisture retrieval over agricultural fields from multi-polarized and multi-angular RADARSAT-2 SAR data. Remote Sens. Environ. 115, 33–43. http://dx.doi.org/10.1016/j.rse.2010.07.011.

Gillies, R.R., Carlson, T.N., 1995. Thermal remote-sensing of surface soil-water content with partial vegetation cover for incorporation into climate-models. J. Appl. Meteorol. http://dx.doi.org/10.1175/1520-0450(1995)034<0745:trsoss>2.0.co;2.

Goward, S.N., Tucker, C.J., Dye, D.G., 1985. North American vegetation patterns observed with the NOAA-7 advanced very high resolution radiometer. Vegetatio. http://dx.doi.org/10.1007/BF00033449.

Hadria, R., Duchemin, B., Lahrouni, A., Khabba, S., Er-raki, S., Dedieu, G., Chehbouni, A.G., Olioso, A., 2006. Monitoring of irrigated wheat in a semi-arid climate using crop modelling and remote sensing data: impact of satellite revisit time frequency. Int. J. Remote Sens. 27, 1093–1117. http://dx.doi.org/10.1080/01431160500382980.

Holah, N., Baghdadi, N., Zribi, M., Bruand, A., King, C., 2005. Potential of ASAR/ENVISAT for the characterization of soil surface parameters over bare agricultural fields. Remote Sens. Environ. 96, 78–86. http://dx.doi.org/10.1016/j.rse.2005.01.008.

Jackson, R.D., Pinter, P.J., 1981. Detection of water stress in wheat by measurement of reflected solar and emitted thermal IR radiation. In: Spectral Signatures of Objects in Remote Sensing. Institute National de la Recherche Agronomique, Versailles, France, pp. 399–406.

Jarlan, L., Khabba, S., Er-Raki, S., Le Page, M., Hanich, L., Fakir, Y., Merlin, O., Mangiarotti, S., Gascoin, S., Ezzahar, J., Kharrou, M.H., Berjamy, B., Saaïdi, A., Boudhar, A., Benkaddour, A., Laftouhi, N., Abaoui, J., Tavernier, A., Boulet, G., Simonneaux, V., Driouech, F., El Adnani, M., El Fazziki, A., Amenzou, N., Raibi, F., El Mandour, A., Ibouh, H., Le Dantec, V., Habets, F., Tramblay, Y., Mougenot, B., Leblanc, M., El Faïz, M., Drapeau, L., Coudert, B., Hagolle, O., Filali, N., Belaqziz, S., Marchane, A., Szczypta, C., Toumi, J., Diarra, A., Aouade, G., Hajhouji, Y., Nassah, H., Bigeard, G., Chirouze, J., Boukhari, K., Abourida, A., Richard, B., Fanise, P., Kasbani, M., Chakir, A., Zribi, M., Marah, H., Naimi, A., Mokssit, A., Kerr, Y., Escadafal, R., 2015. Remote sensing of water resources in semi-arid Mediterranean areas: the joint international laboratory TREMA. Int. J. Remote Sens. http://dx.doi.org/10.1080/01431161.2015.1093198.

Julien, Y., Sobrino, J.A., 2009. The Yearly Land Cover Dynamics (YLCD) method: an analysis of global vegetation from NDVI and LST parameters. Remote Sens. Environ. http://dx.doi.org/10.1016/j.rse.2008.09.016.

Karam, M.A., Fung, A.K., Lang, R.H., Chauhan, N.S., 1992. Microwave scattering model for layered vegetation. IEEE Trans. Geosci. Remote Sens. http://dx.doi.org/10.1109/36.158872.

Karjalainen, M., Harri, K., Hyyppä, J., Laurila, H., Kuittinen, R., 2014. The use of Envisat

alternating polarization Sar images in agricultural monitoring in comparison with Radarsat-1 Sar images. In: Proceedings of the ISPRS Congress, Istanbul, Turkey.

Kerr, Y.H., Waldteufel, P., Wigneron, J.P., Delwart, S., Cabot, F., Boutin, J., Escorihuela, M.J., Font, J., Reul, N., Gruhier, C., Juglea, S.E., Drinkwater, M.R., Hahne, A., Martin-Neira, M., Mecklenburg, S., 2010. The SMOS mission: new tool for monitoring key elements of the global water cycle. In: Proceedings of the IEEE, http://dx.doi.org/10.1109/jproc.2010.2043032.

Khabba, S., Jarlan, L., Er-Raki, S., Le Page, M., Ezzahar, J., Boulet, G., Simonneaux, V., Kharrou, M.H., Hanich, L., Chehbouni, G., 2013. The SudMed program and the joint international laboratory TREMA: a decade of water transfer study in the soil-plant-atmosphere system over irrigated crops in semi-arid area. Procedia Environ Sci 19, 524–533.

Kharrou, M.H., Le Page, M., Chehbouni, A., Simonneaux, V., Er-Raki, S., Jarlan, L., Ouzine, L., Khabba, S., Chehbouni, G., 2013. Assessment of equity and adequacy of water delivery in irrigation systems using remote sensing-based indicators in semi-arid region, Morocco. Water Resour. Manag. http://dx.doi.org/10.1007/s11269-013-0438-5.

Kim, J., Hogue, T.S., 2012. Improving spatial soil moisture representation through integration of AMSR-E and MODIS products. IEEE Trans. Geosci. Remote Sens. http://dx.doi.org/10.1109/TGRS.2011.2161318.

Lagouarde, J.P., Dayau, S., Moreau, P., Guyon, D., 2014. Directional anisotropy of brightness surface temperature over vineyards: case study over the Medoc Region (SW France). IEEE Geosci. Remote Sens. Lett. http://dx.doi.org/10.1109/LGRS.2013.2282492.

Le Hégarat-Mascle, S., Zribi, M., Alem, F., Weisse, A., Loumagne, C., 2002. Soil moisture estimation from ERS/SAR data: toward an operational methodology. IEEE Trans. Geosci. Remote Sens. http://dx.doi.org/10.1109/TGRS.2002.806994.

Le Morvan, A., Zribi, M., Baghdadi, N., Chanzy, A., 2008. Soil moisture profile effect on radar signal measurement. Sensors 8, 256–270. http://dx.doi.org/10.3390/s8010256.

Lee, J. Sen, 1999. Polarimetric SAR speckle filtering and its implication for classification. IEEE Trans. Geosci. Remote Sens. http://dx.doi.org/10.1109/36.789635.

Lee, J.S., Jurkevich, L., Dewaele, P., Wambacq, P., Oosterlinck, A., 1994. Speckle filtering of synthetic aperture radar images: a review. Remote Sens. Rev. http://dx.doi.org/10.1080/02757259409532206.

Lievens, H., Verhoest, N.E.C., 2011. On the retrieval of soil moisture in wheat fields from L-band SAR based on water cloud modeling, the IEM, and effective roughness parameters. IEEE Geosci. Remote Sens. Lett. 8, 740–744. http://dx.doi.org/10.1109/LGRS.2011.2106109.

Loew, A., Ludwig, R., Mauser, W., 2006. Derivation of surface soil moisture from ENVISAT ASAR wide swath and image mode data in agricultural areas. IEEE Trans. Geosci. Remote Sens. http://dx.doi.org/10.1109/TGRS.2005.863858.

Mahfouf, J.-F., Noilhan, J., 1991. Comparative study of various formulations of eva-poration from bare soil using in situ data. J. Appl. Meteorol. 30, 1354–1365.

Mahfouf, J.-F., Noilhan, J., 1996. Inclusion of gravitational drainage in a land surface scheme based on the force-restore method. J. Appl. Meteorol. 35, 987–992. http://dx.doi.org/10.1175/1520-0450(1996)035<0987:IOGDIA>2.0.CO;2.

Manabe, S., 1969. Climate and the ocean circulation I. The atmospheric circulation and the hydrology of the earth's surface. Mon. Weather Rev. http://dx.doi.org/10.1175/1520-0493(1969)097<0739:CATOC>2.3.CO;2.

Mathieu, R., Sbih, M., Viau, A.A., Anctil, F., Parent, L.E., Boisvert, J., 2003. Relationships Between Radarsat SAR Data and Surface Moisture Content of Agricultural Organic Soils. Int. J. Remote Sens.. http://dx.doi.org/10.1080/0143116031000115247.

Mattar, C., Wigneron, J.P., Sobrino, J.A., Novello, N., Calvet, J.C., Albergel, C., Richaume, P., Mialon, A., Guyon, D., Jimenez-Munoz, J.C., Kerr, Y., 2012. A combined optical-microwave method to retrieve soil moisture over vegetated areas. IEEE Trans. Geosci. Remote Sens. 50, 1404–1413. http://dx.doi.org/10.1109/TGRS.2011.2179051.

McVicar, T.R., Jupp, D.B., Yang, X., 1992. Linking regional water balance models with remote sensing. In: Proceedings of the 13th Asian Conference on Remote Sensing, Ulaanbaatar, Mongolia.

Merlin, O., 2013. An original interpretation of the wet edge of the surface temperature-albedo space to estimate crop evapotranspiration (SEB-1S), and its validation over an irrigated area in northwestern Mexico. Hydrol. Earth Syst. Sci. 17, 3623–3637. http://dx.doi.org/10.5194/hess-17-3623-2013.

Merlin, O., Walker, J.P., Chehbouni, A., Kerr, Y., 2008. Towards deterministic down-scaling of SMOS soil moisture using MODIS derived soil evaporative efficiency. Remote Sens. Environ. http://dx.doi.org/10.1016/j.rse.2008.06.012.

Merlin, O., Stefan, V.G., Amazirh, A., Chanzy, A., Ceschia, E., Tallec, T., Beringer, J., Gentine, P., Er-Raki, S., Bircher, S., Khabba, S., 2016. Modeling Soil Evaporation Efficiency in a Range of Soil and Atmospheric Conditions: A Downward Approach Based on Multi-site Data. (Submitted to Water Resources Research).

Merlin, O., Olivera-guerra, L., Bouchra, A.H., Amazirh, A., Rafi, Z., Ezzahar, J., Gentine, P., Khabba, S., Gascoin, S., Er-raki, O., 2017. A phenomenological model of soil evaporative efficiency using readily available data. Agric. For. Meteorol (In review).

Molero, B., Merlin, O., Malbéteau, Y., Al Bitar, A., Cabot, F., Stefan, V., Kerr, Y., Bacon, S., Cosh, M.H., Bindlish, R., Jackson, T.J., 2016. Remote sensing of environment SMOS disaggregated soil moisture product at 1 km resolution: processor overview and first validation results. Remote Sens. Environ. http://dx.doi.org/10.1016/j.rse.2016.02.045.

Moran, M.S., Jackson, R.D., Slater, P.N., Teillet, P.M., 1992. Evaluation of simplified procedures for retrieval of land surface reflectance factors from satellite sensor output. Remote Sens. Environ. http://dx.doi.org/10.1016/0034-4257(92)90076-V.

Moran, M.S., Clarke, T.R., Inoue, Y., Vidal, A., 1994. Estimating crop water deficit using the relation between surface-air temperature and spectral vegetation index. Remote Sens. Environ. http://dx.doi.org/10.1016/0034-4257(94)90020-5.

Nemani, R.R., Running, S.W., 1989. Estimation of regional surface resistance to

evapotranspiration from NDVI and thermal-IR AVHRR data. J. Appl. Meteorol. http://dx.doi.org/10.1175/1520-0450(1989)028<0276:EORSRT>2.0.CO;2.

Nishida, K., Nemani, R.R., Glassy, J.M., Running, S.W., 2003. Development of an eva-potranspiration index from Aqua/MODIS for monitoring surface moisture status. IEEE Trans. Geosci. Remote Sens. http://dx.doi.org/10.1109/TGRS.2003.811744.

Oh, Y., 2004. Quantitative retrieval of soil moisture content and surface roughness from multipolarized radar observations of bare soil surfaces. IEEE Trans. Geosci. Remote Sens. http://dx.doi.org/10.1109/TGRS.2003.821065.

Oh, Y., Sarabandi, K., Ulaby, F.T., 1992. An empirical model and an inversion technique for radar scattering from bare soil surfaces. IEEE Trans. Geosci. Remote Sens. http://dx.doi.org/10.1109/36.134086.

Omer, S.K., Al Bitar, A., Sekhar, M., Zribi, M., Bandyopadhyay, S., 2015. Retrieval and Multi-scale Validation of Soil Moisture From. pp. 8128–8153. http://dx.doi.org/10.3390/rs70608128.

Peng, J., Loew, A., Merlin, O., Verhoest, N.E.C., 2017. A Review of Spatial Downscaling of Satellite Remotely-sensed Soil Moisture. http://dx.doi.org/10.1002/2016RG000543. (Submitted to Reviews of Geophysics).

Price, J.C., 1990. Using spatial context in satellite data to infer regional scale evapo-transpiration. IEEE Trans. Geosci. Remote Sens. http://dx.doi.org/10.1109/36.58983.

Qin, J., Yang, K., Lu, N., Chen, Y., Zhao, L., Han, M., 2013. Spatial upscaling of in-situ soil moisture measurements based on MODIS-derived apparent thermal inertia. Remote Sens. Environ. http://dx.doi.org/10.1016/j.rse.2013.07.003.

Quesney, A., Le Hégarat-Mascle, S., Taconet, O., Vidal-Madjar, D., Wigneron, J.P., Loumagne, C., Normand, M., 2000. Estimation of watershed soil moisture index from ERS/SAR data. Remote Sens. Environ. http://dx.doi.org/10.1016/S0034-4257(99)00102-9.

Rakotoarivony, L., Taconet, O., Vidal-Madjar, D., 1996. Radar backscattering over agri-cultural bare soils. J. Electromagn. Waves Appl. 10, 187–209.

Remond, A., Beaudoin, A., King, C., 1999. SAR imagery to estimate roughness parameters when modelling runoff risk. Int. J. Remote Sens. http://dx.doi.org/10.1080/014311699211967.

Roerink, G.J., Su, Z., Menenti, M., 2000. S-SEBI: a simple remote sensing algorithm to estimate the surface energy balance. Phys. Chem. Earth Part B 25, 147–157.

Sandholt, I., Rasmussen, K., Andersen, J., 2002. A simple interpretation of the surface temperature/vegetation index space for assessment of surface moisture status. Remote Sens. Environ. 79, 213–224. http://dx.doi.org/10.1016/S0034-4257(01)00274-7.

Santamaria-Artigas, A., Mattar, C., Wigneron, J.P., 2016. Application of a combined op-tical-passive microwave method to retrieve soil moisture at regional scale over Chile. IEEE J. Sel. Top. Appl. Earth Obs. Remote Sens. 9, 1493–1504. http://dx.doi.org/10.1109/JSTARS.2015.2512926.

Schmugge, T., 1978. Remote sensing of surface soil moisture. Design. http://dx.doi.org/10.1029/JC080i021p03044.

Shi, J., Wang, J., Hsu, A.Y., O'Neill, P.E., Engman, E.T., 1997. Estimation of bare surface soil moisture and surface roughness parameter using L-band SAR image data. IEEE Trans. Geosci. Remote Sens. http://dx.doi.org/10.1109/36.628792.

Smith, R.C.G., Choudhury, B.J., 1991. Analysis of normalized difference and surface temperature observations over southeastern Australia. Remote Sens. http://dx.doi.org/10.1080/01431169108955234.

Sobrino, J.A., Franch, B., Mattar, C., Jiménez-Muñoz, J.C., Corbari, C., 2012. A method to estimate soil moisture from Airborne Hyperspectral Scanner (AHS) and ASTER data: application to SEN2FLEX and SEN3EXP campaigns. Remote Sens. Environ. http://dx.doi.org/10.1016/j.rse.2011.10.018.

Srivastava, H.S., 2007. Development and Validation of an Improved Methodology for Operational Monitoring of Soil Moisture Over Large Agricultural Area Using Multi-incidence Angle Radarsat-1 Sar Data and M ....

Srivastava, H.S., Patel, P., Manchanda, M.L., Adiga, S., 2003. Use of multiincidence angle RADARSAT-1 SAR data to incorporate the effect of surface roughness in soil moisture estimation. IEEE Trans. Geosci. Remote Sens. http://dx.doi.org/10.1109/TGRS.2003.813356.

Srivastava, H.S., Patel, P., Sharma, Y., Navalgund, R.R., 2008. Retrieval of surface roughness using multi-polarized Envisat-1 ASAR data. Geocarto Int. 23, 67–77. http://dx.doi.org/10.1080/10106040701538157.

Srivastava, H.S., Patel, P., Sharma, Y., Navalgund, R.R., 2009. Large-area Soil Moisture Estimation Using. vol. 47. pp. 2528–2535.

Stefan, V.G., Merlin, O., Er-Raki, S., Escorihuela, M.J., Khabba, S., 2015. Consistency between in situ, model-derived and high-resolution-image-based soil temperature endmembers: towards a robust data-based model for multi-resolution monitoring of crop evapotranspiration. Remote Sens. http://dx.doi.org/10.3390/rs70810444.

Susaki, J., 2008. Calibration of IEM model for the soil moisture mapping of non-in-undated paddy fields using ALOS/PALSAR data. In: Sites the Journal of 20th Century Contemporary French Studies. Junichi Susaki Graduate School of Global Environmental Studies, pp. 753–756.

Tardy, B., Rivalland, V., Huc, M., Hagolle, O., Marcq, S., Boulet, G., 2016. A Software Tool for Atmospheric Correction and Surface Temperature Estimation of Landsat Infrared Thermal Data. pp. 1–24. http://dx.doi.org/10.3390/rs8090696.

Torres, R., Snoeij, P., Geudtner, D., Bibby, D., Davidson, M., Attema, E., Potin, P., Rommen, B., Floury, N., Brown, M., Traver, I.N., Deghaye, P., Duesmann, B., Rosich, B., Miranda, N., Bruno, C., L'Abbate, M., Croci, R., Pietropaolo, A., Huchler, M., Rostan, F., 2012. GMES Sentinel-1 mission. Remote Sens. Environ. http://dx.doi.org/10.1016/j.rse.2011.05.028.

Ulaby, F.T., Batlivala, P.P., Dobson, M.C., 1978. Microwave backscatter dependence on surface roughness, soil moisture, and soil texture: part I–bare soil. IEEE Trans. Geosci. Electron. http://dx.doi.org/10.1109/TGE.1978.294586.

Ulaby, F.T., Bradley, G.A., Obson, M.C., 1979. Microwave backscatter dependence on

surface roughness, soil moisture, and soil texture: part II–vegetation-covered soil. IEEE Trans. Geosci. Electron. http://dx.doi.org/10.1109/TGE.1979.294626.

Ulaby, F.T., Moore, R.K., Fung, A.K., 1986. Microwave remote sensing: active and passive. In: Volume 3 - From Theory to Applications, Microwave Remote Sensing Active and Passive.

Van Oevelen, P.J., Hoekman, D.H., 1999. Radar backscatter inversion techniques for estimation of surface soil moisture: EFEDA-Spain and HAPEX-SAHEL case studies. IEEE Trans. Geosci. Remote Sens. http://dx.doi.org/10.1109/36.739141.

Vereecken, H., Huisman, J.A., Bogena, H., Vanderborght, J., Vrugt, J.A., Hopmans, J.W., 2008. On the Value of Soil Moisture Measurements in Vadose Zone Hydrology: A Review. 44. pp. 1–21. http://dx.doi.org/10.1029/2008WR006829.

Verstraeten, W.W., Veroustraete, F., Feyen, J., 2008. Assessment of Evapotranspiration and Soil Moisture Content Across Different Scales of Observation. pp. 70–117.

Wagner, W., Lemoine, G., Borgeaud, M., Member, S., Rott, H., 1999a. A Study of Vegetation Cover Effects on ERS Scatterometer Data. vol. 37. pp. 938–948.

Wagner, W., Lemoine, G., Rott, H., 1999b. A method for estimating soil moisture from ERS scatterometer and soil data. Remote Sens. Environ. 4257.

Wan, Z., Wang, P., Li, X., 2004. Using MODIS land surface temperature and normalized difference vegetation index products for monitoring drought in the Southern Great Plains, USA. Int. J. Remote Sens. http://dx.doi.org/10.1080/0143116031000115328.

Wang, K., Li, Z., Cribb, M., 2006. Estimation of evaporative fraction from a combination of day and night land surface temperatures and NDVI: a new method to determine the Priestley-Taylor parameter. Remote Sens. Environ. http://dx.doi.org/10.1016/j.rse.2006.02.007.

Wickel, A.J., Jackson, T.J., Wood, E.F., 2001. Multi-temporal monitoring of soil moisture with RADARSAT SAR during the 1997 Southern Great Plains hydrology experiment. Int. J. Remote Sens. http://dx.doi.org/10.1080/01431160120291.

Zhang, D., Zhou, G., 2016. Estimation of Soil Moisture From Optical and Thermal Remote Sensing: A Review. http://dx.doi.org/10.3390/s16081308.

Zhang, F., Zhang, L.W., Shi, J.J., Huang, J.F., 2014. Soil moisture monitoring based on land surface temperature-vegetation index space derived from MODIS data. Pedosphere 24, 450–460. http://dx.doi.org/10.1016/S1002-0160(14)60031-X.

Zribi, M., Dechambre, M., 2003. A new empirical model to retrieve soil moisture and roughness from C-band radar data. Remote Sens. Environ. 84, 42–52. http://dx.doi.org/10.1016/S0034-4257(02)00069-X.

Zribi, M., Taconet, O., Le Hégarat-Mascle, S., Vidal-Madjar, D., Emblanch, C., Loumagne, C., Normand, M., 1997. Backscattering behavior and simulation comparison over bare soils using SIR-C/X-SAR and ERASME 1994 data over Orgeval. Remote Sens. Environ. http://dx.doi.org/10.1016/S0034-4257(96)00158-7.

Zribi, M., Baghdadi, N., Holah, N., Fafin, O., 2005. New methodology for soil surface moisture estimation and its application to ENVISAT-ASAR multi-incidence data inversion. Remote Sens. Environ. http://dx.doi.org/10.1016/j.rse.2005.04.005.

Zribi, M., André, C., Decharme, B., 2008. A method for soil moisture estimation in Western Africa based on the ERS scatterometer. IEEE Trans. Geosci. Remote Sens. http://dx.doi.org/10.1109/TGRS.2007.904582.

Zribi, M., Chahbi, A., Shabou, M., Duchemin, B., Baghdadi, N., Amri, R., 2011. Soil Surface Moisture Estimation Over a Semi-arid Region Using ENVISAT ASAR Radar Data for Soil Evaporation Evaluation. pp. 345–358. http://dx.doi.org/10.5194/hess-15-345-2011.
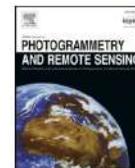
Including Sentinel-1 radar data to improve the disaggregation of MODIS land surface temperature data

Abdelhakim Amazirh[a,b,*], Olivier Merlin[b], Salah Er-Raki[a]

[a] LP2M2E, Département de Physique Appliquée, Faculté des Sciences et Techniques, Université Cadi Ayyad, Marrakech, Morocco
[b] CESBIO, Université de Toulouse, CNES/CNRS/IRD/UPS, Toulouse, France

ABSTRACT

The use of land surface temperature (LST) for monitoring the consumption and water status of crops requires data at fine spatial and temporal resolutions. Unfortunately, the current spaceborne thermal sensors provide data at either high temporal (e.g. MODIS: Moderate Resolution Imaging Spectro-radiometer) or high spatial (e.g. Landsat) resolution separately. Disaggregating low spatial resolution (LR) LST data using ancillary data available at high spatio-temporal resolution could compensate for the lack of high spatial resolution (HR) LST observations. Existing LST downscaling approaches generally rely on the fractional green vegetation cover (f_{gv}) derived from HR reflectances but they do not take into account the soil water availability to explain the spatial variability in LST at HR. In this context, a new method is developed to disaggregate kilometric MODIS LST at 100 m resolution by including the Sentinel-1 (S-1) backscatter, which is indirectly linked to surface soil moisture, in addition to the Landsat-7 and Landsat-8 (L-7 & L-8) reflectances. The approach is tested over two different sites – an 8 km by 8 km irrigated crop area named "R3" and a 12 km by 12 km rainfed area named "Sidi Rahal" in central Morocco (Marrakech) – on the seven dates when S-1, and L-7 or L-8 acquisitions coincide with a one-day precision during the 2015–2016 growing season. The downscaling methods are applied to the 1 km resolution MODIS-Terra LST data, and their performance is assessed by comparing the 100 m disaggregated LST to Landsat LST in three cases: no disaggregation, disaggregation using Landsat f_{gv} only, disaggregation using both Landsat f_{gv} and S-1 backscatter. When including f_{gv} only in the disaggregation procedure, the mean root mean square error in LST decreases from 4.20 to 3.60 °C and the mean correlation coefficient (R) increases from 0.45 to 0.69 compared to the non-disaggregated case within R3. The new methodology including the S-1 backscatter as input to the disaggregation is found to be systematically more accurate on the available dates with a disaggregation mean error decreasing to 3.35 °C and a mean R increasing to 0.75.

1. Introduction

Land surface temperature (LST) derived from thermal infrared remote sensing is an essential input variable for various environmental and hydro-meteorological applications. LST data are practically used for modeling the land surface processes and monitoring the functioning of agro-ecosystems (Anderson et al., 2008; Brunsell and Gillies, 2003; Karnieli et al., 2010; Kustas and Anderson, 2009; Zhang et al., 2008). Therefore, LST data have been used in a variety of applications such as, among others, climate studies (Hansen et al., 2010; Kustas and Anderson, 2009), the monitoring of crop water consumption (Amazirh et al., 2017; Bastiaanssen et al., 1998; Boulet et al., 2007; Er-Raki et al., 2018; Olivera-Guerra et al., 2018; Price, 1982), vegetation monitoring (Kogan, 2001; Williamson, 1988), soil moisture estimation (Amazirh

et al., 2018; Merlin et al., 2010; Sandholt et al., 2002), and hydrological studies (Crow and Wood, 2003). However, there is a limitation in the existing satellite thermal sensors, since those with high revisit cycles (e.g., MODerate resolution Imaging Spectro-radiometer 'MODIS') do not offer high spatial resolution (HR), and those offering HR (e.g., Landsat-8) generally have low temporal resolution (Agam et al., 2007b). In contrast, the visible and near infrared (VNIR) reflectance data are available at a resolution finer than that of most thermal sensors (Ha et al., 2013). To bridge the gap, the finer-resolution VNIR data have hence been extensively used as ancillary data to disaggregate low-resolution (LR) LST at HR.

Recently, various efforts have been devoted to disaggregate LST to a finer – typically 100 m – resolution. Techniques are generally based on a relationship between LST and ancillary (vegetation cover indexes,

* Corresponding author at: LP2M2E, Département de Physique Appliquée, Faculté des Sciences et Techniques (FSTG), Cadi Ayyad University, Av. Abdelkarim Elkhattabi, B.P 549, 40000 Marrakech, Morocco.
E-mail addresses: abdelhakim.amazirh@ced.uca.ma (A. Amazirh), olivier.merlin@cesbio.cnes.fr (O. Merlin), s.erraki@uca.ma (S. Er-Raki).

emissivity and/or albedo) data, the obtained relationship being assumed to be scale invariant (and thus applied at both HR and LR). The statistical downscaling methods in particular, developed by Kustas et al. (2003) over a homogenous vegetated area, has been widely used. This method is based on a linear regression relationship between LST and NDVI (Normalized Difference Vegetation Index) calibrated at LR. The relation between LST and NDVI is also used in Bindhu et al. (2013), with the aim of developing a nonlinear method to estimate LST at HR. Agam et al. (2007a) used the fraction of green vegetation cover instead of NDVI. This method showed its capability and good performance over areas with relatively uniform soil and vegetation hydric status, where the temperature of bare soil is set to the average between the dry and wet soil over the studied area. Other studies reported that NDVI (or f_{gv}) shows some limitations and cannot explain all the variations in LST over agricultural areas (Agam et al., 2007b, 2007a; Inamdar and French, 2009; Merlin et al., 2010; Olivera-Guerra et al., 2017). Especially, Agam et al. (2007b) and Merlin et al. (2010) observed a shortcoming when using the LST-NDVI or LST-f_{gv} relationship over areas with high moisture content, or with various photosynthetic activity vegetation types. Merlin et al. (2010) adapted this method to heterogeneous vegetation status, by adding the fraction of senescent vegetation cover to include the photosynthesis activity of vegetation, and to distinguish between areas of bare soil and dry vegetation cover. Dominguez et al. (2011) integrated the surface albedo to estimate HR LST by fitting the relationship between LST, NDVI and surface albedo. Following the same idea of adding other information that affect the spatial distribution of LST, Merlin et al. (2012) used the projection technique theoretically developed in Merlin et al. (2005) that aims to strengthen the correlation between two variables (LST and NDVI) by representing the dependence of these variables on other additional variables, based on a radiative transfer equation. Moreover, other studies were further presented involving additional factors that reflect the vegetation type (Merlin et al., 2010; Sandholt et al., 2009; Zhan et al., 2011). Sandholt et al. (2002) summarized the variables that affect LST variability, and they mentioned that, surface soil moisture (SM) mainly controls evapotranspiration and thermal properties of the surface, which affect LST. Therefore, optimal LST disaggregation approaches should include the variability of SM in addition to NDVI (or f_{gv}), in order to represent the variability of the bare soil temperature bounded by its wet and dry endmembers. Advanced regression tools using spectral bands, have been successfully used in different studies produce better disaggregation results than simple polynomial functions (Ghosh and Joshi, 2014).

Recently, some studies have attempted to represent the SM effect. Liu and Zhu (2012) used a normalized multi-band drought index (NMDI) for monitoring soil and vegetation moisture, based on the absorption properties of the vegetation water in the NIR and the sensitive characteristics of water absorption differences between soil and vegetation in the short-wave infrared (SWIR). However, NMDI has inconsistent relationships with vegetation and soil moisture changes (i.e. positive correlation with vegetation water content and negative correlation with SM changes). Therefore, it poorly performed over mixed pixels of vegetation and soil. Chen et al. (2010) took into account SM variations using a soil wetness index (SWI) estimated based on the interpretation of the triangular LST–NDVI space. However, the errors were found to be larger with low fractional vegetation cover. In the same manner, Yang et al. (2010) discussed the impact of SM variations using the LST-NDVI space and assumed uniform SM conditions in a coarse pixel. Therefore this technique is only appropriate in regions where SM varies at large scale and in pixels with high f_{gv}. In general, the previously proposed proxies or indexes that aim to incorporate the SM effect on LST poorly performed over the areas with low vegetation cover.

In this context, a new algorithm is proposed to improve the disaggregation of LR LST by explicitly taking into the variability of SM at

HR. Incorporating SM information to disaggregate LST has the advantage of distinguishing between the dry and the wet soil especially in areas with low vegetation cover, where the soil moisture status is the main factor controlling the LST variability. The novelty of this work is to integrate a spaceborne radar-derived soil moisture proxy in the disaggregation of 1 km resolution LST. This research relies on the Sentinel-1 (S-1) mission, which provides C-band radar data at both high-spatial and high-temporal resolutions. The approaches are tested over an 8 km by 8 km and 12 km by 12 km semi-arid areas near Marrakech-Morocco. The chosen sites allows for testing the algorithm over a heterogonous landscape in terms of vegetation type and SM status where LST highly varies in both space and time. The methodologies are applied to aggregated Landsat LST and to MODIS LST data separately, and the HR ancillary data are derived from radar S-1 and VNIR Landsat data. Finally the disaggregated LST is evaluated at 100 m resolution against Landsat LST.

2. Site description and data set

2.1. Study area

The study areas are located in the semi-arid Haouz plain, situated near Marrakech city, in central Morocco (Fig. 1). This region is characterized by irregular and low rainfall of about 250 mm/year with a high evaporative demand that exceeds 1600 mm/year.

In recent years, several field campaigns and experiments have been carried out and numerous studies have been conducted over this area with different objectives related to agricultural water management (Amazirh et al., 2018, 2017; Chehbouni et al., 2008; Er-Raki et al., 2010; Jarlan et al., 2015; Khabba et al., 2013; Duchemin et al., 2008).

The first site is an irrigated agricultural zone (called R3) known by its heterogeneity and occupied by different culture types (alfalfa, wheat, olive, orange and horticulture), where wheat crops is the dominating culture (50%). Flood irrigation is the main irrigation mode used in this area.

The second area is a rainfed agricultural area (called Sidi Rahal) mainly dominated by trees (about 80%) while the remaining surface is comprised of bare soil, small forest and impervious surfaces (e.g., buildings and roads). The dark area mainly represents parcels maintained in bare soil conditions (due to a lack of rainfall in late December) and building. Based on soil analysis (Er-Raki et al., 2007), soil texture is clayey and sandy in the majority of fields within the R3 and Sidi Rahal areas, respectively.

2.2. Ground data

Two automatic meteorological stations have been installed, one over an alfalfa cover in the R3 perimeter and another over a rainfed wheat crop at the Sidi Rahal site providing local data including air temperature (T_{air}), relative humidity (rha) wind speed (ua), wind direction and global solar radiation (rg) measured at 2 m above ground level. For the Sidi Rahal site, the weather station is located in a rainfed wheat crop (bare soil during the study) in the lower right plot (Fig. 1).

2.3. Satellite data

In this study, seven dates of quasi coincident VNIR/thermal and radar images were used (Table 1). The L-7 and L-8 images were downloaded from the USGS website, which freely provides surface reflectances and thermal radiances data in different spectral bands. The level-1 products are calibrated radiometrically and orthorectified using digital elevation model. The revisit time of each sensor is 16 days. Combining both satellites potentially (in cloud free conditions) provides optical data every 8 days. S-1 mission is composed of a constellation of two twin satellites. Both S-1A and S-1B operate in C-band synthetic
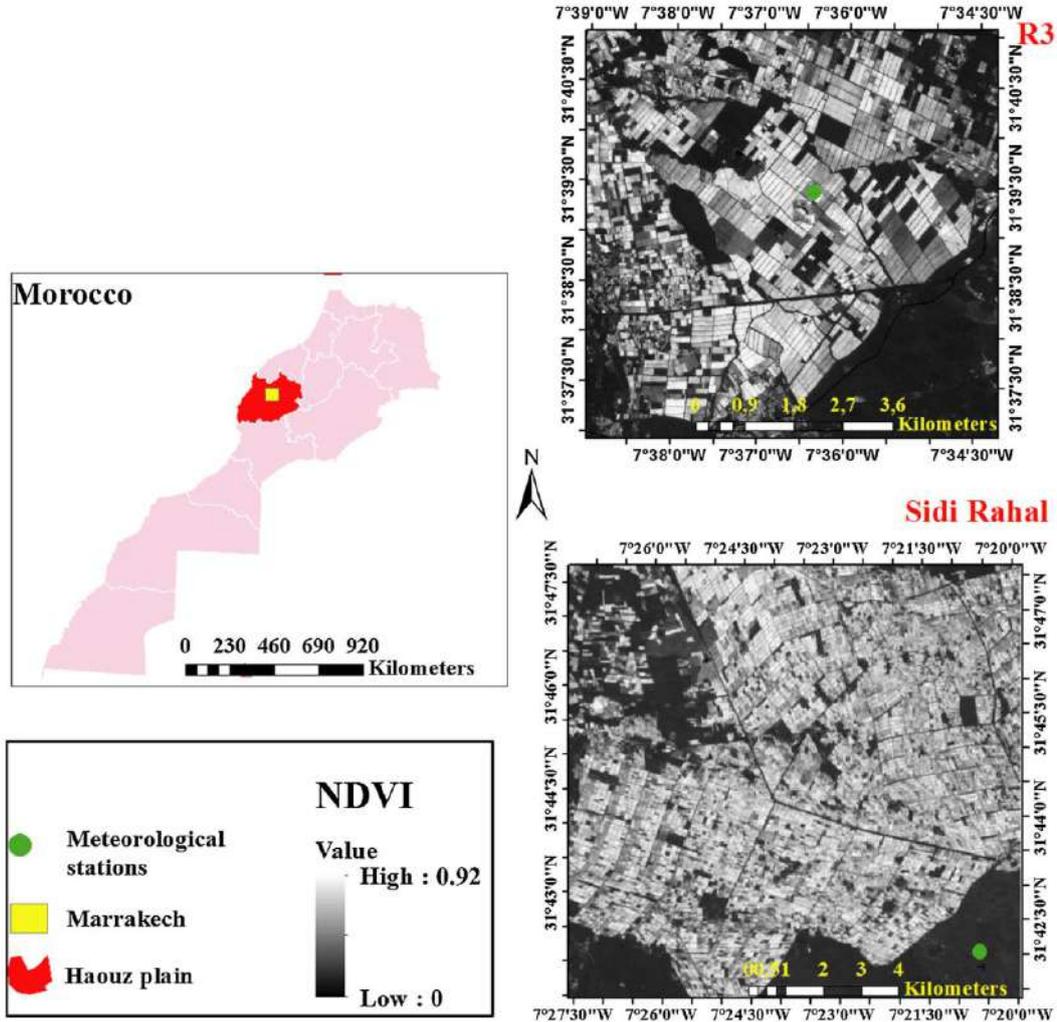
Fig. 1. Location of Marrakech in the Tensift Al Haouz region, Morocco (left) and the study areas (right) including the weather station installed (green circles) during the 2015–2016 agricultural season. The images are derived from Landsat data, the 07 February and the 24 July for Sidi Rahal and R3 sites, respectively. (For interpretation of the references to colour in this figure legend, the reader is referred to the web version of this article.)

Table 1
The seven dates between January 01 and December 31, 2016 when S-1 data are collected one day after Landsat data (in clear sky conditions) are selected.

S-1 σ_{VV}^0	Landsat LST and NDVI
07 January 2016	06 January 2016*
08 February 2016	07 February 2016*
19 March	18 March*
07 June	06 June+
01 July	30 June*
25 July	24 July+
18 August	17 August*

* Landsat-8.
+ Landsat-7.

aperture radar (SAR), providing data in four operational modes (Strip Map, Interferometric Wide Swath, Extra wide swath and Wave) and different polarizations for all modes. The S-1 constellation offers data with high revisit frequency (every 3–6 days).

2.3.1. High resolution reflectances

In our feasibility study, Landsat VNIR data are used because the Landsat LST is, in any case, required for evaluating the disaggregated LST. In real-life, however, the disaggregation approaches should be implemented using high spatio-temporal resolution VNIR data collected from Sentinel-2. The VNIR Landsat reflectances are aggregated at 100 m resolution, consistent with Landsat LST spatial resolution. Surface reflectances are used to calculate the NDVI, defined as the ratio of the difference between the spectral reflectance measurements acquired in NIR and red to their sum. The fractional green vegetation cover is estimated from an empirical relationship with NDVI (Gutman and Ignatov, 1998):

$$f_{gv} = \frac{NDVI - NDVI_{bs}}{NDVI_{gv} - NDVI_{bs}} \tag{1}$$

where $NDVI_{gv}$ and $NDVI_{bs}$ are the NDVI over full-cover green vegetation and bare soil, respectively. The NDVI end-members are derived from the time series of Landsat data as the minimum and maximum

13

value of the 100 m resolution NDVI within the whole selected areas for the bare soil and full-cover green vegetation case, respectively.

2.3.2. Thermal infrared (TIR) data

2.3.2.1. MODIS data. The daily 1 km resolution LST (version 6) MOD11A1 product is available through the U.S. Land Processes Distributed Active Archive Center (LP DAAC, https://lpdaac.usgs.gov/). The generalized split-window algorithm (Wan, 1996; Wan et al., 2002) has been used to retrieve MODIS LST products and a correction step was performed using the surface band emissivity provided also by MODIS spectral data. The LST data were re-projected from sinusoidal to geographic latitude/longitude using the Universal Transverse Mercator (UTM), Zone 29N, World Geodetic System (WGS) 84 coordinate system.

2.3.2.2. Landsat data. L-7 and L-8 sensors provide TIR data with a spatial resolution of 60 m and 100 m, respectively. The TIR radiance is used to calculate LST. To this end, all the followed correction steps and the processing chain are described in Tardy et al. (2016).

The L-7 LST is averaged (aggregated) at 100 m resolution, which is the lowest spatial resolution between S-1 and Landsat data. Note that the reliability of the Landsat-derived LST was checked in Amazirh et al. (2017) by comparing remotely sensed LST with local *in situ* measurements (not shown here) at two TIR stations located within the study area. A relatively good match between satellite and ground LST data was obtained for both sites with an error smaller than 1.0 an 2.4 °C.

The Landsat LSTs are linearly aggregated at 1 km resolution to match the spatial resolution of MODIS observations. The linear averaging technique (without accounting for the nonlinear relationship between physical temperature and radiance) is chosen based on the work of (Liu et al., 2006), which found that the maximum difference between the temperature aggregated using different upscaling approaches is 0.2 °C.

2.3.3. Sentinel-1 radar data

Between January 01 and December 31, 2016, among the 49 images collected over the study area, seven were approximately coincident (with a 1-day precision) with clear sky Landsat images (Table 1). The S-1 level 1 SAR scenes were collected in both ascending and descending pass directions over the study site. The S-1 satellite provides data in both VV and VH polarization modes at an incidence angle of 40° over the study area. The S-1 Ground Range Detected (GRD) images were acquired in interferometric wide swath mode (IW), with an original spatial resolution of 5 m by 20 m. Several processing steps are applied before using the original S-1 data, in order to convert the radar signal to a backscatter coefficient using the Sentinel Application Platform (SNAP). A detailed description of the retrieved processing steps is reported in Amazirh et al. (2018). Among the two available polarizations, the VV polarization is selected in this study for downscaling LST. The rationale behind using VV instead of VH, is that in Amazirh et al. (2018), the VV polarization was found to be more sensitive to SM variability over bare soil than VH over the same study area. S-1 VV backscatter (σ_{vv}^0) is aggregated at 100 m resolution, consistent with Landsat LST spatial resolution.

Table 2 summarizes the characteristics of the satellite data products used as input to, and for validation of disaggregation approaches.

Fig. 2 shows an example of the spatial variability of LST, f_{gv} and σ_{vv}^0

over the study site. Two growing stages (initial, and mid-season) are chosen for illustration purposes. For the initial stage most of the fields are under bare soil conditions with low fraction of green vegetation and the backscatter coefficient is mainly influenced by the SM and roughness, while LST mainly depends on atmospheric conditions and the soil water availability. During the mid-season, f_{gv} reaches its maximum value and the non-cultivated parcels generate higher value of LST (40 °C). The spatial variability of the backscatter is attributed to a combined effect of SM and vegetation (water content). Over cultivated areas, vegetation decreases the radar signal while SM increases it.

3. Disaggregation methods

Two disaggregation techniques are applied in this work using the same input data derived from microwave (radar) and optical (NDVI) data. The methodologies are tested over two different study areas, including a range of conditions (land use, soil hydric status, …). The two versions are named multi-linear regression (MLR) and radiative transfer model (RTM) techniques. Both methodologies are based on a scale invariant relationship between LST and other ancillary variables, which are statistically correlated to LST pixel by pixel. In this work the disaggregation methodologies were applied to aggregated Landsat derived-LST (as a first assessment by minimizing uncertainties in LR LST) and then applied to MODIS/Terra LST (as a real case application). The 100 m resolution was chosen as the target downscaling because it is the lowest spatial resolution at which all the input HR data are available. The diagram in Fig. 3 summarizes briefly the different disaggregation algorithms used in this work.

D0 algorithm requires no ancillary data. By cons, D1 (MLR), D1′ (MLR) and D2′ (RTM) need additional data to disaggregate LST. D1 algorithm is based on f_{gv} only, while D1′ and D2′ are based on both f_{gv} and σ_{vv}^0. A description of the MLR and RTM techniques is presented in the following subsections.

3.1. Multi-linear regressions (MLR) technique

The MLR technique is based on a linear regression at LR between LST and auxiliary data. This method was firstly developed by Kustas et al. (2003) using NDVI as a biophysical indicator of LST. In practice, a least-squares fit is performed between LST (T) and the f_{gv} aggregated at 1 km. Formally, The D1 algorithm is expressed as:

$$D1T_1 = LST_{km} + a \times (f_{gv} - f_{gv,km}) \tag{2}$$

with a being the regression coefficient of the least squares regression between LST_{km} and $f_{gv,km}$, and LST_{km} and $f_{gv,km}$ the LR LST and the aggregated f_{gv}, respectively.

The $D_1^{'}$ disaggregation algorithm is proposed to improve the D1 algorithm by inserting additional information about SM (information derived from the S-1 data). A MLR is performed between LST, f_{gv} and σ_{vv}^0 at LR:

$$D_1^{'}T_1 = LST_{km} + a^{'} \times (f_{gv} - f_{gv,km}) + b^{'} \times (\sigma_{vv}^0 - \sigma_{vv,km}^0) \tag{3}$$

With $a^{'}$ and $b^{'}$ being the slopes of the MLR equation at kilometric resolution, and $\sigma_{vv,km}^0$ the aggregated σ_{vv}^0.

Table 2
Technical characteristics of satellite products.

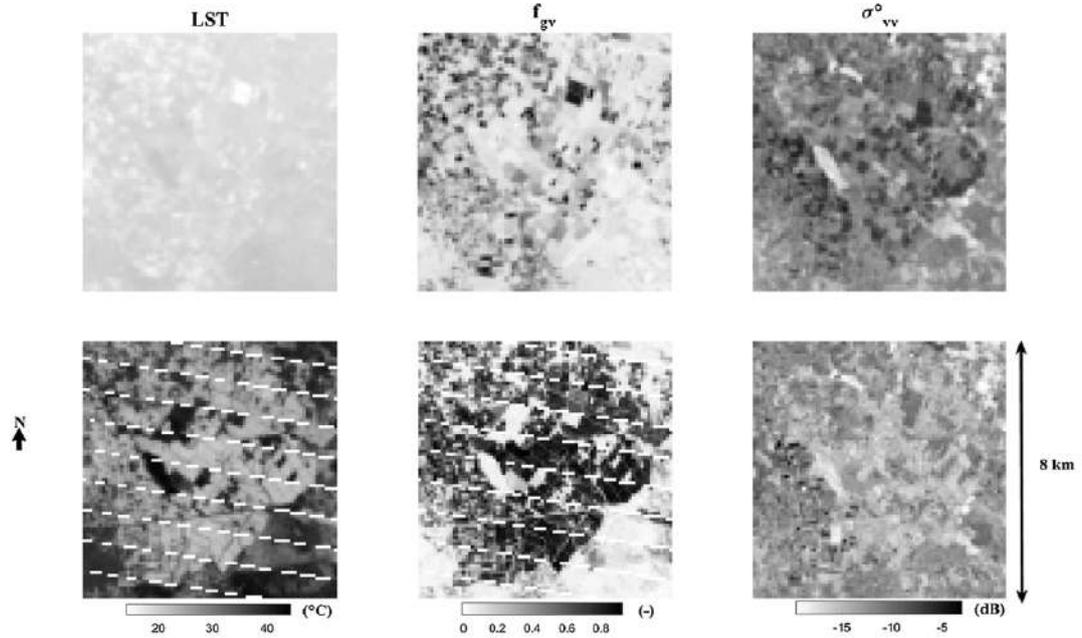| Sensors/Mission	Acquisition Time	Bands	Spatial resolution (m)	Temporal resolution (Day)
S-1 A/B	06:30 AM (descending) and 06:30 PM (ascending)	SAR/C-band	20	3–6
L-7/-8	−11:30 AM	– VNIR (L-7: B3 & B4; L-8: B4 & B5) – TIR (B6 for L-7 and B10 & B11 for L-8)	60 and 100 for TIR 30 for VNIR	8
MODIS/Terra	~11:30 AM	– TIR	~1000	1

14

Fig. 2. LST, f_{gv} and σ^0_{vv} 100 m resolution maps over R3 area at dates corresponding to the initial and mid-season growing stages: January 06 (top) and March 18 (bottom).

3.2. RTM technique

The RTM approach (Merlin et al., 2012) is based on the equation which is formally written as:

$$D_2^{'}T_2^{'} = LST_{km} + \Delta T_2^{'} \tag{4}$$

With the corrective term $\Delta T_2^{'}$ estimated using a RTM forced by HR input data derived from f_{gv} and σ^0_{vv}:

$$\Delta T_2^{'} = T_{sim}(f_{gv}, P_{\sigma^0_{vv}}) - \langle T_{sim}(f_{gv}, P_{\sigma^0_{vv}})\rangle_{KM} \tag{5}$$

With T_{sim} being the LST simulated by the RTM, $\langle\rangle_{KM}$ the resampling function from 100 m to 1 km resolution and $P_{\sigma^0_{vv}}$ a SM proxy derived from S-1 data:

$$P_{\sigma^0_{vv}} = \frac{\sigma^0_{vv} - \sigma^0_{vv,min}}{\sigma^0_{vv,max} - \sigma^0_{vv,min}} \tag{6}$$

where $\sigma^0_{vv,max}$ and $\sigma^0_{vv,min}$ are the maximum and minimum σ^0_{vv} during the

season and over the study area. $\sigma^0_{vv,min}$ and $\sigma^0_{vv,max}$ hence represent the driest and the wettest pixels observed at 100 m resolution over the study site, respectively.

The $T_{sim}(f_{gv}, P_{\sigma^0_{vv}})$ is calculated as:

$$T_{sim}(f_{gv}, P_{\sigma^0_{vv}}) = f_{gv} \times T_{fc,gv} + (1 - f_{gv}) \times T^{sm}_{bs} \tag{7}$$

With $T_{fc,gv}$ is the temperature of pixel with fully-covered vegetation and T^{sm}_{bs} the bare soil temperature estimated using a linearized RTM:

$$T^{sm}_{bs} = T_{bs,w} \times P_{\sigma^0_{vv}} + T_{bs,d} \times (1 - P_{\sigma^0_{vv}}) \tag{8}$$

where $T_{bs,w}$ and $T_{bs,d}$ are the wet and dry bare soil temperatures, respectively. Note that the temperature end-members ($T_{fc,gv}$, $T_{bs,w}$ and $T_{bs,d}$) are estimated based on a synergy between the LST-f_{gv} space, the LST-σ^0_{vv} space and a soil energy balance (EB) model. The sub-section below details the steps followed for estimating σ^0_{vv} and temperature endmembers.
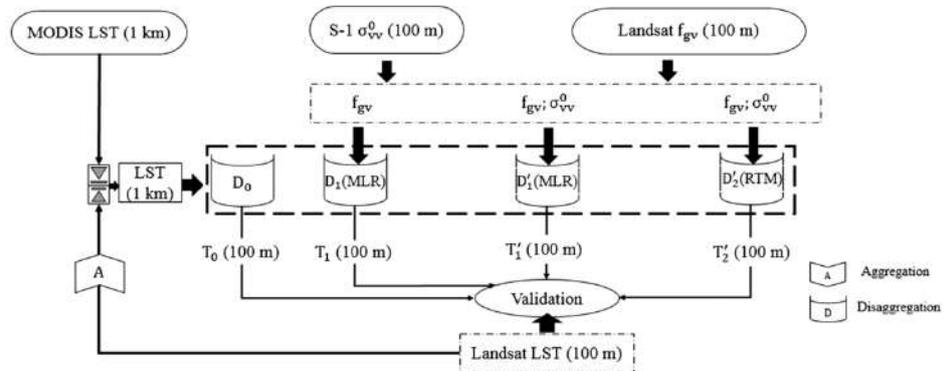

Fig. 3. Diagram showing the different disaggregation algorithms and their input/output data.
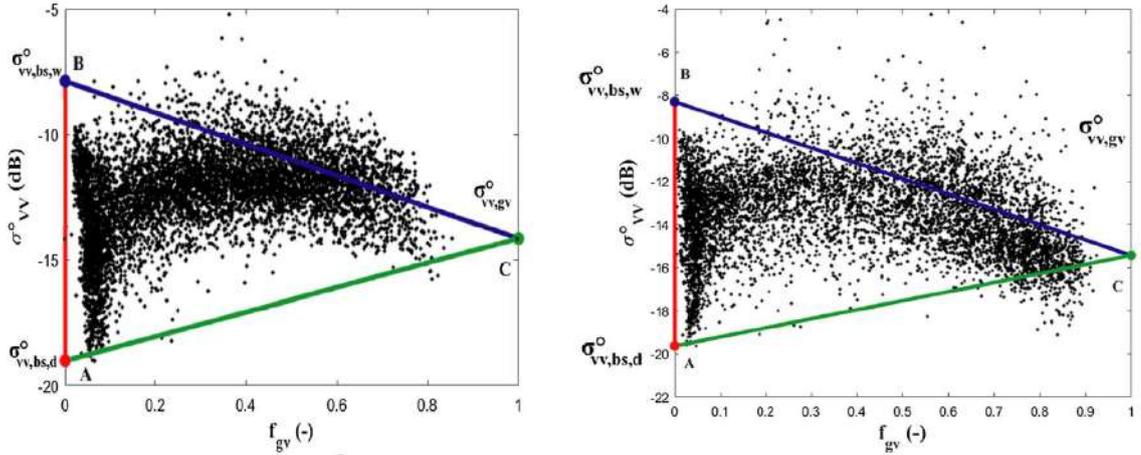
Page | 198

Fig. 4. Identification of the σ_{vv}^0 end-members using the S-1 backscatter plotted against fractional of green vegetation cover f_{gv} space for data on February 07 (left) and March 18 (right) over R3 site.
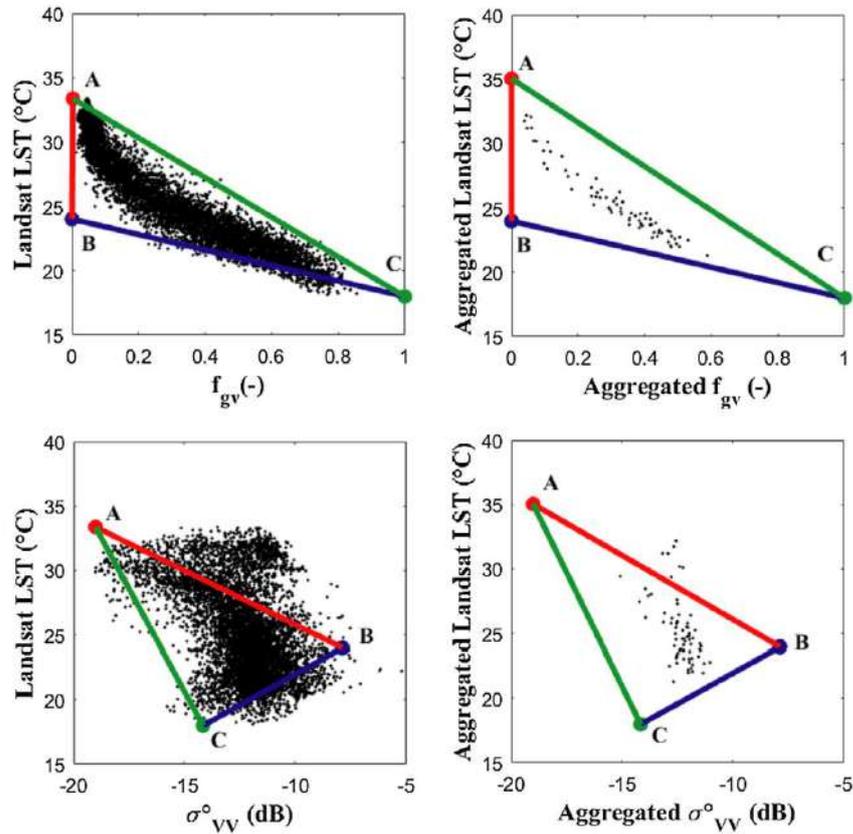
Fig. 5. Scatterplot of LST-f_{gv} and LST-σ_w^0 spaces at 100 m (left) and 1 km (right) resolution. In the LR case, extreme temperatures are estimated using a soil EB model on February 07 over R3 site.

3.2.1. End-members estimation

Before applying the disaggregation methodologies, the endmembers required in the RTM method, namely the three temperatures ($T_{fc,gv}$, $T_{bs,d}$ and $T_{bs,w}$) and the three backscatter coefficients (green vegetation $\sigma_{vv,gv}^0$, bare dry soil $\sigma_{vv,bs,d}^0$ and bare wet soil $\sigma_{vv,bs,w}^0$), are determined from available information. Temperature endmembers vary from date to date depending on the growing stage of vegetation and the soil hydric status over differences landscapes within the selected areas.

16

Page | 199

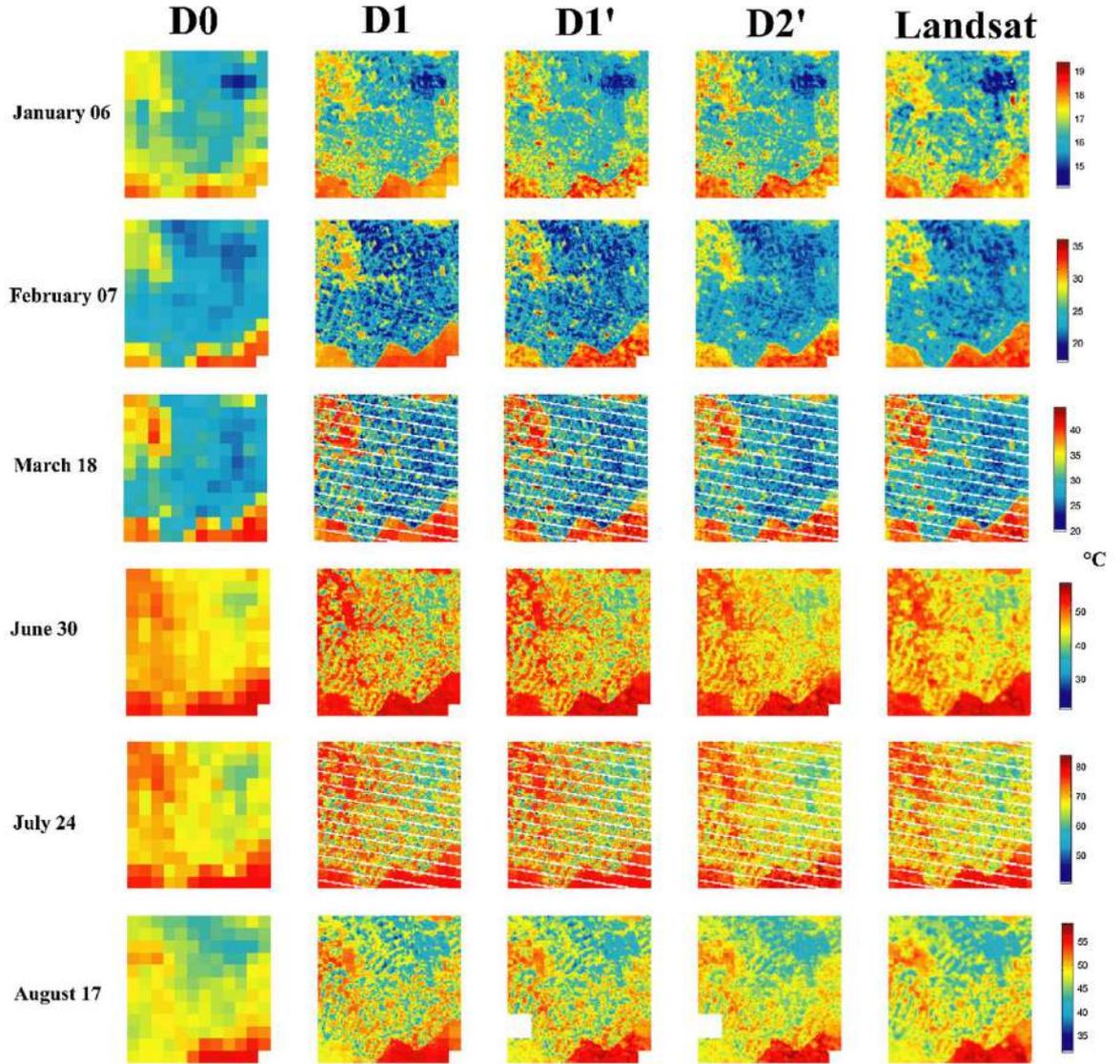**Fig. 6.** Maps of the LR (Landsat-aggregated) LST disaggregated by the four algorithms compared to the Landsat reference HR LST on six selected clear dates separately over Sidi Rahal area.

3.2.1.1. Backscatter endmembers. Fig. 4 presents the spatial variability of σ_{vv}^0 pixel by pixel compared to f_{gv}. Based on the observed $\sigma_{vv}^0 - f_{gv}$ space, the vegetation backscatter coefficient $\sigma_{vv,gv}^0$ is estimated as the σ_{vv}^0 corresponding to $f_{gv} = 1$, vertex C $(1, \sigma_{vv,gv}^0)$ in the σ_{vv}^0-f_{gv} space. The backscatter of bare soil in dry $(\sigma_{vv,bs,d}^0)$ and wet $(\sigma_{vv,bs,w}^0)$ conditions is considered as the minimum and maximum backscatters observed at low f_{gv} (< 0.2), vertex A $(0, \sigma_{vv,bs,d}^0)$ and B $(0, \sigma_{vv,bs,w}^0)$, respectively.

3.2.1.2. LST endmembers. In this study, the LST at HR is assumed to be unknown and therefore, extreme temperatures should be derived from LR LST and possibly other ancillary (meteorological, f_{gv}) data. Two different techniques are combined to estimate the LST endmembers: the contextual LST-f_{gv} space and an EB model forced by available meteorological data (Amazirh et al., 2018). In order to estimate soil extreme temperatures independently of remote sensing data a soil EB model is run to estimate $T_{bs,w}$ and $T_{bs,d}$. In practice, the wet and dry

conditions are simulated by setting the evaporation resistance r_{ss} values equal to zero and infinity, respectively. The EB model is outlined in the Appendix A.

On some days, the maximum temperature estimated by EB modeling appears relatively low compared to the maximum (both HR and LR) observed LST especially on the hottest days (summer) as founded in Amazirh et al. (2018). This is explained by the fact that the meteorological data used as forcing to EB model are collected at a wet alfalfa site, thus underestimating the 2-m air temperature over very dry and hot surface conditions. To correct for such a slight underestimation, the $T_{bs,d}$ is set to the maximum between the maximum value (T_{max}) observed at LR and EB estimation:

$$T_{bs,d} = \max[T_{max}, EB(r_{ss} = \infty)] \qquad (9)$$

The temperature of full cover vegetation ($T_{fc,gv}$) is set to the air temperature (Bastiaanssen et al., 1998; Gillies and Carlson, 1995;

Page | 200

Merlin, 2013; Roerink et al., 2000; Stefan et al., 2015).

A visual representation of the LST-f_{gv} and LST-σ_{vv}^0 spaces at a LR and HR are plotted in Fig. 5. The LST-f_{gv} space identifies three extremes values for f_{gv} (0, 1), while the LST-σ_{vv}^0 space is surrounded by the three extremes backscatter values ($\sigma_{vv,gv}^0$, $\sigma_{vv,bs,d}^0$ and $\sigma_{vv,bs,w}^0$) derived previously from the $\sigma_{vv}^0 - f_{gv}$ space. Note that the triangle formed in the sigma-f_{gv} space is not as well defined as in the LST-f_{gv} space. In fact, the spatial correlation between sigma and f_{gv} is affected by variabilities of both SM and soil roughness. Therefore, $\sigma_{vv,bs,d}^0$ more precisely

corresponds to a smooth (low roughness) dry soil and larger sigma values are expected over dry bare soil pixels with larger surface roughness (the data points on the other side of the AB segment).

The point A in Fig. 5 in the low resolution (aggregated LST) case is estimated using the soil energy balance model, which estimates LST in dry soil condition using meteorological data only i.e. independently from Landsat observations. For that reason, the simulated dry soil temperature is hence not necessarily equal to the maximum value observed within the study area from Landsat LST.
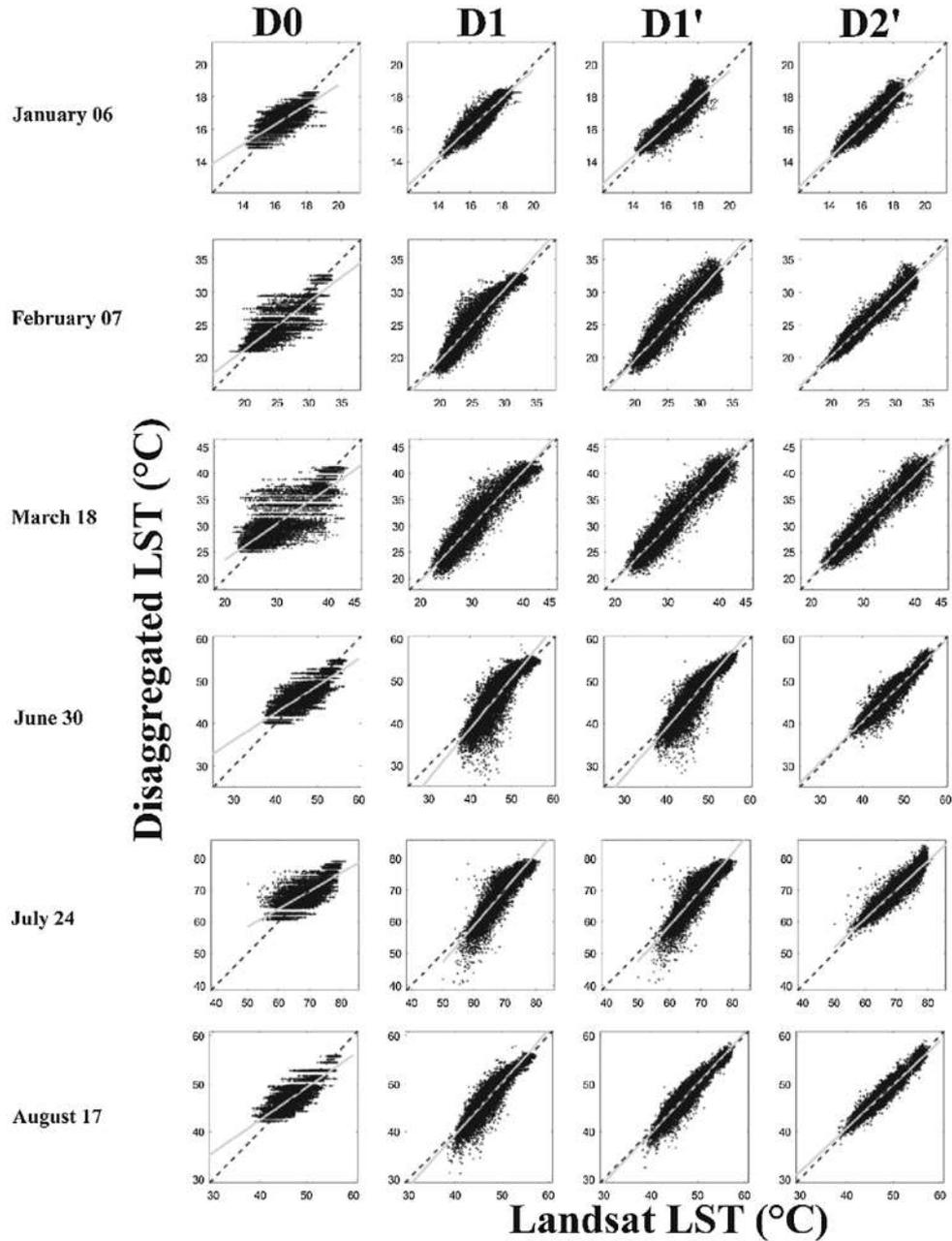

Fig. 7. Comparison between the LST disaggregated using each algorithm against the HR Landsat LST over Sidi Rahal area.

18

Table 3
Summary statistics of the disaggregation algorithms. Temperature endmembers are estimated from HR Landsat data over the Sidi Rahal site.

Date	R (–)				RMSE (°C)				Slope (–)			
	D0	D1	D1′	D2′	D0	D1	D1′	D2′	D0	D1	D1′	D2′
February 07	0.87	0.94	0.95	0.97	1.68	1.31	1.25	0.82	0.73	1.07	1.06	0.94
March 18	0.83	0.95	0.95	0.96	2.94	1.79	1.69	1.39	0.68	1.04	1.03	0.96
June 30	0.81	0.88	0.90	0.95	2.29	2.67	2.27	1.30	0.63	1.18	1.14	0.95
July 24	0.75	0.91	0.91	0.93	3.34	2.80	2.72	1.88	0.56	1.14	1.13	0.90
August 17	0.84	0.92	0.95	0.96	1.86	1.63	1.26	0.99	0.68	1.08	1.04	0.91
All	0.82	0.92	0.93	0.95	2.42	2.04	1.83	1.27	0.65	1.10	1.08	0.93

4. Results

The disaggregation approaches MLR (D1 and D1′) and RTM (D2′) are applied to the seven dates when all the satellite data are available. The disaggregated LST is evaluated against Landsat LST and in each case, disaggregation results are compared with those obtained in the no-disaggregation case (D0). A stepwise approach is presented by using the (1 km resolution) aggregated Landsat LST as the LR LST input prior
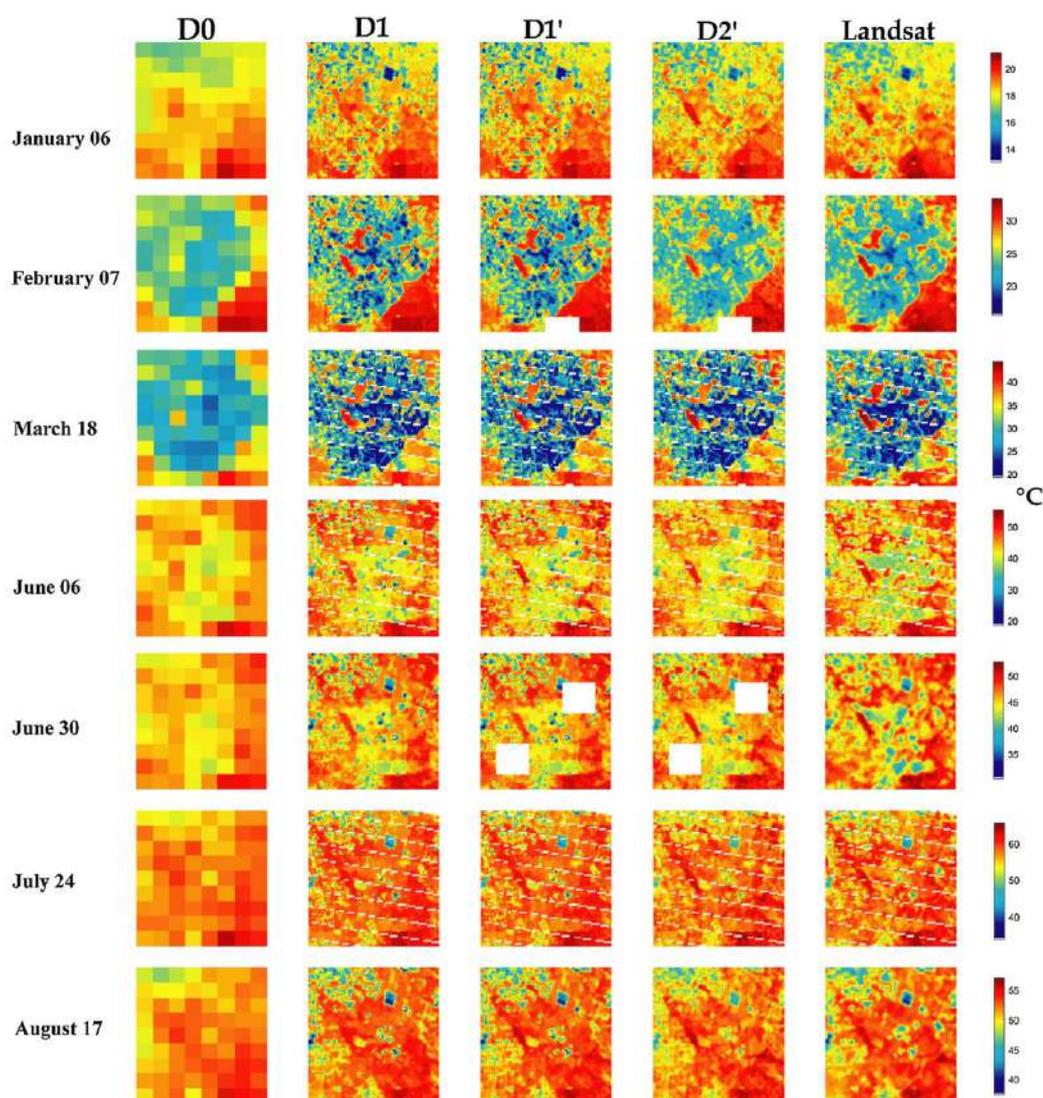

Fig. 8. Maps of the LR (Landsat-aggregated) LST disaggregated by the four algorithms compared to the Landsat reference HR LST on the seven selected dates separately over R3 area. The data gaps on February 07 and June 30 for D1′ and D2′ are attributed to S-1 raw data (no data value).

19

to the application to MODIS LST.

4.1. Application to aggregated Landsat-7/-8 data

As a first assessment, the disaggregation approaches are applied to aggregated Landsat LST. Moreover, in the case of RTM (D2′), the LST

end-members are estimated from the spaces built from HR data in order to reduce possible uncertainties. The disaggregation results are evaluated visually and quantitatively using the 100 m Landsat LST image as reference. Fig. 6 shows the LST images obtained from D0, D1, D1′ and D2′ for the six dates over Sidi Rahal rainfed site. The high spatial heterogeneity in soil properties and the land use over the selected areas
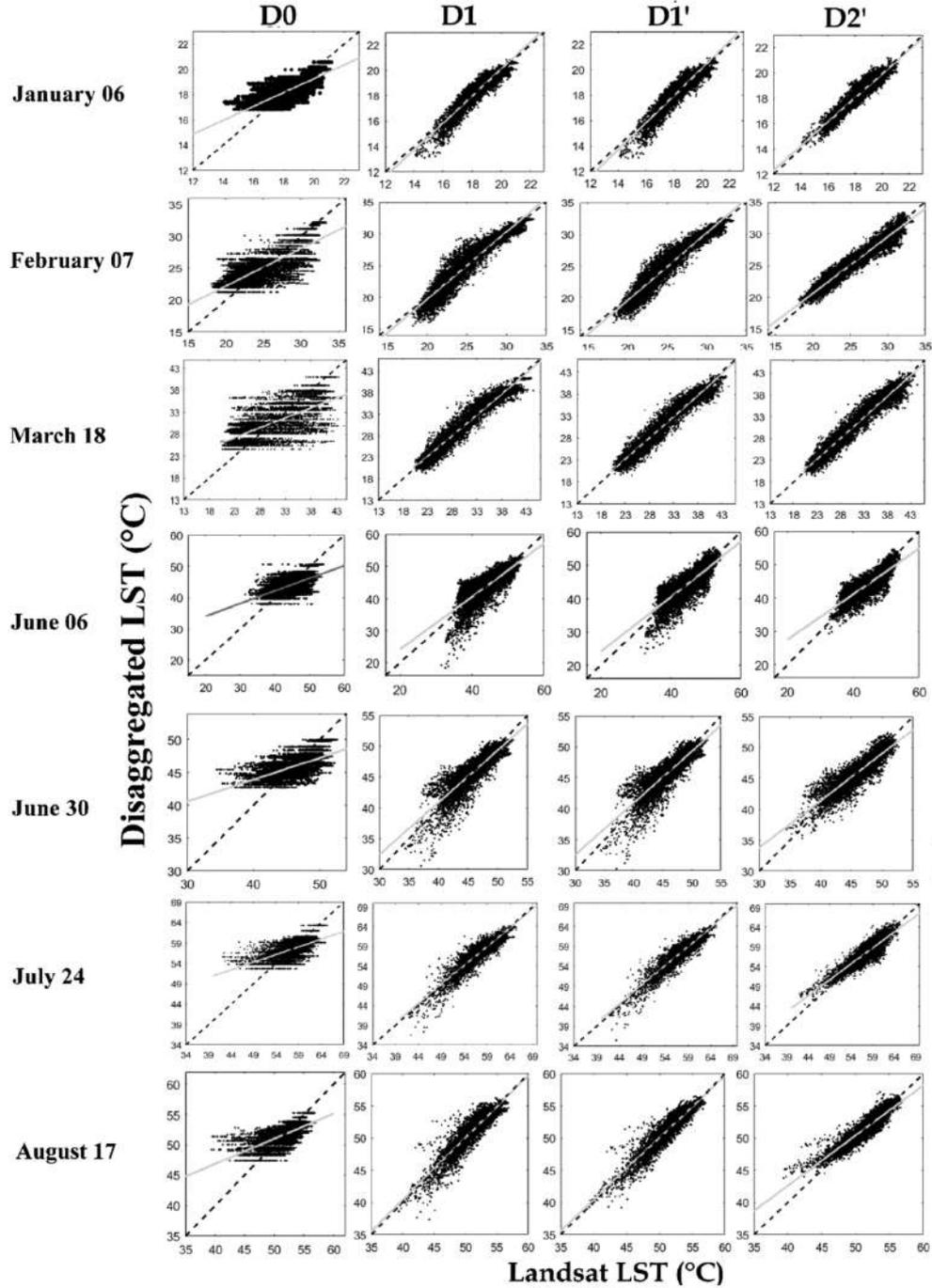

Fig. 9. Comparison between the LST disaggregated using each algorithm against the HR Landsat LST for the seven dates over R3 area.

Table 4

Summary statistics of the disaggregation algorithms. For D2′, LST endmembers are derived from the contextual spaces defined by HR ancillary data.

Date	R (–)				RMSE (°C)				Slope (–)			
	D0	D1	D1′	D2′	D0	D1	D1′	D2′	D0	D1	D1′	D2′
January 06	0.76	0.93	0.93	0.94	0.71	0.45	0.47	0.36	0.55	1.06	1.06	0.95
February 07	0.78	0.95	0.96	0.97	2.26	1.26	1.15	0.91	0.59	1.06	1.06	0.89
March 18	0.66	0.97	0.97	0.97	4.42	1.48	1.44	1.46	0.45	0.96	0.97	0.96
June 06	0.63	0.80	0.82	0.83	3.31	2.78	2.61	2.37	0.40	0.82	0.82	0.68
June 30	0.61	0.86	0.86	0.88	2.25	1.47	1.54	1.39	0.33	0.84	0.84	0.76
July 24	0.61	0.91	0.92	0.90	2.54	1.37	1.27	1.40	0.37	0.96	0.95	0.80
August 17	0.67	0.92	0.94	0.92	1.81	1.01	0.87	0.97	0.41	0.96	0.96	0.78
All	0.67	0.90	0.91	0.91	2.47	1.40	1.33	1.26	0.44	0.95	0.95	0.83

Table 5

Statistics of the disaggregation algorithms using temperature endmembers estimated by EB modeling (estimated by LST-f_{gv} spaces defined using HR data in parenthesis).

Date	R (–)	RMSE (°C)	Slope
January 06	0.87 (0.94)	0.85 (0.36)	1.27 (0.95)
February 07	0.97 (0.97)	0.89 (0.91)	0.92 (0.89)
March 18	0.96 (0.97)	1.60 (1.46)	0.88 (0.96)
June 06	0.83 (0.83)	2.40 (2.37)	0.66 (0.68)
June 30	0.87 (0.88)	1.43 (1.39)	0.73 (0.76)
July 24	0.86 (0.90)	1.65 (1.40)	0.79 (0.80)
August 17	0.87 (0.92)	1.21 (0.97)	0.80 (0.78)
All	0.89 (0.91)	1.43 (1.26)	0.86 (0.83)

induces strong variations in LST at the HR. All three D1, D1′ and D2′ algorithms provide more variability of LST than D0 algorithm which does not take into account the spatial variability at HR. It is also observed that the boxy artifact, meaning the block effect that still remains in the disaggregated LST at the LR (Agam et al., 2007b; Merlin et al., 2010), is reduced for D2′.

Results (Fig. 7) listed in Table 3, shows that the D2′ performs systematically better than the classical approach in all the cases, and provides more accurate results over the rainfed agriculture site. 1.27 °C is the minimum mean error it has been assessed using the D2′ algorithm compared to 2.04 °C by using the classical D1 approach.

A significant underestimation is observed for the low LST values during the hottest days (June 30, July 24 and August 17) using D1 and D1′. In contrast, the RTM D2′ LST fits correctly the Landsat observation. The most significant difference in performance is found for the February 07 image, when the bare soil dominates and the soil moisture variation controls the LST distribution. This means that radar data provide useful and independent information about the LST variability that the f_{gv} does not provide. The results indicate that the additional SM proxy used in the RTM algorithm allows more of the variability in LST to be captured over this scene.

The used algorithms in this paper have been tested over the 8 km by 8 km R3 site, in order to test the stability of the new approaches. Here we test the capacity of the new algorithm to capture LST variability over the complex fields. Fig. 8 show the spatial distribution and the temporal variation across the season of the disaggregated and Landsat LST over the R3 site for seven clear sky selected dates. We can observe a high variability of LST, which depends on the spatial heterogeneity of f_{gv} and/or SM.

To facilitate the comparison between the algorithms, they are plotted against the Landsat-derived temperature over the R3 site in Fig. 9. The statistical results for each algorithm are summarized in Table 4.

Data points in the scatterplot of the new (D2′) algorithm fall closer to the 1:1 line. Based on Table 4, D1, D1′ and D2′ generate better results than D0. The improved disaggregation algorithms show a decrease in

the root mean square error (RMSE) with 1.26, 1.15 and 0.91 °C using the D1, D1′ and D2′ algorithms, respectively compared to D0, which shows an error up to 2.2 °C on 07 February as an example.

The results change from date to date, but in general in our study case we found that, the MLR D1′ and RTM D2′ algorithms provide better results in term of correlation coefficient (R) and RMSE than the original approach D1. A better slope of the linear regression between disaggregated and Landsat LST is provided by D1 and D1′ whereas D2′ degrades slightly the slope on the same dates. The good results provided by the D1′ algorithm are attributed to an efficient calibration at LR of the coefficients of the regression fit between LST, f_{gv} and the radar backscatter. Moreover, the RTM model is sensitive to uncertainties in extreme LST, which in this case, were derived using HR Landsat data. The Landsat-derived temperature endmembers may be significantly biased in the case where/when surface conditions are relatively homogeneous (in particular over rainfed sites like Sidi Rahal).

The mean R between disaggregated and Landsat LST slightly increases from 0.90 to 0.91, and the mean RMSE decreases from 1.40 °C to 1.26 °C using the D1 and D2′ algorithms, respectively. In contrast, the mean slope is decreased from 0.95 to 0.83 using D1 and D2′ algorithms, respectively.

Since HR Landsat LST is assumed to be unavailable in our disaggregation exercise, the LST endmembers are now derived from LR LST data only (instead of using HR LST data as previously). Table 5 lists the RMSE, R, and slope of the linear regression between disaggregated and Landsat LST for D2′ algorithm, using the temperature endmembers derived from LR LST data combined with EB model estimates.

A valuable discussion is presented in this paragraph that helps to see the impact of the LST endmembers estimation on the disaggregation results. Looking at the Table 5, the statistical results clearly show that the disaggregated LST is more accurate when using the LST endmembers derived from Landsat HR data than those derived from EB modeling (combined with LR data). In contrast, using EB-derived extreme LST provides a slightly better mean slope (0.86) than when using HR data (0.83). In order to assess the main causes behind that, the $T_{bs,d}$ estimated by the EB model is compared to the maximum value observed at HR. On January 06, an overestimation of about 8 °C of $T_{bs,d}$ is observed when using the EB model (data not shown here), which leads to slightly poorer results compared to when using temperature endmembers derived from HR spaces. It is suggested that the temperature endmembers derived from EB modeling are more uncertain than those derived from HR spaces, especially over a highly heterogeneous area like R3.

4.2. Application to MODIS data

In this section, the disaggregation methodologies D0, D1, D1′ and D2′ are applied to MODIS/Terra (MOD11-A1) LST product over only the R3 site. It is reminded that only the MODIS images acquired on the same dates as Landsat data are used for the evaluation. For the rainfed Sidi Rahal site, the MODIS LST data are affected by clouds where the
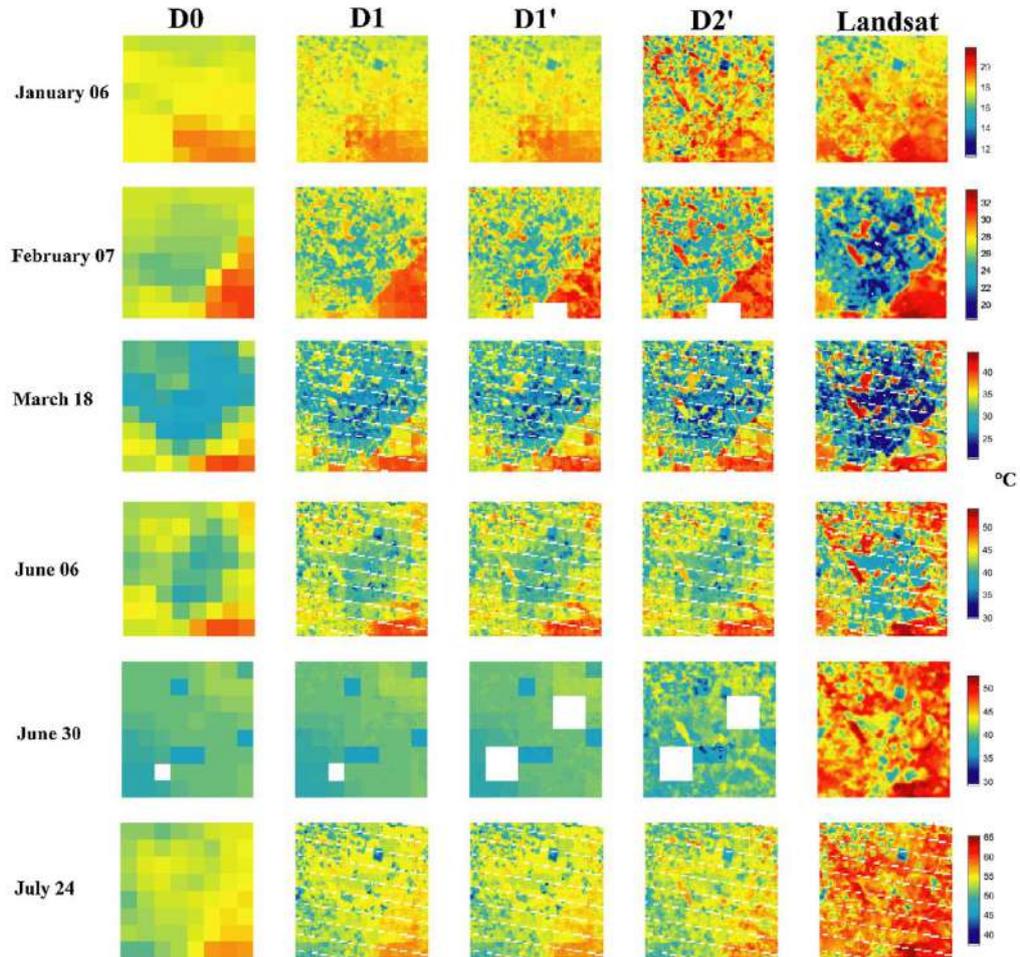
Fig. 10. Maps of the MODIS LST disaggregated at HR by the four algorithms compared to the Landsat reference LST map on the six clear sky dates over R3 area.

contaminated pixel are masked with the MODIS cloud mask product. Therefore no MODIS image is clear, which limits the application to MODIS data over this site. Fig. 10 compares the disaggregation images with the 100 m resolution Landsat LST for six selected dates. Note that the MODIS image on August 17 is affected by clouds and was thus removed. In the implementation of D2′, the temperature end-members are estimated using EB modeling.

Looking at the spatial patterns of disaggregated LST maps, the values in all maps range from 14 °C to 60 °C. The boxy effect anomalies are less apparent for D2′ algorithm compared to the original algorithms. Generally, the disaggregation algorithms of MODIS LST show a lower maximum and higher minimum than Landsat LST.

The downscaling results and statistics are shown in Fig. 11 and reported in Table 6. The D2′ algorithm provides better results than the MLR approaches (D1 and D1′). Results in Table 6 shows that the minimum mean RMSE is 3.35 °C and the highest mean R is 0.75, which are both obtained with D2′ algorithm. A systematic negative bias is apparent in the disaggregated temperature using MODIS LST, quite consistent with the mean bias between MODIS and Landsat LST estimated as 4 °C in this work. As expected the disaggregation method does not yield similar results when applied to MODIS/Terra LST instead of aggregated Landsat data. This is due to the discrepancy between MODIS and Landsat data, and to different sensitivities of MLR and RTM algorithms to uncertainties (including bias) in LR input data. However, in

our study case over the selected irrigated perimeter, the new algorithm D2′ clearly improves the disaggregated LST against the classical approaches. When comparing the new algorithm D2′ to the classical one D1, D2′ generally shows the best results with an increase of R from 0.83 to 0.86 and a decrease in the RMSE from 3.57 to 2.20 °C, respectively (18 March as an example). By comparing the performance of the disaggregation algorithms using aggregated Landsat and real MODIS LST, the aggregated Landsat LST provides better results than MODIS LST. The reason is due to the fact that real images have an additional noise in the LST data which may be related to sensor registration (Essa et al., 2013). In addition, part of the error could be attributed to differences in the algorithms used to retrieve LST, which are not the same (split-window for MODIS and single-channel for Landsat). A relatively poor performance is observed for D1 and D1′ on 30 June compared to the new D2′ methodology. On that date MODIS LST largely underestimates Landsat LST. However, D2′ provides a much better R (0.55 instead of 0.1 for all the other approaches). We argue that the RTM method (D2′), is more accurate and more robust than MLR method (D1′) especially when applying it to real data (MODIS LST). In particular, it is much less sensitive to uncertainties in LR LST than MLR method. Based on the acquired results, RTM algorithm performed better than the classical algorithm and in most cases than the RTM method where it stabilizes the errors and systematically increases the R between disaggregated and Landsat LST.
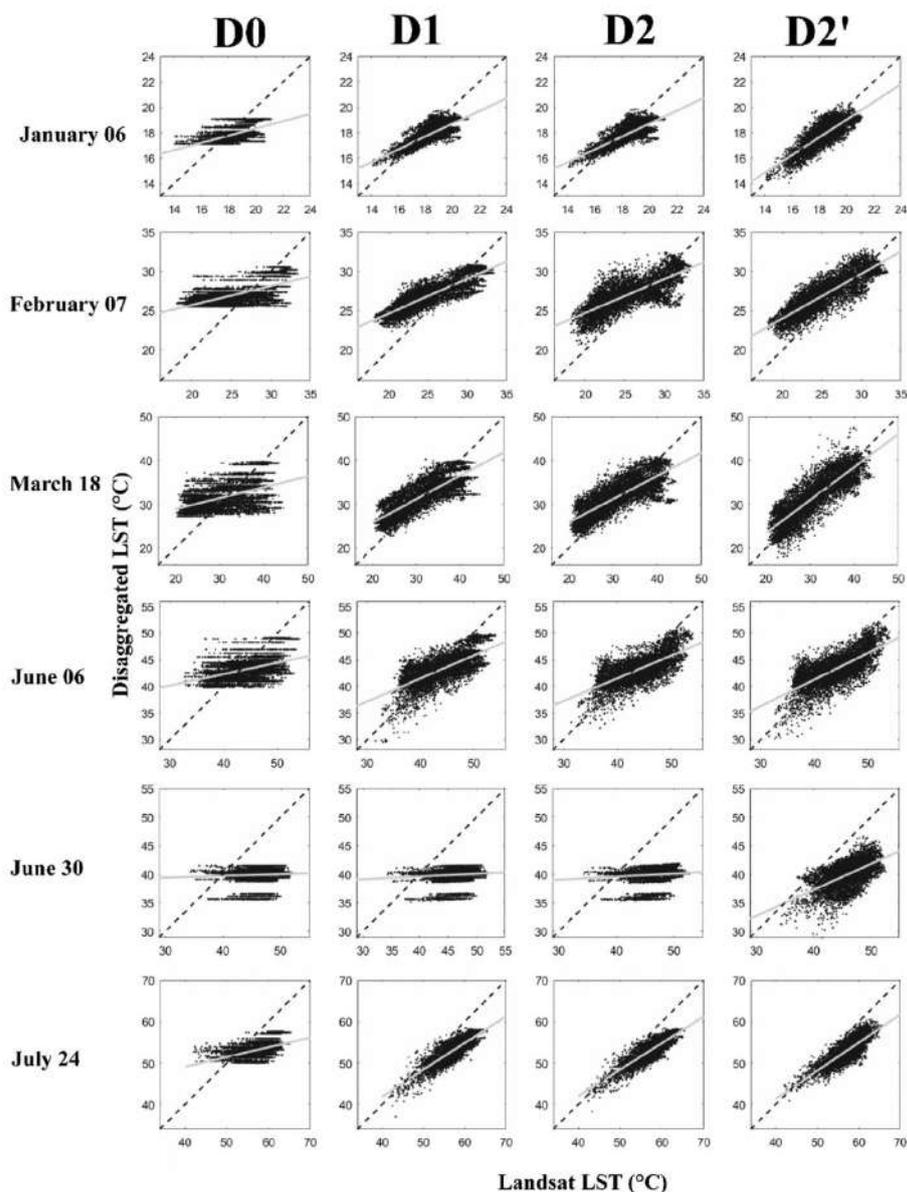
Fig. 11. Comparison between the disaggregated LST using each algorithm against the HR Landsat LST for the seven dates over R3 area.

Table 6

Summary statistics of the disaggregation algorithms. Temperature endmembers are estimated from EB modeling.

Date	R (–)				RMSE (°C)				Slope			
	D0	D1	D1′	D2′	D0	D1	D1′	D2′	D0	D1	D1′	D2′
January 06	0.56	0.80	0.80	0.75	1.03	0.83	0.83	1.09	0.28	0.50	0.50	1.01
February 07	0.65	0.87	0.76	0.86	3.34	2.73	2.94	2.57	0.24	0.44	0.43	0.59
March 18	0.51	0.83	0.80	0.86	5.16	3.57	3.71	2.20	0.24	0.53	0.53	0.65
June 06	0.47	0.70	0.71	0.71	3.84	3.16	3.14	3.09	0.21	0.43	0.42	0.44
June 30	0.07	0.12	0.13	0.55	6.71	6.68	6.71	6.44	0.03	0.05	0.05	0.38
July 24	0.47	0.84	0.84	0.78	5.14	4.64	4.64	4.71	0.23	0.64	0.64	0.58
All	0.45	0.69	0.67	0.75	4.20	3.60	3.66	3.35	0.20	0.43	0.43	0.61

23

5. Conclusion

The objective of this paper is to disaggregate MODIS/Terra LST data to 100 m resolution over an irrigated semi-arid area. The idea is to include the high spatial resolution soil moisture variability in the dis-aggregation algorithm, in addition to the classical fraction of green vegetation cover. The approaches are tested over two heterogonous sites: 8 km by 8 km irrigated perimeter and a 12 km by 12 km rainfed area south of Marrakech during the 2015–2016 growing season. The algorithms are firstly tested using the 1 km aggregated Landsat-7/-8 surface temperature as input to avoid the errors and random un-certainty produced by the registration of LR sensors like MODIS. Then, the performance of the used algorithms is assessed using MODIS/Terra daytime LST as input. The Landsat LST at 100 m resolution is mainly used for validation purposes.

Best results are obtained with the new algorithm denoted D2′ when using MODIS LST data based on the RTM equation, compared to the procedure based on a linear regression between f_{gv} and LST, and also compared to the multi-linear regression between f_{gv}, σ_{vv}^0 and LST. Since the selected area showed a heterogeneity in terms of vegetation type and soil water status, we conclude that the new algorithm produces more stable and robust results during the selected year. 0.83 °C and 0.86 were the lowest RMSE and the highest correlation coefficient as-sessed using the new algorithm. These results are encouraging and can be used to reinforce and to improve the application of downscaling procedure to low resolution thermal sensors. Sentinel-2 (S-2) is a continuity of Landsat reflectances with an improvement in the spatio-temporal resolution. Therefore, the application of the disaggregation algorithm to MODIS LST using S-2 ancillary data will improve the temporal resolution to 5 days. This work also can be considered as a basis for new missions dedicated to provide TIR data at high spatio-temporal resolution (India-France joint satellite mission, Trishna). Further research must be undertaken to incorporate the vegetation water stress into the disaggregation methods, possibly by integrating the S-1 VH polarization data, which are more sensitive to vegetation water content effects than VV polarization.

Appendix A

To run EB model, the soil temperature is set to air temperature (T_{air}) and an iterative loop on the soil temperature is made until the thermal equilibrium is reached by minimizing the cost function (F(LST)) by finding the LST value corresponding to the EB closure:

$$F(LST) = (R_n - G - H - LE)^2 \tag{A.1}$$

Starting from the EB model equation, where the available energy is set equal to the turbulent fluxes:

$$R_n - G = LE + H \tag{A.2}$$

with R_n is the surface net radiation is expressed as:

$$R_n = (1 - \alpha)r_g + \varepsilon(R_{atm} - \sigma T_s^4) \tag{A.3}$$

with $\sigma = 5.67 \times 10^{-8}$ the Stephan-Boltzmann constant (W m^{-2} K^{-4}). α (–) being the surface albedo (set to 0.15), r_g (W m^{-2}) is the global radiation, ε (–) is the surface emissivity (set to 0.95), R_{atm} is the atmospheric longwave radiation (W m^{-2}) and. The downward atmospheric radiation at surface level is expressed as:

$$R_{atm} = \varepsilon_a \times \sigma T_{air}^4 \tag{A.4}$$

where ε_a is the atmospheric emissivity (Brutsaert, 1975):

$$\varepsilon_a = 1.24 \times \left(\frac{e_a}{T_{air}}\right)^{\frac{1}{7}} \tag{A.5}$$

with $\quad e_a = e_s(T_{air}) \times \frac{rh_a}{100} \tag{A.6}$

rh_a (%) being the air relative humidity and e_s the saturated water vapour pressure (kPa) given by:

$$e_s = 0.611 \times e^{\left(\frac{17.27 \times T_{air}}{T_{air} + 273.3}\right)} \tag{A.7}$$

The ground flux G is estimated as a fraction of net radiation at the surface R_n:

$$G = cg. R_n \tag{A.8}$$

with cg being a fractional empirical coefficient set to 0.2.

The sensible heat flux is given by:

$$H = \rho c_p \frac{T_s - T_{air}}{r_{a,h}} \tag{A.9}$$

24

The latent heat flux is estimated as:

$$LE = \frac{\rho c_p}{\gamma} \frac{e_s - e_a}{r_{a,h} + r_{ss}}$$

(A.10)

References

Agam, N., Kustas, W.P., Anderson, M.C., Li, F., Colaizzi, P.D., 2007a. Utility of thermal sharpening over Texas high plains irrigated agricultural fields. J. Geophys. Res. Atmos. 112, 1–10. https://doi.org/10.1029/2007JD008407.

Agam, N., Kustas, W.P., Anderson, M.C., Li, F., Neale, C.M.U., 2007b. A vegetation index based technique for spatial sharpening of thermal imagery. Remote Sens. Environ. 107, 545–558. https://doi.org/10.1016/j.rse.2006.10.006.

Amazirh, A., Er-Raki, S., Chehbouni, A., Rivalland, V., Diarra, A., Khabba, S., Ezzahar, J., Merlin, O., 2017. Modified Penman-Monteith equation for monitoring evapotranspiration of wheat crop: relationship between the surface resistance and remotely sensed stress index. Biosyst. Eng. 164, 68–84. https://doi.org/10.1016/j.biosystemseng.2017.09.015.

Amazirh, A., Merlin, O., Er-raki, S., Gao, Q., Rivalland, V., Malbeteau, Y., Khabba, S., José, M., 2018. Retrieving surface soil moisture at high spatio-temporal resolution from a synergy between Sentinel-1 radar and Landsat thermal data: a study case over bare soil. Remote Sens. Environ. 211, 321–337. https://doi.org/10.1016/j.rse.2018.04.013.

Anderson, M.C., Norman, J.M., Kustas, W.P., Houborg, R., Starks, P.J., Agam, N., 2008. A thermal-based remote sensing technique for routine mapping of land-surface carbon, water and energy fluxes from field to regional scales. Remote Sens. Environ. 112, 4227–4241. https://doi.org/10.1016/j.rse.2008.07.009.

Bastiaanssen, W.G.M., Menenti, M., Feddes, R.A., Holtslag, A.A.M., 1998. A remote sensing surface energy balance algorithm for land (SEBAL). J. Hydrol. https://doi.org/10.1016/S0022-1694(98)00253-4.

Bindhu, V.M., Narasimhan, B., Sudheer, K.P., 2013. Development and verification of a non-linear disaggregation method (NL-DisTrad) to downscale MODIS land surface temperature to the spatial scale of Landsat thermal data to estimate evapotranspiration. Remote Sens. Environ. 135, 118–129. https://doi.org/10.1016/j.rse.2013.03.023.

Boulet, G., Chehbouni, A., Gentine, P., Duchemin, B., Ezzahar, J., Hadria, R., 2007. Monitoring water stress using time series of observed to unstressed surface temperature difference. Agric. For. Meteorol. 146, 159–172. https://doi.org/10.1016/j.agrformet.2007.05.012.

Brunsell, N.A., Gillies, R.R., 2003. Length scale analysis of surface energy fluxes derived from remote sensing. J. Hydrometeorol. 4, 1212–1219. https://doi.org/10.1175/1525-7541(2003) 004<1212:lsaose>2.0.co;2.

Brutsaert, W., 1975. On a derivable formula for long-wave radiation from clear skies. Water Resour. Res. 4, 742–744. https://doi.org/10.1029/WR011i005p00742.

Chehbouni, A.H., Escadafal, R., Duchemin, B., Boulet, G., Simonneaux, V., Dedieu, G., Mougenot, B., Khabba, S., Kharrou, H., Maisongrande, P., Merlin, O., Chaponnière, A., Ezzahar, J., Er-Raki, S., Hoedjes, J., Hadria, R., Abourida, A., Cheggour, A., Raibi, F., Boudhar, A., Benhadj, I., Hanich, L., Benkaddour, A., Guemouria, N., Chehbouni, A.H., Lahrouni, A., Olioso, A., Jacob, F., Williams, D.G., Sobrino, J.A., 2008. An integrated modelling and remote sensing approach for hydrological study in arid and semi-arid regions: the SUDMED Programme. Int. J. Remote Sens. 29, 5161–5181. https://doi.org/10.1080/01431160802036417.

Chen, L., Yan, G.J., Ren, H.Z., Li, A.H., 2010. A modified vegetation index based algorithm for thermal imagery sharpening. In: 2010 IEEE International Geoscience and Remote Sensing Symposium, https://doi.org/10.1109/igarss.2010.5651428.

Crow, W.T., Wood, E.F., 2003. The assimilation of remotely sensed soil brightness temperature imagery into a land surface model using Ensemble Kalman filtering: a case study based on ESTAR measurements during SGP97. Adv. Water Resour. 26, 137–149. https://doi.org/10.1016/S0309-1708(02)00088-X.

Dominguez, A., Kleissl, J., Luvall, J.C., Rickman, D.L., 2011. High-resolution urban thermal sharpener (HUTS). Remote Sens. Environ. 115, 1772–1780. https://doi.org/10.1016/j.rse.2011.03.008.

Duchemin, B., Hagolle, O., Mougenot, B., Benhadj, I., Hadria, R., Simonneaux, V., Ezzahar, J., Hoedjes, J., Khabba, S., Kharrou, M.H., Boulet, G., Dedieu, G., Er-Raki, S., Escadafal, R., Olioso, A., Chehbouni, A.G., 2008. Agrometeorological study of semiarid areas: an experiment for analysing the potential of time series of FORMOSAT-2 images (Tensift-Marrakech plain). Int. J. Remote Sens. 29, 5291–5299. https://doi.org/10.1080/01431160802036482.

Er-Raki, S., Amazirh, A., Ayyoub, A., Khabba, S., Merlin, O., Ezzahar, J., Chehbouni, A., 2018. Integrating thermal surface temperature into Penman-Monteith model for estimating evapotranspiration and crop water stress of orange orchard in semi-arid region. Acta Horticult. https://doi.org/10.17660/ActaHortic. 2018.1197.12.

Er-Raki, S., Chehbouni, A., Boulet, G., Williams, D.G., 2010. Using the dual approach of FAO-56 for partitioning ET into soil and plant components for olive orchards in a semi-arid region. Agric. Water Manage. 97, 1769–1778. https://doi.org/10.1016/j.agwat.2010.06.009.

Er-Raki, S., Chehbouni, A., Guemouria, N., Duchemin, B., Ezzahar, J., Hadria, R., 2007. Combining FAO-56 model and ground-based remote sensing to estimate water consumptions of wheat crops in a semi-arid region. Agric. Water Manage. 87, 41–54. https://doi.org/10.1016/j.agwat.2006.02.004.

Essa, W., van der Kwast, J., Verbeiren, B., Batelaan, O., 2013. Downscaling of thermal images over urban areas using the land surface temperature–impervious percentage relationship. Int. J. Appl. Earth Observ. Geoinform. 23, 95–108. https://doi.org/10.1016/j.jag.2012.12.007. ISSN 0303-2434.

Ghosh, A., Joshi, P.K., 2014. Hyperspectral imagery for disaggregation of land surface temperature with selected regression algorithms over different land use land cover scenes. ISPRS J. Photogramm. Remote Sens. 96, 76–93. https://doi.org/10.1016/j.isprsjprs.2014.07.003.

Gillies, R.R., Carlson, T.N., 1995. Thermal remote-sensing of surface soil-water content with partial vegetation cover for incorporation into climate-models. J. Appl. Meteorol. 34, 745–756. https://doi.org/10.1175/1520-0450(1995) 034<0745:trsoss>2.0.co;2.

Gutman, G., Ignatov, A., 1998. The derivation of the green vegetation fraction from NOAA/AVHRR data for use in numerical weather prediction models. Int. J. Remote Sens. 19, 1533–1543. https://doi.org/10.1080/014311698215333.

Ha, W., Gowda, P.H., Howell, T.A., 2013. A review of downscaling methods for remote sensing-based irrigation management: Part I. Irrig. Sci. 31, 831–850. https://doi.org/10.1007/s00271-012-0331-7.

Hansen, J., Ruedy, R., Sato, M., Lo, K., 2010. Global surface temperature change. Rev. Geophys. 48. https://doi.org/10.1029/2010RG000345.

Inamdar, A.K., French, A., 2009. Disaggregation of GOES land surface temperatures using surface emissivity. Geophys. Res. Lett. 36, L02408. https://doi.org/10.1029/2008GL036544.

Jarlan, L., Khabba, S., Er-Raki, S., Le Page, M., Hanich, L., Fakir, Y., Merlin, O., Mangiarotti, S., Gascoin, S., Ezzahar, J., Kharrou, M.H., Berjamy, B., Saaïdi, A., Boudhar, A., Benkaddour, A., Laftouhi, N., Abaoui, J., Tavernier, A., Boulet, G., Simonneaux, V., Driouech, F., El Adnani, M., El Fazziki, A., Amenzou, N., Raibi, F., Escadafal, R., 2015. Remote sensing of water resources in the semi-arid Mediterranean areas: the joint international laboratory TREMA. Int. J. Remote Sensing.

Karnieli, A., Agam, N., Pinker, R.T., Anderson, M., Imhoff, M.L., Gutman, G.G., Panov, N., Goldberg, A., 2010. Use of NDVI and land surface temperature for drought assessment: merits and limitations. J. Clim. 23, 618–633. https://doi.org/10.1175/2009JCLI2900.1.

Khabba, S., Jarlan, L., Er-Raki, S., Le Page, M., Ezzahar, J., Boulet, G., Simonneaux, V., Kharrou, M.H., Hanich, L., Chehbouni, G., 2013. The SudMed program and the joint international laboratory TREMA: a decade of water transfer study in the soil-plant-atmosphere system over irrigated crops in semi-arid area. Procedia Environ. Sci. 19, 524–533.

Kogan, F.N., 2001. Operational space technology for global vegetation assessment. Bull. Am. Meteorol. Soc. 82, 1949–1964. https://doi.org/10.1175/1520-0477(2001) 082<1949:OSTFGV>2.3.CO;2.

Kustas, W., Anderson, M., 2009. Advances in thermal infrared remote sensing for land surface modeling. Agric. For. Meteorol. 149, 2071–2081. https://doi.org/10.1016/j.agrformet.2009.05.016.

Kustas, W.P., Norman, J.M., Anderson, M.C., French, A.N., 2003. Estimating subpixel surface temperatures and energy fluxes from the vegetation index-radiometric temperature relationship. Remote Sensing Environ. 85, 429–440. https://doi.org/10.1016/S0034-4257(03)00036-1.

Liu, D., Zhu, X., 2012. An enhanced physical method for downscaling thermal infrared radiance. IEEE Geosci. Remote Sens. Lett. 9, 690–694. https://doi.org/10.1109/LGRS.2011.2178814.

Liu, Y., Hiyama, T., Yamaguchi, Y., 2006. Scaling of land surface temperature using satellite data: a case examination on ASTER and MODIS products over a heterogeneous terrain area. Remote Sens. Environ. 105, 115–128. https://doi.org/10.1016/j.rse.2006.06.012.

Merlin, O., 2013. An original interpretation of the wet edge of the surface temperature-albedo space to estimate crop evapotranspiration (SEB-1S), and its validation over an irrigated area in northwestern Mexico. Hydrol. Earth Syst. Sci. 17, 3623–3637. https://doi.org/10.5194/hess-17-3623-2013.

Merlin, O., Chehbouni, A.G., Kerr, Y.H., Njoku, E.G., Entekhabi, D., 2005. A combined modeling and multispectral/multiresolution remote sensing approach for disaggregation of surface soil moisture: application to SMOS configuration. IEEE Trans. Geosci. Remote Sens. 43, 2036–2050. https://doi.org/10.1109/TGRS.2005.853192.

Merlin, O., Duchemin, B., Hagolle, O., Jacob, F., Coudert, B., Chehbouni, G., Dedieu, G., Garatuza, J., Kerr, Y., 2010. Disaggregation of MODIS surface temperature over an agricultural area using a time series of Formosat-2 images. Remote Sens. Environ. 114, 2500–2512. https://doi.org/10.1016/j.rse.2010.05.025.

Merlin, O., Jacob, F., Wigneron, J., Member, S., Walker, J., Chehbouni, G., 2012. Multidimensional disaggregation of land surface and microwave-L bands 50, 1864–1880.

Olivera-Guerra, L., Mattar, C., Merlin, O., Durán-Alarcón, C., Santamaría-Artigas, A., Fuster, R., 2017. An operational method for the disaggregation of land surface temperature to estimate actual evapotranspiration in the arid region of Chile. ISPRS J. Photogramm. Remote Sens. 128, 170–181. https://doi.org/10.1016/j.isprsjprs.2017.03.014.

Olivera-Guerra, L., Merlin, O., Er-Raki, S., Khabba, S., Escorihuela, M.J., 2018. Estimating the water budget components of irrigated crops: combining the FAO-56 dual crop coefficient with surface temperature and vegetation index data. Agric. Water Manage. 208, 120–131. https://doi.org/10.1016/j.agwat.2018.06.014.

25

Price, J.C., 1982. Estimation of regional scale evapotranspiration through analysis of satellite thermal-infrared data. IEEE Trans. Geosci. Remote Sens. 20, 286–292. https://doi.org/10.1109/TGRS.1982.350445.

Roerink, G.J., Su, Z., Menenti, M., 2000. S-SEBI: a simple remote sensing algorithm to estimate the surface energy balance. Phys. Chem. Earth Part B-Hydrol. Oceans Atmos. 25, 147–157. https://doi.org/10.1016/S1464-1909(99)00128-8.

Sandholt, I., Nielsen, C., Stisen, S., 2009. A simple downscaling algorithm for remotely sensed land surface temperature. American Geophysical Union, Spring Meeting 2009, Abstract id. H24A-04.

Sandholt, I., Rasmussen, K., Andersen, J., 2002. A simple interpretation of the surface temperature/vegetation index space for assessment of surface moisture status. Remote Sens. Environ. 79, 213–224. https://doi.org/10.1016/S0034-4257(01)00274-7.

Stefan, V.G., Merlin, O., Er-Raki, S., Escorihuela, M.J., Khabba, S., 2015. Consistency between in situ, model-derived and high-resolution-image-based soil temperature endmembers: towards a robust data-based model for multi-resolution monitoring of crop evapotranspiration. Remote Sensing 7, 10444–10479. https://doi.org/10.3390/rs70810444.

Tardy, B., Rivalland, V., Huc, M., Hagolle, O., Marcq, S., Boulet, G., 2016. A software tool for atmospheric correction and surface temperature estimation of landsat infrared thermal data 8, 696. https://doi.org/10.3390/rs8090696.

Wan, Z., 1996. A generalized split-window algorithm for retrieving land-surface temperature from space. IEEE Trans. Geosci. Remote Sens. 34, 892–905. https://doi.org/10.1109/36.508406.

Wan, Z., Zhang, Y., Zhang, Q., Li, Liang, Z., 2002. Validation of the land-surface temperature products retrieved from terra moderate resolution imaging spectroradiometer data. Remote Sens. Environ. 38, 163–180. https://doi.org/10.1016/S0034-4257(02)00093-7.

Williamson, H.D., 1988. Evaluation of middle and thermal infrared radiance in indices used to estimate GLAI. Int. J. Remote Sens. 9, 275–283. https://doi.org/10.1080/01431168808954851.

Yang, H., Cong, Z., Liu, Z., Lei, Z., 2010. Estimating sub-pixel temperatures using the triangle algorithm. Int. J. Remote Sens. 31, 6047–6060. https://doi.org/10.1080/01431160903376373.

Zhan, W., Chen, Y., Zhou, J., Li, J., Liu, W., 2011. Sharpening thermal imageries: a generalized theoretical framework from an assimilation perspective. IEEE Trans. Geosci. Remote Sens. 49, 773–789. https://doi.org/10.1109/TGRS.2010.2060342.

Zhang, R., Tian, J., Su, H., Sun, X., Chen, S., Xia, J., 2008. Two improvements of an operational two-layer model for terrestrial surface heat flux retrieval. Sensors 8, 6165–6187. https://doi.org/10.3390/s8106165.

Glossary

Symbols: signification and unit

$P_{\theta_{gv}}$: Soil moisture proxy
$\sigma^0_{vv,max}$: Backscatter coefficient correspond to the wettest pixel during the season
$\sigma^0_{vv,min}$: Backscatter coefficient correspond to the driest pixel during the season
$\sigma^0_{vv,gv}$: Green vegetation backscatter coefficient
$\sigma^0_{vv,bs,d}$: Bare dry soil backscatter coefficient
$\sigma^0_{vv,bs,w}$: Bare wet soil backscatter coefficient
$T_{fc,gv}$: The temperature of pixel with fully-covered vegetation
T^{lin}_{bs}: Temperature estimated using a linearized RTM
$T_{bs,w}$: Wet bare soil temperature
$T_{bs,d}$: Dry bare soil temperature
σ^0_{vv}: VV polarized backscatter coefficient
$\sigma^0_{vv,km}$: Aggregated VV polarized backscatter coefficient
ΔT_2: Corrective term
r_{ss}: Evaporation surface resistance, s m^{-1}
R_n: Net radiation, W m^{-2}
G: Soil heat flux, W m^{-2}
H: Sensible heat flux, W m^{-2}
LE: Latent heat flux, W m^{-2}
ua: Wind speed, m s^{-1}
r_g: Solar radiation, W m^{-2}
rh_a: Relative humidity, %
T_{air}: Air temperature, °C
ε: Surface emissivity
γ: Psychrometric constant, kPa °C^{-1}
ρ: Mean air density at constant pressure, kg m^{-3}
c_p: Stands for the specific heat of air, MJ kg^{-1} °C^{-1}
e_a: Actual vapour pressure, kPa
e_s: Saturation vapour pressure, kPa
$r_{a,h}$: Aerodynamic resistance, s m^{-1}
a: Surface albedo
R_{atm}: Atmospheric longwave radiation, W m^{-2}
σ: Stephan-Boltzmann constant equal to 5.67×10^{-8}, W m^{-2} K^{-4}
ε_a: Atmospheric emissivity
c_g: Fractional empirical coefficient set to 0.2
f_{gv}: Fraction of green vegetation cover
$f_{gv,km}$: Aggregated fraction of green vegetation cover
$NDVI_{gv}$: Full-cover green vegetation index
$NDVI_{bs}$: Bare soil vegetation index
$F (LST)$: Cost function